OPTIMISATION OF THE SYNTHESIS OF Mg-Al-CO_3 LAYERED DOUBLE HYDROXIDE AND THE PARTIAL SUBSTITUTION OF Mg/Ca-BASED LAYERED DOUBLE HYDROXIDES

UNIVERSITEIT VAN PRETORIA
UNIVERSITY OF PRETORIA
YUNIBESITHI YA PRETORIA

Hendrik P. Venter

OPTIMISATION OF THE SYNTHESIS OF Mg-Al-CO_3 LDH AND THE PARTIAL SUBSTITUTION OF Mg/Ca-BASED LDHS

Hendrik P. Venter

UNIVERSITEIT VAN PRETORIA
UNIVERSITY OF PRETORIA
YUNIBESITHI YA PRETORIA

Submitted in partial fulfilment of part of the requirements for the degree of Master of Engineering in the Faculty Engineering, the Built Environment and Information Technology, University of Pretoria, Pretoria

2014

OPTIMISATION OF THE SYNTHESIS OF Mg-Al-CO_3 LDH AND THE PARTIAL SUBSTITUTION OF Mg/Ca-BASED LDHS

by: Hendrik P. Venter

Supervisor: Dr. FJWJ Labuschagné

Department: Chemical Engineering

Degree: MEng (Chemical Engineering)

SYNOPSIS

A green synthesis method for the synthesis of hydrotalcite has been previously developed but this process has not yet been optimised. The main focus of this dissertation was on aluminium-based LDHs. The purpose of this investigation were; to determine optimum synthesis conditions for the formation of hydrotalcite using the dissolution-precipitation method and to determine the possibility of partial substituting the divalent metal species in hydrotalcite and hydrocalumite with other metal species.

During the optimisation process for the formation of hydrotalcite using the dissolution precipitation method, the formation of hydromagnesite was proved to be dominant reaction at lower reaction temperatures. With the increase in reaction time and temperature the

decomposition of hydromagnesite occurred to form magnesite. At low temperatures the formation of M*g-Al-CO_3* LDH is limited due to the low solubility of gibbsite. *Mg-Al-CO_3* LDH formation of 80 % was achieved at 140 ^{o}C after 2 hours reaction time, but crystallinity was low. To achieve an *Mg-Al-CO_3* LDH conversion higher than 96 % a reaction temperature of 160 ^{o}C for a minimum of 4 hours is required, but is achieved within 1 hour at 180 ^{o}C. A 99.37 % conversion was achieved at 180 ^{o}C for 5 hours with a high crystallinity and homogeneity. The surface area for *Mg-Al-CO_3* LDH at 180 ^{o}C after 5 hours reaction time proved to be 9.19 m^2/g. The average particle size obtained for a high crystalline LDH was in the range of approx. 3 µm and 6.8 µm at temperatures of 160 ^{o}C and above for a minimum of 3 hours reaction time. The following are recommended for future work:

- Determine the effect of mixing speed on the shape of the platelets.
- Determine the difference between freshly precipitated metal oxides/hydroxides as reagents compared to aged metal oxides/hydroxides.

The presence of *$Mg(OH)_2$* and *$Ca(OH)_2$* in solution (respectively) did increase the pH enough for the dissolution of gibbsite and most of the M^{x+} metal species. A reaction time and temperature of 5 hours at 180 ^{o}C in a carbonate environment proved to be close to the ideal conditions for the formation of *Mg/Mo-Al-CO_3* LDH and *Mg/Zn-Al-CO_3* LDH. The results for the formation of Mg/Ti-Al-CO_3 LDH were inconclusive. Isolation of the possible *Mg/Ti-Al-CO_3* LDH is recommended to determine the degree of substitution. The conditions for the dissolution of the metal species for the following experiments were proven to be successful:

- *Ca/Mn(IV)-Al*
- *Ca/Mo-Al*
- *Ca/Ni-Al*
- *Ca/Ti-Al*

The following recommendations are made for the improvement on the formation of an M^{x+}-impregnated LDH/precursor:

- Determine the effect of different reaction time and temperature.
- Determine the effect of adding the carbonate source at temperatures above 100 ^{o}C under pressure.

- Determine the effect of synthesising at different pH conditions.

Cobalt and tin showed no/negligible amount of possible solubility.

KEYWORDS: Layered double Hydroxides, co-precipitation, dissolution-precipitation, crystal phase, solubility.

Acknowledgement

The Author would like to thank:

- My Creator and Saviour for the talents and grace bestowed on me.
- Jonel for all her help, support, love and friendship.
- My family and friends for their moral support during the difficult times.
- My supervisor, Dr. FJWJ Labuschagné for all his time, help and knowledge.
- Mr. F. van der Westhuizen and Mrs. M. van Graan for their contribution to this research.
- All the helpful people at the Leibniz-Institut für Polymerforschung Dresden e.V. for all their help, time, inputs and financial support during the time spent in Germany: Prof. Dr. U. Wagenknecht and Dr. A. Leuteritz.
- Mr. B. Kutlu for all the XRD analysis done and the interpretation thereof during the period in Germany.
- Mrs. M. Auf der Landwehr for all the SEM-EDS analysis done and the interpretation thereof during the period in Germany.
- Mrs. W. Grote for all the XRD analysis done and the interpretation thereof at the University of Pretoria.
- Mrs. Jeanette Dykstra for all the XRF analysis done at the University of Pretoria.
- The NRF and Thrip for financial support.
- The people of the department of Chemical Engineering for their support.

Contents

List of Tables

List of Figures

Nomenclature

Symbol	Property	Unit
A	Specific anion in interlayer	[-]
a	Width of unit cell	Angstrom [Å]
c	Unit cell total thickness	Angstrom [Å]
c'	d-spacing	Angstrom [Å]
d	d-spacing	Angstrom [Å]
M	Total divalent- trivalent mole amount	[-]
M^{II}	Divalent metal mole amount	mole
M^{III}	Trivalent metal mole amount	mole
m	Crystal water in lattice	[-]
n	Anion formal charge	[-]
x	Divalent/Trivalent metal mole ratio	[-]
λ	XRD beam wavelength	Angstrom [Å]
θ	Beam angle	Degrees [^{o}]

Abbreviations

BET	Brunauer-Emmett and Teller
EDS	energy-dispersive X-ray spectroscopy
HMT	hexamethylenetetramine
HTC	hydrotalcite
HTlc	hydrotalcite-like compounds
ICP	inductively coupled plasma
LDH	layered double hydroxide
MHL	metal hydroxide layer
PVC	poly(vinyl chloride)
PSA	particle size analysis
SDBS	sodium dodecyl benzene sulphonate
SEM	scanning electron microscope
WAXS	wide angle X-ray scattering
XRD	X-ray diffraction

1. Introduction

The impact of polymers in industry is increasing daily and the demand to produce a stable polymer product using a more environmentally friendly way is becoming more important.

The *Environmental Impact Assessment Regulation 385-8(i)* states that the impact an activity has on the environment should be investigated and also states that measures should be taken to protect the environment from harm as a result of the activity (DEAT (2006)). This has a major impact on the industry due to the high cost involved upgrading current processes to comply with the law. Therefore, continuous research is being performed on the improvement and the development of new processes.

Additives are used with polymers to increase the mechanical properties of the polymer; increase the stability of the polymer under specific weathering conditions and also to introduce additional properties to the polymer such as electrical conductivity, colour additive, anti-bacterial/fungal and also hydrophilic/ hydrophobic properties.

A layered double hydroxide (LDH) is a lamellar type of anionic clay consisting of metal hydroxyl groups with an anionic group in the interlayer. The application of LDHs in the industry is increasing significantly (Das and Samal, 2004).

Hydrotalcite, a well-known LDH, is known for its use as an additive in polyvinyl chloride (PVC) as a heat stabiliser. It was first discovered in Sweden in 1842 (Rives, 2001:217), but only 90 years after the discovery did researchers reveal its true potential. The first synthesis was performed by Feitknecht in the mid 1930's and was soon followed by researchers like Miyata, Ross and Kodawa (Reichle, 1986). Intensive research has already revealed numerous applications for LDH as shown in Figure 1.

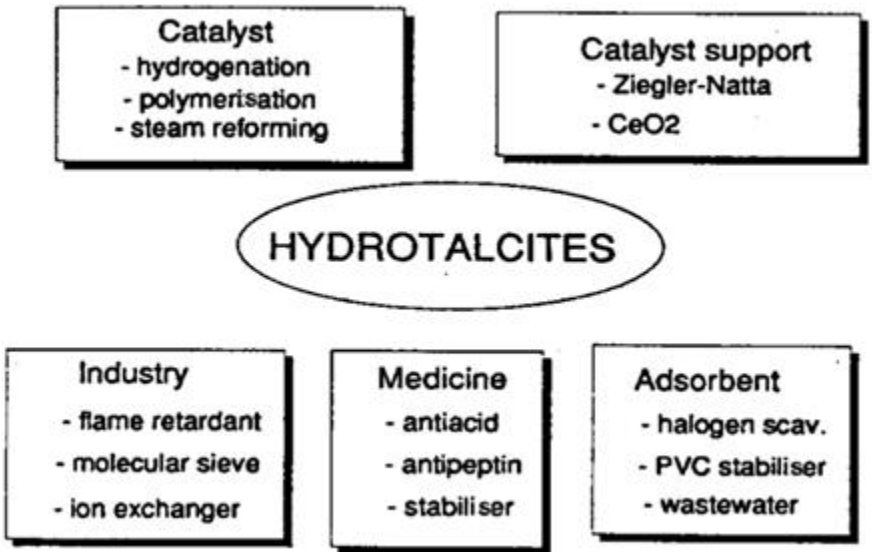

Figure 1: Possible applications for layered double hydroxides in the industry (Cavani, Trifiró and Vaccari, 1991).

The main focus of this dissertation will be on aluminium-based LDHs.

2. Literature

Feitknecht proposed that the *Mg-Al-CO_3* LDH consists out of two metal hydroxide of the same metal species which is then intercalated with a layer of the second metal hydroxide species from another species (Feitknecht and Fischer, 1935). Alleman *et al.* (1968) and Pastor-Rodriguez & Taylor (1971) proved through X-ray diffraction (XRD) analysis that the two cation species are localised in the same layer and that water and carbonate anions are situated in the interlayer. It was this discovery that initiated the intense research on the synthesis and possible application abilities for LDHs.

2.1 Layered double hydroxide structure

2.1.1. Pre-cursor

The general structure of the LDH, also referred to as mixed metal hydroxides, is derived from either the structure of the mineral brucite [*$Mg(OH)_2$*] layer or from gibbsite/bayerite [*$Al(OH)_3$*] layer, as shown in Figure 2.

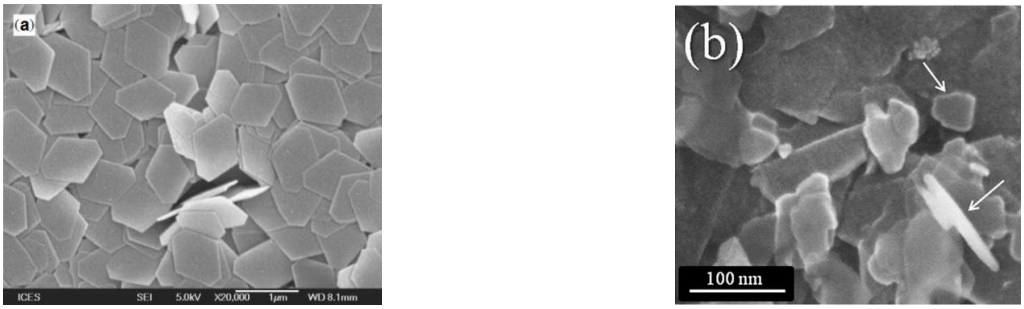

(a) (b)

Figure 2: Scanning electron microscope (SEM) images of brucite/gibbsite platelets respectively. (a) Gibbsite platelets (Shen et al, 2006). (b) Brucite platelets (Moreira et al, 2013).

The brucite structure consists of Mg^{2+} ions which are co-ordinated octahedrally by hydroxyl groups to form infinite sheets. The brucite structure is shown in Figure 3. The charge of the brucite platelets is neutral, but is stacked on top of each other and is held together by

hydrogen bonding (Cavani, Trifiró and Vaccari, 1991). The order of stacking of the brucite layers can be rombohedral (hydrotalcite-like) or hexagonal (manasseite-like). A more in depth description on the structure of LDHs regarding the crystal morphology is found in Section 2.2.

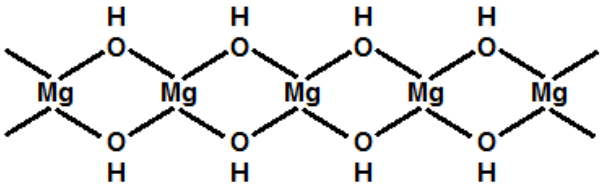

Figure 3: General structure of brucite [$Mg(OH)_2$] (adapted from Reichle, 1986).

2.1.2. Layered double hydroxide

When a fraction of the magnesium ions in the brucite structure are replaced by trivalent metal cations with an ionic radius similar to that of Mg^{2+}, a charge is created on the platelets, as shown in Figure 4.

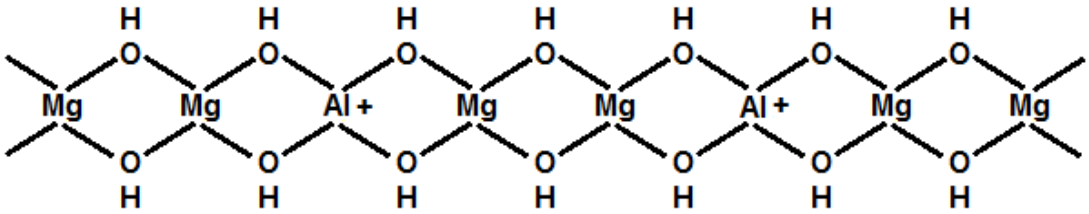

Figure 4: Brucite layer partially impregnated with aluminium [$(Mg_6Al_2(OH)_{16})^{+2}$] (adapted from Reichle, 1986).

The charge of these platelets are neutralised by placing an anionic group, in the interlayer such as a carbonate (CO_3^{2-}) group. Crystal water is also present in the interlayer. Figure 5 is a graphical representation of a neutralised LDH structure, hydrotalcite.

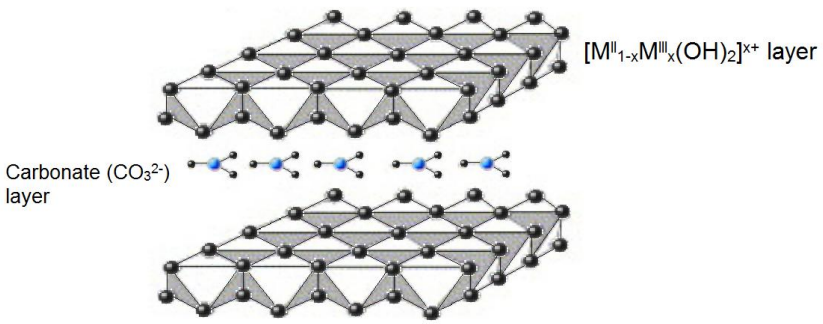

Figure 5: Idealised structure of hydrotalcite (adapted from Qi, Amphlett and Peppley, 2006).

The chemical formula for LDH is represented by Equation 1 and 2 (Del Arco *et al.*, 2004).

$$\left[M^{II}_{1-x}M^{III}_{x}(OH)_2\right]^{x+}\left[A_{x/n}\right]^{n-}\cdot mH_2O \qquad (1)$$

$$x = M^{III}/\sum M \qquad (2)$$

In Equation 1 and 2, x is the molar fraction of the M^{III} cation species, A is the specified anion within the interlayer, n is the formal charge of the anion and m indicates the crystal water within the interlayer. The molar fraction (x) may vary between 0.11 and 0.5, but the range to obtain a pure Hydrotalcite-like LDH is $0.2 \leq x \leq 0.33$ (Cavani *et al.,* 1991).

The layers of an LDH are formed due to the electrostatic forces from the interstitial anions, holding the covalently bonded metal hydroxide sheets together. The repeated units constituted by an octahedral layer and an interlayer can be arranged rhombohedrally or hexagonally, creating the crystal lattice of the LDH. The main characteristics of LDHs are determined by the nature of the brucite-like layers; the type and position of anions in the interlayer and by the type of stacking of these layers.

2.1.3. Chemical composition of LDH

2.1.3.1. Metal hydroxide layer (MHL)

Most research has been performed on Hydrotalcite (HTC) compared to other LDHs. The metal hydroxide layer (MHL) for HTC contains a mixture of an alkaline earth metal ion (Mg^{2+}) and a post-transition metal ion (Al^{3+}). According to the research performed by Miyata & Kumura (1973), it was found that the difference in ion radius between the divalent and trivalent ions must be as small as possible. The mole ratio of the divalent/trivalent metal ions plays an important role. If the value of x (Equation 2) is outside of the range specified, either pure metal hydroxides or other metal complexes with different structures than LDHs are

formed. For example, if the value of *x* is less than 0.33, the *Al*-octahedra will not be neighbouring, resultantly increasing the possibility of forming an LDH. As the value of *x* increases, the possibility of forming $Al(OH)_3$ increases, and the same holds for the formation of $Mg(OH)_2$ if the value of *x* becomes too small. Yamaguchi *et al.* (1987) indicated that a magnesium aluminium double hydroxide species forms in the presence of limited aluminium. This compound does have a structure similar to brucite but is not an LDH. Figure 6 illustrates this ruling for the formation of homogenous hydrotalcite. The layer thickness of the LDH is depended on the amount of partial substitution of the divalent metal species.

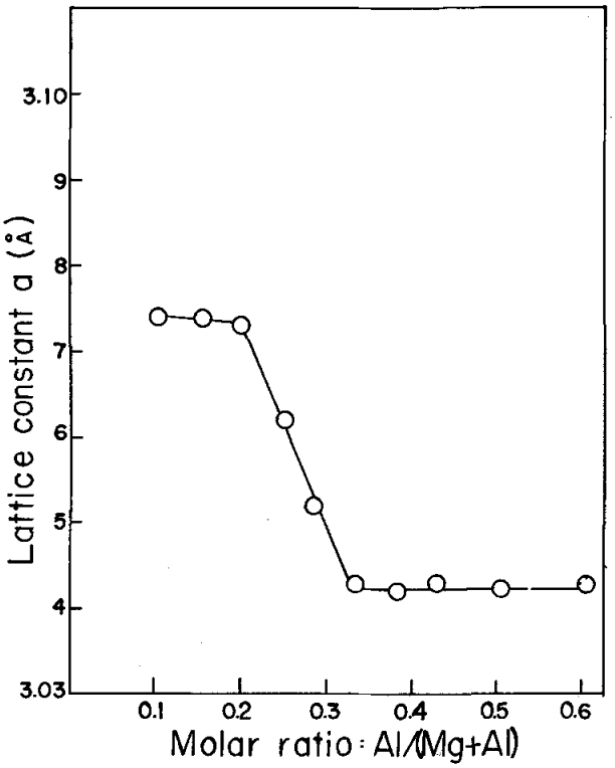

Figure 6: The thickness of the brucite-like layer as a function of the aluminium ion (Adapted from Miyata, 1980).

It is also proven that transition metal ions (Britto and Kamath, 2009) as well as alkali metal ions (French *et al.,* 2010) can be used to form an LDH. Most of the possible ion species that is known to form an LDH are listed in Table 1 (Forano, 2006 and Sposito, 2008:31). The LDHs formed from these elements are called Hydrotalcite-like compounds (HTlc).

Table 1: Ionic radii for some metal cation species (adapted from Forano, 2006 and Sposito, 2008:31).

Metal Species	Valence	Ionic Radius (nm)	Metal Species	Valence	Ionic Radius (nm)
Li	1	0.076	*Co*	2	0.075
Mg	2	0.072		3	0.061
Al	3	0.054	*Ni*	2	0.069
Ca	2	0.112	*Cu*	2	0.057
Ti	4	0.061	*Zn*	2	0.074
Cr	3	0.062	*Sr*	2	0.118
	6	0.026	*Mo*	6	0.041
Mn	2	0.083	*Ag*	1	0.115
	3	0.065	*Cd*	2	0.095
	4	0.053			
Fe	2	0.078			
	3	0.065			

As is seen in Table 1, there is a possibility to combine metal cations with a large difference in ionic radii. The synthesis of Ca-Al-LDH where an ionic radius difference for covalent bonding of approximately 0.058 nm is observed (James & Lord, 1992) compared to that of *Mg-Al* LDH of only 0.018 nm. Nayak *et al.* (1997) reported the formation of *Li-Al* LDH which is a special case for a monovalent cation LDH with an ionic radius difference of 0.022 nm. According to Forano (2006), there are no limits to the combinations of metal cations. Binary, ternary and even quaternary cations can be used. Nayak *et al.* (1997) reported of a *Li-Al* LDH which is a special case for a monovalent cation LDH.

The main focus of this dissertation will be on aluminium-based LDH.

2.1.3.2. Interlayer

The parameters that influence the thickness of the interlayer are the number, size, orientation and strength of the bonds between the interstitial anion and the hydroxyl group of the brucite-like layer. The anion in the interlayer does not affect the thickness of the metal hydroxyl layer. The interspatial layer can be modified by replacing the interstitial anion with organic or inorganic anions. The interspatial layer modification is performed to give the LDH specific properties for specified applications. LDH is a hydrophilic structure which has a difficulty compounding into non-polar polymeric matrices. Organic anions like the surfactant sodium dodecyl sulphate (SDS), are intercalated to overcome this problem. The long C_{12} tail of the SDS molecule aids bonding with the polymer whereas the anionic end of the surfactant reacts with the charge of the LDH (Crepaldi *et al.*, 2002). There is no definite limit to the type of anionic species that could be used. According to Chitrakar *et al.* (2005) and Miyata (1983), the order of preference of the anionic groups in the interlayer is as follows:

Monovalent anions: $OH^- > F^- > Cl^- > Br^- > NO_3^- > I^-$

Divalent anions: $CO_3^{2-} > SO_4^{2-} > HPO_4^{2-}$

and divalent anionic species are preferred in the interlayer above monovalent anions (Moyer & Singh, 2004). A significant change in the interlayer is observed when organic anions are situated within the interlayer. The thickness of the interlayer increases linearly with the number of carbon atoms for a saturated, single chained organic group, as show in Figure 7.

The interlayer for the carbonate anions is smaller than the diameter of the CO_3^{2-} molecule (comparable with that found with monovalent ions) due to the strong hydrogen bonds between the metal hydroxyl layers and the anion. The shape of the carbonate anion is also planar, resulting in easy fitting between the layers. The opposite is noted for NO_3^- anions where a bigger distance is noted compared to what is expected. This phenomenon is due to the fact that more monovalent anions are required to compensate for the charge which forces

the NO_3^- anions to arrange to favour the closest packing. This causes significant repulsion inside the layers with the increase in concentration of NO_3^-. (Cavani *et al.*, 1991)

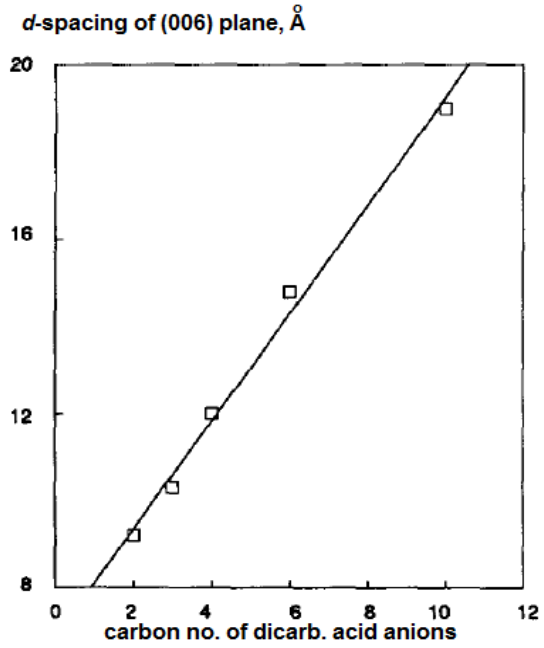

Figure 7: The relationship between the carbon number of the anion species in the interlayer and the d-spacing (Adapted from Cavani et al, 1991)

The position of the anions and crystal water is random within the interlayer and has the possibility to relocate within the interlayer by breaking bonds and forming new ones, similar to liquid water (Cavani *et al.*, 1991).

2.2. Crystal morphology

2.2.1. X-ray Diffraction (XRD)

Hull (1919) reported that when a crystalline structure is exposed to X-rays, a series of unique patterns is obtained by analysing the reflecting rays. He also discovered that even in a mixture containing different substances which have crystalline structures, each substance reflects a unique pattern of its own. Therefore, it is evident that a specific crystalline

substance in a mixture could be identified by its unique fingerprint pattern using X-ray diffraction.

The reflected beam from the sample is picked up by the detector and the intensity of the beam reflected is stored. When a second beam is reflected from the sample (which is in phase with the first beam) the total intensity will be increased (Waseda, Matsubara and Shinoda, 2011:74). An example of an XRD result for a typical LDH is shown in Figure 8 and the results are based on *Cu*- K_α values.

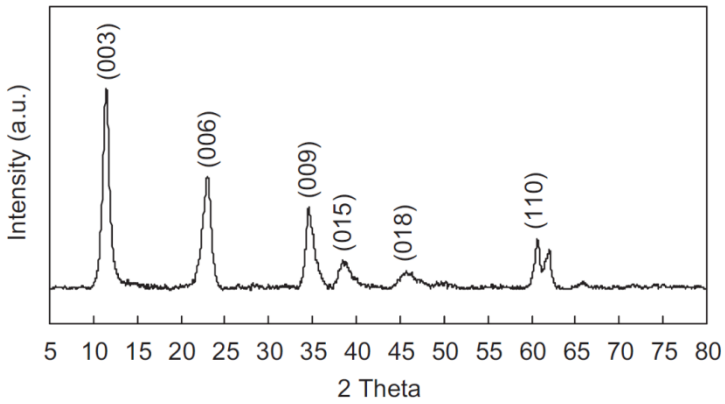

Figure 8: Typical characteristic XRD result of an LDH (*Cu*- K_α). (Goh, Lim and Dong, 2008).

For this research *Co*- K_α values are used. For the conversion between the *Cu* and *Co* values, refer to Section 2.2.2.

When a peak is shown on the results, it indicates that a crystal structure is present. As the amount of reflected beams (which is in phase with each other) increases, the intensity of the peak will increase; the distribution width of each peak will decrease and will therefore show an increase in crystallinity of that sample. The pattern for each substance consists of several individual peaks. (Waseda, Matsubara and Shinoda, 2011:73-74)

XRD analysis can also be used to identify layers and also to determine whether a layered structure had been formed during an LDH synthesis. An important note is that this method only works for crystalline products. This method may furthermore be used for to calculate the

approximate perpendicular distance between each layer (known as the d-spacing) of the LDH by using Bragg's law, as shown in Equation 3. (Waseda, Matsubara and Shinoda, 2011:74)

Bragg's law: $2d_{[003]}sin\theta=n\lambda$ (3)

where n is the order of reflection; λ is the wavelength used during analysis; θ is the position of the reflected laser beam and d the basal spacing (the thickness of one complete layer).

Rietveld refinement is a kind of state analysis of which the positions, thermal displacements and occupancies of atomic sites in crystalline materials are quantitatively determined. The precise determination on the composition and ratio in mixtures is possible using this analysis. (Gohshi and Saisho, 1996:407-408)

Quantative analysis with regards to the composition of the sample based on crystalline compounds is done by the Rietveld refinement analysis using the peak height, peak width and the position of the peaks on a XRD pattern. (Rietveld, 1968)

2.2.2 Layered double hydroxide crystal structure (Cavani *et al.*, 1991)

The stacking of the brucite-like layers has two possible stacking orders: rombohedral or hexagonal. It is known that hydrotalcite-like LDHs crystallise in the rombohedral 3R symmetry (having three sheets in the unit cell) with the parameters of the cell being a and c, as shown in Figure 9.

Hydrotalcite-like LDHs are mainly known to be rhombohedral in nature; with the hexagonal polytype being the high temperature synthesis form of the rhombohedral shape. The parameter a refers to the width of one side of the unit crystal and $c=3c'$ refers to the total thickness of the unit cell. The $c' = d_{[003]}$ parameter refers to the thickness of one layer which consists of a brucite-like sheet and one interlayer. For pure hydrotalcite (*Mg*:*Al* ratio of 3:1), the a parameter is 3.05 Å and $d_{[003]}$ is 7.63 Å.

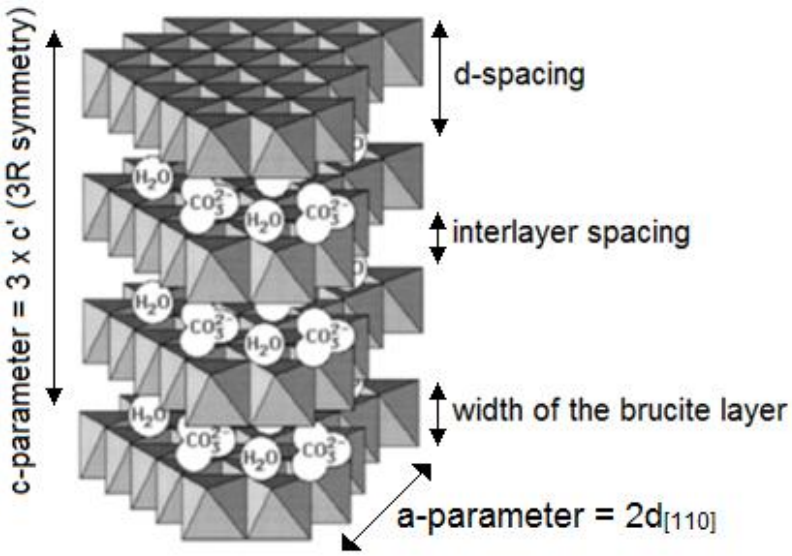

Figure 9: The structure of hydrotalcite-like LDHs with defined cell parameters (Rives and Ulibarri, 1999).

Looking at Figure 8, the first peak located on the left refers to the basal spacing (d_{003}) which indicates the stacking of the platelets.

To be able to compare XRD results when a cobalt beam was used instead of copper, Equation 4 is used:

2θ conversion: $$\theta_X = sin^{-1}\left(\frac{\lambda_X Sin\theta_Y}{\lambda_Y}\right) \quad (4)$$

where λ_x and λ_Y are the wavelengths of the desired beam (1.78901 Å for *Co*) and the used beam (1.5418 Å for *Cu*) respectively.

The reflections in Figure 8 (d_{006} and d_{009}) are the repetitive peaks corresponding to the d_{003} basal reflection peak. The counts for each repetitive peak and the narrowing at the base indicate the crystallinity of the LDH. The two peaks grouped together on the right side of Figure 8 correspond to the d_{110} reflection (Rives, 2001). The corresponding *2θ*-values for both *Cu*-K_α and *Co*-K_α are shown in Table 2.

Table 2: Calculated *Co*-K_α 2θ-values corresponding to *Cu*-K_α values.

Basal spacing	*Cu*-K_α Value (^{o})	*Co*-K_α Value (^{o})
d_{003}	11.0^o	13.5^o
d_{006}	23.0^o	28.0^o
d_{009}	35.0^o	41.0^o
d_{110}	60, 65^o	70^o, 75^o

If only a single peak is noted within this range, a well-formed hexagonal shaped unit cell is formed. However, it is known that in some cases double peaks are reported, indicating distorted hexagonal crystal platelets. These peaks are used to calculate the *a* parameter of the unit cell structure in angstrom (Å) using the following correlation in Equation 5:

$$a=2d_{110} \quad (5)$$

The crystallographic parameters for hydrotalcite and hydrocalumite are shown in Table 3:

Table 3: Crystallographic parameters for hydrotalcite and hydrocalumite.

Parameters	Hydrotalcite (Rhombohedral)	Hydrocalumite (Rhombohedral)
Reference source	Cavani *et al.* (1991)	Buttler, Glasser & Taylor (1959)
Spacial Group	3R	3R
a (Å)	3.05	3.32
c (Å)	22.81	23.76
$d_{[003]}$ (Å)	7.603	7.92

2.2.3 Crystal Shapes

The morphology of crystals plays a very important role in mechanical (Bao *et al.*, 2008), sorption (Dudek *et al.*, 2012), as well as properties in polymers. It also describes whether the conditions during synthesis crystallisation were ideal or not. There are three main crystal habits which are listed below and are illustrated in Figure 10:

- Euhedral crystals
- Subhedral crystals
- Anhedral crystals

Euhedral crystals are defined as crystals that display perfect polyhedral surfaces with regular and characteristic interfacial angles. These crystals experienced sufficient room to grow. Anhedral crystals are the opposite of euhedral crystals, a geometric solid with irregular surfaces. Crystals that are partially recognised are called subhedral crystals. The growth of these crystals was limited due to space. (Wenk and Bulakh, 2004: 85, 265)

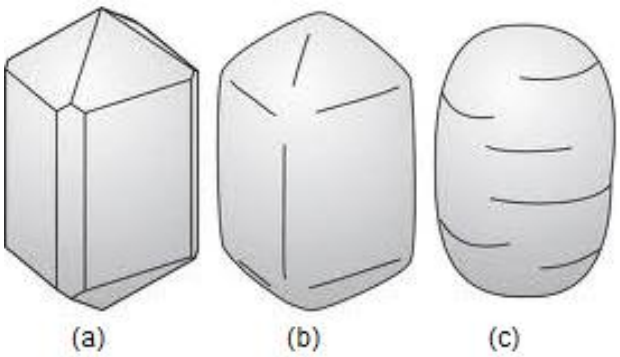

Figure 10: The three main crystal habits. (a) Euhedral. (b) Subhedral. (c) Anhedral. (Schott, 2009)

Well-formed hydrotalcite has euhedral hexagonal platelets (Grim and Güven, 1978:256). During the synthesis of layered double hydroxides, different crystal morphologies can be expected by changing the conditions such as pH, temperature and the rate at which the reaction takes place. Three different crystal structures for hydrotalcite are shown in Figure 11; the doughnut crystals, rose crystals and the normal hexagonal platelets.

Zhao, Xiao and Jiao (2011) showed through the synthesis of *Ni-Al*-LDH that it is possible to form rod-like crystals which have the same XRD patterns as normal LDH, as shown in Figure 12.

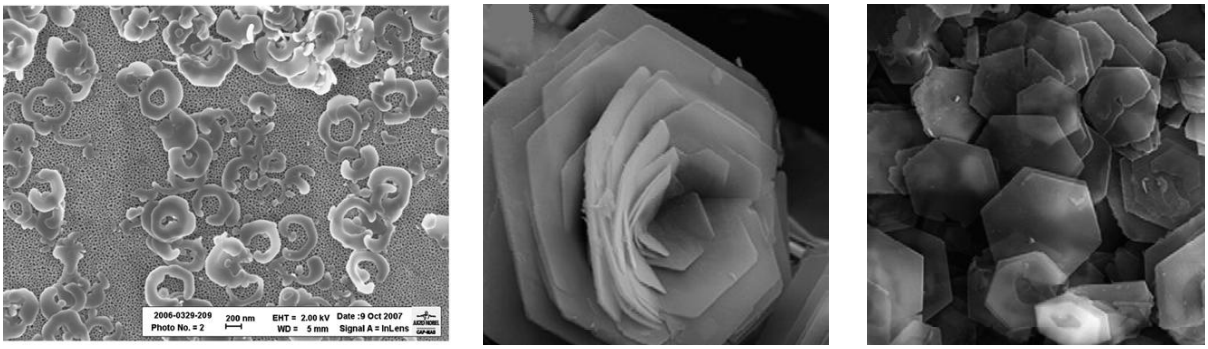

(a) (b) (c)

Figure 11: Different crystal morphologies for layered double hydroxide – hydrotalcite. (a) Doughnut shape (Budhysutanto *et al.*, 2011). (b) Rose formation (Okamoto *et al.*, 2007). (c) Hexagonal platelets (Okamoto *et al.*, 2007).

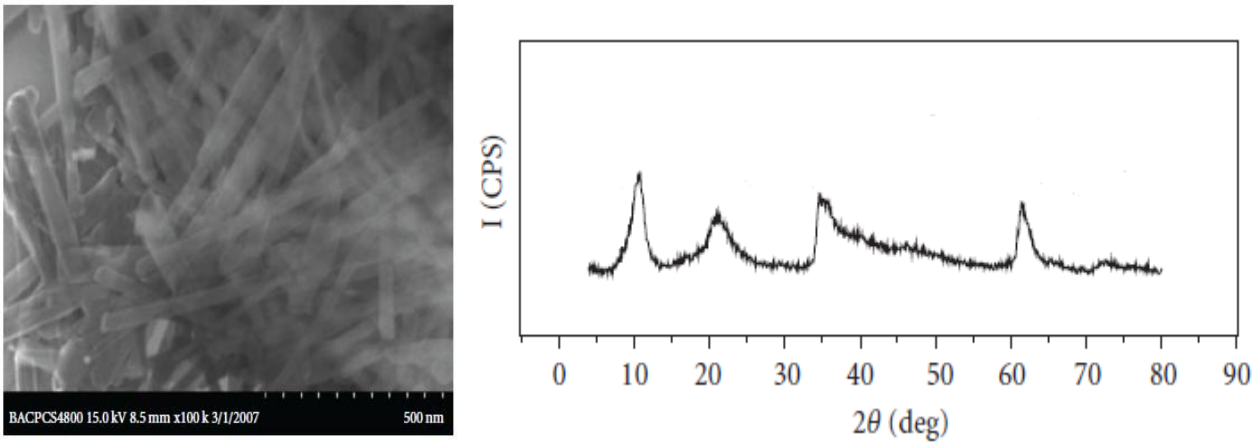

(a) (b)

Figure 12: (a) SEM image and (b) XRD powder pattern for Ni-Al-LDH (adapted from Zhao, Xiao and Jiao, 2011).

One phenomenon that often occurs during the crystal growth of platelets (as well as other crystal shapes) is called crystal twinning. This occurs when two or more separate crystals started to form from the same nucleation point and share some of the same crystal lattices. This induces the intergrowth of two separate crystals which arranges itself into specific crystal configurations, as shown in Figure 13:

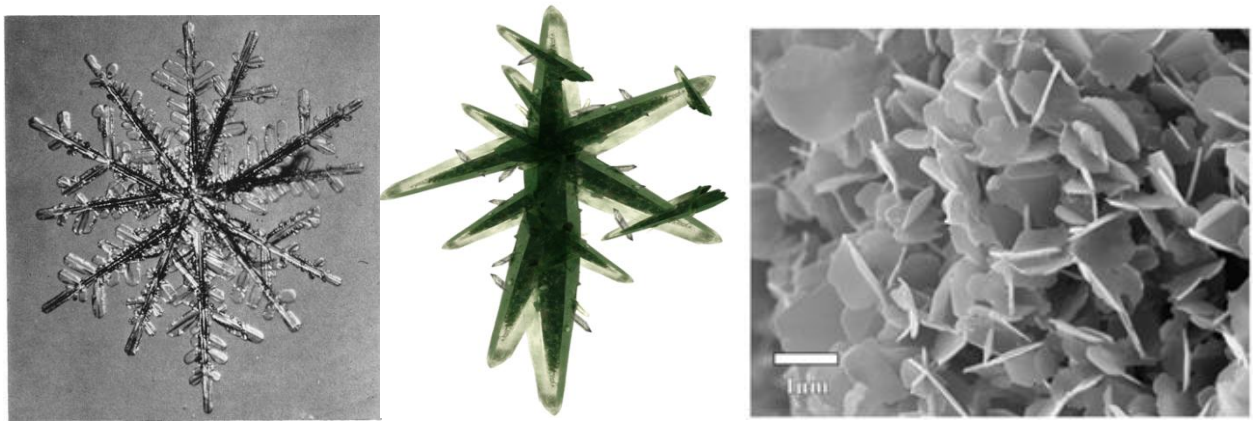

(a) (b) (c)

Figure 13: Crystal twinning. (a) Snow flake formation due to contact twinning (Kobayashi and Furukawa, 1975). (b) Penetration crystal twinning. (c) cyclic twinning of pure Mg^{2+}/Fe^{3+} LDH (Schütz et al, 2011)

Contact twinning occurs when two crystals share a single composition surface and appears to be mirror images of each other. The phenomenon when two individual crystals seem to grow through each other in a symmetrical manner is called penetration twinning. Cyclic twinning is almost the same as penetration twinning, with the exception that the alignment of the crystals is irregular.

2.3. Synthesis Methods

The first synthesis of hydrotalcite was performed by Feitknecht and Fischer (1935) using a method which is referred to as the co-precipitation method today.

Interest in the different synthesis methods and the parameters that affects the formation of LDHs has become more and more popular. The major factors which influence the formation of LDHs are listed below (Othman, 2009):

- pH
- Temperature
- Reaction time
- Aging period

- Nature of the metal ions used
- The ratio between the metal ions
- The nature of the anion to be found in the interlayer

All of these factors play part in what type of LDH will be formed. As an example, Forano (2006) reported that the pH during co-precipitation has a significant effect on the chemical, structural and textural properties of the phases. For instance, if the divalent-trivalent metal ratios change, the total surface area per unit mass could increase/decrease and the crystal size could be influenced. It all depends on the conditions under which the synthesis is performed.

Table 4 shows a small portion of the aluminium-based LDHs found in literature with its method of synthesis. There are a variety of LDHs that have been synthesised for different applications. When looking at Table 4, it is noted that most of the experiments were performed using the co-precipitation method. Only *Mg-Al*-LDH and *Ca-Al*-LDH were synthesised previously using the dissolution precipitation method. No other literature could be found on the synthesis of the rest of the metal species using this method. The two reagents; *MgO* and *CaO*, when dissociated in water, increase the pH above 10 which is known to be required for the synthesis of an LDH.

Extensive research has been performed on *Mg-Al*-LDHs through a variety of synthesis techniques and it has been proven that a very stable and highly crystalline LDH could be formed. This specific LDH has become the primary backbone for a large variety of LDHs in the catalyst industry by partial substitution of the *Mg*-ions with other metal species (Othman, 2009).

Table 4: Previous synthesised *Al*-based LDHs and its methods.

Metal Species	Products synthesized	Synthesis method	Reference
Ca	*Ca-Al-NO_3* *Ca-Al-CO_3* *Ca-Mg-Al-NO_3*	Sol-gel Dissolution precipitation Co-precipitation	Yu, Bian and Plank (2010) Van der Westhuizen (2011) Zhou *et al.* (2011)
Co	*Mg-Co-Al-NO_3* *Co-Al-SO_4*	Co-precipitation Co-precipitation	Tanasoi *et al.* (2011) Magagula, Nhlapo and Focke (2009)
Cu	*Mg-Cu-Al-NO_3*	Co-precipitation	Tanasoi *et al.* (2011)
Mg	*Mg-Al-NO_3* *Mg-Al-NO_3* *Mg-Al-CO_3*	Urea Co-precipitation Dissolution precipitation	Okamoto, Lyi and Sasaki (2007) Miyata (1975) Martin *et al.* (1999)
Mn	*Mg-Mn-Al-NO_3* *Mn_2-Al-SO_4* *Mg-Mn-Cl*	Co-precipitation Co-precipitation Co-precipitation	Tanasoi *et al.* (2011) Magagula, Nhlapo and Focke (2009) Chitrakar *et al.* (2005)
Mo	*Mg-Mo-Al-Fe-NO_3*	Urea	Zhao *et al.* (2011)
Ni	*Mg-Ni-Al-NO_3*	Co-precipitation	Tanasoi *et al.* (2011)
Sn	*Mg-Sn-Al-NO_3*	Co-precipitation	Velu *et al.* (1999)
Ti	*Mg-Ti-Al-NO_3* *Zn-Ti-Al-Cl*	Co-precipitation Co-precipitation	Das and Samal (2004) Saber and Tagaya (2008)
Zn	*Mg-Zn-Al-Fe-NO_3* *Zn-Al-Cl* *Zn-Ti-NO_3* *Mg-Zn-Al-NO_3*	Co-precipitation Co-precipitation Co-precipitation Urea	Tanasoi *et al.* (2011) Oliva *et al.* (2012) You, Vance and Zhao (2001) Saber and Tagaya (2008)

Yu, Bian & Plank (2010) showed that the *Ca-Al-NO_3* LDH can be synthesised using the co-precipitation method and also proved to be very stable. Zhou *et al.* (2011) demonstrated that partial substitution of the Mg with Ca is also achievable.

Van der Westhuizen (2011) did extensive research on the synthesis of *Ca-Al-CO_3* LDH (hydrocalumite) using a process similar to the dissolution-precipitation which was done by Labuschagne *et al* (2006). The experiments were performed to determine the solid concentration at which the synthesis is proposed to be carried out, the temperature required as well as the preferred sequence in which the synthesis must be done. A mixture of *CaO* and *$Al(OH)_3$* was first allowed to react for two days before the slurry was exposed to a carbonate source.

It was proven that the presence of a carbonate source during the synthesis process caused the formation of *$CaCO_3$* which seems to be more thermodynamically stable than that of LDH, therefore, preventing the formation of the synthetic clay.

An intermediate product, Katoite [*$Ca_3Al_2((OH)_4)_3$*], was synthesised in an inert atmosphere (*N_2*) at 80 ^{o}C by stirring the 30 wt% slurry for two days before sodium bicarbonate is added for the formation of the LDH. Boclair and Braterman (1999) stated through the co-precipitation method that there is the possibility for the formation of a precursor product before the formation of an LDH. Figure 14 shows the intermediate product as well as the hydrocalumite which were synthesised by Van der Westhuizen (2011).

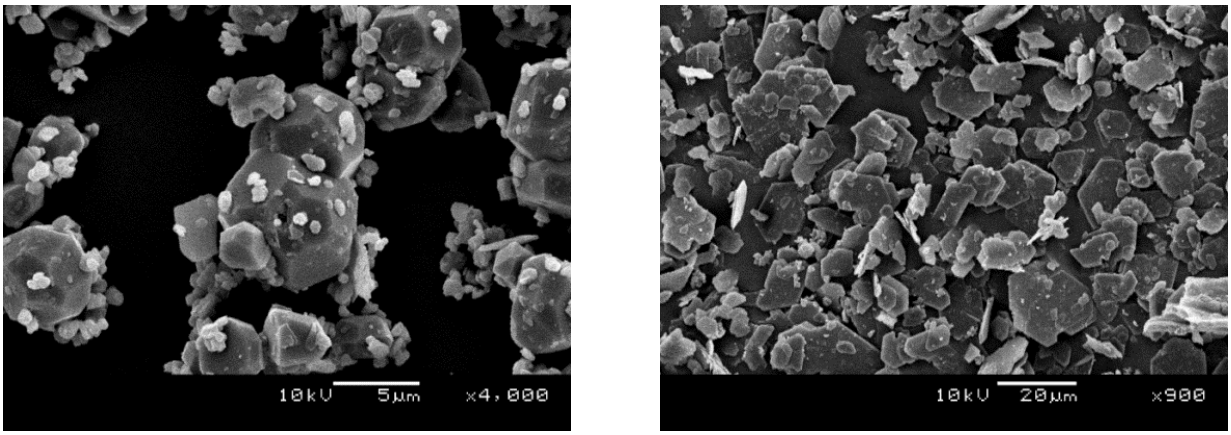

(a) (b)

Figure 14: The formation of hydrocalumite by first synthesizing an intermediate product. (a) Katoite. (b) Hydrocalumite. (Van der Westhuizen, 2011)

Van Graan (2012) confirmed that a 2-step process is required for the formation of hydrocalumite if the dissolution-precipitation process is preferred. The synthesis of hydrocalumite was optimised in order to form hydrocalumite in a reasonable time.

The effect of increasing temperature was investigated and it was found that it is possible to synthesise katoite in a 20 wt% solid concentration and at 180 ^{o}C for 6 hours in an inert atmosphere using a pressure vessel. After the katoite had formed, the slurry was exposed to a carbonate source (sodium bicarbonate) and within 30 min hydrocalumite was formed. Figure 15 shows the katoite and hydrocalumite that had formed under high pressure and temperature.

The well-formed layered structure can be seen in Figure 15. This process generates high yield, well crystalline hydrocalumite. Van Graan (2012) proposed the following two-step hydrothermal synthesis mechanism for the formation of hydrocalumite which is similar to the mechanism proposed by Martin *et al*. (1996):

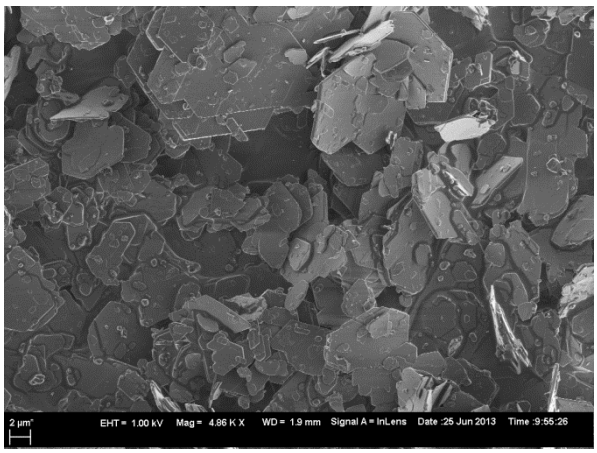

(a)

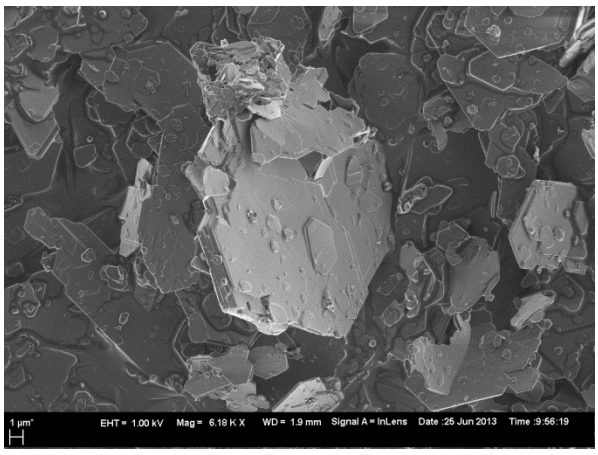

(b)

Figure 15: The formation of hydrocalumite [(a) and (b)] from katoite at 180 oC after 6 hours.

The first step (Equation 6) is the dissolution of $Al(OH)_3$ and $Ca(OH)_2$ followed by the precipitation of the precursor material.

$$3Ca(OH)_2+2Al(OH)_3 \rightarrow Ca_3Al_2(OH)_{12} \quad (6)$$

The second step (Equation 7) involves the dissolution of the precursor in the presence of a carbonate source and therefore consequently the precipitation of hydrocalumite.

$$Ca_3Al_2(OH)_{12}+Ca(OH)_2+NaHCO_3+4H_2O\rightarrow Ca_4Al_2(OH)_{12}CO_3\cdot 5H_2O+NaOH \quad (7)$$

The following main findings obtained from Van der Westhuizen (2011) as well as from Van Graan (2012) are listed below which serves to great interest to the current study:

- A temperature of approx.1 80 ^{o}C and 6 hours reaction time is required for the complete dissolution of $Al(OH)_3$ and the precipitation of hydrocalumite.
- The presence of a carbonate source during the in situ synthesis of $Ca\text{-}Al\text{-}CO_3$ LDH caused the formation of $CaCO_3$, therefore, preventing the formation of hydrocalumite.
- The formation of a precursor mixed metal hydroxide (katoite) in an inert atmosphere results in a high yield hydrocalumite conversion after the precursor is exposed to a carbonate source in solution.

2.3.1 Co-precipitation

2.3.1.1. Standard co-precipitation

Metal salt solutions are used as starting reagents for this synthesis method. The general reaction equation for a mixed divalent/trivalent LDH synthesis is shown in Equation 8 (Forano, 2006).

$$(1\text{-}x)M^{II}A^{n-}_{2/n}+xM^{III}A^{n-}_{3/n}+2NaOH+mH_2O\rightarrow M^{II}_{1-x}M^{III}_{x}(OH)_2A^{n-}_{x/n}\cdot mH_2O+2NaA^{n-}_{1/n} \quad (8)$$

The standard co-precipitation process is performed by the following method (Miyata 1975, Othman *et al.,* 2009):

Aqueous solutions of the metal salts used to synthesise the desired LDH (like magnesium and aluminium salts for producing hydrotalcite) are slowly added together in a specific ratio

while stirring vigorously, keeping the temperature constant (preferably above 40 °C). Zang *et al.* (2008) and Clause *et al.* (1991) reported that doing co-precipitation at too high supersaturating conditions results in a product with low crystallinity, due to the large amount of nuclei sites.

According to Forano (2006) it is recommended to do co-precipitation at constant pH in order to obtain high chemical homogeneity. Othman (2009) reported that when synthesising at too low pH values, certain metal ions may not precipitate and to the contrary, for synthesising at too high pH values. This is shown in Figure 16 where Boclair & Braterman (1999) determined the titration curves for *Mg-Al*-LDH and *Co-Al*-LDH.

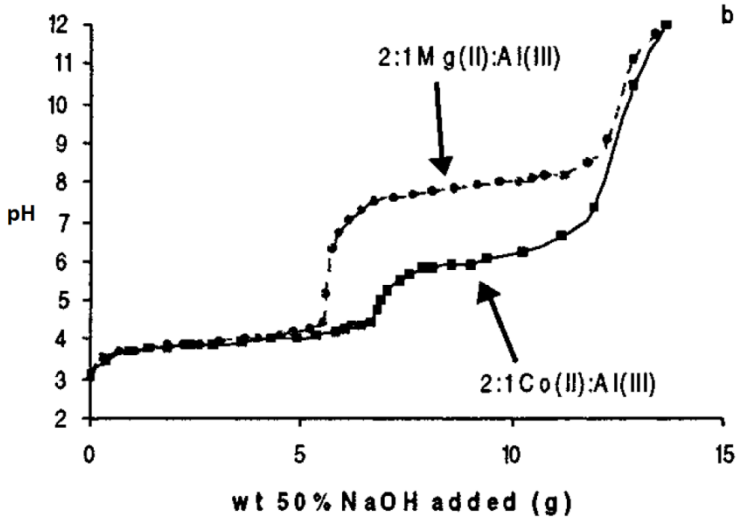

Figure 16: Titration curves of ratio 2:1 $MgCl_2$-$AlCl_3$ and 2:1 $CoCl_2$-$AlCl_3$ solutions (Boclair & Braterman, 1999)

From Figure 16, it is observed that most of the precipitate is formed at a pH of approximately 12, for both Mg-Al-LDH and Co-Al-LDH. It depends on the types of cations that are used and at what pH value the precipitation curve is horizontal. Sodium hydroxide (*NaOH*) is normally used to control the pH above 10 (for hydrotalcite) and is added drop-wise to the solution.

After the precipitate is formed, the mixture is stirred for a while at constant temperature before aging. The aging process (which in this case may be referred to as the hydrothermal treatment process) is necessary when using the co-precipitation method. This final step of the

synthesis uses the Ostwald ripening effect to increase the crystallinity and homogeneity of the product by dissolving the small crystals in the mixture and to re-precipitate onto larger crystals (Auerbach, Carrado & Dutta*, 2004: 418*). It is normally performed at temperatures above 110 °C for approximately 24 hours. The product is then washed until the pH is close to 7 to get rid of unwanted *NaOH* and other salts, filtered and dried for application.

The advantages of this process are the following:

- High crystallinity of product (after aging)
- Small particle size (before aging)
- High specific area (before aging)
- High average pore diameter (before aging)

The main disadvantages of this method are the high production of salt effluent (Othman, 2009) and the compensation between crystallinity and particle size/high specific area/ average pore diameter.

2.3.1.2. Urea method

The Urea method was first performed by Umberto Costantino and his co-workers (1998). This method is very close to the normal co-precipitation with only one major difference. Urea is used instead of a strong inorganic chemical base like *NaOH*. The advantage urea has over *NaOH* is that the urea hydrolysis process is slow, which prohibits a high degree of super saturation to occur during precipitation. The hydrolysis reaction of urea can lead to a carbonate source in an acidic medium or in a basic medium when heated, as illustrated in Equation 9 to 11 (Rao *et al.*, 2005).

$$H_2N\text{-}CO\text{-}NH_2 \rightarrow NH^{4+} + NCO^{-} \quad (9)$$

Basic: $$NCO^{-} + 2H_2O \rightarrow NH^{4+}CO_3^{2-} \quad (10)$$

Acidic: $$NCO^{-} + 2H^{+} + 2H_2O \rightarrow NH^{4+} + H_2CO_3 \quad (11)$$

Ogawa and Kaiho (2002) reported that by controlling the reaction temperature and concentration of the reactants, the range of the particle size can be reduced, compared to the wide particle distribution obtained by co-precipitation. Another advantage using this method is that the washing process is much faster. Due to the absence of inert metal cations like Na^+ and *Na*-based salts, the washing can be performed in one step instead of repeated washing which must be performed with co-precipitation (Othman, 2009).

Inayat, Klumpp and Schwieger (2011) reported that one major disadvantage for using this method is the production of CO_3^{2-}-only LDHs. The reason for this is due to the high affinity of the LDH to a carbonate source.

2.3.1.3. Sol-Gel method (Jitianu *et al.*, 2000 and Prince *et al.*, 2009)

The Sol-Gel method is a well-known method that is used for producing LDHs which must comply with certain criteria for applications in the medical field such as an alternative drug-delivery system (Lee & Cheng, 2006). Valente *et al.* (2007) showed that control over the structural and textural properties of the LDH is possible to provide a product which has a certain specific area, pore size distribution and good purity.

A metal alkoxide (Magnesium methoxide) is dissolved in ethanol which contains a low concentration of *HCl* (HNO_3 can also be used). The acid acts as a hydrolysis catalyst. The solution is then cooled to 0 °C before adding acetone which contains the metal-acetonate (aluminium acetylacetonate) while stirring. The pH is adjusted using a base (*NaOH* or NH_3 solution can be used) in order to form an LDH. The solution is then allowed to naturally reach room temperature while stirring. During this step, alkoxide (RO^-) exchange takes place between the metal alkoxide and alcohol which then forms a gel, containing the LDH (Valente, 2007). An important note is that the LDH contains a charge when it is suspended in the gel. After stirring for 18 hours, the gel is isolated by filtering and washed for purification of the LDH. The washed product can then be introduced to the desired interstitial anion solution for possible intercalation. The product is then filtered and washed again before drying.

There is a variety of organic compounds which could be used for this synthesis, but the two most common organic compounds used are metal alkoxides and acetonates. Jitianu *et al.* (2000) proved that using a metal-isopropylate as precursor instead of an acetonate-compound also leads to the formation of LDH.

2.3.2 Dissolution precipitation method

The dissolution precipitation method, also referred to as the two powder synthesis method, is a method where metal oxides/hydroxides are used as reagents for the synthesis of LDH. Martin *et al.* (1996) came up with a purposed method for the synthesis of hydrotalcite using the method in Equations 12 – 13.

Step 1:

$$(1\text{-}x)MgO + x/2\,Al_2O_3 + (1 + x/2 + w)H_2O \rightarrow [Mg_{(1-x)}Al_x(OH)_2](OH)_x \cdot wH_2O \quad (12)$$

Step 2:

$$2\left[Mg_{(1-x)}Al_x(OH)_2\right](OH)_x \cdot wH_2O + x/2\,CO_2 \rightarrow 2\left[Mg_{(1-x)}Al_x(OH)_2\right]\left(CO_3^{2-}\right)_{x/2} \cdot wH_2O + H_2O \quad (13)$$

A purposed general reaction mechanism was given by Martin *et al.* (1996) from the above mentioned reaction steps for the synthesis of an LDH and is shown in Equations 14 and 15.

$$M_aO_b + Al_2O_3 \cdot gH_2O \rightarrow MX \quad (14)$$

$$MX + HA \rightarrow LDH + H_2O \quad (15)$$

where *MX* is referred to the mixed metal hydroxyl layered compound and *HA* is the anion source. As can be noted from the reactions shown above, the major drawback of this synthesis is the limitation caused by the solubility of the metal oxides. Dyer Scrivner & Dentel (1998) mentioned that there are a few parameters that influence the solubility of metal oxides/hydroxides:

- Particle size distribution
- Crystalline form of solid phase present
- Temperature
- pH
- Residence time

The solubility of a metal compound can be illustrated on a solubility graph, also referred to as a Pourbaix diagram. A Pourbaix diagram is a visual illustration of the relative stabilities and also show the solubility concentrations of a metal compound in water (unless different specified) with respect to its ions and its hydrous and anhydrous oxide (Garverick, 1995). Another name referring to these diagrams is “Equilibrium diagrams” (Wulfsberg, 1991).

Using these diagrams, the most thermodynamically stable form of the specified element at the specific potential and corresponding pH could be determined. The Nernst equation is usd to convert the potential on the diagram to the concentration. Another advantage the pourbaix diagram has is the visual representation of the oxidising and reducing abilities of the major stable compounds of the specific element. (Wulfsberg, 1991)

The Pourbaix diagram is affected by the temperature of the solution and the concentration of the solvated ions in the solution and the equilibrium lines will shift to accommodate these changes. Diagrams consisting of combinations of different compounds such as *Mg* in the presence of a carbonate source are also available indicating the equilibrium stages between the different compounds. Magnesium and aluminium is used to illustrate how the Pourbaix diagram is used (Figure 17).

The lines on each Pourbaix diagram represent the equilibrium conditions for the species on each side of the line. Below the top, sloped line in Figure 17(a) and between the two lines (labelled (a) and (b)) in Figure 17(b) is the area in which water is stable for these two elements. As shown in Figure 17(a), the stability of magnesium is below the stability of water (sloped line), creating this large “area” where *Mg* could dissolve as Mg^{+} and Mg^{2+} with

accompanying hydrogen evolution (Fekry, 2011). For aluminium the results are slightly different.

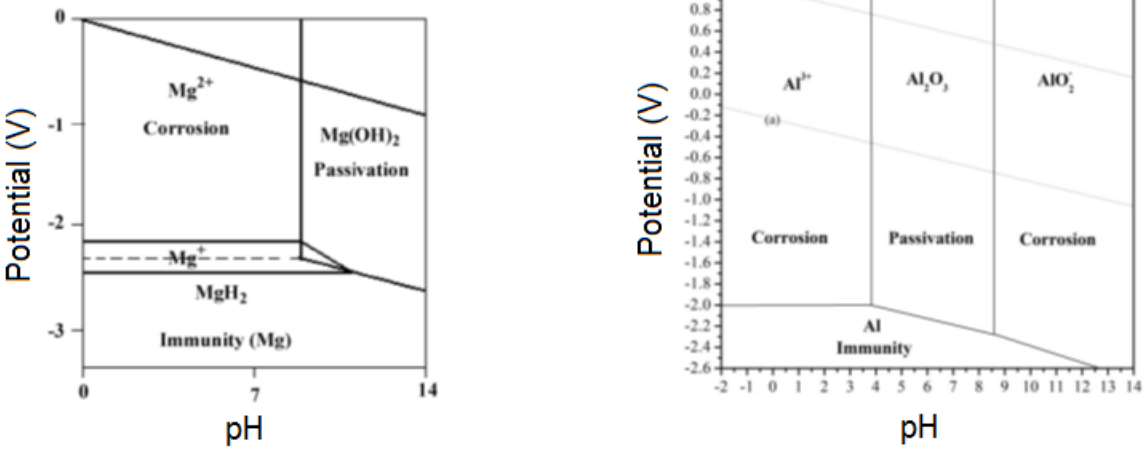

(a) (b)

Figure 17: Pourbaix diagrams for Mg and Al at 25 ^{o}C. (a) Magnesium-water (Fekry and Tammam, 2011). (b) Aluminium-water (Sukiman et. al., 2013).

Aluminium is overall passive in the pH range of 4 to 9 due to the presence of an Al_2O_3 film which covers the surface of the solid. The solubility of aluminium increases as the pH increases from approx. 4 to approx. 9 due to the dissolution of the alloy film as can be seen in Figure 17(b). In the acidic range the aluminium is oxidised by forming Al^{3+} metal cations, whereas in an alkaline range the formation of AlO^{2-} occurs. (Sukiman *et. al.*, 2013)

In general the Pourbaix diagrams indicates the conditions at which the metal either does not react (immunity) or can possibly react to form a specific oxide or complex ions but the diagrams does not indicate the kinetic rate at which the reactions may occur. (Garverick, 1995)

The pH-solubility curves for a couple of metal species are shown in Figure 18:

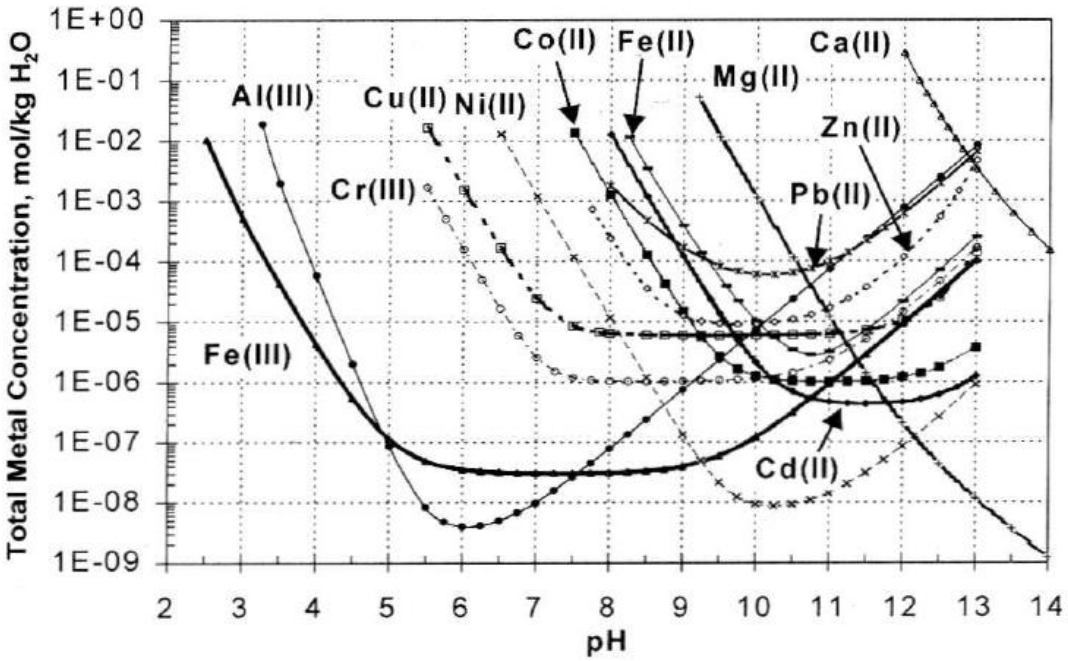

Figure 18: Solubility graph of metal oxides/hydroxides at 25 ^{o}C (Dyer, Scrivner and Dentel, 1998).

With the dissolution precipitation method, Labuschagne, Giesekke & Van Schalkwyk (2006) invented a one-step synthesis process with zero effluent for the production of hydrotalcite. It is suggested that the temperature within the range from 140 °C to 200 °C is recommended between 4 to 6 hours and at a pressure of from 10 bar to 14 bar in order to produce hydrotalcite. The carbonate source is in the form of sodium bicarbonate ($NaHCO_3$) which reacts to form CO_2 and sodium carbonate (Na_2CO_3). The sodium carbonate is regenerated by bubbling CO_2 through the Na_2CO_3 solution. Castet *et al.* (1993) indicated that with the increase in temperature the hydrolysed reaction of boehmite (a form of $Al(OH)_3$) is favoured. Castet and his co-workers (1993) also indicated a possible shift to the left of the minimum solubility point of boehmite when the temperature is increased, increasing the solubility with the increase in pH. These results were later confirmed by Bénézeth, Palmer & Wesolowski (2001). Therefore, it can be concluded that an alkaline aqueous environment would favour the solubility of $Al(OH)_3$ at higher temperatures (as can be seen from Figure 18) for the synthesis of LDHs.

It is also evident that too high pH could prevent certain metal species to dissolve, as shown for magnesium in Figure 18. Therefore, the optimum conditions of pH and temperature varies, depending on the type and ratio of metal species used.

The main advantage of this method when comparing it to the previous methods is that it only requires the metal oxides / hydroxides, which could easily be obtained and it also decreases the cost. There is also no formation of metal salts, which makes it a zero-effluent process. The disadvantage using this method is the amount of energy required to generate the optimum conditions for the solubility of the reagents.

2.4. Interlayer modification techniques

There are three main methods used for modification:

- Memory effect
- In situ
- Ion-exchange

It is sometimes difficult to synthesise directly an LDH containing the required anionic species. Therefore, these methods are used to solve the problem.

2.4.1. Memory effect

This technique is done by heating up an LDH containing an anion in the interlayer which could easily be converted through temperature. The LDH is heated to high temperatures which results in the formation of an amorphous oxide phase. When the amorphous phase is added to a solution containing the required anionic species, it rehydrates and has the ability to transform back into the layered structure. This phenomenon is called "*memory effect*". (Auerbach, Carrado & Dutta, 2004:383)

The modification is performed through a process called calcination. This is done by heating the LDH to between 350 ^{o}C to 500 ^{o}C. During calcination the interlayer water, interlayer anion

(e.g. CO_3^{2-} for hydrotalcite) and also the hydroxyl groups of the metal layers are removed through dehydroxylation, leaving the amorphous oxide phase behind. [Duan and Evans (2006), Auerbach, Carrado & Dutta (2004:417)]

This method is sensitive to temperature; therefore, the temperature must be controlled in order to prevent spinel formation which is resistant to rehydration (Auerbach, Carrado & Dutta, 2004:383). After calcination, the product is added to a water solution containing the specified anion to be used in the interlayer under an inert atmosphere to prevent CO_3^{2-} contamination. During mixing, the calcined product absorbs water, reconstructing the hydroxide metal layers. It is during this process where the anionic species in the solution is incorporated into the layered structure, neutralising the charge from the trivalent cation within the layers. The three different intermediate steps are shown in Figure 19.

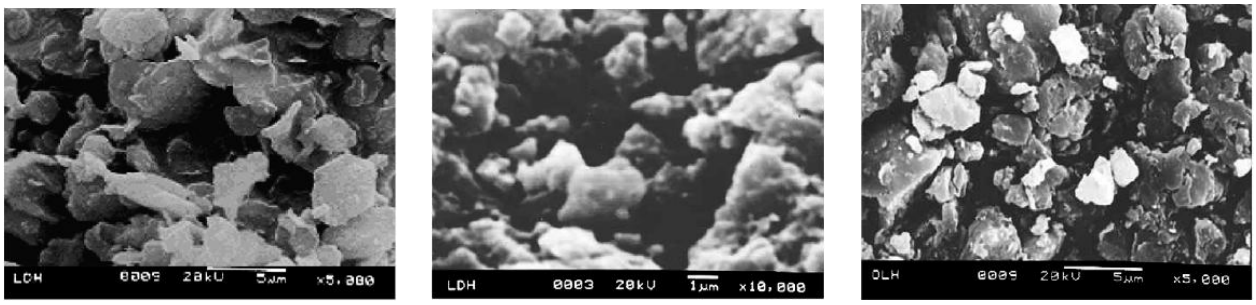

(a) (b) (c)

Figure 19: (a) Pure Mg-Al-LDH. (b) Calcined Mg-Al-LDH. (c) Organically modified *Mg-Al* LDH through memory effect (Acharya, Srivastava & Bhowmick, 2007).

2.4.2. In situ modification

In-situ modification is performed during the synthesis of the LDH. The specific anion required in the interlayer is dissolved in de-ionised water. It is difficult to dissolve certain organic acids. Therefore, sodium hydroxide may be used as well as heating the water to 70 ^{o}C to aid the process (Zhao and Nagy, 2004). After the organic acid is dissolved, the solution is purged with nitrogen gas to get rid of the last carbonate ions in the solution. The divalent and trivalent metal-ion salts are then slowly added to the solution (using the co-precipitation method) and *NaOH* is also added to control the pH. The anion forming part of the metal salt must have a

lower affinity to the LDH than the required anionic species (Wang *et al.*, 2009). As the LDH is starting the form (precipitation starts), the guest anion (A^{n-}) is absorbed into the layered structure to neutralise the positive charge, as shown in Figure 20. The guest anionic species could be a monovalent or divalent species.

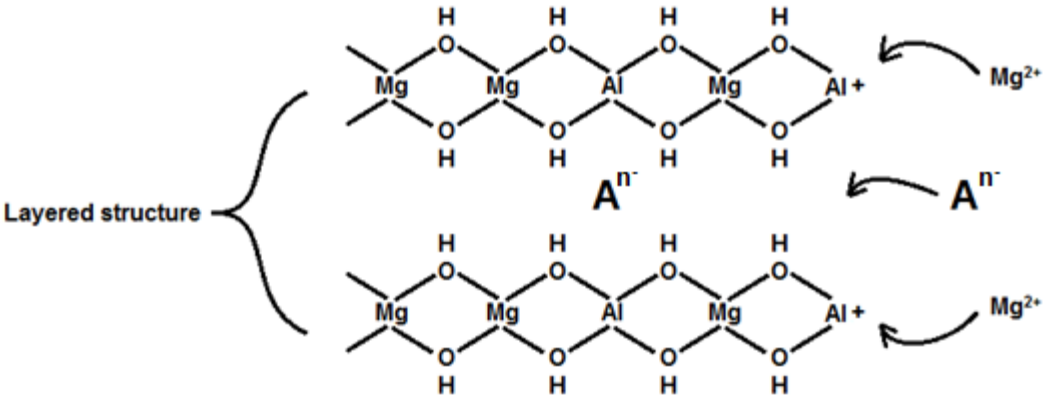

Figure 20:In-situ LDH modification (adapted from Reichle, 1986).

2.4.3. Ion-exchange modification

In order to produce an LDH containing an interlayer anion apart from carbonate, post-synthetic treatments with salt and acid (Iyi *et al.*, 2004) could also be performed to replace the carbonate ions with less affine anions like chloride. Costantino *et al.* (1998) illustrated that carbonate-LDH may be avoided by treating the LDH produced by the urea method with dilute *HCl* gas between 140 ^{o}C and 160 ^{o}C after synthesis while stirring for 8 hours. During this modification process, the guest anion (A^{n-}) situated in the interlayer acts as a guest ion in the interlayer and is then replaced by the required anionic species B^{n-}, as illustrated in Figure 21.

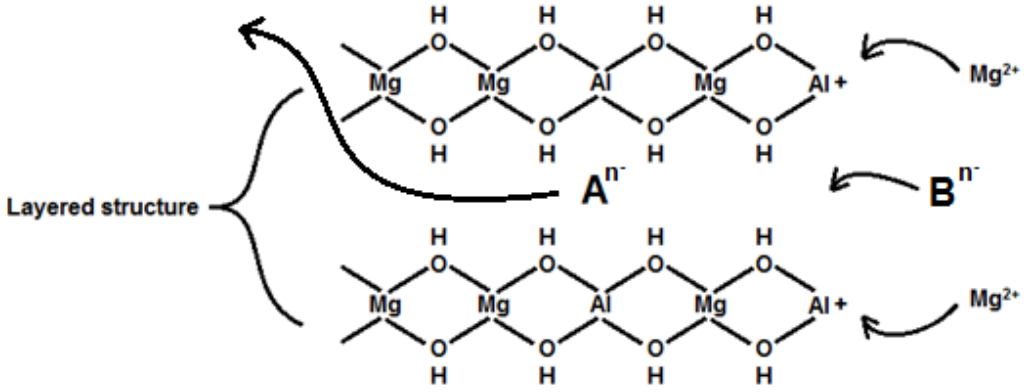

Figure 21: Ion-exchange modification (adapted from Reichle, 1986).

Wang *et al.* (2009) used *Mg-Al* LDH containing NO_3^- and Cl^- respectively as guest anions to be replaced by sodium dodecylbenzenesulfonate (SDBS). Zhao and Nagy (2004) used sodium dodecyl sulphate (SDS) as organo-modifier and the reaction took place at 65 ^oC for approx. 2 days to allow sufficient time for ion-exchange to take place.

2.4.4. Advantages/Disadvantages for each modification technique.

The advantages and disadvantages of these two modification techniques are listed in Table 5:

Table 5: Advantages and disadvantages for the three interlayer modification techniques; Memory effect, In-situ modification and ion-exchange modification.

Technique	Advantages	Disadvantages
Memory effect	1. A high percentage modification yield is achieved. 2. Almost stoichiometric amount of anion required for modification.	1. It is a high demand for energy required for the temperature required for calcination. 2. It is a 2-step process. 3. Temperature must be controlled to avoid the formation of spinel.
In-situ	1. This modification is part of the LDH synthesis, therefore, eliminating one processing step. 2. It is a faster method for modification than afterwards modification. 3. A reasonable high percentage modification yield is achieved.	1. This process requires working in an inert atmosphere. 2. More than stoichiometric amount required to ensure high yield.

Technique	Advantages	Disadvantages
Ion-exchange	1. This method does not have to be performed in an inert atmosphere.	1. It is difficult to achieve 100% anion replacement. 2. This method is time consuming. 3. A large excess amount of anion required to ensure high yield.

3. Experimental

3.1 Planning

In this research, *Mg-Al* LDH and *Ca-Al* LDH were used as primary LDHs. The method for synthesizing *Ca-Al* LDH using the dissolution-precipitation method has already been optimized, but not yet for *Mg-Al* LDH. The first part of this research is to determine the effect of temperature and time on the synthesis of *Mg-Al-CO_3* LDH using the dissolution-precipitation method.

LDHs that are either consisting of or that have been partially substituted with the species listed below has already been synthesised using the co-precipitation or urea method, but have not yet been done using the dissolution-precipitation method.

- *Co*
- *Cu*
- *Mn*
- *Mo*
- *Ni*
- *Sn*
- *Ti*
- *Zn*

The second part of this research will be based on the possibility of partially substituting the *Mg/Ca* cations with the above mentioned metal species via the dissolution-precipitation process. The reason for the method of choice is to determine whether it is possible to synthesise LDHs containing these metal species using a zero-effluent process.

According to Van der Westhuizen (2011) and Van Graan (2012), for the *Ca*-based experiments, the presence of a carbonate source favours the formation of calcite (*$CaCO_3$*). Therefore, for the *Ca*-based experiments, the samples will first be synthesised in an inert atmosphere before it is exposed to a carbonate source. Through this method it could be possible to determine whether an intermediate product containing both the *Ca* and M^{2+}/M^{3+} metal species has formed.

3.2 Apparatus

3.2.1 Dissolution-precipitation method

All the syntheses were performed using the Versoclave pressure reactor (type 3/5L) from Büchiglasuster, as shown in Figure 22.

(a) (b)

Figure 22: Versoclave pressure reactor from Büchiglasuster. (a) Reactor vessel with magnetic drive on top, temperature controller and speed controller on the right. (b) Complete reactor setup with Petite Fleur Tango 1.5 kW oil heater from Huber at the bottom for heating.

The setup was equipped with two reactor vessels (operating volumes of 1 L and 5 L respectively for temperatures not exceeding 200 ^{o}C) depending on the quantity to be synthesised. The reactor was equipped with one magnetic drive mixer containing one impeller at the bottom of the shaft. A baffle is added to increase turbulent flow inside the reactor. The reactor contained two 0.5 L liquid dosing pods above which is operated manually, one sample tube which is mounted at the top of the reactor that reaches a quarter-length from the bottom of the reactor.

A Petite Fleur heater with a 1.5 kW heater and 0.48 kW cooler (Refrigerant – R290) was connected to the reactor. This heater used oil for indirect heating of the reactor via a circulation pump (33 L/min at 0.9 bar). The specifications of the reactor are listed below:

- Operating temperature (-40 ^{o}C to 200 ^{o}C max.) - controllable
- Operating pressure (0 bar to 40 bar max.)
- Operating stirrer speed (0 rpm to 1200 rpm max.) - controllable
- pH probe (0 ^{o}C to 120 ^{o}C max.) - controllable

Figure 23: Complete setup for co-precipitation method.

The reaction vessel (Erlenmeyer flask with a magnetic stirrer inside) was placed inside an oil bath which was heated by the hotplate. A flat metal shaft wasis placed inside the oil bath (underneath the flask with enough space to rotate) which was also stirred by the magnetic stirrer in order to increase the heating rate of the oil inside the oil bath.

Two dropping funnels were used (One for *NaOH* solution and one for divalent metal salt solution).

3.2.4 Analysis equipment

3.2.4.1 X-ray Diffraction analysis

Wide angle X-ray scattering (WAXS) measurements were performed with the X'pert-Pro Diffractometer system from PANalytical with continuous scanning using a step size of 0.001^{o} between the ranges 5.0084^{o} and 89.9914^{o} 2θ. *Co*-K_{α} radiation was generated with a wavelength of 0.1789 nm at 50 mA and 35 kV by a diffractometer. The irradiated length was kept at 15 mm with a specimen length of 10 mm. The distance Focus-diverge slit was kept at 100 mm and the measuring time was kept Δt = 14.52 s for each point.

3.2.4.2 Scanning electron spectroscopy (SEM) and energy-dispersive X-ray spectroscopy (EDS) analysis

SEM analysis at the Institut für Polymer Forschung Dresden e.V., Germany was performed on the Ultra Plus Series from Zeiss. The samples were sputter-coated with 3nm platinum and the gun voltage status was set between 2 kV and 10 kV, depending on the sample.

EDS (energy dispersive X-ray spectroscopy) analysis is an addition to the SEM. X-radiation is emitted from the interaction of the electron beam with the sample. This radiation is detected using an X-ray detector, which then converts this data to quantitavive data such as composition on an elemental basis (by visual mapping). EDS analysis were done on the XFlash Quad 5040 EDS detector in Germany.

The samples that were analysed at the Council for Scientific and Industrial Research (CSIR-Pretoria, South Africa) were done on the Zeiss Auriga FIB SEM. The samples were sputter-coated with carbon and the gun voltage status was set between 2 kV and 10 kV, depending on the sample. EDS analysis were done on the Oxford X-max EDS detector.

3.2.4.3 Particle size analysis (PSA)

The Hydro 2000MU (A) particle size analyser with a size range of 0.1 µm to 1000 µm from Malvern was used for this analysis. The analysis model was General purpose – spherical. Water was used as dispersant (dispersant Reflex Index of 1.330) and ultra-sonic vibration was used for 30 seconds during each run to break down agglomerates and preventing new ones from forming. Each sample was analysed five times before an average was calculated.

3.2.4.4 Brunauer-Emmett-Teller (BET) Analysis

BET-analysis was done using a Tristar ll. Liquid nitrogen (N_2) was used as analysis adsorptive agent with an analysis temperature of -195.8 ^{o}C. Degassing was done at 100 ^{o}C oer night using Helium gas. The equilibration interval was set to 5 s for each run and a total run took approx. 4 hours.

3.2.4.5 Inductively Coupled Plasma (ICP) Analysis

An ARCOS model, Inductively Coupled Plasma Optical Emission Spectrometer (ICP-OES) from SPECTRO was used for the determination of aluminium and magnesium concentrations in solution. An Argon gas plasma was used. 1 g of each sample was dissolved in 20 ml of 37% hydrochloric acid which was then diluted with distilled water in a 1:10 ratio. A Multi-element standard ICP grade from Merck was used for comparison. ICP analysis was done in triplets.

3.3 Method

3.3.1. *Mg-Al-CO_3* LDH synthesis optimization

The reactions were performed in the reactor using stoichiometric ratios and a 10 wt% product solid concentration (100 g LDH formed per litre batch reaction) for the mixture as basis. The effect of temperature and time was performed according to Table 6 shown below:

Table 6: Time-temperature matrix for *Mg-Al-CO_3* LDH synthesis optimisation.

Time (h)	Temperature (^oC)			
	120	140	160	180
1	MgAl120-1	MgAl140-1	MgAl160-1	MgAl180-1
2	MgAl120-2	MgAl140-2	MgAl160-2	MgAl180-2
3	MgAl120-3	MgAl140-3	MgAl160-3	MgAl180-3
4	MgAl120-4	MgAl140-4	MgAl160-4	MgAl180-4
5	MgAl120-5	MgAl140-5	MgAl160-5	MgAl180-5

The chemical reagents that were used are listed in Table 7.

Table 7: Chemical regaents for *Mg-Al-CO_3* LDH synthesis optimization.

Chemical species	Compound	Supplier
Magnesium (*Mg*)	*MgO*	Sigma-Aldrich, CAS nr. 1309-48-4, 99.99%
Aluminium (*Al*)	*$Al(OH)_3$*	Merck Millipore, Cas nr. 1.01093.1000, >95%
Carbonate (CO_3^{2-})	*$NaHCO_3$*	Merck Millipore, Cas nr. 144-55-8, 99%

The following steps were performed for each run:

1. Stoichiometric amount *MgO* (34.36 g), *$Al(OH)_3$* (33.23 g), were added individually and in small quantities to 1 L distilled *H_2O* on a magnetic stirrer.
2. 20 mole% excess *$NaHCO_3$* (42.96 g) was then added in small quantities to ensure sufficient carbonate is present.
3. The mixture was allowed to stir for 5 minutes before the pH is measured.
4. After stirring, the mixture was added to the reactor while the stirrer was set at a low speed (100 rpm) rate to keep the solids suspended.
5. Once all the content is inside the reactor, the stirrer was set to 600 rpm and the temperature was set to the specific set point according to Table 5.
6. The reaction time started as soon as the temperature was within 5% of the set point.
7. After the reaction was completed (according to the time scale in Table 5) the reactor was left to cool down.
8. Once the temperature inside the reactor was below 70 ^oC (safe to handle) the reactor was drained.

9. The slurry was then filtered and washed until the pH was below 8. (The washing was done by adding distilled H_2O, 4 to 6 times the volume of total cake thickness, to the filter – this process is called total cake displacement).
10. After washing the sample was dried in a convection drying oven set at 70 ^{o}C over night before it was crushed in a mortar and pestle for analysis.

3.3.2. M^{x+}-*Mg/Ca-Al*-CO_3 LDH synthesis

The reactions were performed in the reactor using stoichiometric ratios and a 10 wt% product solid concentration (100 g LDH formed per litre batch reaction) for the mixture as basis.

Partial substitution of the divalent metal ions used for the primary LDH's (*Mg-Al* LDH and *Ca-Al* LDH) was investigated. From literature it was found that some divalent metal species oxidise and has the potential to replace the trivalent metal species (Table 3, Section 2.3). Therefore, the experiments were categorised under two main sections: 25 mole% substitution and 8.3 mole% substitution.

The 25 mole% substitution was used for divalent and transition metal ions which are used to replace the *Mg/Ca* ions and don't have the potential to partially replace the *Al*-cations in the metal hydroxide layers. The 8.3 mole% substitution was only used for transition metal species which has the potential to partially replace the *Al* ions. The 8.3 mole% substitution was calculated by keeping the divalent/trivalent metal ratio within 2:1 to 3:1 and by changing the mole fraction of the substitution metal ion species to meet the ratio requirements. The metal species that were investigated are shown in Table 8.

The set-point temperature of the heater was set to 200 ^{o}C in order to reach reaction temperatures of 180 ^{o}C. During the winter season the reactor temperature wasn't able to reach the initial reaction temperature above 170 ^{o}C. The initial reaction temperature was then assumed to be any value above 165 ^{o}C and the reaction time was set from then. Insulation was added later on during the experiments. A 50 mm thick glass fibre pad was used for insulation, covered with aluminium foil to prevent fibres from breaking off during operation. As the season passed, the reactor was able to reach temperatures above 180 ^{o}C.

Table 8: Metal species used for Mg/Ca partial substitution.

Metal species	Compound	Supplier
Magnesium (*Mg*)	MgO	Sigma-Aldrich, CAS nr. 1309-48-4, 99.99%
Calcium (*Ca*)	CaO	Sigma-Aldrich, CAS nr. 1305-78-8, Reagent grade
Aluminium (*Al*)	$Al(OH)_3$	Merck Millipore, CaS nr. 1.01093.1000, >95%
Titanium (*Ti*)	TiO_2	Sigma-Aldrich, CAS nr. 1317-70-0, 99.8% Anatase
Manganese (*Mn*)	MnO	Sigma-Aldrich, CAS nr. 1344-43-0, >99.99%, Mn(ll)
	MnO_2	Sigma-Aldrich, CAS nr. 1313-13-9, 99.99%, Mn(lV)
Cobalt (*Co*)	Co_3O_4	Sigma-Aldrich, CAS nr. 1308-06-1, 99,995%
Nickel (*Ni*)	NiO	Sigma-Aldrich, CAS nr. 1313-99-1, 99.99%
Copper (*Cu*)	CuO	Sigma-Aldrich, CAS nr. 1317-38-0, 99.99%, Cu(ll)
	Cu_2O	Sigma-Aldrich, CAS nr. 1317-39-1, >99.99%, Cu(l)
Zinc (*Zn*)	ZnO	Sigma-Aldrich, CAS nr. 1314-13-2, Analytical grade
Molybdenum (*Mo*)	MoO_3	Sigma-Aldrich, CAS nr. 1313-27-5, 99.99%
Tin (*Sn*)	SnO_2	Sigma-Aldrich, CAS nr. 18282-10-5, >99.99%

For these experiments an initial reaction temperature of approx. 180 ^{o}C was used. The following steps were performed for each run:

3.3. 2.1. *Ca/M^{x+}-Al* LDH synthesis

1. Using a magnetic stirrer, stoichiometric amount CaO, $Al(OH)_3$ and the metal oxide/hydroxide used for substitution were added individually in small quantities at a time to pre-heated Distilled H_2O (1 L, 70 ^{o}C). The H_2O is pre-heated to prevent CO_3^{2-} contamination.
2. After all the metal oxides/hydroxides were added, the mixture was stirred for 5 minutes before the pH was measured. A glass lid was placed on top during mixing to prevent unwanted CO_3^{2-} contamination.
3. $NaOH$ was added to the mixture if the pH was not above 10.
4. After pH measurement the mixture was added to the reactor.

5. The reactor was purged with nitrogen gas (N_2) up to gauge pressure of 100 kPa to ensure the absence of CO_3^{2-}.
6. The temperature was set to 200 ^oC and the stirrer speed was set to 600 rpm.
7. When the temperature was within 5% of the set point temperature, the reaction time was set for 5 hours.
8. After reaction time the heating was stopped and the reactor was allowed to cool down through natural convection.
9. After the temperature inside the reactor was below 70 ^oC (for safe handling) the reactor is drained and the pH was measured again.
10. The batch was then split into two samples; to one a carbonate source was added and to the other nothing. The samples were labelled “Inert” and “Carbonate”.
11. $NaHCO_3$ (20 mole% excess) was added to the carbonate labelled sample on a magnetic stirrer and was allowed to stir overnight to ensure enough reaction time.
12. Both the samples were then individually filtered and washed until the pH was below 8. (The washing was done by adding distilled H_2O, 4 to 6 times the volume of total cake thickness, to the filter.
13. After washing, both the samples were dried overnight in a vacuum oven set at 70 ^oC before it was grinded with a mortar and pestle for analysis.

3.3.2.2. *Mg/M^{x+}-Al* LDH synthesis

1. Using a magnetic stirrer, stoichiometric amount MgO, $Al(OH)_3$, $NaHCO_3$ and the metal oxide/hydroxide used for substitution were added individually in small quantities at a time to Distilled H_2O (1 L).
2. After all the reagents were added, the mixture was stirred for 5 minutes before the pH was measured.
3. $NaOH$ was added to the mixture if the pH was not above 10.
4. After pH measurement the mixture was added to the reactor.
5. The temperature was set to 200 ^oC and the stirrer speed was set to 600 rpm.
6. When the temperature was within 5% of the set point temperature, the reaction time was set for 5 hours before letting it cool down.

7. After the temperature inside the reactor was below 70 ^{o}C (for safe handling) the reactor was drained and the pH was measured again.
8. The sample was then split into two individual samples.
9. The carbonate sample was the exposed to a carbonate source in solution and was allowed to react overnight.
10. Only carbonate samples were washed until the pH is below 8. (The washing was done by adding distilled H_2O, 4 to 6 times the volume of total cake thickness, to the filter.
11. Both the inert and carbonate samples were filtered before it were dried in a convection drying oven set at 70 ^{o}C overnight.

4. Results and Discussions

It is believed that the formation of hydrotalcite via the reaction of insoluble or low solubility metal oxides, hydroxides or carbonates with each other is a dissolution-precipitation reaction. For example, the magnesium oxide loaded to the reactor must dissolve to some extent and react with water to form and precipitate as brucite (magnesium hydroxide) – the base layer of the LDH material. The aluminium hydroxide (added as gibbsite) must also dissolve to form aluminium ions that replace some of the magnesium ions in the brucite layers to form the unbalanced layers of the hydrotalcite structure. Finally, the anion (in this case carbonate released form the sodium bicarbonate) can balance the positively charged layers, trap come crystal water and hydrotalcite can precipitate. This is a good example of Le Chatelier's principal (Atkins & De Paula, 2009: 162 & 188). If hydrotalcite is the least soluble specie at the system temperature and pressure, it will preferentially precipitate and remove the relevant ions from solution, causing more of the ions to be dissoluted. But this is however only possible if the ions were in solution to some extent to begin with.

4.1. Effect of reaction temperature and time on the synthesis of Mg-Al-CO3 LDH

The detailed XRD patterns obtained for all the runs are shown individually in Appendix A.1. Figure 24 is the combination of all the XRD results obtained for the synthesis of *Mg-Al*CO_3 LDH at different reaction temperatures and time.

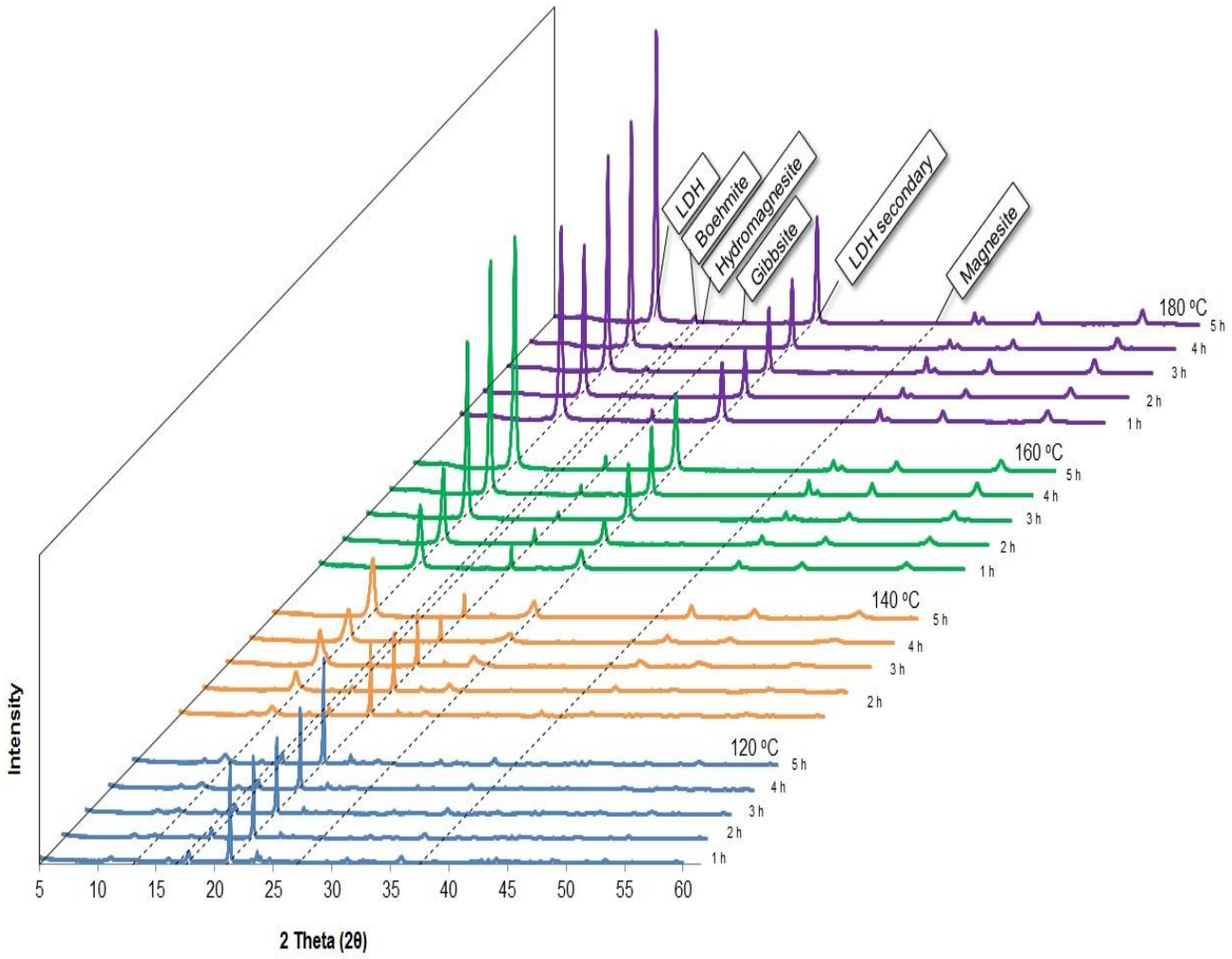

Figure 24: XRD Results obtained for the synthesis of *Mg-AlCO$_3$* LDH at different reaction temperatures and time.

4.1.1. 120 °C Reaction temperature

The XRD patterns obtained for the experiments performed at 120 °C and at different reaction times are shown in Figure 24. The first peak that is noted is the large peak situated at the 2θ value of 21° which corresponds to the gibbsite which is present in the sample. The intensity of the peak indicates that there is a significant amount of gibbsite which is still crystalline and did not dissolve. A small peak is noticed at the 2θ value of 13° which corresponds to that of LDH. The secondary peak of LDH which normally occurs around the 2θ position of 27° is barely noticeable, indicating low yield and/or low crystallinity LDH. The XRD pattern for

hydromagnesite ($Mg_5(CO_3)_4(OH)_2{\cdot}4H_2O$, a basic carbonate of magnesium) is close to hydrotalcite with a primary peak around the 2θ position of 18° and a secondary peak around 16° (Focke *et al*., 2009) and visible in all reactions at 120 °C.

The Rietveld analyses for these five experiments are shown in Table 9.

Table 9: Rietveld analysis for *Mg-Al-CO_3* LDH synthesised at 120 °C.

Reaction time (hrs)		Compound				
		***Mg-Al-CO_3* LDH**	***$Al(OH)_3$***	***$MgCO_3$***	***$Mg_5(CO_3)_4(OH)_2{\cdot}4H_2O$***	***$Mg(OH)_2$***
1	Weight Fraction (%)	**10.28**	**40.11**	**-**	**49.61**	-
	3 σ error	0.69	1.11	-	1.14	-
2	Weight Fraction (%)	**6.67**	**39.47**	**-**	**53.86**	-
	3 σ error	0.84	1.17	-	1.23	-
3	Weight Fraction (%)	**8.42**	**36.52**	**-**	**55.06**	-
	3 σ error	0.84	1.23	-	1.32	-
4	Weight Fraction (%)	**8.41**	**36.43**	**-**	**55.16**	-
	3 σ error	1.08	1.41	-	1.53	-
5	Weight Fraction (%)	**25.54**	**32.70**	**-**	**41.76**	-
	3 σ error	0.66	0.78	-	0.90	-

From the Rietveld analysis the low yield of LDH corresponds to the results shown in Figure 24. It is evident that there is a significant amount of gibbsite still left in the sample, indicating that time was not enough for sufficient dissolution and reaction time at the low reaction temperature of 120 °C. But a decrease in the amount of gibbsite is shown. Due to the low solubility of the gibbsite compared to that of $Mg(OH)_2$, it makes gibbsite the limiting reagent for the formation of the LDH at these conditions.

According to Hartmann-Petersen, Gerrans and Hartmann-Petersen (2007) $MgCO_3$ is a more stable form of *Mg* compared to that of $Mg(OH)_2$ and is produced by bubbling CO_2 through a $Mg(OH)_2$ slurry. This process is a relatively quick process. Magnesite ($MgCO_3$) is then precipitated out. When excess CO_2 is bubbled through an $MgCO_3$ solution, carbonic acid is formed causing the solution to become more acidic. This aids in the solubility of the $MgCO_3$ and forms hydrated magnesium carbonate which is a more soluble form of magnesium (Singhal, 2010:4.16). The formation of hydrated magnesium carbonates generally occurs at low temperatures in an excess carbonate environment and is referred to as "the magnesite problem" (Deelman, 2011). The following reaction mechanism is derived from the above mentioned literature (Equation 18 to Equation 20):

$$MgO + H_2O \rightarrow Mg(OH)_2 \quad (18)$$

$$Mg(OH)_2 + CO_2 \rightarrow MgCO_3 + H_2O \quad (19)$$

$$4MgCO_3 + Mg(OH)_2 + 4H_2O \rightarrow Mg_5(CO_3)_4(OH)_2 \cdot 4H_2O \quad (20)$$

To confirm if the formation of magnesite or hydromagnesite is temperature driven in a closed system, the same synthesis was done at the same reaction temperaures (5 hours reaction time) but with no aluminium source added as reagent. This is further discussed in Section 4.1.5.

From the mechanism derived above, it is possible that the formation of magnesium hydroxy carbonate in these experiments were due to excess carbonates in solution and low temperature. There were no $Mg(OH)_2$ or $MgCO_3$ detected, however, the presence of hydromagnesite ($Mg_5(CO_3)_4(OH)_2 \cdot 4H_2O$), which is a metastable hydrated magnesium carbonate mineral (Vágvölgyi *et al*., 2008), did show in the Rietveld results. The XRD pattern for hydromagnesite is close to hydrotalcite with a primary peak around 18 ^{o} at the 2θ position and a secondary peak around 11 ^{o} (Focke *et al*., 2009). These two peaks can clearly be seen in Figure 24 for MgAl120-1 which is at a reaction time of 1 hour. As the time is increased, the decrease in the hydromagnesite peaks in Figure 24 can be seen with the corresponding increase in the primary and secondary LDH peaks. The decrease in the formation of hydromagnesite with the increase in reaction time indicated that at low temperatures, short

reaction time and excess carbonates in solution does favour this reaction. The solubility of gibbsite was also negligible at these low reaction temperature.

4.1.2. 140 °C Reaction temperature

A significant difference was noted when comparing the Rietveld results obtained for the reaction temperature of 140 °C to that of 120 °C, as shown in Table 10.

Table 10: Rietveld analysis for *Mg-Al-CO_3* LDH synthesised at 140 °C.

Reaction time (hrs)		Compound				
		***Mg-Al-CO_3* LDH**	***$Al(OH)_3$***	***$MgCO_3$***	***$Mg_5(CO_3)_4(OH)_2{\cdot}4H_2O$***	***$Mg(OH)_2$***
1	Weight Fraction (%)	**79.52**	**15.38**	**5.10**	**-**	-
	3 σ error	0.83	0.83	0.62	-	-
2	Weight Fraction (%)	**80.94**	**13.86**	**5.20**	**-**	-
	3 σ error	0.79	0.66	0.66	-	-
3	Weight Fraction (%)	**83.16**	**12.11**	**4.73**	**-**	-
	3 σ error	0.39	0.57	0.33	-	-
4	Weight Fraction (%)	**86.48**	**10.21**	**3.31**	**-**	-
	3 σ error	0.90	0.78	0.39	-	-
5	Weight Fraction (%)	**91.49**	**7.34**	**1.17**	**-**	-
	3 σ error	0.75	0.60	0.49	-	-

The LDH showed a significant increase with a yield obtained of almost 80 % just after 1 hour reaction time and over 90 wt% after 5 hours reaction time. The presence of gibbsite decreased with more than 50 wt%, indicating that the increase in temperature has a major advantage on its solubility and therefore the formation of the LDH. This is considerably lower

than the ca. 40 % for the 120 ^{o}C reaction temperature. Also observed is the absence of hydromagnesite and the presence of $MgCO_3$. Calculated from the Rietveld data, the change in distribution of the *Mg* and *Al* is shown Figure 25 (120 ^{o}C) and Figure 26 (140 ^{o}C).

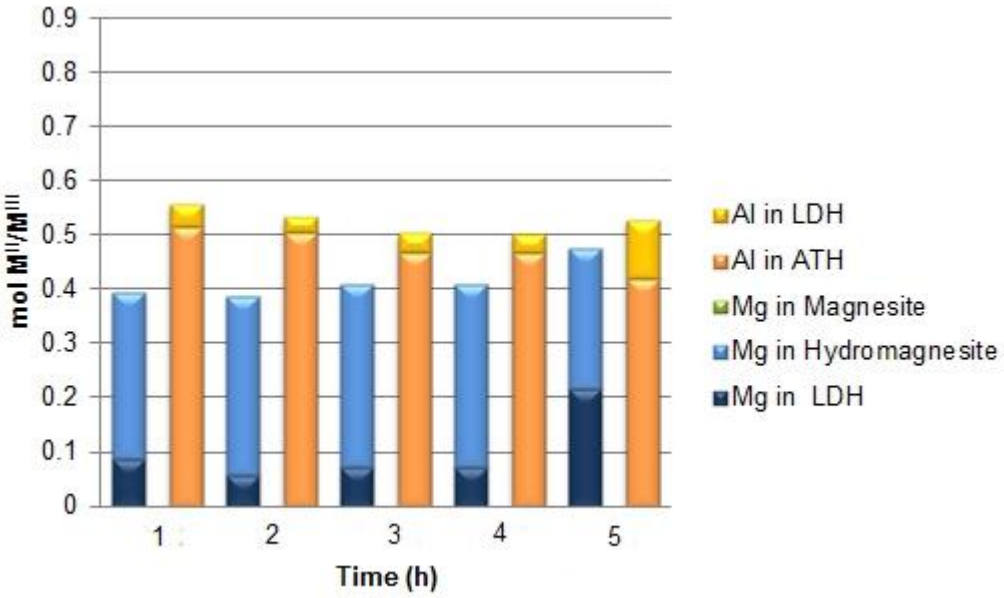

Figure 25: *Mg* and *Al* distribution at 120 ^{o}C reaction temperature.

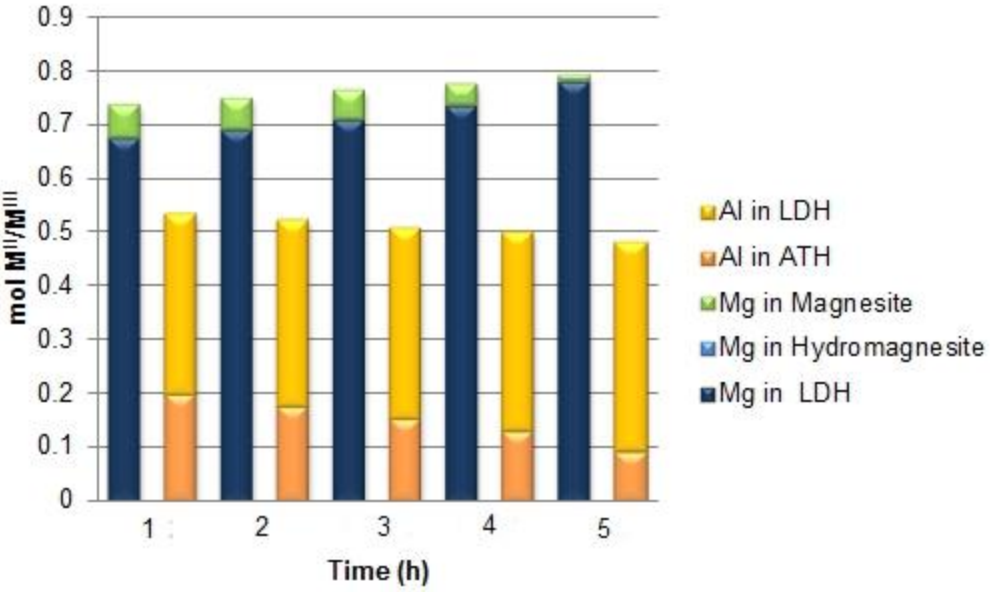

Figure 26: *Mg* and *Al* distribution at 140 ^{o}C reaction temperature.

The results above corresponds to the theory mentioned by Hartmann-Petersen, Gerrans and Hartmann-Petersen (2007) as well as the results obtained which is discussed in Section 4.1.5.

At 120 ^{o}C the majority of the *Mg* is noted to take part in the formation of hydromagnesite. Gibbsite (represented as ATH in Figure 25 and Figure 26) also showed low solubility. At 140 ^{o}C, there is a significant shift in the distribution of the *Mg* and *Al* ions. Most of the *Mg* which took part in the formation of hydromagnesite at the lower reaction temperature took part in the formation of magnesite and LDH. Also, no $Mg(OH)_2$ were detected in the samples. As the solubility of the *Al* is increased with the increase in reaction temperature and time (140 ^{o}C and 5 hours), more *Mg* took part in the formation of LDH, therefore, explaining the decrease in the presence of magnesite, hydromagnesite and gibbsite.

This also indicates that the increase in reaction temperature suppresses the formation of hydromagnesite and favours magnesite ($MgCO_3$) formation. And as the reaction time is increased, the magnesite then starts to dissolve and reacts with the dissolved gibbsite to form the LDH.

The primary peak at the 2θ position of 13^{o} showed a significant increase in peak intensity as the reaction time is increased (Figure 24). The significant decrease in the gibbsite peak at 2θ position of 21^{o} is also clear. The decrease in the magnesite peak (2θ position of 38^{o}) can clearly be seen in the raw XRD patterns shown in Figure 62 to Figure 66 in Appendix A.1.1. As the reaction time is increased, the intensity of the primary and secondary peaks for the LDH increases, indicating the improvement on crystallinity of the LDH.

4.1.3. 160 ^{o}C Reaction temperature

Significant improvement on the synthesis of *Mg-Al-*CO_3 LDH is seen in Figure 24. The primary, secondary and the rest of the LDH peaks (41^{o}, 46^{o} and 55^{o}) are well-defined with high intensity and small broadening at the base, indicating a good crystalline product. There are still gibbsite present, but significant improvement was achieved. The Rietveld data obtained for these experiments is shown in Table 11.

Table 11: Rietveld analysis for *Mg-Al-CO_3* LDH synthesised at 160 ^{o}C.

Reaction time (hrs)		Compound				
		***Mg-Al-CO_3* LDH**	***$Al(OH)_3$***	***$MgCO_3$***	***$Mg_5(CO_3)_4(OH)_2{\cdot}4H_2O$***	***$Mg(OH)_2$***
1	Weight Fraction (%)	**91.25**	**8.75**	**-**	**-**	-
	3 σ error	0.51	0.51	-	-	-
2	Weight Fraction (%)	**95.27**	**4.73**	**-**	**-**	-
	3 σ error	0.48	0.48	-	-	-
3	Weight Fraction (%)	**95.17**	**4.83**	**-**	**-**	-
	3 σ error	0.75	0.57	-	-	-
4	Weight Fraction (%)	**96.01**	**3.99**	**-**	**-**	-
	3 σ error	0.33	0.33	-	-	-
5	Weight Fraction (%)	**96.5**	**3.5**	**-**	**-**	-
	3 σ error	0.54	0.54	-	-	-

From the results obtained, it is clear that the reaction for the formation of LDH is becoming more preferred at the high temperatures than the formation of *$MgCO_3$* and *$Mg_5(CO_3)_4(OH)_2{\cdot}4H_2O$*. The amount of gibbsite in the sample also had decreased to approx. 4 wt% after 5 hours. Compared to the previous temperature runs, the amount of *$MgCO_3$* in the 160 ^{o}C runs had significantly decreased to almost negligible after 5 hours reaction time. As can be noted, only *Mg* which doesn't form part of the LDH reacted to form *$MgCO_3$* and *$Mg_5(CO_3)_4(OH)_2{\cdot}4H_2O$*. Therefore, as more *Al* dissolves, the ratio of *Mg:Al* becomes ideal (2:1) and then LDH is precipitated and less *$MgCO_3$* and *$Mg_5(CO_3)_4(OH)_2{\cdot}4H_2O$* are present.

4.1.4. 180 °C Reaction temperature

Table 12 represents the Rietveld data obtained for the set of experiments that were done at 180 °C with different reaction times.

Table 12: Rietveld analysis for *Mg-Al-CO₃* LDH synthesised at 180 °C.

Reaction time (hrs)		Compound				
		***Mg-Al-CO₃* LDH**	***Al(OH)₃***	***MgCO₃***	***Mg₅(CO₃)₄(OH)₂·4H₂O***	***Mg(OH)₂***
1	Weight Fraction (%)	**96.37**	**3.63**	**-**	**-**	-
	3 σ error	0.84	0.57	-	-	-
2	Weight Fraction (%)	**96.37**	**3.63**	**-**	**-**	-
	3 σ error	0.39	0.28	-	-	-
3	Weight Fraction (%)	**96.88**	**3.12**	**-**	**-**	-
	3 σ error	0.36	0.36	-	-	-
4	Weight Fraction (%)	**96.18**	**3.82**	**-**	**-**	-
	3 σ error	0.28	0.28	-	-	-
5	Weight Fraction (%)	**99.37**	**0.63**	**-**	**-**	-
	3 σ error	0.48	0.48	-	-	-

There were no *MgCO₃, Mg₅(CO₃)₄(OH)₂·4H₂O* or *Mg(OH)₂* present in the samples which were synthesised at 180 °C, but there were still small amounts of gibbsite present. The synthesis of *Mg-Al-CO₃* LDH improved significantly with the increase in temperature and the increase in reaction time.

After two hours reaction time, the peaks representing gibbsite disappeared, but, after three hours the peaks of boehmite (another crystal form of *Al(OH)₃*) appeared at the 2θ positions of

17°, 33° and 45°. This indicates that the gibbsite had completely dissolved and had re-precipitated as boehmite. This is a possible indication that the limiting reagent may have been the Mg-source. The repetitive peaks of the LDH are dominant with narrow broadening at the base of the peaks, indicating that the LDH has a high crystalline structure.

When looking at the detailed XRD results, it is believed that aging and an increase in crystallinity occurs at the high temperatures during the final hours of reaction time where the small LDH crystals dissolve and re-precipitate to form a much more crystalline product through the process called Ostwald ripening (Yao *et al*., 1993).

4.1.5. The effects of temperature or carbonate concentration on the formation of magnesite and hydromagnesite

To confirm if the formation of magnesite or hydromagnesite is temperature or carbonate concentration driven in a closed system, the same synthesis was done at the same reaction temperatures (5 hours reaction time) but with no aluminium source added as reagent.

The XRD patterns obtained for the experiments are shown in Figure 27 below as well as in Appendix A.2. All the peaks on the XRD patterns were identified. Rietveld analysis were also done on the samples and the results obtained are shown in Table 2 with weight % 3σ errors indicated in italics.

The first observation is the formation of hydrotalcite at 180 °C. This is impossible as no aluminium was added to the reactor (intentionally) and must thus be due to unwanted contamination. The trace amounts of *MgO* (less than 1 wt%) left in the samples is surprising and may be a highly crystalline and unreactive form of *MgO* impurity in the feed material. It is to be expected that all the *MgO* added to the reactor would react with the water to form brucite ($Mg(OH)_2$). Both the XRD and Rietveld refinement data confirms the presence of large quantities of brucite in all the samples. Of interest is what happens with the carbonate added and in which form it precipitates at a given temperature.

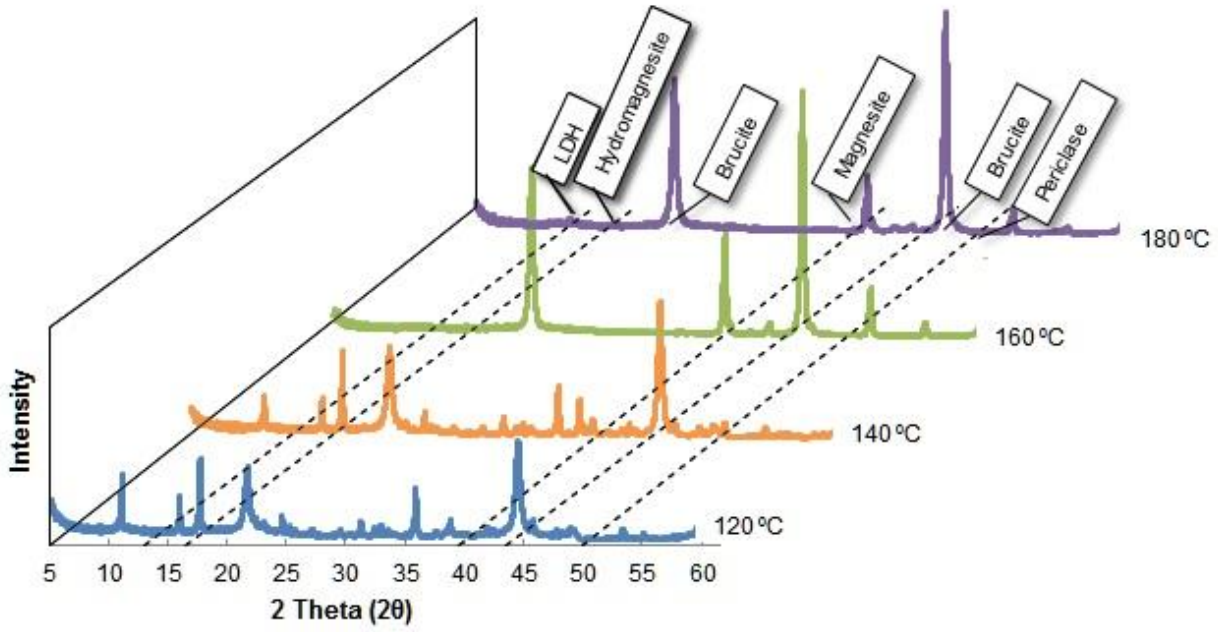

Figure 27: Combined XRD results for all experimental runs without aluminium hydroxide as reagent indicating primary peaks of phases.

Table 13: Rietveld analysis for magnesium species reacted at different reaction temperatures for 5 hours.

Reaction Temperature (°C)	Compound				
	***MgAl-CO_3* LDH**	***MgO***	***$MgCO_3$***	***$4MgCO_3 \cdot Mg(OH)_2 \cdot 2(H_2O)$***	***$Mg(OH)_2$***
120	-	-	-	**37.11**	**62.89**
	-	-	-	*0.57*	*0.57*
140	-	**0.4**	**6.88**	**33.48**	**59.23**
	-	*0.19*	*0.51*	*0.72*	*0.75*
160	-	**0.9**	**29.38**	-	**69.71**
	-	*0.3*	*0.57*	-	*0.51*
180	**4.38**	**0.76**	**16.06**	-	**78.8**
	0.54	*0.23*	*0.54*	-	*0.66*

From the data in Table 2 and XRD patterns in Figure 27, it is evident that the formation of magnesite is favoured at higher temperatures and hydromagnesite at lower temperatures, as described in literature – and their formation is not carbonate concentration driven. A reaction temperature of 140 °C and 5 hour reaction time is an intermediate condition where both species are formed in the absence of an *Al* source.

4.1.6. Comparison of reaction temperature

The Rietveld data for all the experiments were plotted for overall visual comparison and are shown in Figure 28. Figure 28(a) and (b) almost look like the inverse of the other, clearly showing how the formation of LDH is limited by the solubility of gibbsite. As the temperature is increased, the solubility of gibbsite is increased as well as the formation of the LDH.

As soon as the reaction temperature is above 140 ^{o}C, the formation of LDH and the reaction of $Al(OH)_3$ reaches a plateau and the conversion for LDH formation is almost 80 %. The majority of the reaction had already taken place, but the LDH which had formed doesn't have a high crystallinity, according to the XRD patterns. When looking at the top black line on the plateau in Figure 28(a), the rate of LDH formation is shown. As the temperature is increased the high yield of LDH takes place at a much shorter time.

Figure 28(c) shows the formation of hydromagnesite and correspond to the literature and Section 4.1.5, stating that the formation of this compound do prefer low temperatures. The formation of magnesite (Figure 28(d)) shows an interesting trend. Between 120 ^{o}C and 160 ^{o}C the formation is high in short reaction times, but, as soon as the reaction time or reaction temperature is increased the amount of magnesite decreases. Also, as the solubility of the gibbsite is increased with the increase in reaction temperature and time, the presence of magnesite decreases, indicating that the magnesium precipitates with the aluminium as an LDH which is a more stable form.

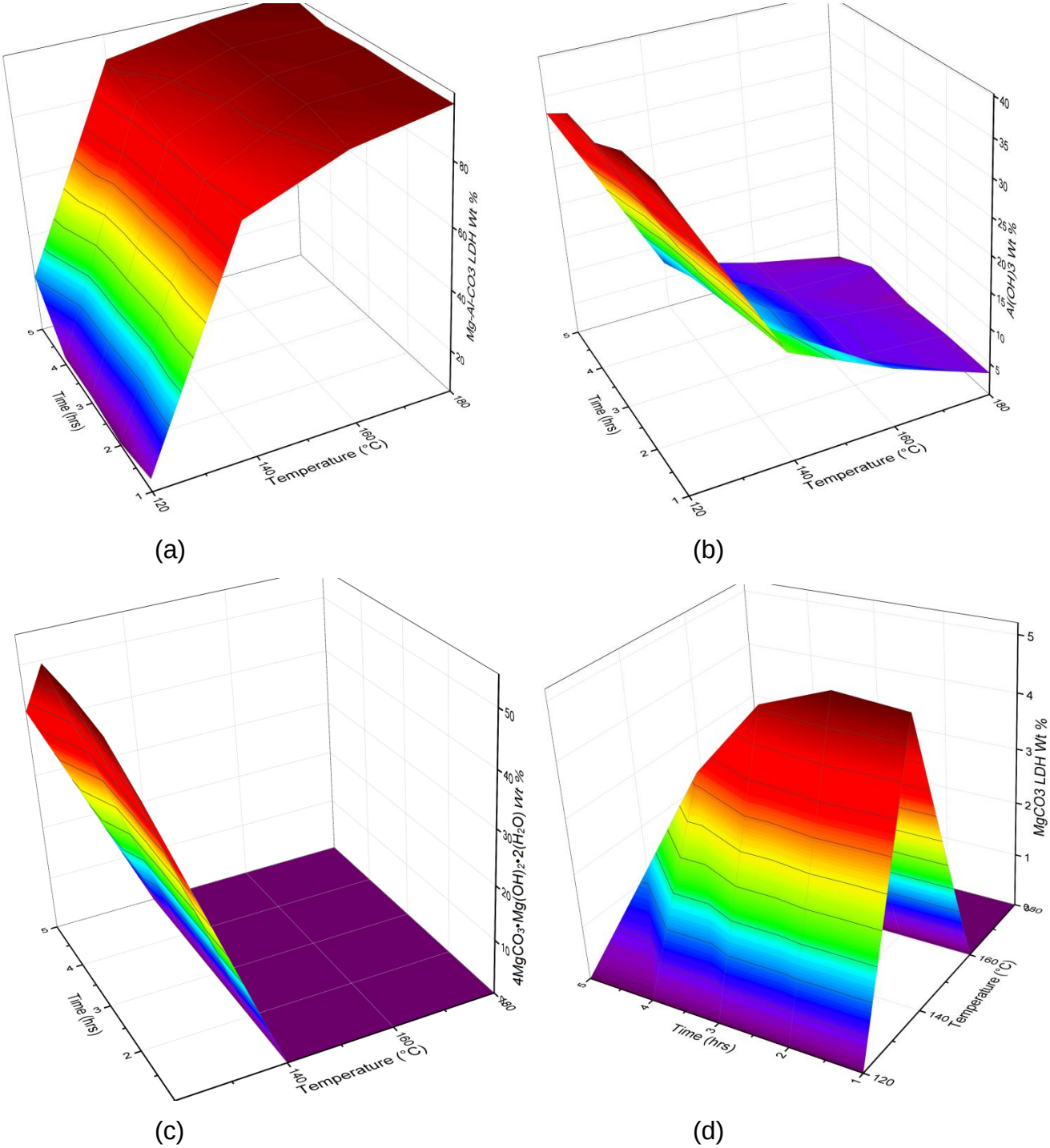

Figure 28: 3D representation of the Rietveld data obtained for the synthesis of *Mg-Al-CO$_3$* LDH at different reaction times and temperatures.

4.1.7. Inductively Coupled Plasma Mass Spectrometry analysis (ICP)

The detailed ICP analysis is shown in Appendix B. Figure 29 is a visual representation of the difference in the *Mg:Al* ratio as the temperature and time are increased.

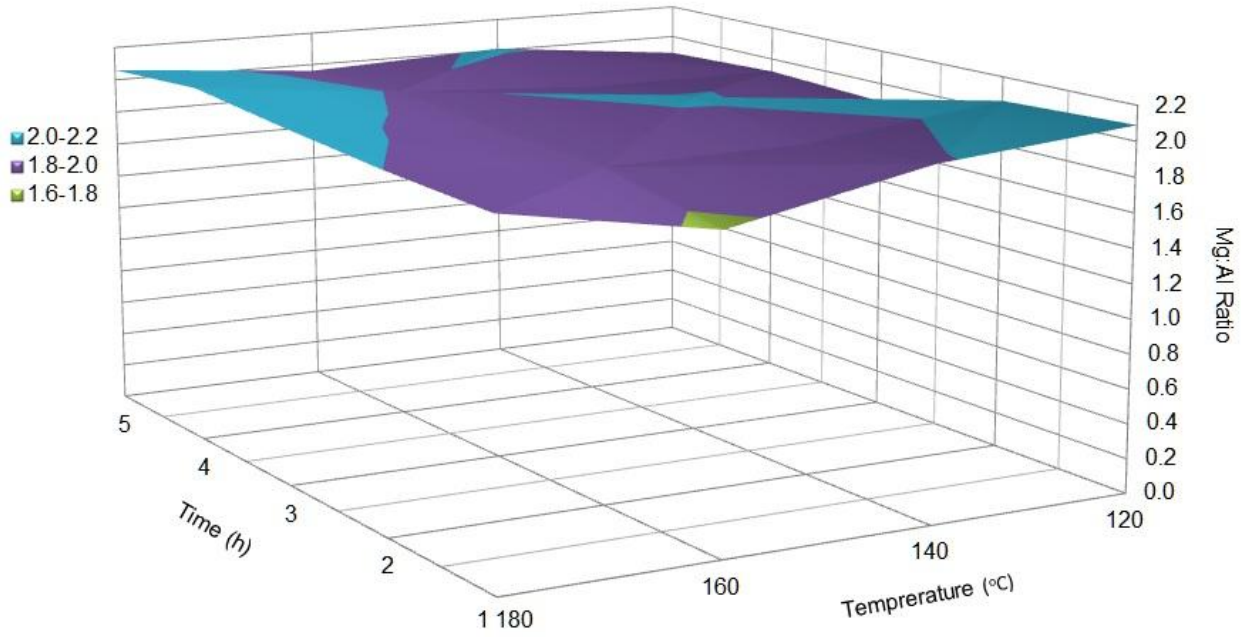

Figure 29: Ratio of *Mg:Al* obtained by ICP analysis.

It was expected that a plateau would have formed due to the high yield of LDH (which has a metal ratio of 2:1) and also the low presence *of* $Al(OH)_3$, $MgCO_3$ and $MgCO_3(OH)_2$ as the temperature and time increased above 160 ^oC and 3 hour. At 160 ^oC and after 1 hour reaction time a sudden decrease is noted. This could be possible due to dissolved *Mg* which had been washed out during filtering.

According to Figure 18 the solubility of *Mg* decreases with the increase in pH and for *Al* the solubility increases. At room temperature, the solubility of *Mg* is lower than *Al* for pH above 11. This could indicate that the solubility of the *Al* became more than *Mg* at 180 ^oC. It is known that pH does not stay constant with the change in temperature. The reason why the metal ratio increased for the 180 ^oC could possibly be due to the washout of *Al* during the filtering.

4.1.8. Brunauer-Emmett-Teller analysis (BET)

Brunauer-Emmett-Teller analysis (BET) was done and the results are shown in Appendix C. Figure 30(a) is a 3-dimensional illustration summary of the results obtained.

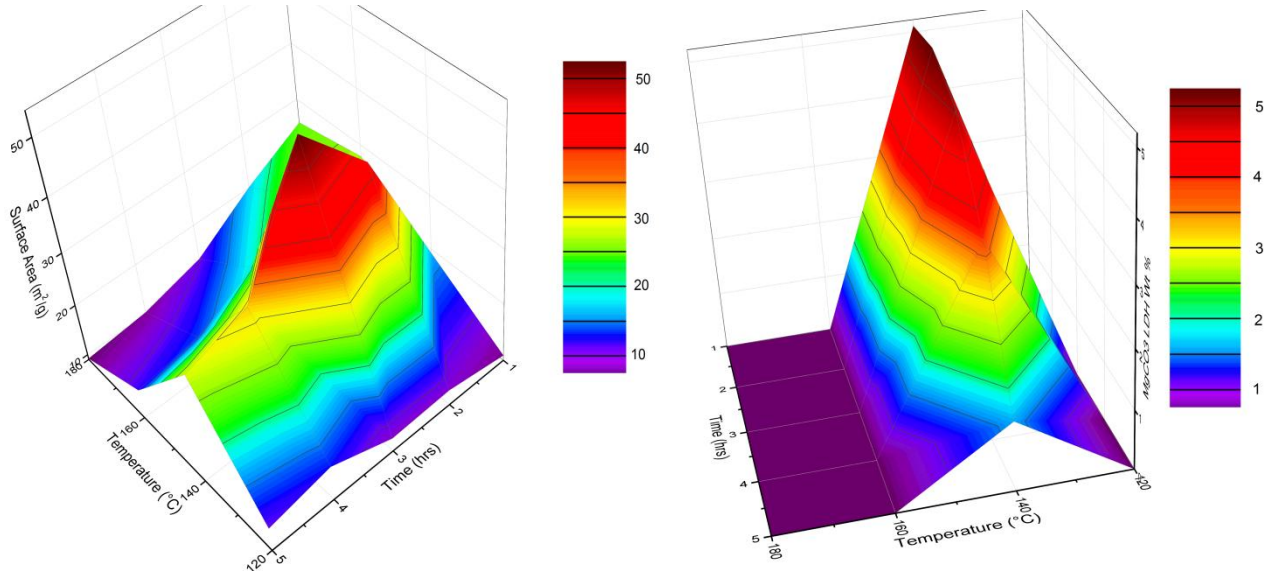

(a) (b)

Figure 30: Synthesis of *Mg-Al-CO3* LDH with the change in temperature and reaction time. (a) BET analysis. (b) Formation of magnesite.

A graduate decrease in surface area was expected to show on the results due to the increase in crystallinity of LDH, but, when looking at Figure 30, the results showed something different. When looking at the data shown in Appendix C, it is evident that at the lower range temperature (120 ^{o}C) the surface area increases with the formation of hydromagnesite. at 140 ^{o}C an inflection point occur for the surface area. at the lower reaction times (1-3 hours) there is an increase in surface area which corresponds to the Rietveld data which shows the increase in magnesite formation at the higher reaction times (4 to 5 hours) a sudden decrease in surface area is noted. These results corresponds to the decrease in magnesite formation and the increase in LDH formation. Therefore, it is evident that a decrease in surface area is expected with the increase in LDH formation. At the higher reaction temperatures the surface area is decreased as the crystallinity of the LDH is increased.

A surface area of 9.19 m^2/g was achieved at 180 ^{o}C after 5 hours reaction time.

4.1.9. Particle size analysis (PSA)

The detailed particle distribution analyses are shown in Appendix D. Figure 31 is constructed using the average particle size distribution (d_{50}).

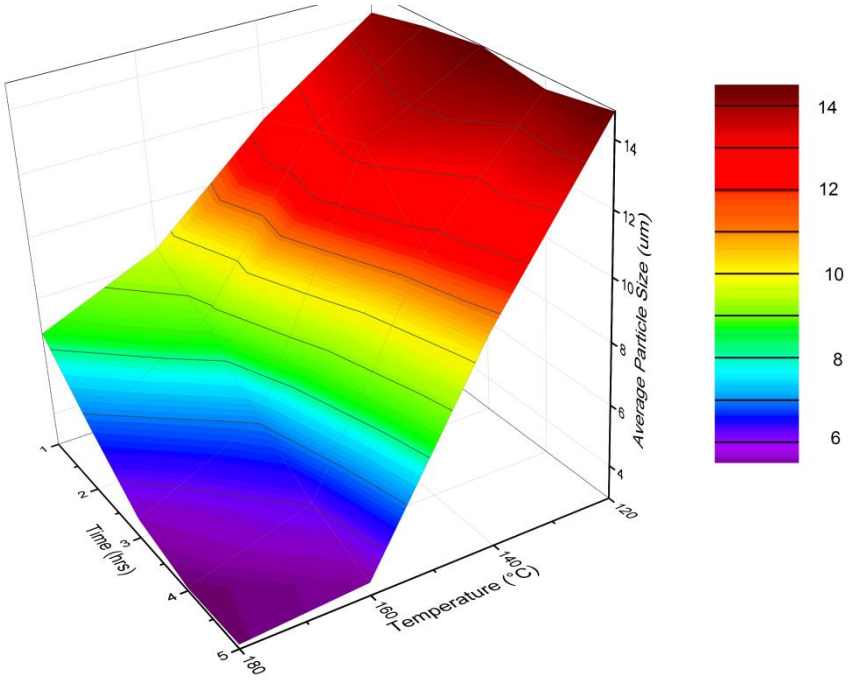

Figure 31: d_{50} values from the PSA for the synthesis of *Mg-Al-CO₃* LDH synthesis at different reaction time and temperatures.

The PSA result shown in Figure 31(a) is different than what was expected. An inflection line was expected indicating where the average particle size of all the reagents was overtaken by the growth of the LDH platelets during the ageing process at higher temperatures and reaction times. But instead, a graduate decrease in the particle size occurred, with the lowest particle size distribution of d_{50} = 3.05 µm occurring at 180 ^{o}C and after 5 hours reaction time.
The change in the particle size distribution as a function of reaction time at a constant reaction temperature was plotted and shown in Figure 32, Figure 33, and Figure 34 for comparison. The comparison between the particle size distributions for the synthesis that were done at 120 ^{o}C did not show any significant difference; therefore, it is not shown.

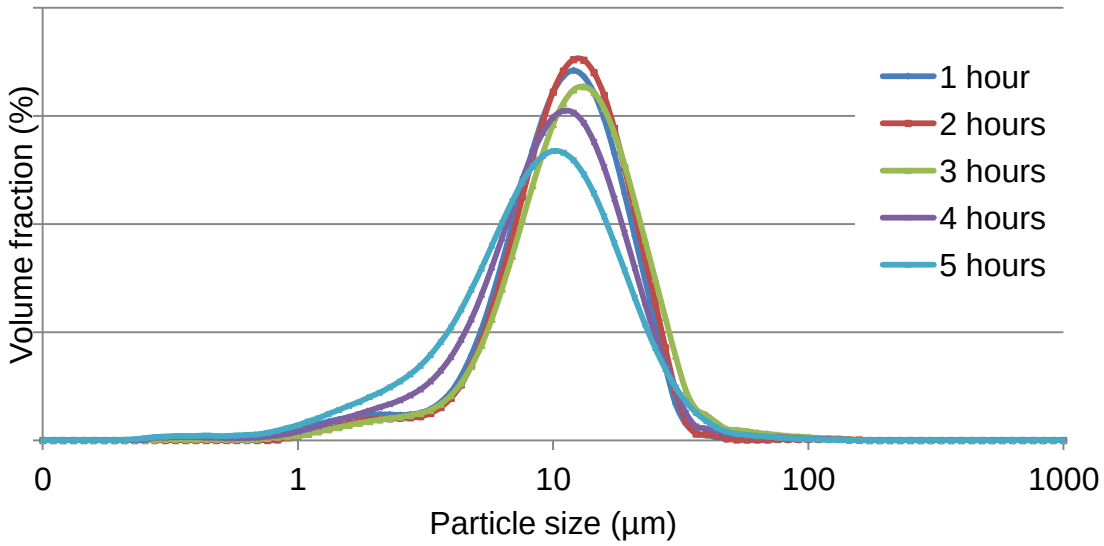

Figure 32: Particle size distribution for experimental runs at 140 ^{o}C.

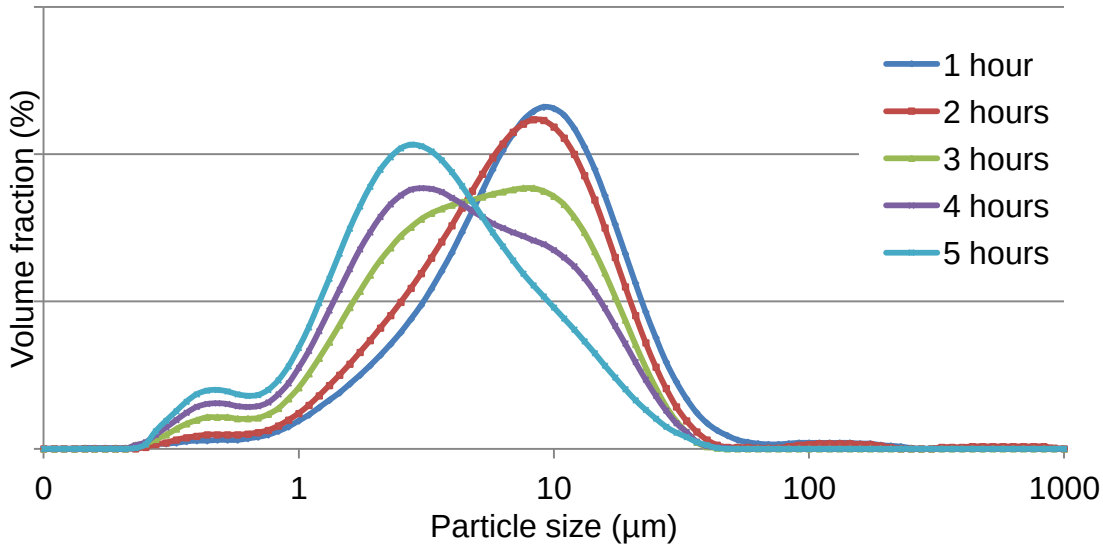

Figure 33: Particle size distribution for experimental runs at 160 ^{o}C.

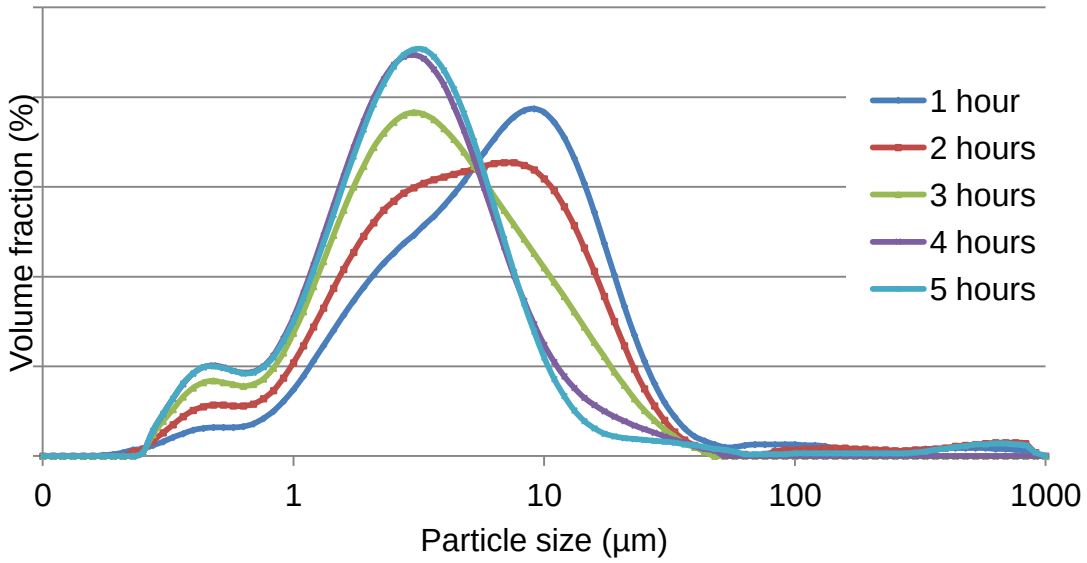

Figure 34: Particle size distribution for experimental runs at 180 ^{o}C.

The 140 ^{o}C reaction experiments show a slight decrease in the average particle size (d_{50}) of 2 µm (from 12 µm to 10 µm) and there is also an increase in the broadening of the base in the peaks. This could correspond to a mixture of hydromagnesite and the formation of the magnesite which has a lower surface area than that of hydromagnesite (results discussed in BET analysis).

The real difference is seen at temperatures of 160 ^{o}C and 180 ^{o}C respectively. Figure 33 shows a very nice particle size distribution. After 3 hours a bimodal peak is formed which shifts to the left (decrease in particle size) to finally form a normal distribution around 3 µm after 5 hours. The exact same results are obtained at 180 ^{o}C but only after 2 hours reaction time. The reason for the formation of these bimodal distributions followed by the normal distribution could be due to the following:

As the LDH starts to form within the first hour of reaction time, amorphous phase metal complexes starts to bond these platelets, forming these large agglomerates. As the reaction time is increased the amorphous compounds dissolves which results in the breaking of the agglomerates and the dissolved complexes precipitate to form new LDH crystals, under the Ostwald ripening method. There is a small peak which appears in Figure 33 and Figure 34.

This could be the presence of single formed LDH crystals in the sample, therefore, indicating that the size of a single LDH platelet could be less than 1 µm (approx. 500 nm).

4.1.10. Scanning electron microscopy (SEM) analysis

SEM was also done on only on some of the samples just to visually confirm the results obtained by the previous analysis. The images are shown in Appendix E.1. The presence of platelet structures can be seen corresponding to the hydromagnesite formation at low temperatures. It is difficult to completely distinguish between the different crystals, whether it is platelets or another form, indicating that there is a possibility for a mix between the subhedral hydromagnesite platelets, LDH platelets and possible gibbsite platelets (according to Rietveld data and XRD patterns). Other anhedral crystal structures are also noted in the sample which is difficult to distinguish. At short reaction time periods the occurrence of cyclic twinning is clear. As the reaction time and temperature is increased the size of the agglomerates starts to decrease (also less cyclic twinning present), therefore, confirming that it is possible that amorphous phase complexes bounding the LDH platelets. This corresponds to the results obtained by the particle size distribution analysis. The SEM images (160 ^{o}C and 180 ^{o}C) shows the presence of single LDH crystals in the sample which relates to the first peak (around 500 nm) of the particle size distribution graphs shown in Figure 33 and Figure 34. The platelets formed during the dissolution-precipitation process are not well-shaped hexagonal platelets compared to that of co-precipitated platelets. It looks like cyclic twinning that occurred for the experimental run that was done at 180 ^{o}C after 4 hours, but when looking very close it is noticed that the platelets are only joined at the edges, confirming the hypothesis proposed in the PSA results based on the assumption that amorphous phase complexes bounding the platelets together.

4.2 Partial substitution through dissolution precipitation method

The partial substitution experiments were conducted based on the results obtained from the *Mg-Al-CO_3* LDH optimisation and from the work done by Van der Westhuizen (2011) and Van

Graan (2012). From the *Mg-Al-CO_3* LDH synthesis it was proven that the formation of an LDH is limited by the following three parameters (arranged in sequence of significance):

1. The solubility of *$Al(OH)_3$*.
2. The solubility of the M^{2+} metal oxide
3. The formation of the LDH structure

The detailed XRD patterns obtained for each metal oxide are shown in Appendix A.3. Rietveld analysis could not be done on any of the samples due to unidentified peaks being present. The SEM-EDS results for all the experiments are shown in Appendix E.2. Some of the EDS spectrum graphs are not shown because it did not not add significant additional information to the results. The parameters that were monitored before, during and after each synthesis run are shown In Table 14 (*Ca*-substituted) and Table 14 (*Mg*-substituted).

Table 14: Reaction conditions for *Ca*-based samples during each run.

Sample	Temperature (°C)	Pressure (bar)	Mixer Speed (rpm)	pH	
				Before	After
Ca/Co(II)-Al (25 mole% subst.)	182	9.4	600	>13	>11
Ca/Co(III)-Al (25 mole% subst.)	182	9.4	600	>13	>13
Ca/Cu(II)-Al (25 mole% subst.)	175-178	7.8-8.4	600	>13	>11
Ca/Cu(I)-Al (25 mole% subst.)	173-178	7.3-8.5	600	>13	>10
Ca/Mn(II)-Al (25 mole% subst.)	176-178	8.0-8.5	600	>13	>10
Ca/Mn(II)-Al (8.3 mole% subst.)	174-182	7.5-9.2	600	>13	>13
Ca/Mn(IV)-Al (25 mole% subst.)	176-178	7.8-8.5	600	>13	>11
Ca/Mo-Al (25 mole% subst.)	170-182	6.8-9.4	600	>13	>13
Ca/Ni-Al (25 mole% subst.)	182-183	9.2-9.4	600	>13	>10
Ca/Ni-Al (8.3 mole% subst.)	175-178	7.7-8.4	600	>13	>13
Ca/Sn-Al (25 mole% subst.)	176-179	8.0-8.6	600	>12	>12
Ca/Sn-Al (8.3 mole% subst.)	174-176	7.5-8.0	600	>12	>12
Ca/Ti-Al (25 mole% subst.)	172-178	7.2-8.3	600	>13	>10
Ca/Ti-Al (8.3 mole% subst.)	176-178	7.9-8.5	600	>13	>13
Ca/Zn-Al (25 mole% subst.)	186	11.8-12.3	600	>12	>12

Table 15: Reaction conditions for *Mg*-based samples during each run.

Sample	Temperature (°C)	Pressure (bar)	Mixer Speed (rpm)	pH	
				Before	After
Mg/Co(II)-Al (25 mole% subst.)	181	9.0	600	>10	>9
Mg /Co(III)-Al (25 mole% subst.)	181	8.9-9.0	600	>10	>10
Mg /Cu(II)-Al (25 mole% subst.)	165-172	6.1-7.1	600	>10	>10
Mg /Cu(I)-Al (25 mole% subst.)	177	8.2	600	>10	>11
Mg /Mn(II)-Al (25 mole% subst.)	170-173	6.7-7.4	600	>10	>10
Mg /Mn(II)-Al (8.3 mole% subst.)	180	8.8	600	>10	>12
Mg /Mn(IV)-Al (25 mole% subst.)	181	9.0	600	>10	>10
Mg /Mo-Al (25 mole% subst.)	181	9.1	600	>10	>11
Mg /Ni-Al (25 mole% subst.)	181	9.1	600	>10	>10
Mg /Ni-Al (8.3 mole% subst.)	177-180	8.1-8.7	600	>12	>12
Mg /Sn-Al (25 mole% subst.)	162-165	6.5-6.9	600	>10	>10
Mg /Sn-Al (8.3 mole% subst.)	163-170	6.7-7.9	600	>10	>12
Mg /Ti-Al (25 mole% subst.)	166-168	6.2-6.5	600	>10	>10
Mg /Ti-Al (8.3 mole% subst.)	175-176	7.7-8.0	600	>10	>10
Mg /Zn-Al (25 mole% subst.)	166-168	6.2-6.5	600	>10	>10

During all the experiments mentioned above, the pH was achieved by the presence of *MgO*/*CaO* with its partial dissociation in water respectively. Because *Mg* and *Ca* are both alkaline earth metals, pH values of 10.3 and 13 respectively were achieved and therefore no *NaOH* was needed to achieve the minimum pH requirement of 10.

4.2.1. *Al*-solubility

Due to the fact that the solubility of $Al(OH)_3$ increases with the increase in pH (Figure 18), it was assumed that the *Ca*-based experiments would not have an *Al*-solubility problem because of the high pH the $Ca(OH)_2$ provides (Van Graan, 2012) required for the solubility of *Al*. It is evident from Table 14 that the *Ca* did provide enough pH. Because *Al* was used as primary trivalent metal species, it was assumed that the main factor influencing the formation of LDH was the solubility of the *Al*.

Most of the XRD patterns in Appendix A.3. (*Ca*- and *Mg*-based) indicate that the gibbsite used for each experiment had dissolved and some of the gibbsite had either precipitated in the form of boehmite or another metal hydroxide compound. There are some experiments that showed the presence of gibbsite (*Mg-Sn* as well as *Mg-Zn* partial substitution), indicating that the conditions for the dissolution of gibbsite were far from ideal. Apart from these two samples the formation of an LDH for the majority of the samples was not limited by gibbsite.

4.2.2. M^{x+}-solubility

This section focusses on the solubility of the M^{x+} metal species and not the formation of LDH, therefore, the inert samples were mainly used and the carbonate samples were only used to determine whether the presence of a carbonate source had influenced the solubility of the metal species. For the solubility of the desired M^{x+} metal species used there were a couple of samples which showed no/negligible solubility (according to the XRD patterns shown in Appendix A.3.).

4.2.2.1. *Ca*-based experiments

Figure 35 represents the XRD patterns obtained for the *Ca-Co* substitution experiments. The presence of a carbonate source also did not have any effect the solubility of the cobalt. The primary peak for the silica-free hydrogarnet is situated at the 2θ position of approx. 20°, followed by the seconday peak at 46°. Hydrogarnet has a similar composition and XRD pattern to that of Katoite (Van der Westhuizen, 2011), indicating that it is another crystal form of this *Ca-Al* compound (katoite).

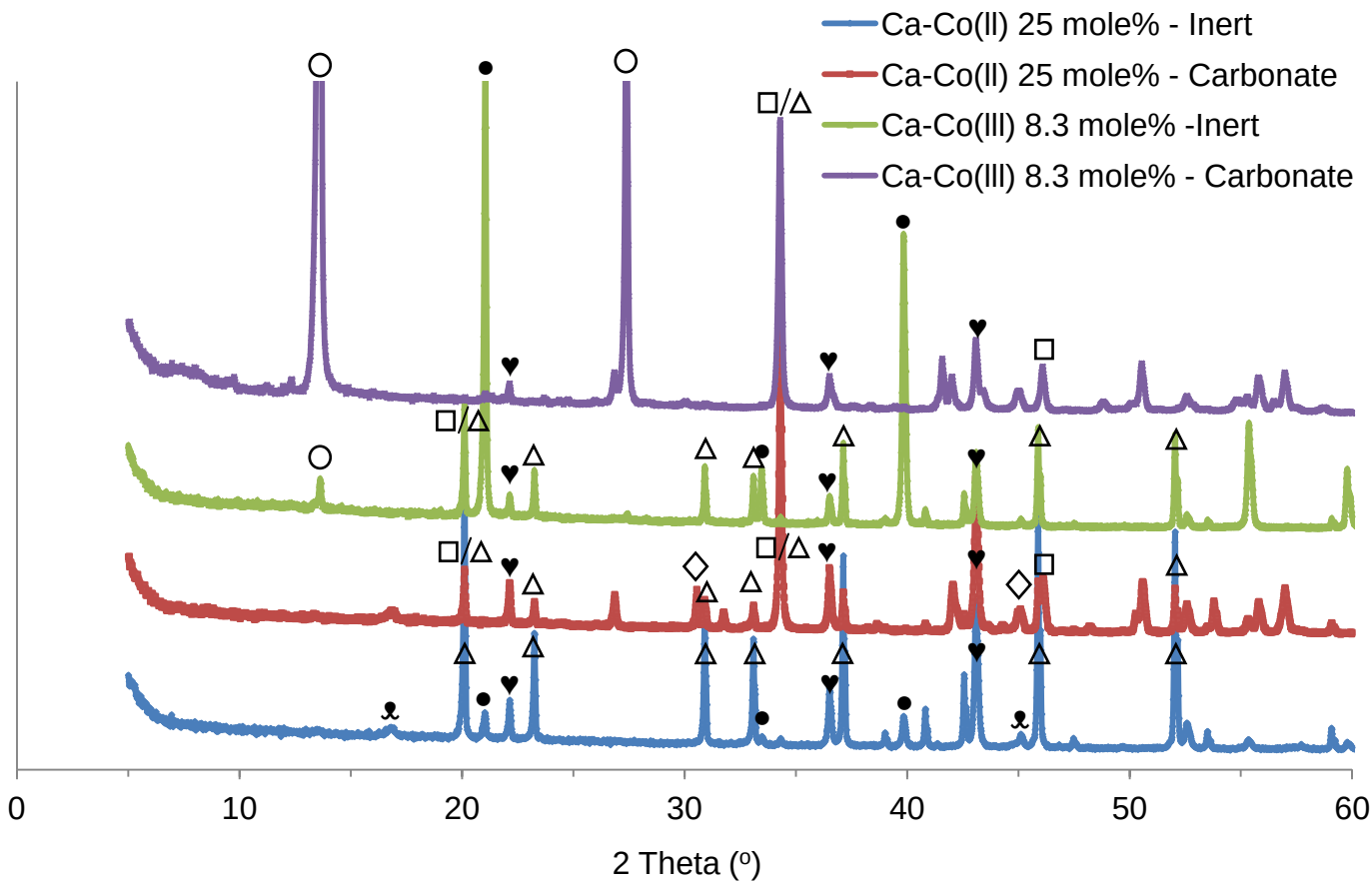

Figure 35: XRD patterns for *Ca-Co* partial substitution. (△) Hydrogarnet. (♥) Co_3O_4. (□) Calcite. (○) LDH. (ᵹ) Boehmite. (●) Portlandite. (◇) Aragonite.

When comparing the 25 mole% inert substitution to the 8.3 mole% inert substitution samples, it is observed that the peak intensity for the hydrogarnet is not that intense at the higher cobalt concentration compared to the 8.3 mole% sample. Although the peak intensities on XRD patterns don't give quantitative results, it can give a possible indication on the composition. Therefore, the presence of the cobalt(ll and lll) in the reactor did have an influence on the stability of the *Ca*. It is also observed that when the samples were exposed to a carbonate source, the formation of calcite ($CaCO_3$) were much more favoured at lower cobalt concentrations. This could be due to the fact that there is more portlandite ($Ca(OH)_2$) present and able to form calcite. It is noted that some of the hydrogarnet peaks coincide with that of calcite; therefore, there is a possibility that the carbonate samples may contain some unreacted hydrogarnet. The formation of aragonite (another crystal phase of $CaCO_3$) noticed

in the 25 mole% *Ca-Co* substitution sample might be influenced by the presence of cobalt. At the lower concentration the presence of aragonite could not be determined. Figure 36 shows the Pourbaix diagram for cobalt in water at 25 ^{o}C.

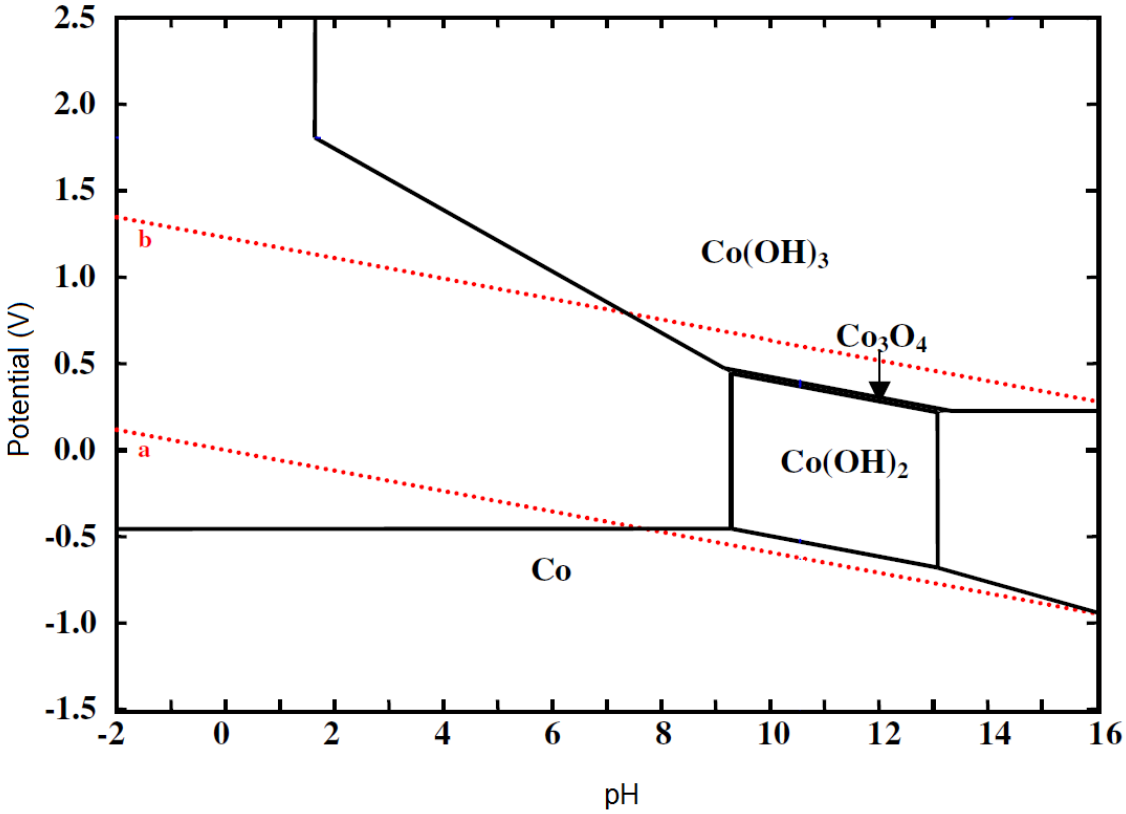

Figure 36: Pourbaix diagram for *Co-H_2O* at 25 ^{o}C (Adapted from Chivot *et al.*, 2008)

Looking at Figure 36 the solubility is rather low and according to Chivot *et al.* (2008) the solubility of cobalt does not show a significant increase with the increase in temperature. Also, it seems that the stable phase for cobalt is *Co_3O_4* which is the reagent used for the experiments which occurs within the pH range of just below 10 to approx. 13. This explains why cobalt did not show any sign of solubility.

The following substitution experiments also indicated no/negligible signs of solubility for the M^{x+} metal species (See Appendix A.3.):

- *Ca-Cu(II)* 25 mole%
- *Ca-Ni* 25 mole%

- *Ca-Sn* 25 mole%
- *Ca-Sn* 8.3 mole%
- *Ca-Zn* 25 mole%

The SEM-EDS images correspond to the XRD patterns, as shown in Appendix E.2.

The *Ca-Cu(I)* 25 mole% partial substitution experiments showed different results on the XRD patterns(Figure 89 and Figure 90 in Appendix A.3.). Cuprite (Cu_2O) was used as reagent for the experiment and, according to the results; partial dissolution of the copper oxide did occur and had re-precipitated as tenorite (*CuO*). Looking at the pH values before and after the substitution experiments for both copper(I) and copper(II), a decrease in the final pH was noted (Table 14). When comparing this to Figure 37, it is noted that the boundary between copper(I) and copper(II) is in the pH range of 10 to 12. However, it is known that the phases of the species on the phase diagram shifts with the increase in temperature. This also holds true for the samples which indicated no/negligible solubility.

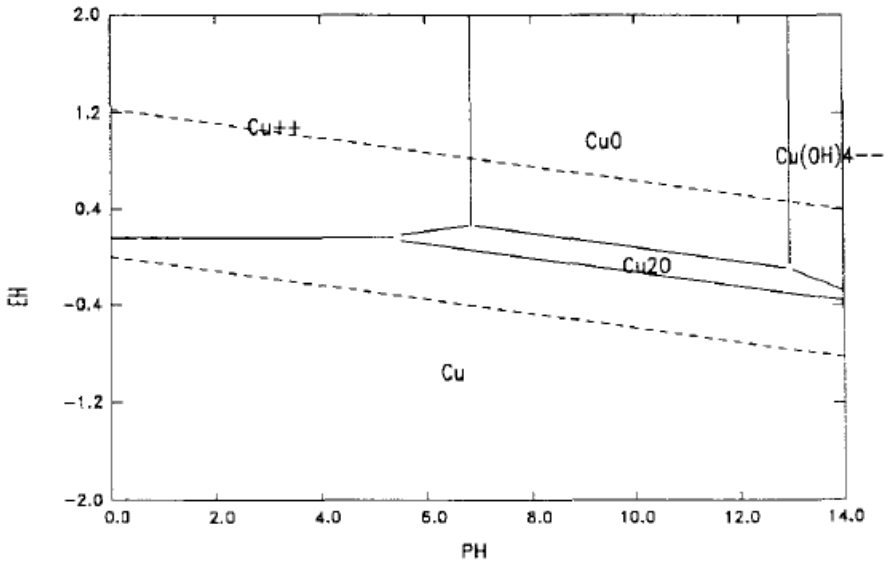

Figure 37: Pourbaix diagram for *Cu-H_2O* at 25 ^{o}C (Osseo-Asare and Mishra, 1996).

When comparing the XRD pattern peak intensities for the *Ca-Cu(I)* 25 mole%-inert sample, it seems like a small amount of cuprite had dissolved and re-precipitated.

The SEM-EDS image obtained for the inert sample is shown in Figure 38. The “ball”-like crystals in Figure 38 correspond to that of the precursor (katoite) mentioned by Van der Westhuizen (2011). From the SEM-EDS image it is clear that the composition of these “ball”-like crystals is mainly *Ca* and *Al*, indicating that is katoite. Large *Cu*-agglomerates is noted on the surface of the katoite crystals, indicating that there is no copper present in the precursor. Some unreacted $Al(OH)_3$ and $Ca(OH)_2$ is noted when looking at the highly concentrated areas on the metal species mapping images.

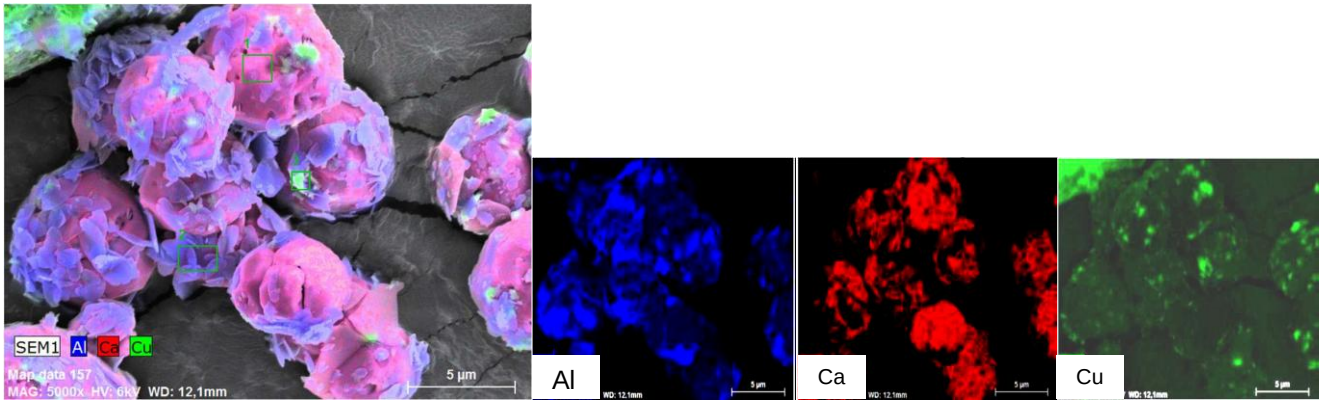

(a) (b)

Figure 38: SEM-EDS image for *Ca-Cu(I)* 25 mole%-inert partial substitution. (a) Overall metal species mapping. (b) Individual mapping for each metal species.

Significant difference is observed when comparing this result to the 25 mole%-carbonate sample. It seems like the presence of a carbonate source aids in the solubility of cuprite when comparing the peak intensities.

The partial substitution using *Mn* showed promising results, apart from the *Ca-Mn(II)* 25 mole% mentioned earlier. Figure 39 shows the XRD patterns obtained for the manganese substitution experiments.

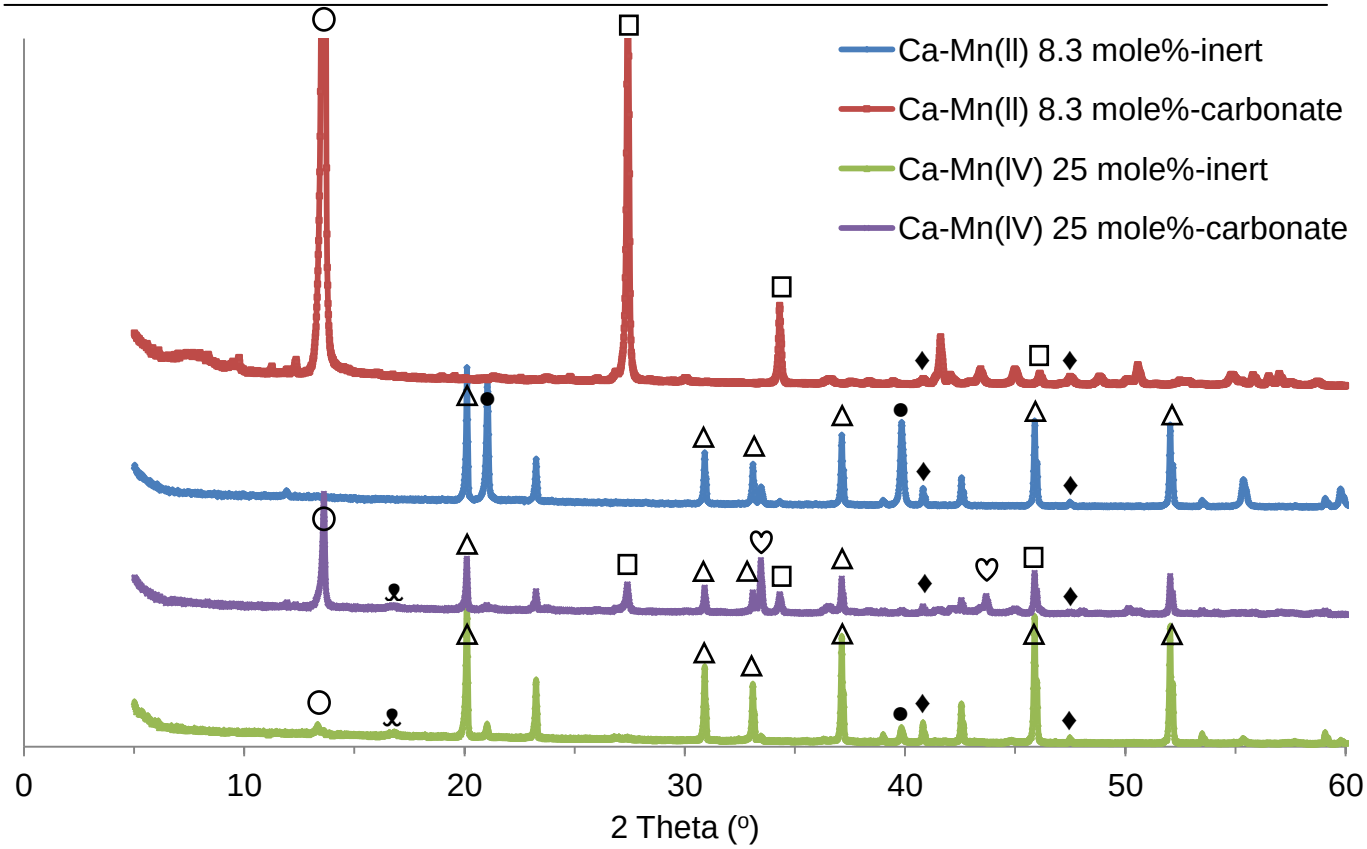

Figure 39: XRD patterns for *Ca-Mn* partial substitution experiments. (△) Hydrogarnet. (♡) Pyrolusite. (□) Calcite. (○) LDH. (♦) Manganosite. (ᵴ) Boehmite. (●) Portlandite.

Starting with the manganese(ll) 8.3 mole%-inert sample, according to the XRD patterns obtained there are significantly low manganosite in the sample. But when looking closely at the XRD patterns, it is noted that the hydrogarnet peaks coincide with that of manganosite (with the primary peak situated at approx. 47.5^{o} and secondary peak at approx. 40.5^{o}, see Appendix A.3.). This made it very difficult to distinguish between the two species on the XRD patterns. Therefore, there is probably manganosite present in the sample. The sample also has significantly high portlandite present. SEM-EDS image obtained for this sample is shown in Figure 40.

The image clearly shows the presence of large manganese crystals, therefore, confirming that there is manganosite present in the sample. Although SEM-EDS images are based on a small quantity of the sample, the same results were obtained repeatedly for a number of small sample quantities. When looking at the distribution of the metal species (Figure 40(b)) it is

noted that there is a possibility that manganese is part of the precursor product. This indicates that partial dissolution of the manganese did occur. The sample that was exposed to a carbonate source (*Ca-Mn(II)* 8.3 mole%-carbonate) clearly shows the manganosite peaks, making it easy to identify. A large quantity of the hydrogarnet did react to form calcite, but the calcite peak intensity is relatively small compared to that that was found in the *Ca-Co* substitution experiments. This result possibly indicates that the presence of manganese may lower the reaction rate for the formation if calcite.

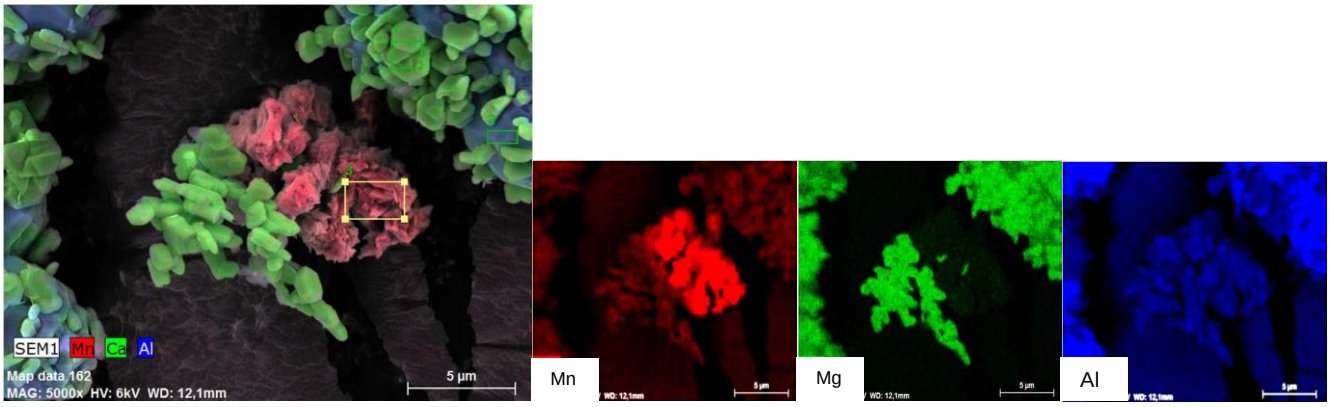

(a) (b)

Figure 40: SEM-EDS image for *Ca-Mn(II)* 8.3 mole%-inert partial substitution. (a) Overall metal species mapping. (b) Individual mapping for each metal species.

Pyrolusite (MnO_2) was used as reagent for the *Ca-Mn(IV)* 25 mole% partial substitution experiment. The primary and secondary peaks for pyrolusite in the XRD pattern are situated at approx. 33.5^o and 43.5^o respectively as shown in Figure 39. On the XRD pattern for the Co-Mn(IV)-inert 25 mole% sample, a small peak is noticed indicating the presence of manganosite and the peaks representing pyrolusite is negligible. This indicates that the dissolution of pyrolusite did occur and that the conditions were good. There is a small peak shift to the left noticeable for the hydrogarnet, indicating the possible presence of manganese. Figure 41 shows the SEM-EDS image obtained.

The “ball”-like crystals noticed in the SEM-EDS image correspond to that of hydrogarnet. The distribution of the metal species clearly indicates the homogeneous distribution of the manganese. It is possible that the manganese is situated on the surface of the precursor, but,

it is believed that the manganese is part of the precursor. After exposing the sample to a carbonate source the precipitation of pyrolusite was significant. According to the XRD graph a large amount of the hydrogarnet did not react to form calcite, indicating that the presence of manganese during the carbonate reaction had possibly an inhibiting effect. These results correspond to the SEM-EDS image shown in Figure 174, Appendix A.3.

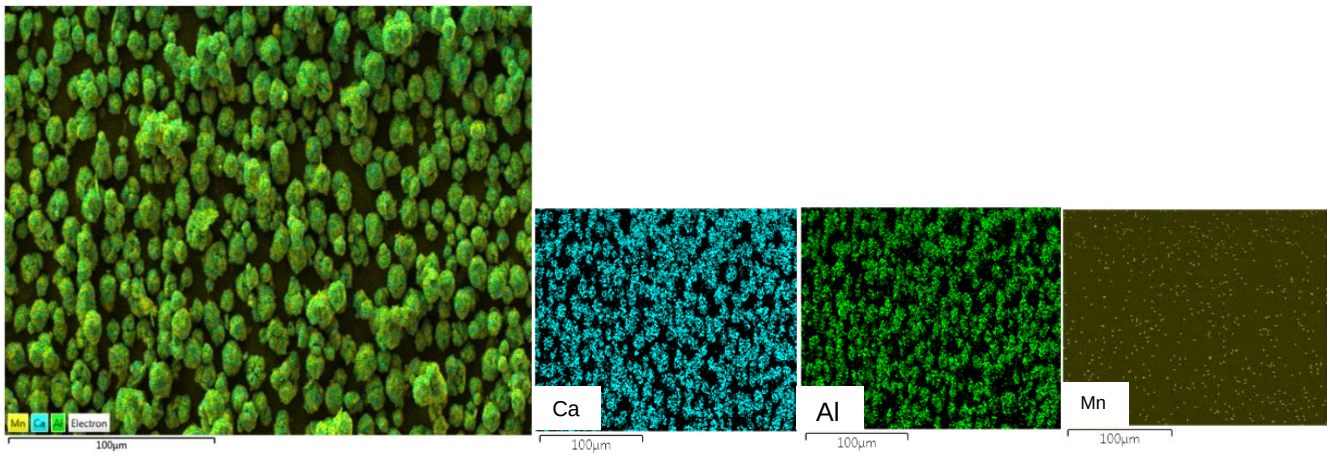

(a) (b)

Figure 41: SEM-EDS image for *Ca-Mn(IV)* 25 mole%-inert partial substitution. (a) Overall metal species mapping. (b) Individual mapping for each metal species.

The dissolution conditions for molybdenum proved to be ideal for the *Ca-Mo* 25 mole% partial substitution. The both the inert and carbonate XRD patterns (Figure 102 and Figure 103, Appendix A.2) picked up molybdenum as powellite ($CaMoO_4$). This is a good indication that the molybdenum has the potential to bond with the *Ca*. When looking closely at the powellite, hydrogarnet and LDH patterns, it seems that there is a slight misfit. The SEM-EDS image for both the inert and carbonate samples are shown in Figure 42 and Figure 43 respectively.

From the image it seems that molybdenum took part in the formation of the precursor in the inert sample. The precursor clearly shows the homogeneous distribution of molybdenum. The carbonate sample shows a relatively large molybdenum concentration at the lower middle of the image (*Mo*-distribution in Figure 43(b)). These SEM-EDS results conclude that the conditions for the dissolution of molybdenum were good.

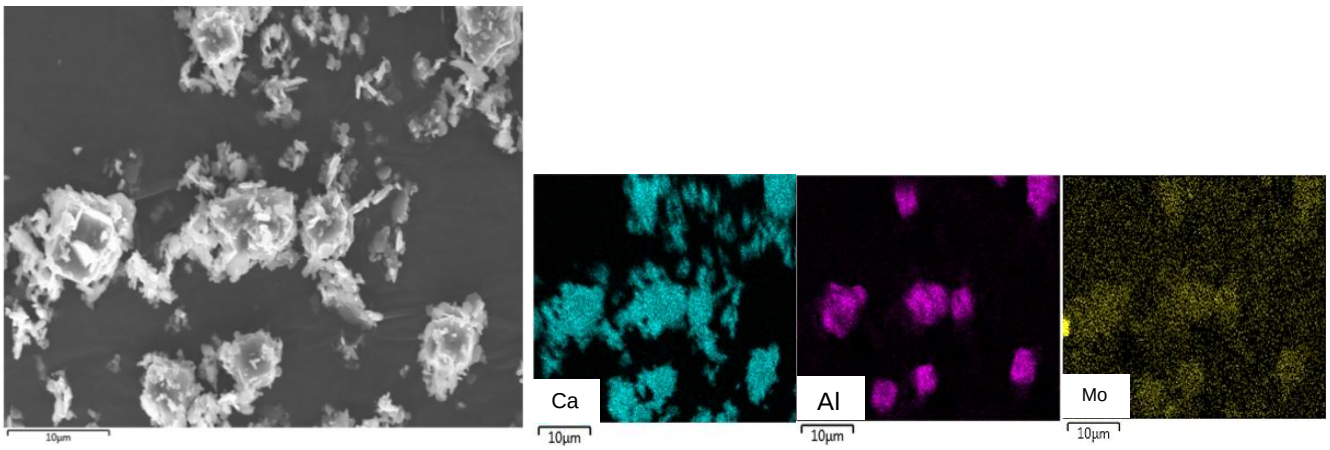

(a) (b)

Figure 42: SEM-EDS image for *Ca-Mo* 25 mole%-inert partial substitution. (a) Area used for metal species mapping. (b) Individual mapping for each metal species.

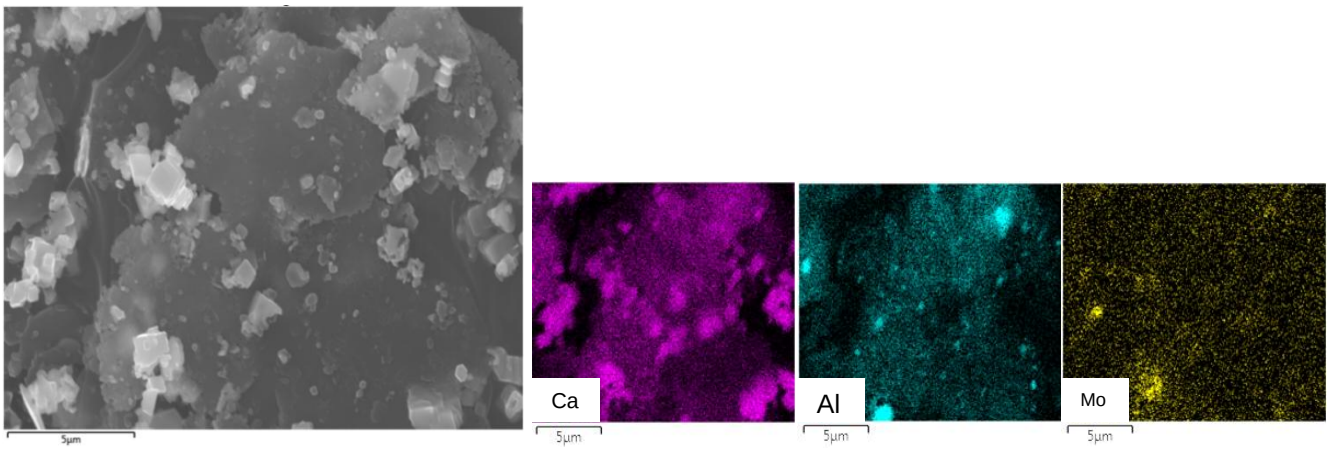

(a) (b)

Figure 43: SEM-EDS image for *Ca-Mo* 25 mole%-carbonate partial substitution. (a) Area used for metal species mapping. (b) Individual mapping for each metal species.

The XRD pattern obtained for the *Ca-Ni* 8.3 mole%-inert partial substitution displayed high intensity peaks for *NiO* indicating that there are still reagent present (Figure 107 in Appendix A.3.). When looking closely at the hydrogarnet peaks there is a small misfit. This shows that the compound could possibly contain nickel. The SEM-EDS image shown in Figure 44 showed a different result.

Looking at the distribution for nickel, it is clear that it took part in the formation of the 'ball'-like shape precursor. This corresponds to the slight peak shift on the XRD pattern for the hydrogarnet.The image also indicates that a *Ca-Ni* complex had formed, but isn't reported on the XRD pattern, although all the peaks on the XRD pattern have all been identified. This could be a *Ca-Ni* crystal/amorphous complex which had possibly formed and the XRD pattern for the crystal phase could coincide with that of hydrogarnet, portlandite, bunsenite (*NiO*) or hydrocalumite. Or, the peaks of this compound coincide with the species mentioned. The formation of calcite also occurred when the sample was exposed to a carbonate source.

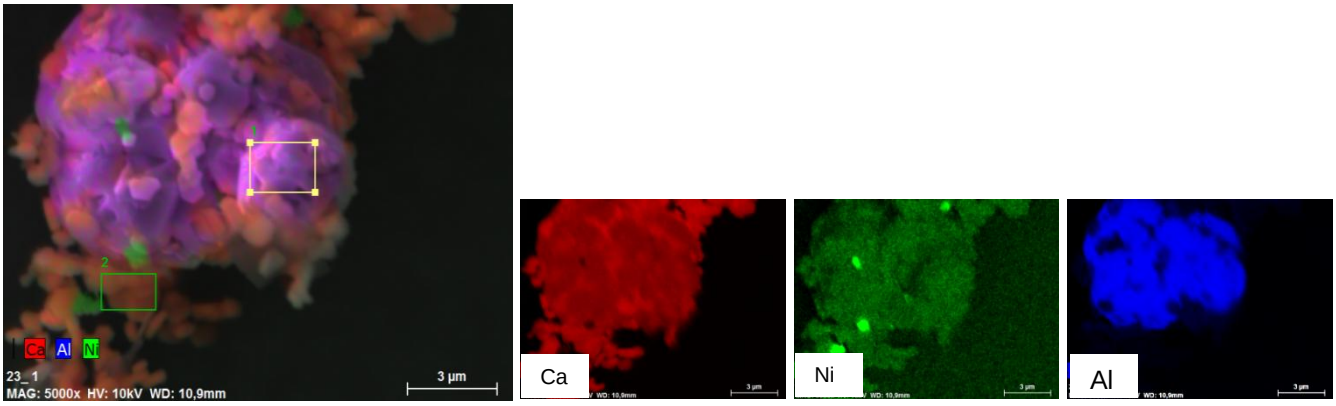

(a) (b)

Figure 44: SEM-EDS image for *Ca-Ni* 8.3 mole%-inert partial substitution. (a) Overall metal species mapping. (b) Individual mapping for each metal species.

The XRD pattern for the carbonate sample indicates the formation of an *Al-Ni-OH* complex (Figure 108). This is not true due to the significant misfit. There are also a large number of unidentified peaks which couldn't be identified. Overall, the results indicated that the conditions were not optimal, but good for the dissolution of nickel.

Figure 45 shows the XRD patterns obtained for the *Ca-Ti* partial substitution experiments. It appears that almost no anatase had dissolved during the 25 mole%-inert experiment. The peak intensity is still large for anatase and no other form of titanium were detected. But the SEM-EDS image obtained for this specific experiment showed a different result, as can be seen in Figure 46. Similar results were observed in a number of different sites of the sample during analysis. There is a possibility that the titanium had precipitated in smaller crystals onto

the surface of the precursor or that the titanium took part in the formation of the precursor. Both these options indicate that the conditions to dissolve the titanium were good, but not optimal.

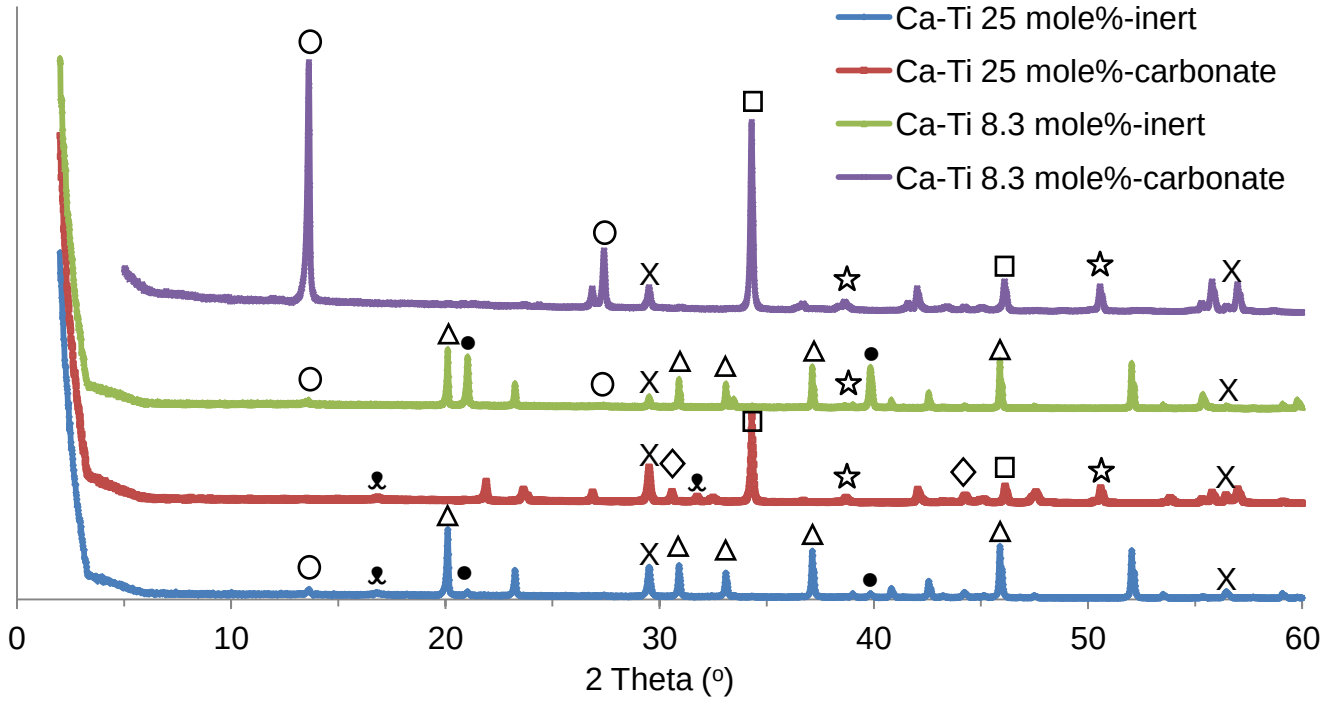

Figure 45: XRD patterns for *Ca-Ti* partial substitution. (△) Hydrogarnet. (X) Anatase. (□) Calcite. (○) LDH. (☆) Perovskite. (◇) Aragonite. (⚷) Boehmite. (●) Portlandite.

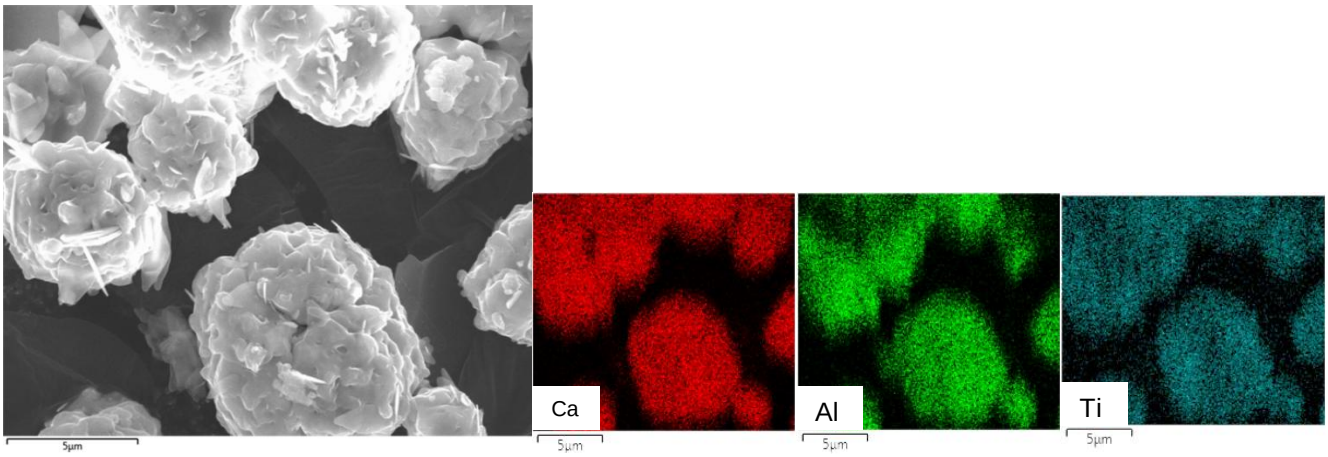

(a) (b)

Figure 46: SEM-EDS image for *Ca-Ti* 25 mole%-inert partial substitution. (a) Area used for metal species mapping. (b) Individual mapping for each metal species.

A number of sights during the SEM-EDS analysis displayed the same results, but some areas showed the presence of large titanium crystals, as shown in Figure 191 (Appendix E.2.). When comparing these results to the 25 mole%-carbonate sample (XRD - Figure 118, EDS - Figure 192), most of the precursor had reacted to form calcite and the aluminium had precipitated as boehmite.

There is also a slight increase in the peak intensity of the anatase. The carbonate sample also indicates the formation of a *Ca-Ti* metal complex (Perovskite) which also indicates that some of the anatase had dissolved. The SEM-EDS images for the Ca-Ti 8.3 mole% partial substitution experiments are shown in Appendix E.2. (Figure 193 and Figure 194) and correspond with the results obtained by the XRD patterns. Both the inert and carbonate samples for the 8.3 mole% partial substitution experiments showed similar results. The inert sample also indicated the presence of titanium in the precursor (Figure 193), but the concentration of the titanium appeared to be lower. The exposure to a carbonate source resulted in the formation of calcite. Comparing the peak intensities between the two titanium-carbonate samples, it clearly indicates that more calcite had formed at a lower titanium concentration. This corresponds to the amount of $Ca(OH)_2$ initially added to the reactor. The 8.3 mole%-carbonate sample also indicates the presence of aragonite in the sample.

Overall, it is confirmed that the conditions for the dissolution of titanium were good, but the initial concentrations added for each run might not have been ideal.

4.2.2.2. *Mg*-based experiments

The detailed XRD patterns and SEM-EDS images obtained for all the *Mg-*M^{x+} partial substitution experiments are shown in Appendix A.1. and in Appendix E.2. respectively. The *Mg-Co* partial substitution experiments showed similar results compared to that which were obtained by the *Ca*-based experiments. Figure 47 displays the XRD patterns obtained for the *Mg-Co* partial substitution experiments.

When looking at the detailed XRD patterns in Appendix A.3., it is noted that there are a couple of unidentified peaks present. These peaks could resemble any metal complex which

could have formed consisting of either *Mg*, *Al* or *Co*. However, the intensity of these peaks is small and insignificant, indicating that although partial dissolution of the *Co* could have occurred, the conditions were far from ideal.

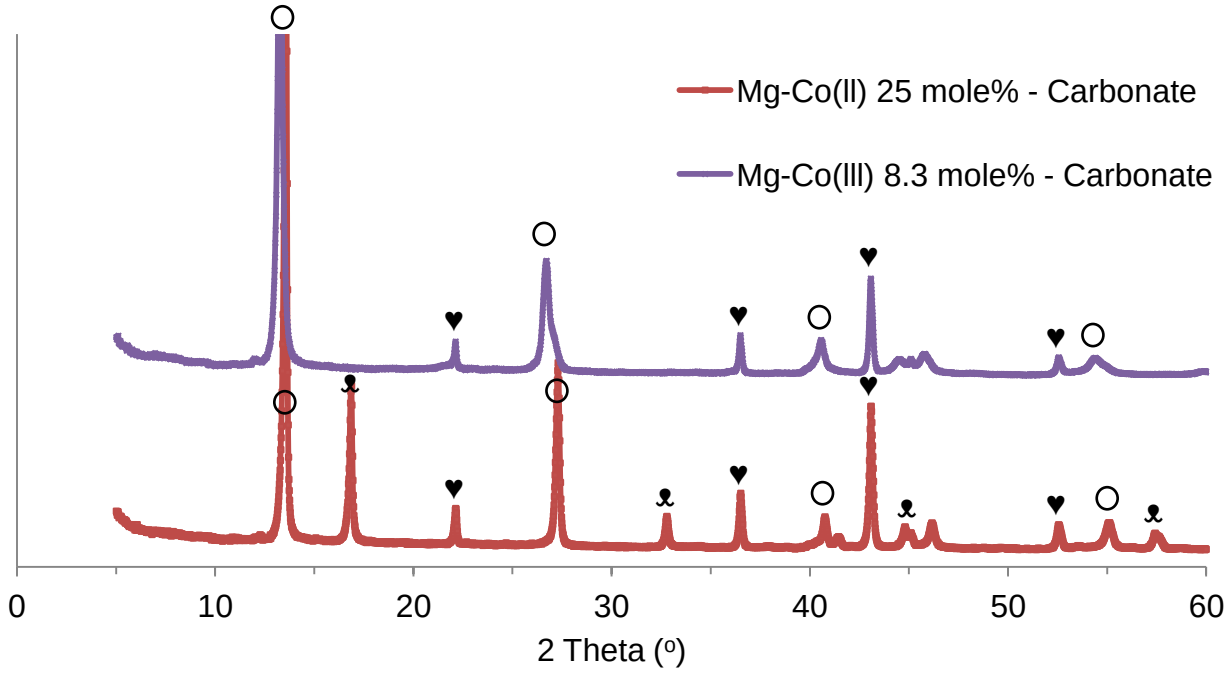

Figure 47: XRD patterns for *Mg-Co* partial substitution. (○) LDH. (♥) $Co3O_4$. (♟) Boehmite.

A shift in the LDH peak is noted between the 25 mole% and 8.3 mole% samples. This result is further discussed in Section 4.2.3: Possible formation of LDH and LDH composition. The 25 mole%-carbonate sample indicates the presence of sodium carbonate (Na_2CO_3). This could be true due to the decomposition of sodium bicarbonate ($NaHCO_3$) to sodium carbonate during the reaction run which was followed by improper washing during the filtering process. The SEM-EDS results shown in Figure 85 and Figure 86 (Appendix A.3.) coincide to these XRD patterns. For both the samples the large Co-crystals are observed, verifying the poor dissolution conditions.

Similar results were obtained for the following experiments and the detailed results are shown in Appendix A.3. and Appendix E.2. for verification.

- *Mg-Cu(II)* 25 mole%
- *Mg-Cu(I)* 25 mole%

- *Mg-Ni* 25 mole%
- *Mg-Ni* 8.3 mole%
- *Mg-Sn* 25 mole%
- *Mg-Sn* 8.3 mole%

The *Mg-Mn(II)* 8.3 mole%-carbonate sample (Figure 98) indicates the presence of both manganosite and periclase (*MgOH*) and the peaks for these two compounds are almost identical. It is assumed that possibility of periclase being part of the sample with such high peak intensity is unlikely, therefore, it is concluded that these peaks on the XRD pattern represents that of manganosite. The same accounts for the *Mg-Mn(IV)* 25 mole% partial substitution experiment. These results correspond to that found in the SEM-EDS images (Figure 97 and Figure 98 in Appendix E.2.). Lepidocrocite (*γ-FeO(OH)*) was picked up in the *Mg-Mn(IV)* 25 mole%-carbonate sample, but the primary and secondary peaks of this Fe-compound is the lay at the same position than that of boehmite (at 17^{o} and 33^{o} respectively). Therefore, it is concluded that boehmite is in the sample and not lepidocrocite due to the fact that no *Fe*-based reagent was used for any of the dissolution-precipitation reactions and the dissolution of the reactor vessel steel is unlikely to occur.

Molybdenum also showed similar results when compared to the *Ca-Mo*-based experiments. The XRD pattern in Figure 104 (Appendix A.3.) shows a significant amount of unidentified peaks which could be possible Mo-containing compounds. According to the SEM-EDS image shown in Figure 178 (Appendix E.2.) it seems as if the molybdenum is all over the sample in a homogeneous distribution. It is possible that the image shown for the distribution of molybdenum could be due to back scattering. A number of different sites were investigated at different magnifications, but no trace could be found. Therefore, further investigation must be done do determine the results.

The *Mg-Ni* 25 mole%-crabonate sample also showed no/negligible signs of dissolution of NiO according to the XRD pattern shown in Figure 109 (Appendix A.3.), however, there is a small peak noticed at around 10^{o}. This corresponds to an interlayer of approx. 10.3 Å. The

difference is significant, and this anomaly is further discussed in Section 4.2.3. The rest of the *Mg-Ni* partial substitution experiments didn't indicate signs of significant importance.

The XRD patterns obtained for the *Mg-Ti* partial substitution experiments are shown in Figure 48.

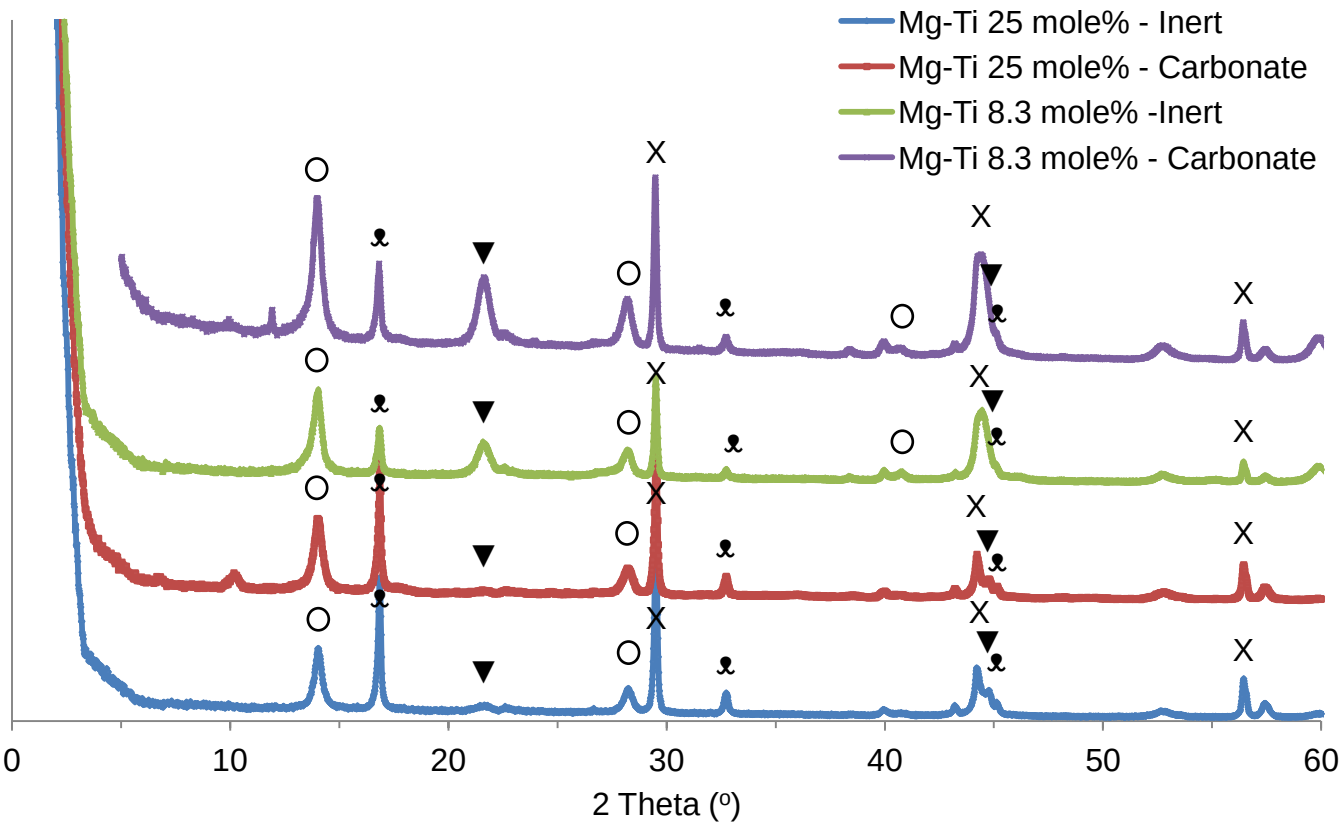

Figure 48: XRD patterns for *Mg-Ti* partial substitution. (▼) Brucite. (X) Anatase. (O) LDH. (♟) Boehmite.

The carbonate samples for the *Ti*-based experiments showed interesting results, therefore, it was decided to also do inert experiments to determine whether it will aid in the interpretation of the results. For the 25 mole% partial substitution, the inert sample showed no sign of dissolution for the anatase, which corresponds to the SEM-EDS image obtained (shown in Figure 195, Appendix E.2.). The carbonate sample showed a slightly different result. Overall the XRD pattern of the carbonate sample still shows an intense peak representing the anatase, but a new peak is displayed at around 10°. This result is similar to the result found in

the *Mg-Ni* experiment. This result is further discussed in Section 4.2.3. From the SEM-EDS image shown in Figure 196 it is difficult to distinguish whether there is titanium present in the other crystals displayed apart from the anatase crystals which are clearly noted. The 8.3 mole%-inert and carbonate sample showed similar XRD patterns obtained compared to the 25 mole%-inert sample. The SEM-EDS image shown in Figure 197 and Figure 198 (Appendix E.2.) also corresponds to the previous results. The carbonate sample also displays a small but noteworthy important peak at around 10^{o} which is further discussed in Section 4.2.3.

Overall, all of the *Mg-Ti* partial substitution experiments indicates that the conditions were far from ideal, but due to the anomalies found in the XRD patterns in combination with the SEM-EDS results, further investigation is recommended.

Lastly, the *Mg-Zn* 25 mole% partial substitution experiment presented very good results. The XRD patterns obtained for this experiment is shown in Figure 49 followed by the SEM-EDS image obtained in Figure 50.

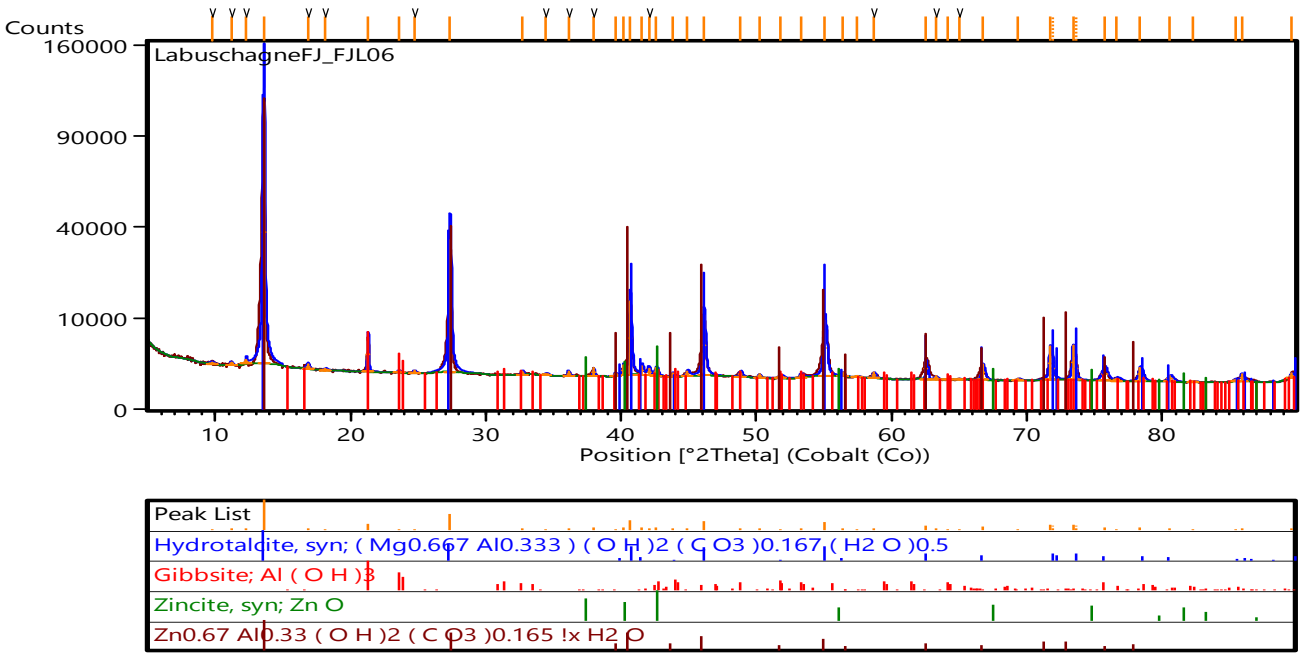

Figure 49: XRD patterns for *Mg-Zn* 25 mole% partial substitution.

The zincite pattern which is shown is not a precise fit, indicating that this form of zincite is not present in the sample. Apart from the significantly high peaks representing an LDH, there is no other unidentified peak which could represent *Zn*. When comparing this result to the SEM-EDS image, the distribution image of *Zn* clearly indicates that it took part in the formation of the LDH, therefore, indicating that the conditions were ideal for the dissolution of the *ZnO* used. The LDH formation is also discussed in Section 4.2.3.

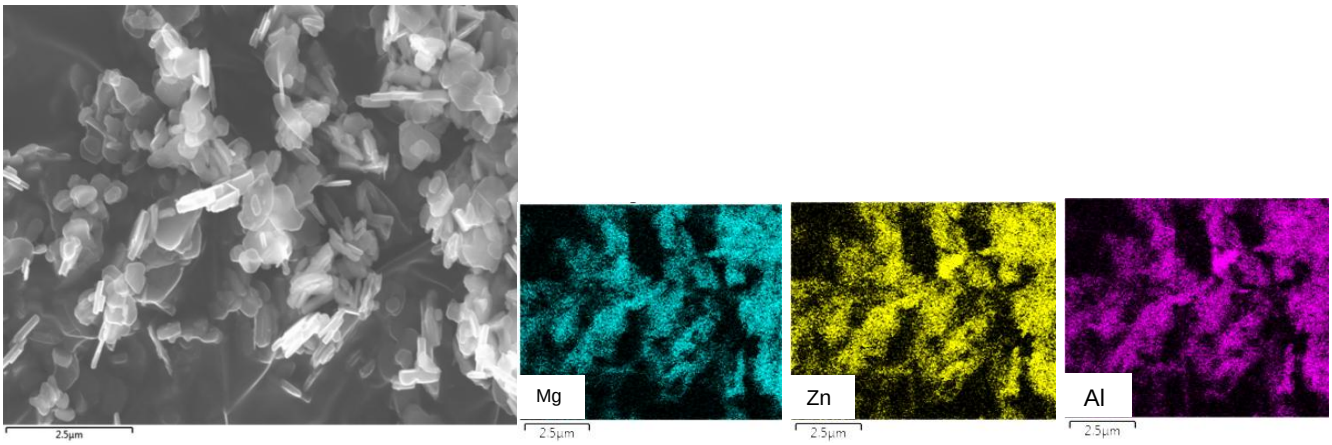

Figure 50: SEM-EDS image for *Mg-Zn* 25 mole% partial substitution. (a) Area used for metal species mapping. (b) Individual mapping for each metal species.

4.2.3. Possible formation of LDH and LDH composition

The three criteria that were used to determine which samples could have indicated signs of possible LDH formation containing the specific metal species or indicated potential formation of an M^{x+}- impregnated LDH were the following:

1. Indications of dissolution for both gibbsite and the specific M^{x+}-oxide/hydroxide.
2. The formation of an intermediate product/precursor potentially containing the specific M^{x+} species according to the XRD and SEM-EDS analysis.
3. Indications of possible peak shift on XRD pattern for the LDH compared to that of hydrocalumite or hydrotalcite or the formation of new peaks in the 2θ range of between 12^{o} and 14^{o}. This range is determined by the results obtained for hydrocalumite and hydrotalcite as well as using the ionic radii for the different metal species.

4. Indications of possible repeat patterns.

The samples listed below in Table 16 met with at least two of the criteria mentioned above, therefore, only these samples are discussed further in this section.

Table 16: M^{x+}-substitution experiments indicating potential formation of LDH.

Primary metal species	M^{x+}-substitution species	Mole % substitution	Environment
Ca	*Cu(I)*	25	Carbonate
	Mn(II)	8.3	Carbonate
	Mn(IV)	25	Carbonate
	Mo	25	Carbonate
	Ni	8.3	Carbonate
	Ti	8.3	Carbonate
Mg	*Mn(II)*	8.3	Carbonate
	Mn(IV)	25	Carbonate
	Mo	25	Carbonate
	Ni	8.3	Carbonate
	Ti	25	Carbonate
		8.3	Carbonate
	Zn	25	Carbonate

The XRD patterns for all the *Ca*-based as well as *Mg*-based samples are shown in Figure 51 and Figure 52 respectively. Table 17 contains the *d*-spacing values calculated from the XRD patterns using Bragg's law (Equation 3). In some cases it is difficult to observe a difference in an LDH peak shift when comparing the primary peaks due to the fact that the hydrotalcite-like compounds are often very poorly crystallised (Cavani, 1991) or that the ionic radii of the metal species could be similar (see Table 1). This is why sometimes the secondary LDH peak is used for comparison. The second peak also represents the sum of two of the *d*-spacing values, therefore, displaying a clearer indication for a possible peak shift.

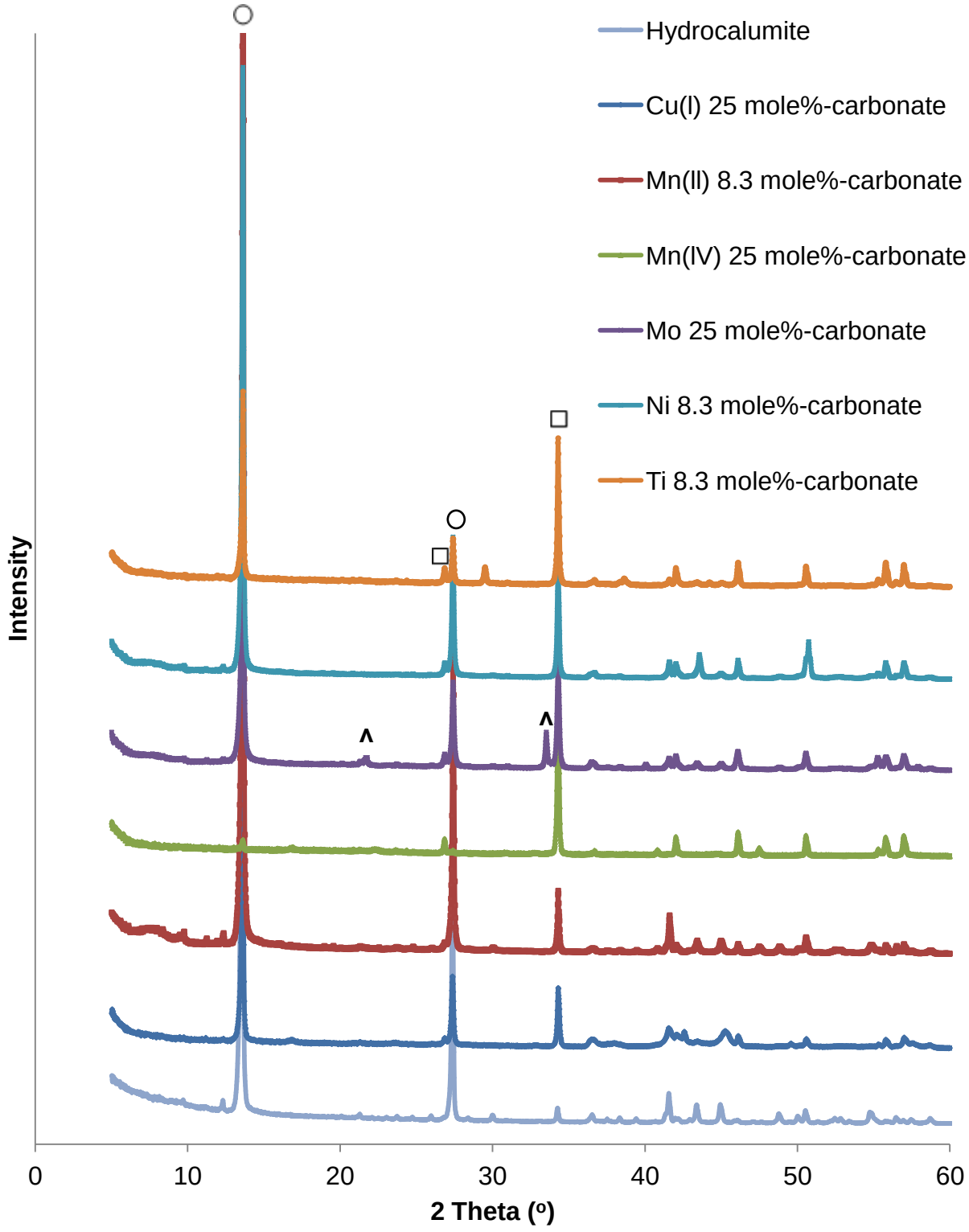

Figure 51: XRD patterns obtained for all the *Ca*-based samples indicating possible M^{x+}-LDH formation. (○) LDH peaks. (□) Calcite. (∧) Powellite.

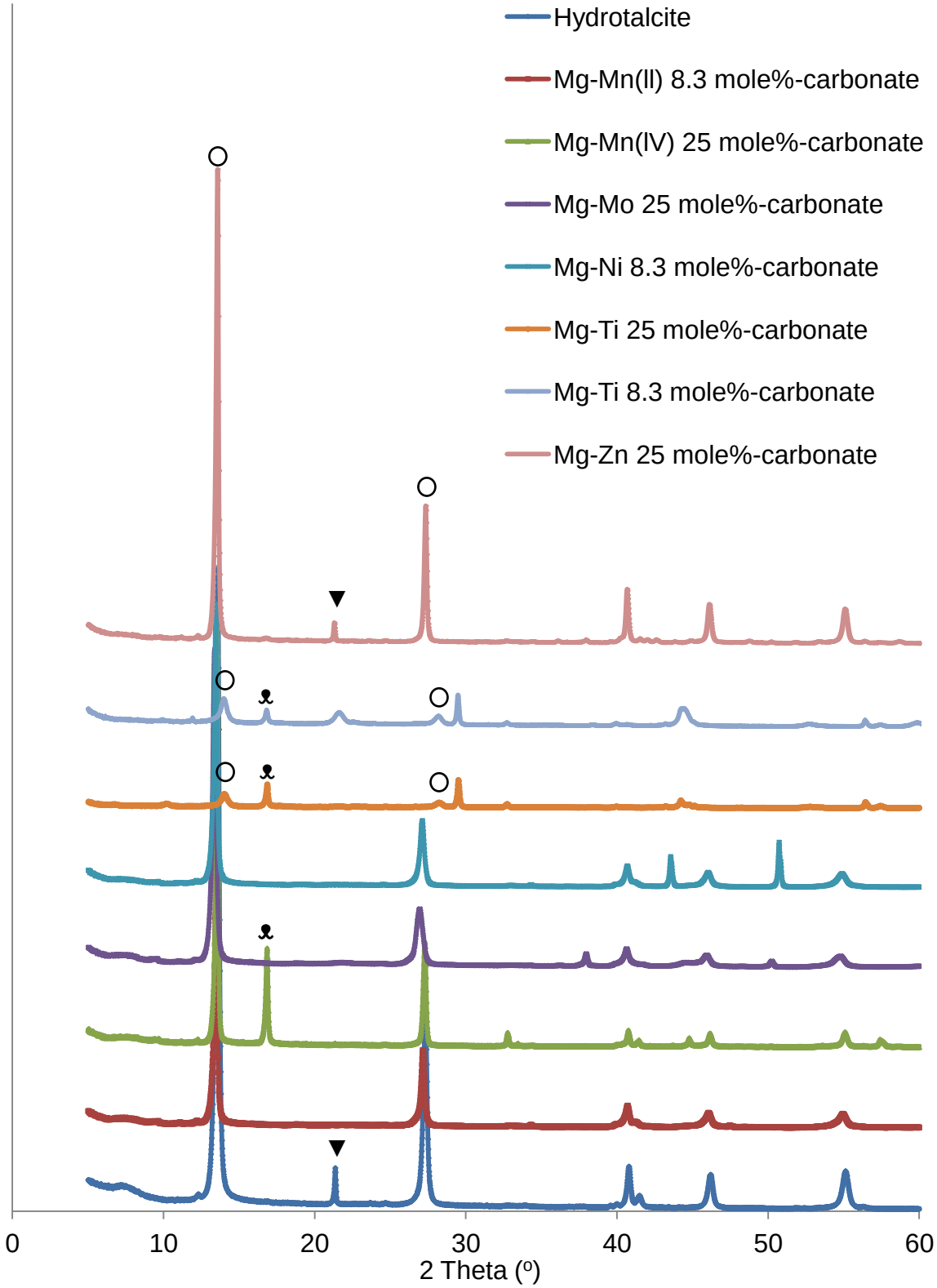

Figure 52: XRD patterns obtained for all the *Mg*-based samples indicating possible M^{x+}-LDH formation. (○) LDH peaks. (♟) Boehmite peaks. (▼) Brucite.

Table 17: *d*-spacing values calculated from the *Ca*- and *Mg*-based samples XRD patterns.

Primary metal species	M^{x+}-substitution species	Mole % substitution	Calculated d-spacing (Å)
Ca	Hydrocalumite		7.56
	Cu(I)	25	7.55
	Mn(II)	8.3	7.54
	Mn(IV)	25	7.55
	Mo	25	7.55
	Ni	8.3	7.55
	Ti	8.3	7.54
Mg	Hydrotalcite		7.58
	Mn(II)	8.3	7.63
	Mn(IV)	25	7.59
	Mo	25	7.70
	Ni	8.3	7.63
	Ti	25	7.40
		8.3	7.37
	Zn	25	7.57

It is difficult to distinguish from the XRD patterns for the *Ca*-based experiments whether the LDH formed does contain the required M^{x+} species, therefore, SEM-EDS images are used in this section to assist in the determination of possible desired LDH formation. The *Ca*-based XRD patterns indicate almost no significant shift in the primary or secondary peaks. The presence of small peaks (at approx. 12^{o}) on the left of the primary hydrocalumite peaks could not be identified. When calculating the possible corresponding *d*-spacing, it is proved to be approx. 8.21 Å. According to Table 17, the *d*-spacing for hydrocalumite is only 7.56Å. The fact that the *Ca*-ions could only have been partially replaced by metal species with lower ionic radii values would have resulted in the decrease in the interlayer spacing. Therefore, it is improbable that peaks outside of the 2θ range of 12^{o} to 14^{o} could indicate the presence of an LDH.

The SEM-EDS image obtained for the Ca-Cu(I) 25 mole%-carbonate sample is shown in Figure 53.

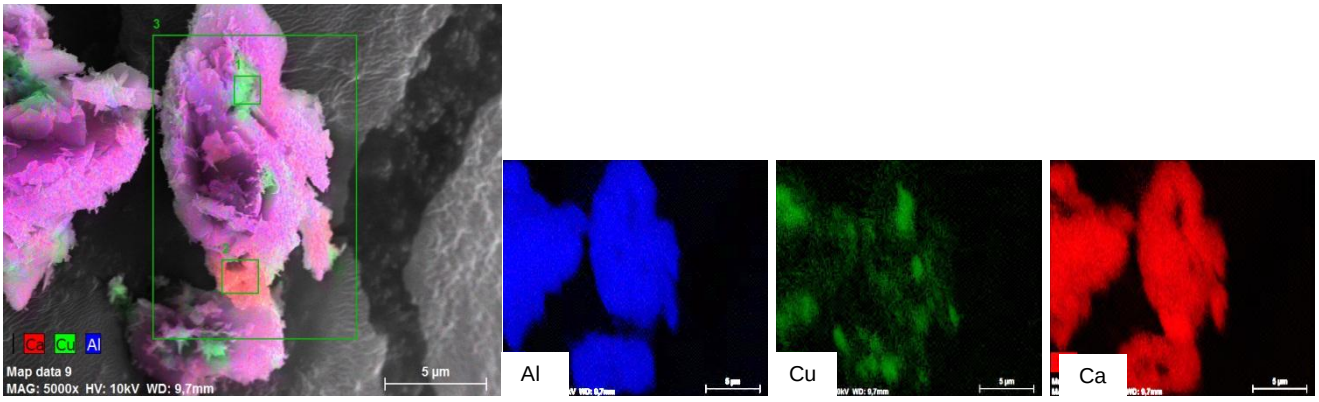

(a) (b)

Figure 53: SEM-EDS image for *Ca-Cu(I)* 25 mole%-carbonate partial substitution. (a) Overall metal species mapping. (b) Individual mapping for each metal species.

The LDH structure picked up by the XRD pattern for Cu(I) is observed on the SEM image and it appears that the platelets formed are significantly small. It is also evident that the LDH only consists out of *Ca* and *Al*. Large *Cu*-crystals are noted all over the sample (also seen in Figure 163, Appendix E.2.), and this result was found in numerous sights during analysis. Therefore, it is concluded that copper(I) did not take part in the formation of the metal hydroxyl layer of the LDH.

Similar results were concluded for the rest of the Ca-based experiments, indicating that the conditions for the formation of an LDH containing the specified M^{x+} species were non-ideal. More detailed SEM-EDS images for these samples are shown in Appendix E.2.

The *Mg*-based experiments showed more promising results compared to the *Ca*-based experiments. Only three of the possible 7 samples indicated negative results for the formation of the preferred LDH and are listed below (determined with the aid of SEM-EDS images):

- *Mg-Mn(II)* 8.3 mole%-carbonate
- *Mg-Mn(IV)* 25 mole%-carbonate
- *Mg-Ni* 25 mole%-carbonate

The SEM-EDS images for these three samples are shown in Appendix E.2. which correspond to the XRD patterns obtained.

There is a small shift noticed in Figure 52 for both the *Mg-Mn(ll)* 8.3 mole%-carbonate as well as the *Mg-Mn(ll)* 25 mole%-carbonate experiment. An increase of approx. 0.04 Å in the *d*-spacing is noticed. This could be possible due t the fact that the ionic radius for *Mn(II)* is 0.083 nm, which is larger than that of both *Mg* and *Al* (according to Table 1). However, the intensity of the peaks for the 25 mole% experiment is lower than that of the 8.3 mole% experiment, indicating that the presence of excess *Mn* could have an antagonistic effect. Therefore, further investigation must be done using less at a lower partial substitution to determine whether improvement would be achieved. Further investigation must also be done to see whether the change in temperature, pressure or pH could improve the *Mg-Mn-Al-*CO_3 LDH yield.

Looking at the distribution image of *Mo* in Figure 54(b) which represents the *Mg-Mo* 25 mole%-carbonate showed very promising results.

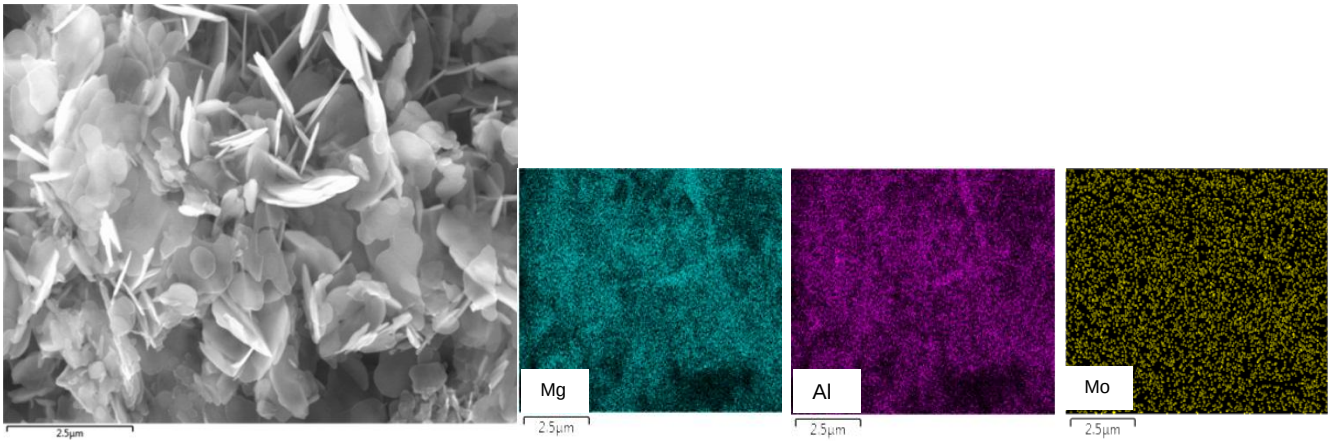

Figure 54: SEM-EDS image for *Mg-Mo* 25 mole%-carbonate partial substitution. (a) Area used for metal species mapping. (b) Individual mapping for each metal species.

Looking at the distribution image of *Mo*, it clearly shows the homogeneous distribution (as mentioned in Section 4.2.2 for the precursor product formation). When comparing the shift of

the possible LDH peak to that of hydrotalcite (Figure 52) it is noted that an enlargement of the interlayer had occurred. The *d*-spacing increased from a possible 7.56 Å to a possible 7.70 Å. However, when looking at the ionic radii for *Mo* (Table 1), it is noted that the ionic radii for *Mo* (0.041 nm) is far less than that of *Ca* (0.112 nm) or *Al* (0.054 nm), which mean that the possibility for an increase of *d*-spacing (0.14 Å) through metal substitution and containing the same interlayer anion is improbable for an LDH. Therefore, this indicates that different *Mg-Mo* or *Mg-Mo-Al* complex had formed, and not an LDH.

This also confirms that the distribution image of *Mo* in Figure 54 is not due to scattering of MoO_3 but rather did display the presence of an *Mg-Mo-Al-*CO_3 complex. Unfortunately the amount of molybdenum present in the LDH is unclear; therefore, further investigation must be done.

To determine whether an *Mg-Ti-Al-*CO_3 had formed during the *Mg-Ti* experiments proved to be much more difficult. Figure 55 and Figure 56 shows the SEM-EDS images obtained for both the 25 mole%-carbonate and the 8.3 mole%-carbonate sample respectively.

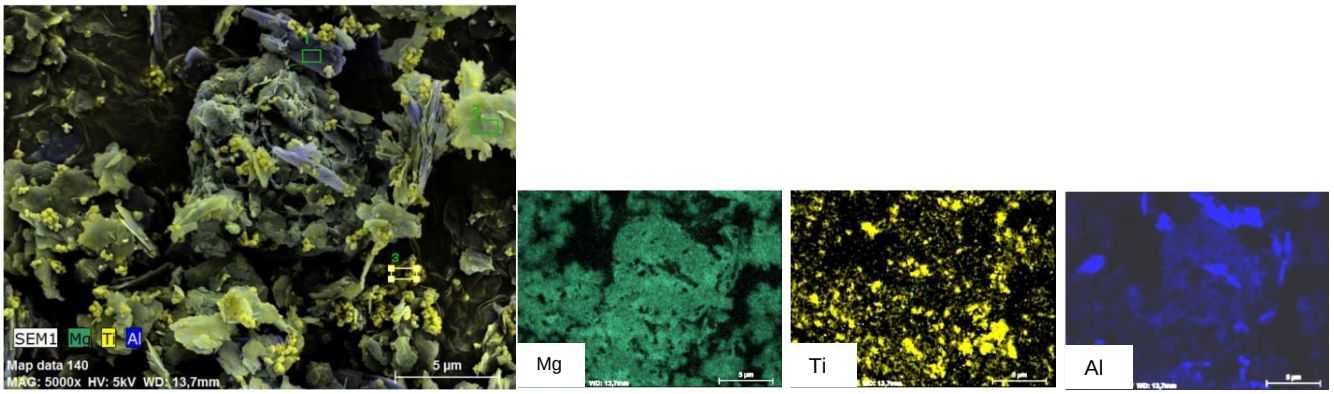

(a) (b)

Figure 55: SEM-EDS image for *Mg-Ti* 25 mole%-carbonate partial substitution. (a) Overall metal species mapping. (b) Individual mapping for each metal species.

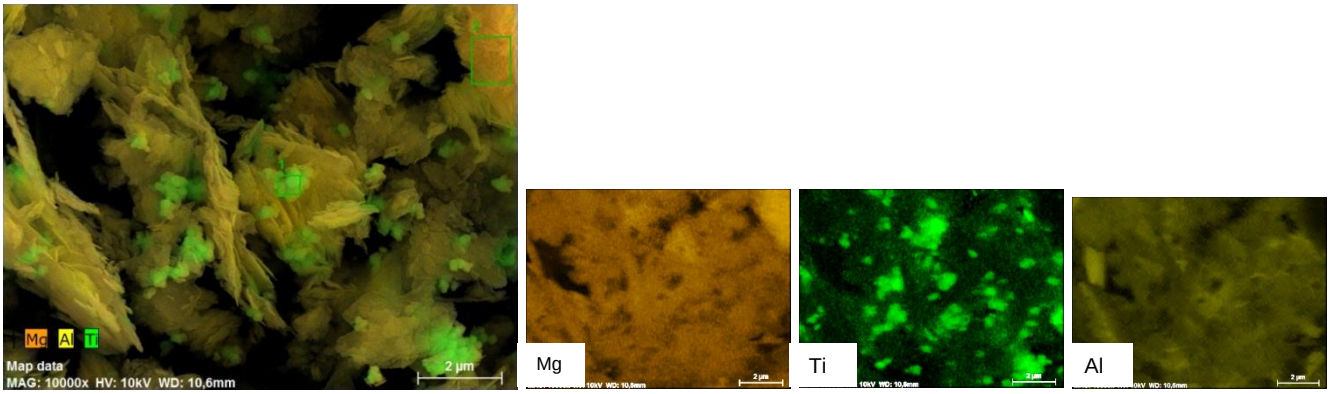

(a) (b)

Figure 56: SEM-EDS image for *Mg-Ti* 8.3 mole%-carbonate partial substitution. (a) Overall metal species mapping. (b) Individual mapping for each metal species.

The first observation is the overall distribution of the titanium crystals shown in the overall metal species mapping image. But, when looking closely at the individual mapping for *Ti*, the 8.3 mole%-carbonate sample indicates traces of titanium in the areas where the platelets are situated, indicating possible *Mg/Ti-Al-*CO_3 LDH. It could also be some titanium crystals behind the platelets which were picked up by the detector. Comparing these results to the results shown in Table 17, there is a possibility that an *Mg/Ti-Al-*CO_3 LDH had formed. The ionic radii of *Ti* is approx. 0.061 nm. There is a slight difference compared to that of *Mg* (0.072 nm). This small difference in ionic radii could possibly be the reason for the decrease in the interlayer spacing of approx. 0.18 Å for *Ti*(II) and 0.21 Å for *Ti*(IV), with the LDH having the same interlayer anion: CO_3. Further investigation needs to be done to confirm these results and also the concentration of the titanium taking part in the possible formation of the metal hydroxyl layers.

The SEM-EDS image shown in Figure 50 (Section 4.2.2.) clearly indicates that Zn was present in high quantity in the formation of the LDH. The *d*-spacing reported in Table 17 did not show a significant shift, but, according to Table 1 the difference is almost negligible. Therefore, indicating that the specific LDH had formed. The misfit of the *ZnO* pattern on the XRD pattern (Figure 127, Appendix A.3.) corresponds to the formation of the LDH which contains high amount of *Zn* and that the presence of another crystalline *Zn*-containing compound could not be found, however, some of the peaks could not be identified. Even the

intensity of the peaks indicates that a high crystallinity, homogeneous LDH had formed; therefore, the conditions for the formation of an *Mg/Zn-Al-CO_3* LDH were close to ideal.

5. Conclusions and Recommendations

5.1. Mg-Al-CO_3 LDH synthesis

During the optimisation process for the formation of hydrotalcite using the dissolution precipitation method, hydromagnesite was proved to be dominant reaction at low temperatures. With the increase in reaction time and temperature the decomposition of hydromagnesite occurred to form magnesite. At low temperatures the formation of *Mg-Al-CO_3* LDH was limited due to the low solubility of gibbsite. *Mg-Al-CO_3* LDH formation of 80 % was achieved at 140 ^{o}C after 2 hours reaction time, but crystallinity is low.

To achieve an *Mg-Al-CO_3* LDH conversion higher than 96% a reaction temperature of 160 ^{o}C for a minimum of 4 hours was required, but was achieved within 1 hour at 180 ^{o}C. A 99.37 % conversion was achieved at 180 ^{o}C for 5 hours with a high crystallinity and homogeneity.

The surface area for *Mg-Al-CO_3* LDH at 180 ^{o}C after 5 hours reaction time proved to be 9.19 m^2/g. The average particle size obtained for a high crystalline LDH was in the range of approx. 3 µm and 6.8 µm. at temperatures of 160 ^{o}C and above for a minimum of 3 hours reaction time.

SEM images in combination with Rietveld analysis and PSA clearly shows how platelets are joined together by amorphous phase metal complexes. To minimise the amount of agglomerates formed due to this bonding, a reaction temperature of 160 ^{o}C and a minimum reaction time of 5 hours is required. The platelets formed during the dissolution-precipitation process are not well-shaped hexagonal platelets compared to that of co-precipitated platelets.

The following are recommended for future work:

- Determine the effect of mixing speed on the shape of the platelets.
- Determine the difference between freshly precipitated metal oxides/hydroxides as reagents compared to aged metal oxides/hydroxides.

5.2. M^{x+}-metal species partial substitution

The presence of $Mg(OH)_2$ and $Ca(OH)_2$ in solution (respectively) did increase the pH enough for the dissolution of gibbsite and most of the M^{x+} metal species. The two main experiments indicating the formation of the required M^{x+}-containing LDH were *Mg/Mo-Al-*CO_3 LDH and *Mg/Zn-Al-*CO_3 LDH. A reaction time and temperature of 5 hours at 180 ^{o}C in a carbonate environment proved to be close to the ideal conditions for the formation of these homogeneous, well-crystalline LDHs. However, small amounts of unreacted reagents were present. The results for the formation of *Mg/Ti-Al-*CO_3 LDH were inconclusive. Further investigation to determine whether the formation of the LDH did occur is recommended by possible isolation of the platelets and to do XRD and Rietveld analysis in order to determine the composition.

The conditions for the dissolution of the M^{x+}-metal species for the following experiments were proven to be successful:

- *Ca/Mn(IV)-Al*
- *Ca/Mo-Al*
- *Ca/Ni-Al*
- *Ca/Ti-Al*
- *Mg/Mo-Al*
- *Mg/Zn-Al*

The *Ca*-based experiments also indicated the possibility for the formation of a precursor. All the above mentioned *Ca*-based experiments showed indications of instability of the precursor when exposed to a carbonate source. The shape of these precurors appeared to look the same as the “ball”-like structure of katoite. For *Mg/Ti-Al* the same “ball”-like structure was noted. Hydrogarnet is a Ca-Al compound that has a similar structure to that of katoite. It is found that hydrogarnet decomposes to form hydrocalumite and calcite in a carbonate atmosphere. The presence of titanium in the *Ca*-based reaction proved to have an inhibiting effect on the formation of hydrocalumite. Most of the *Ca*-based experiments indicated sufficient pH for the dissolution of the M^{x+}-species, but in some instances the M^{x+}metal species had re-precipitated in the more stable oxide/hydroxide phase.

The following are recommended for the improvement on the formation of an M^{x+}-impregnated LDH/precursor:

- Determine the effect of different reaction times and temperature
- The effect of adding the carbonate source at a higher temperature (above 100 ^{o}C under pressure)
- The effect of synthesising at different pH conditions

Cobalt and tin showed no/negligible amount of possible solubility. Improvement on the dissolution for these two species must be further investigated. The only experiment which indicated difficulties in the solubility of gibbsite was the *Mg-Sn* partial substitution experiment. The *Mg-Zn* sample did also show the presence of unreacted gibbsite.

6. References

Acharya, H, Srivastava, SK and Bhowmick, AK (2007) “Synthesis of partially exfoliated EPDM/LDH nanocomposites by solution intercalation: Structural characterization and properties”, Composites Science and Technology, 67, 2807-2816.

DEAT (2006) *Environmental Impact Assessment Regulations in terms of the National Environmental Management Act* (Act No. 107 of 1998) (Government Notice No. R. 385, R. 386, and R. 387 in the Government Gazette of 21 April 2006 refer).

Alleman, R(1968) “The crystal structure of pyroaurite” *Acta Crystallographica*, B24, 972-977.

Atkins, P and De Paula, J (2009) Elements of Physical Chemistry, 5th Ed, W. H. Freeman and Company, New York.

Auerbach, SM, Carrado, KA and Dutta, PK (2004) *Handbook of Layered Materials*, Marcel Decker Inc., New York.

Bao, Y, Zhi-ming, H, Shen-xing, L and Zhi-xue, W (2008) “Thermal stability, smoke emission and mechanical properties of poly(vinyl chloride)/hydrotalcite nanocomposites” Polymer Degradation and Stability, 93(2), 448-455.

Bénézeth, P, Palmer, DA and Wesolowski, DJ (2001) “Aqueous high-temperature solubility studies. II. The solubility of boehmite at 0.03 m ionic strength as a function of temperature and pH as determined by in situ measurements”, Geochimica et Cosmochimica Acta, 65 (13), 2097-2111.

Boclair, JW and Braterman, PS (1999) “Layered double hydroxide stability. 1. Relative stabilities of layered double hydroxides and their simple counterparts”, Chemistry of Materials, 11, 298-302.

Britto, S and Kamath, PV (2009) “Thermal, solution and reductive decomposition of Cu-Al layered double hydroxides into oxide products” Journal of Solid State Chemistry, 182, 1193-1199.

Budhysutanto, WN, Van Den Bruele, FJ, Rossenaar, BD, Van Agterveld, D, Van Enckevort, WJP and Kramer, HJM (2011) “A unique growth mechanism of donut-shaped Mg-Al layered double hydroxides crystals revealed by AFM and STEM-EDX”, *Journal of crystal growth*, 318, 110-116.

Buttler, FG, Glasser, LSD and Taylor, HFW (1959) “Studies on $4CaOAl_2.O_3.13H_2O$ and the related natural mineral Hydrocalumite”, *Journal of the American Ceramic Society*, 42(3), 121-126.

Castet, S, Dandurand, JL, Schott, J and Gout, R (1993) “Boehmite solubility and aqueous aluminum speciation in hydrothermal solutions (90-350^oC): Experimental study and modeling”, Geochimica et Cosmochimica Acta, 57, 4869-4884.

Cavani, F, Trifirò, F and Vaccari, A(1991) “Hydrotalcite-type anionic clays: preparation, properties and applications”, *Catalysis Today*, 11, 173-301.

Chitrakar, R, Tezuka, S, Sonoda, A, Sakane, K, Ooi, K and Hirotsu, T (2005) “Adsorption of phosphate from seawater on calcined MgMn-layered double hydroxides”, Jounrla of Colloid and Interface Science, 290, 45-51.

Chivot, J, Mendoza, L, Mansour, C, Pauporté, T and Cassir, M (2008) “New insight in the behaviour of Co-H_2O system at 25-150 ^oC, based on revised Pourbaix diagrams” *Corrosion Science*, 50, 62-69.

Costantino, U, Marmottini, F, Nocchetti, M and Vivani, R (1998) “New synthetic routes to hydrotalcite-like compounds – Characterisation and properties of the obtained materials”, European Journal of Inorganic Chemistry, 1439-1446.

Crepaldi, EL, Pavan, PC, Tronto, J and Valim, JB (2002) “Chemical, structural and thermal properties of Zn(II)-Cr(III) layered double hydroxides intercalated with sulphated and sulfonated surfactants”, 248, 429-442.

Clause, O, Gazzano, M, Trifiro’, F, Vaccari, A and Zatorski, L (1991) “Preparation and thermal reactivity of nickel/chromium and nickel/aluminium hydrotalcite-type precursors”, Applied Catalysis, 73, 217-236.

Das, N and Samal, A (2004) “Synthesis, characterization and rehydration behaviour of titanium(IV) containing hydrotalcite like compounds” *Microporous and Mesoporous Materials*, 72, 219-225.

Deelman, JC (2011) “Low-temperature formation of dolomite and magnesite”, http://www.jcdeelman.demon.nl/dolomite/bookprospectus.html [2013, October 20].

Del Arco, M, Gutiérrez, S, Martín, C, Rives, V and Rocha, J (2004) “Synthesis and characterisation of layered double hydroxides (LDH) intercalated with non-steroidal anti-inflammatory drugs (NSAID)” Journal of Solid State Chemistry, 177, 3954-3962.

Duan, X and Evans, DG (2006) “Layered double Hydroxides”, *Springer-Verlag*, Volume 119.

Dudek, B, Kuśtrowiski, P, Bialas, A, Natkański, P, Piwowarska, Z, Chmielarz, L, Kozak, M and Michalik, M (2012) “Influence of textural and structural properties of Mg-Al and Mg-Zn-Al containing hydrotalcite derived oxides on Cr(Vl) adsorption capacity”, Materials Chemistry and Physics, 132 (2-3), 929-936.

Dyer, JA, Scrivner, NC and Dentel, SK (1998) “A practical guide for determining the solubility of metal hydroxides and oxides in water”, Environmental Progress, 17(1), 1-8.

Feitknecht, W and Fischer, G (1935) “Zur Chemie und morphologie der basischen salze zweiwertiger metalle lll”, *Helvetica Chimica Acta*, 18(1), 555-569.

Fekry, AM and Tammam, RH (2011) "Corrosion and impedence studies on magnesium alloy in oxalate solution" *Materials Science and Engineering*, 176, 792-798.

Forano, C, Hibino, T, Lerouw, F and Taviot-Guého, C (2006) "Layered double hydroxides", *Handbook of Clay Science*, Bergaya, F, Theng, BKG and Lagaly, G (Eds.), Elsevier, Amsterdam.

French, D, Schifano, P, Cortés-Concepcíon, J and Hargrove-Leak, S (2010) "Li-Al layered double hydroxides as catalysts for the synthesis of flavanone" Catalysis Communications, 12, 92-94.

Garverick, L (1995) *Corrosion in the petrochemical industry*, Materials Park, Ohio.

Goh, KH, Lim, TT and Dong, Z (2008) "Application of layered double hydroxides for removal of oxyanions: A review", Water Research, 42, 1343-1368.

Grim, RE and Güven, N (1978) "Bentonites: Geology, Minerology, Properties and Uses", Amsterdam and New York, Elsevier.

Hartmann-Petersen, P, Gerrans, GC and Hrtman-Petersen, R (2007) *SASOL Encyclopaedia of Science and Technology*, 2nd Ed, New Africa Books, Claremont, South Africa.

Hull, W (1919) "A new method of chemical analysis", Philosophical Magazine, 17, 1168-1175.

Inayat, A, Klumpp, M and Schwieger, W (2011) "The urea method for the direct synthesis of ZnAl layered double hydroxides with nitrate as the interlayer anion", Applied Clay Science, 51, 452-459.

Iyi, N, Matsumoto, T, Kaneko, Y and Kitamura, K (2004) "Deintercalation of carbonate ions from a hydrotalcite-like compound: Enhanced decarbonation using acid-salt mixed solution", Chemistry of Materials, 16, 2926-2932.

James, AM and Lord, MP (1992) *Macmillan's Chemical and Physical Data*, London, UK

Jitianu, M, Bálásoiu, M, Zaharescu, M, Jitianu, A and Ivanov, A (2000) "Comparative study of Sol-Gel and coprecipitated Ni-Al hydrotalcites", Journal of Sol-Gel Science and Technology, 19, 453-457.

Labuschagne, FJWJ, Giesekke, EW and Van Schalkwyk, JD (2006) "Production of Hydrotalcite", *ZA Patent WO 2006/123284 A2*.

Lee, WF and Chen, YC (2006) "Effects of intercalated hydrotalcite on drug release behaviour for poly(acrylic acid-co-N-isopropyl acrylamide)/intercalated hydrotalcite hydrogels", European Polymer Journal, 42, 1634-1642.

Magagula, B, Nhlapo, N and Focke, WW (2009) "Mn_2Al-LDH- and Co_2Al-LDH-stearate as photodegradants for LDPE film",*Polymer Degradation Stability*, 94, 947-954.

Martin, ES, Horn, WE, Stinson, JM and Cedro, V (1999) "Two powder synthesis of hydrotalcite and hydrotalcite-like compounds", *EU Patent PCT/US95/00166*, assigned to Aluminum Company of America, US.

Miyata, S and Kumura, T (1973) "Synthesis of new hydrotalcite-like compounds and their physic-chemical properties" Chemical society of Japan, 843-848.

Miyata, S (1975) "Te synthesis of hydrotalcite-like compounds and their structures and physic-chemical properties" Clay and Clay Minerals, 23, 369-375.

Miyata, S (1980) "Physico-Chemical properties of synthetic hydrotalcites in relation to composition" Clays and Clay Minerals, 28(1), 50-56.

Miyata, S (1983) “Anion-exchange properties of hydrotalcite-like compounds”, Clays and Clay Minerals, 31(4), 305-311.

Moreira, FKV, Pedro, DCA, Glenn, GM, Marconicini, JM and Mattoso, LHC (2013) “Brucite nanoplates reinforced starch bionanocomposites” *Carbohydrate Polymers*, 92, 1743-1751.

Moyer, BA and Singh, RP (2004) “Fundamentals and applications of Anion Separations”, Kluwer Academic / Plenum Publishers, NY, p311.

Nayak, M, Kutty, TRN, Jayaraman, V and Periaswamy, G (1997) “Preparation of the layered double hydroxide (LDH) $LiAl_2(OH)_7{\bullet}H_2O$, by gel to crystallite conversion and a hydrothermal method, and its conversion to lithium aluminates” Journal of Materials Chemistry, 7(10), 2131-2137.

Ogawa, M and Kaiho, H (2002) “Homogeneous precipitation of uniform hydrotalcite particles”, Langmuir, 18, 4240-4242.

Okamoto, K, Iyi, N and Sasaki, T (2007) “Factors affecting the crystal size of the Mg-Al-LDH (layered double hydroxide) prepared by using ammonia-releasing reagents”, *Applied clay science*, 37, 23-31

Oliva, MI, Heredia, A, Zandalazini, CI, Crivello, M and Corchero, E (2012) “Magnetic behaviour of Mg-Al-Zn-Fe mixed oxides from precursors layered double hydroxide” *Physica B*, 407, 3125-3127.

Osseo-Asare, K and Mishra, KK (1996) “Solution chemical constraints in the chemical-mechanical polishing of copper: Aqueous stability diagrams for the $Cu\text{-}H_2O$ and $Cu\text{-}NH_3\text{-}H_2O$ systems” *Journal of Electronic Materials*, 25.

Othman, MR, Helwani, Z, Martunus and Fernando, WJN (2009) “Synthetic hydrotalcites from different routes and their application as catalysts and gas adsorbents: a review”, Applied Organometallic Chemistry, 23, 335-346.

Panda, HS, Srivastava, R and Bahadur, D (2011) “Synthesis and *in situ* mechanism of nuclei growth of layered double hydroxides”, *Bulletin of Material Science*, 34(7), 1599-1604.

Pastor-Rodriguez, J and Taylor, HFW (1971) “Crystal structure of caolingite” *Mineralogical Magazine,* 38, 286-294.

Qi, C, Amphlett, JC and Peppley, BA (2006) “Product composition as a function of temperature over NiAl-layered double hydroxide derived catalysts in steam reforming of methanol” *Applied Catalysis: General*, 302(2), 237-243.

Rao, MM, Reddy, BR, Jaylakshmi, M, Jaya, VS and Sridhar, B (2005) “Hydrothermal synthesis of Mg-Al hydrotalcites by urea hydrolysis” Materials Research Bulletin, 40, 347-359.

Reichle, WT (1986) “Synthesis of anionic clay minerals (Mixed metal hydroxides, Hydrotalcite)” *Solid States Ionics*, 22, 135-141.

Rietveld, HM (1968) “A profile refinement method for nuclear and magnetic structures”, *Journal of Applied Crystallography*, 2(2), 65-71.

Rives, V and Ulibarri, MA (1999) “Layered double hydroxides (LDH) intercalated with metal coordination compounds and oxometalates” *Coordination Chemistry Reviews*, 181, 61-120.

Rives, V (2001) *Layered Double Hydroxides – Present and Future*, Nova Science Publishers Inc., New York.

Saber, O and Tagaya, H (2008) “Preparation and intercalation reactions of nano-structural materials, Zn-Al-Ti LDH” *Materials Chemistry and Physics*, 108, 449-455.

Schott, R (2009) “Crystal habits – Euhedral, subhedral, anhedral”, Personal Communication, Department of Geosciences, Fort Hays State University, Kansas.

Schütz, MR, Schedl, AE, Wagner, FE and Breu, J (2011) “Complexing agent assisted synthesis of high aspect ratio Fe^{3+}/Mg^{2+} layered double hydroxides”, Applied Clay Science, 54, 281-286.

Shen, S, Chow, PS, Chen, F, Feng, S and Tan, RBH (2006) “Synthesis of submicron gibbsite platelets by organic-free hydrothermal crystallization process” *Journal of Crystal Growth*, 292, 136-142.

Singhal, A (2010) *The Pearson guide to inorganic chemistry for the IIT JEE*, Dorling Kindersley, India

Sposito, G (2008) *The Chemistry of soils*, 2nd Ed, Oxford University Press, New York, USA.

Sukiman, NL, Zhou, X, Birbilis, N, Hughes, AE, Mol, JMC, Garcia, SJ, Zhou, X and Thompson, GE (2013) “Durability and Corrosion of Aluminium and its Alloys: Overview, property space, techniques and developments” *Australian Corrosion Association*, Australia.

Tanasoi, S, Mitran, G, Tanchoux, N, Cacciaguerra, T, Fajula, F, Sandulescu, I, Tichit, D and Marco, IC (2011) “Transition metal-containing mixed oxides catalysts derived from LDH precursors for short-chain hydrocarbons oxidation” *Applied Catalysis: General*, 395, 78-86.

Valente, JS, Cantú, MS, Cortez, JGH, Montiel, R, Bokhimi, X and López-Salinas, E (2007) “Preparation and characterization of sol-gel MgAl hydrotalcites with nanocapsular morphology”, 111, 642-651.

Van der Westhuizen, F (2011) “The green engineering of layered double hydroxides” Project Report, Dept Chem Eng, University of Pretoria.

Van Graan, M (2012) “Layered double hydroxide synthesis for utilisation as catalysts” Project Report, Dept Chem Eng, University of Pretoria.

Velu, S, Suzuki, K, Osaki, T, Ohashi, F and Tomura, S (1999) “Synthesis of new Sn incorporated layered double hydroxides and their evolution to mixed oxides” *Materials Research Bulletin*, 34, 1707-1717.

Wang, DY, Costa, FR, Vyalikh, A, Leuteritz, A, Scheler, U, Jehnichen, D, Wagenknecht, U, Häussler, L and Heinrich, G (2009) “One-step synthesis of organic LDH and its comparison with regeneration and anion exchange method”, 21, 4490-4497.

Waseda, Y, Matsubara, E and Shinoda, K (2011) *X-ray Diffraction Crystallography – introduction, examples and solved problems*, Springer-Verlag, Heidelberg, Germany.

Wenk, HR and Bulakh, A (2004) *Minerals – Their constitution and origin*, Cambridge University Press, Cambridge, United Kingdom

Wulfsberg, G (1991) *Principles of descriptive inorganic chemistry*, University Science Books, Sausalito, CA.

Yamaguchi, O, Taguchi, H, Miyata, Y, Yoshinaka, M and Shimizu, K (1987) “Characterisation of magnesium-aluminium double hydroxide prepared from alkoxides and its products of thermolysis” *Polyhedron*, 6(7), 1587-1592.

Yao, JH, Elder, KR, Guo, H and Grant, M (1993) “Theory and simulation of Ostwald ripening” Physical Review B, 47, 14110-14125.

You, Y, Vance, GF and Zhao, H (2001) “Selenium adsorption on Mg-Al and Zn-Al layered double hydroxides” *Applied Clay Science*, 20, 13-25.

Yu, B, Bian, H and Plank, J (2010) “Self-assembly and characterization of Ca-Al-LDH nanohybrids containing casein proteins as guest anions” *Journal of Physics and Chemistry of Solids*, 71, 468-472.

Zang, WH, Guo, XD, He, J and Qian, ZY (2008) “Preparation of Ni(II)/Ti(IV) layered double hydroxide at high supersaturation”, Journal of the European Ceramic Society, 28, 1623-1629.

Zhan, Y, Zhao, R, Lei, Y, Meng, F, Zhong, J and Liu, X (2011) “Preparation, characterisation and electromagnetic properties of carbon nanotubes/Fe_3O_4 inorganic hybrid material”, Applied Surface Science, 257, 4524-4528.

Zhao, H and Nagy, KL (2004) “Dodecyl sulphate-hydrotalcite nanocomposites for trapping chlorinated organic pollutants in water”, Journal of Colloid and Interface Science, 274, 613-624.

Zhao, mQ, Huang, JQ, Zhang, Q, Nie, JQ, Wei, F (2011) “Stretchanle single-walled carbon nanotube double helices derived from molybdenum-containing layered double hydroxides”, *Carbon*, 49, 2141-2161.

Zhao, Y, Xiao, F and Jiao, Q (2011) “Hydrothermal synthesis of Ni/Al aluminium double hydroxide nanorods” *Journal of Nanotechnology*, 2011

Zhou, JZ, Xu, ZP, Qiao, S, Liu, J, Xu, Y, Zhang, J and Qian, G (2011) “Triphosphate removal processes over ternary CaMgAl-layered double hydroxides” *Applied Clay Science*, 54, 196-201.

Appendix A: XRD results

A.1. *Mg-Al-CO$_3$* LDH synthesis

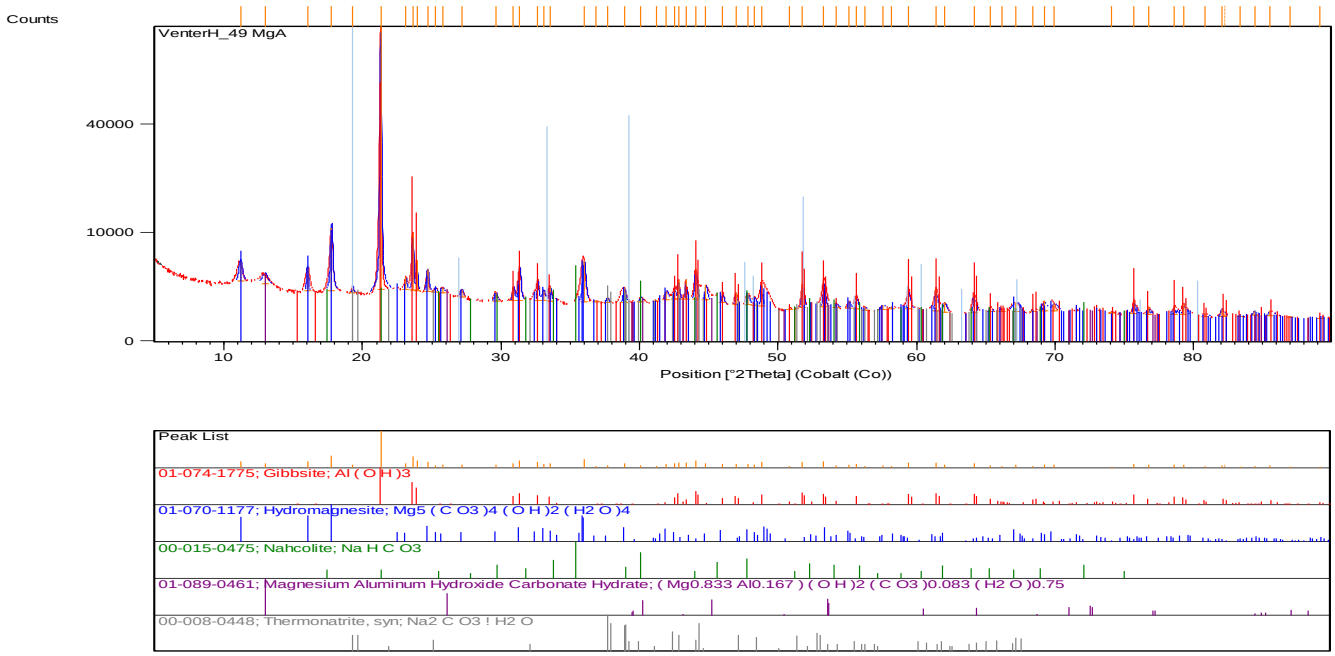

Figure 57: XRD Pattern - MgAl120-1

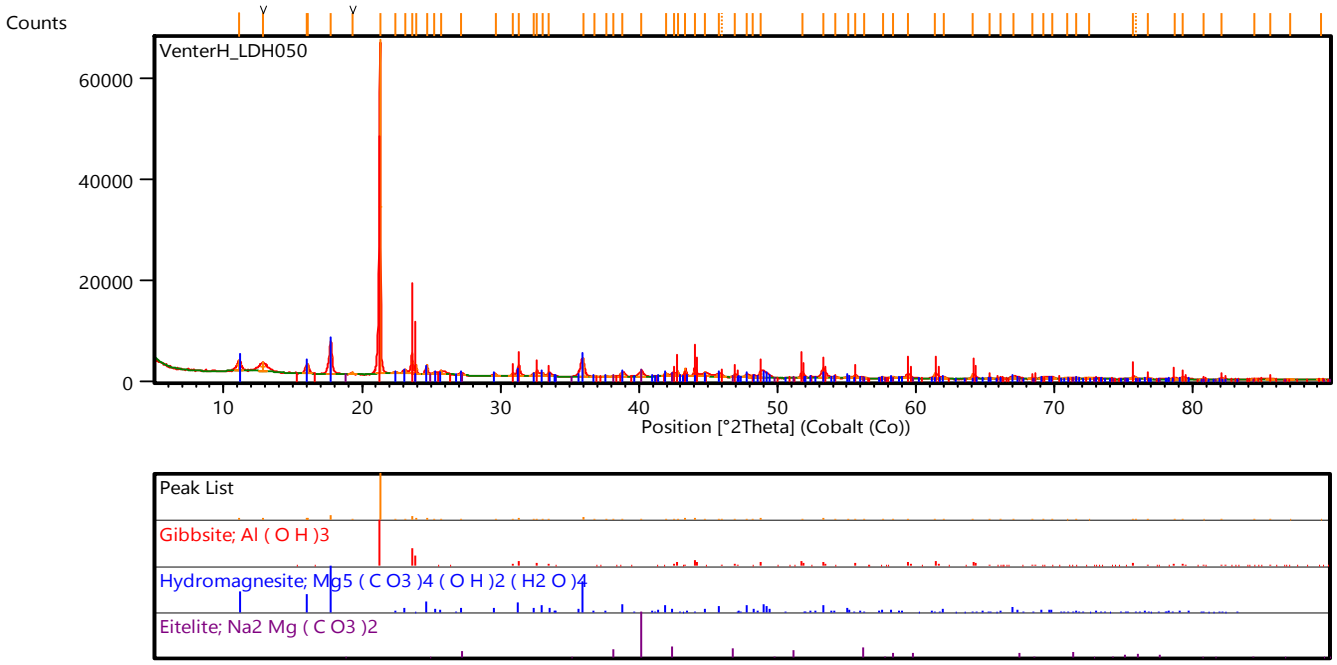

Figure 58: XRD Pattern - MgAl120-2

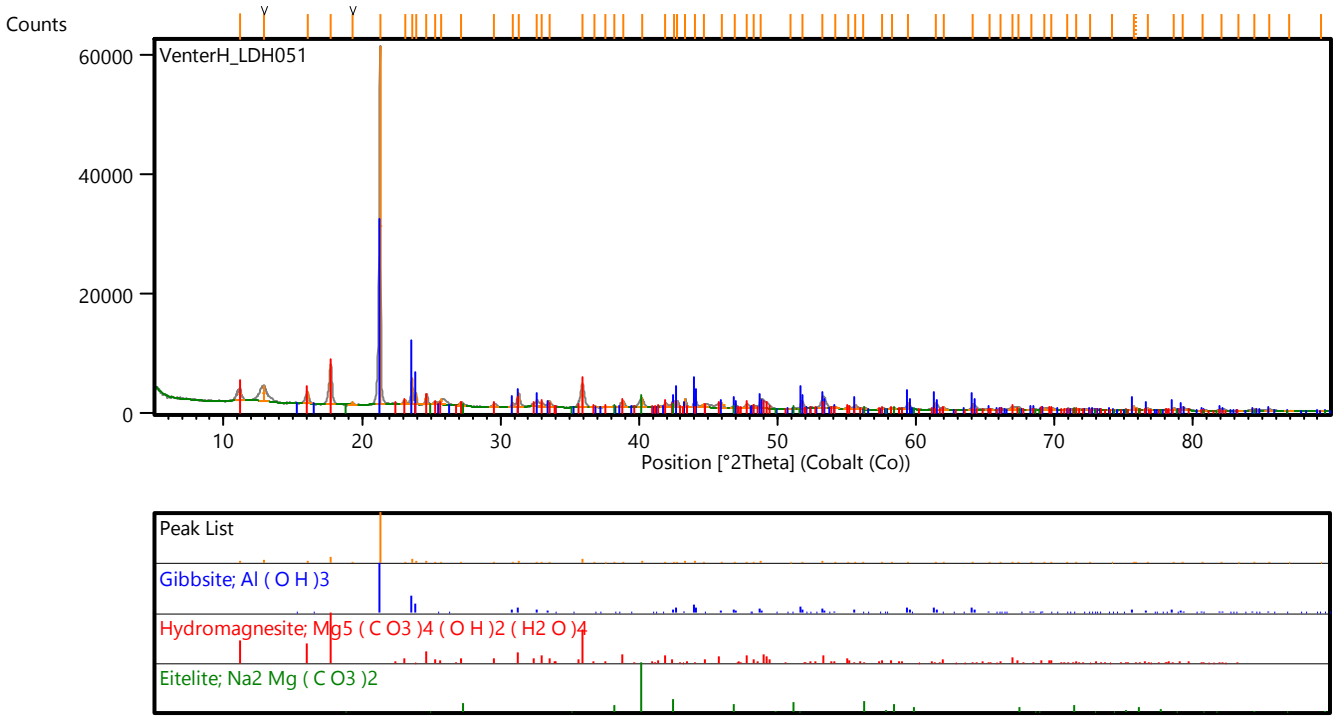

Figure 59: XRD Pattern - MgAl120-3

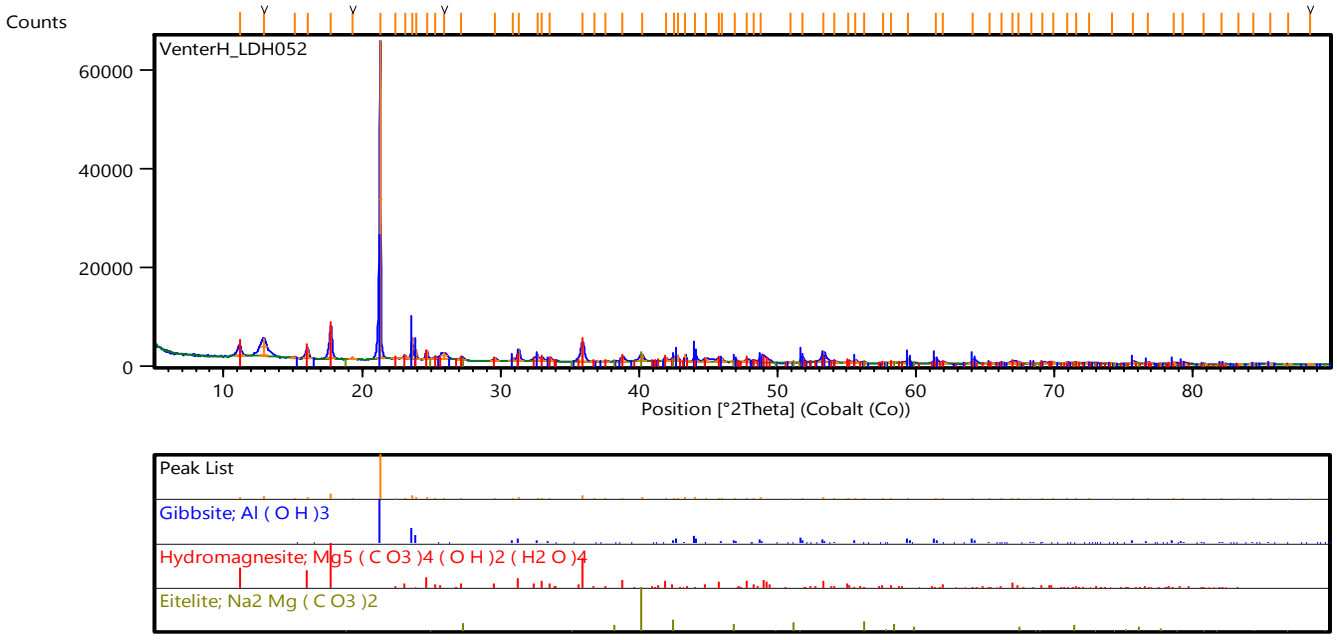

Figure 60: XRD Pattern - MgAl120-4

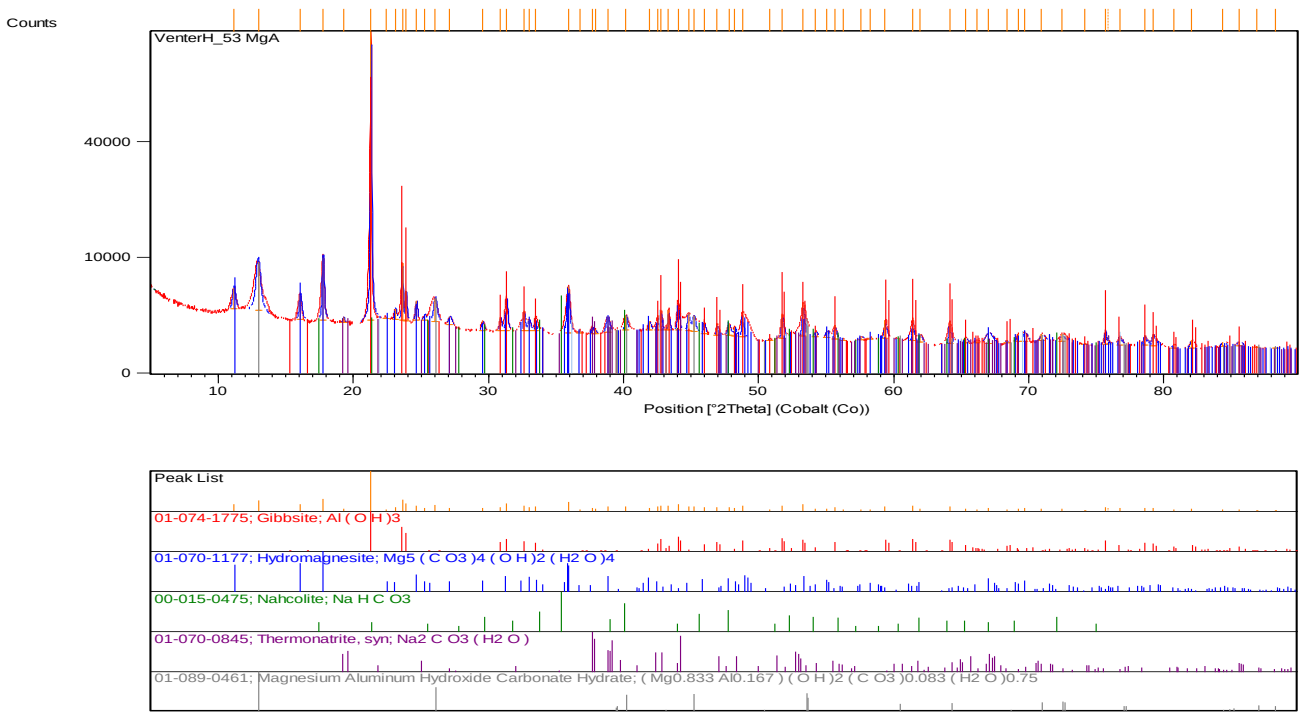

Figure 61: XRD Pattern - MgAl120-5

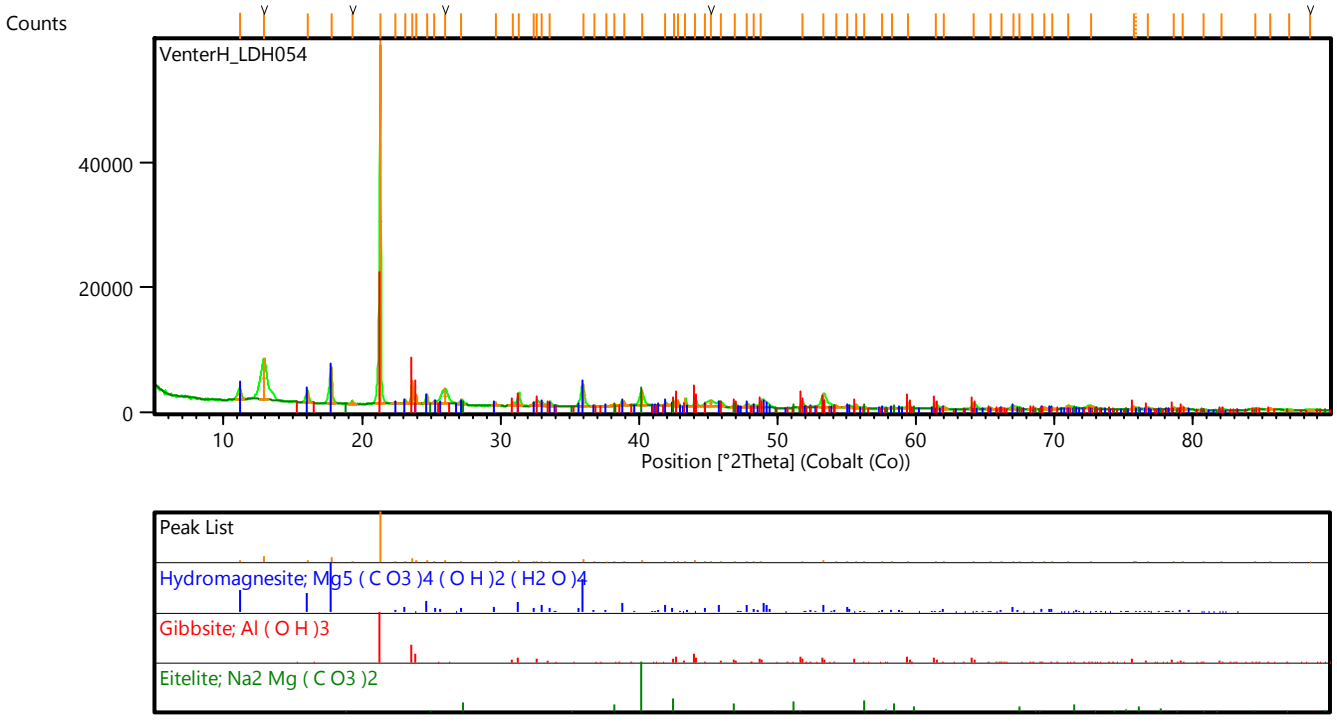

Figure 62: XRD Pattern - MgAl140-1

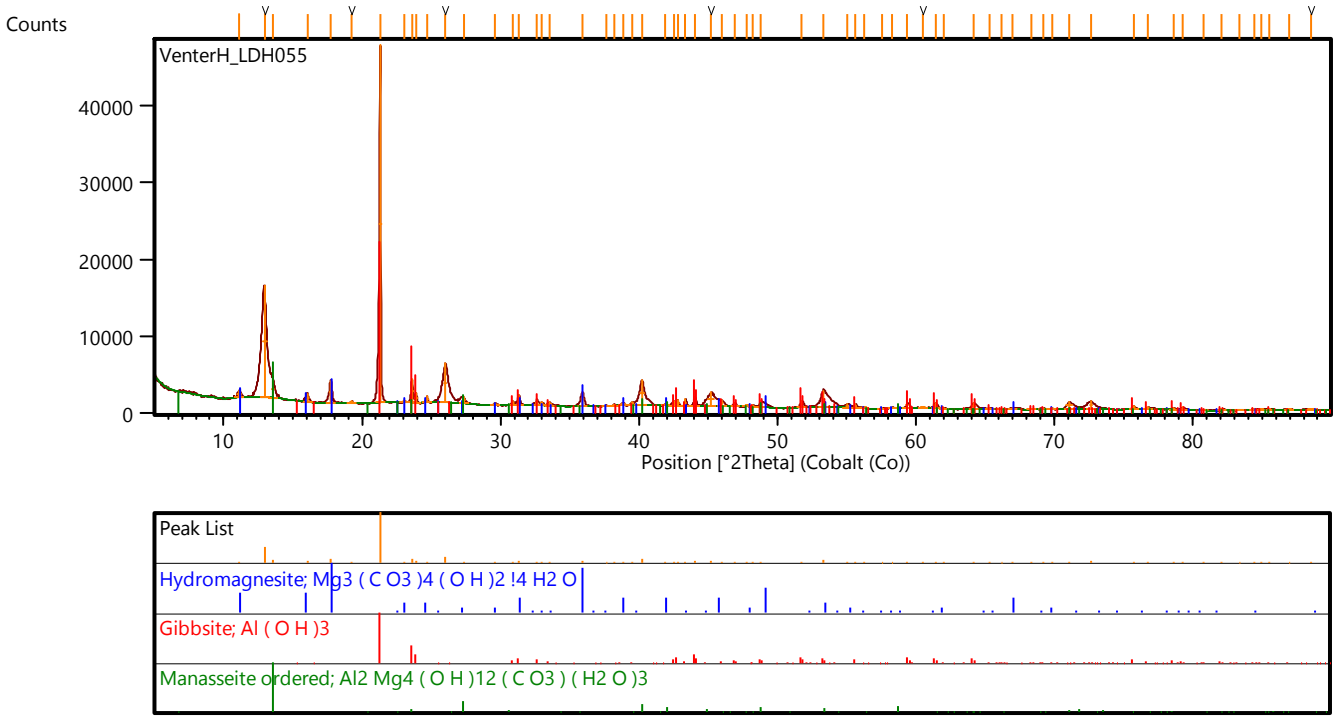

Figure 63: XRD Pattern - MgAl140-2

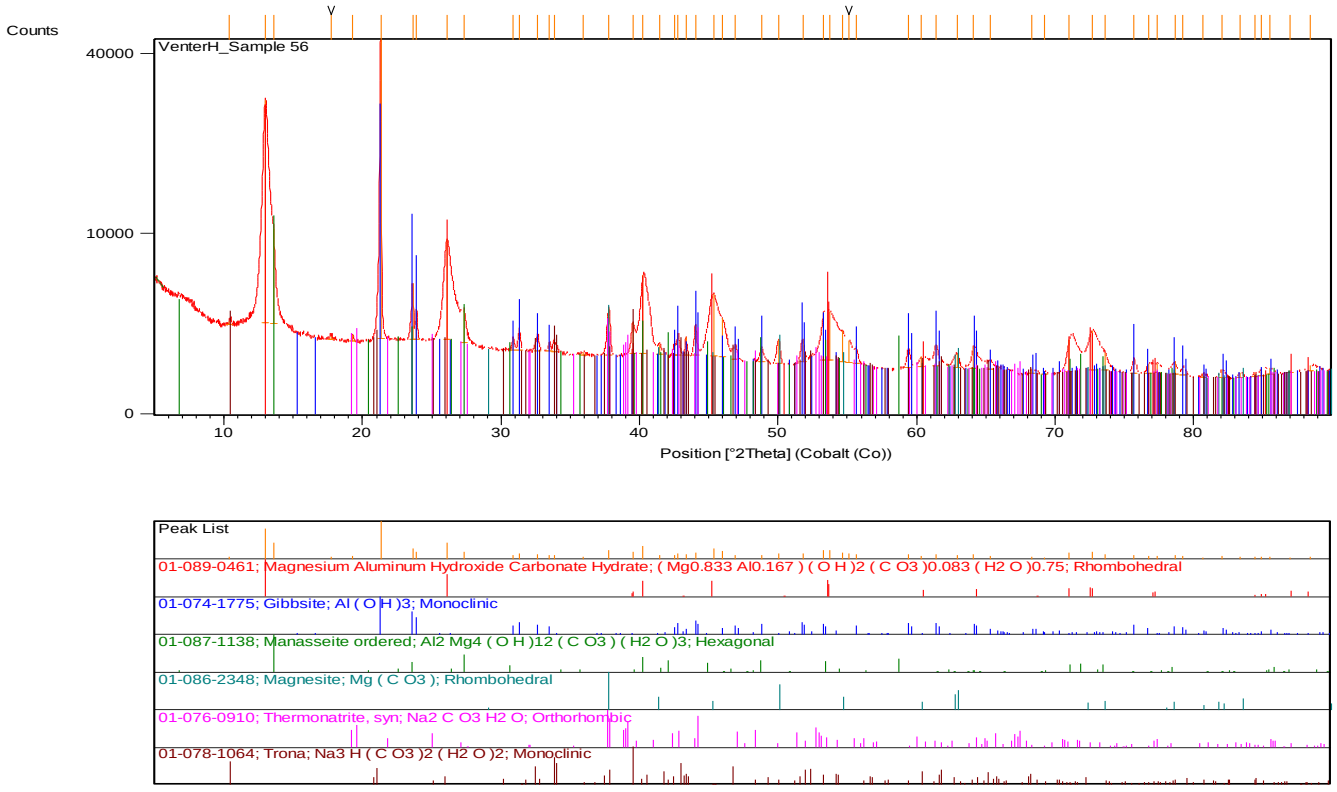

Figure 64: XRD Pattern - MgAl140-3

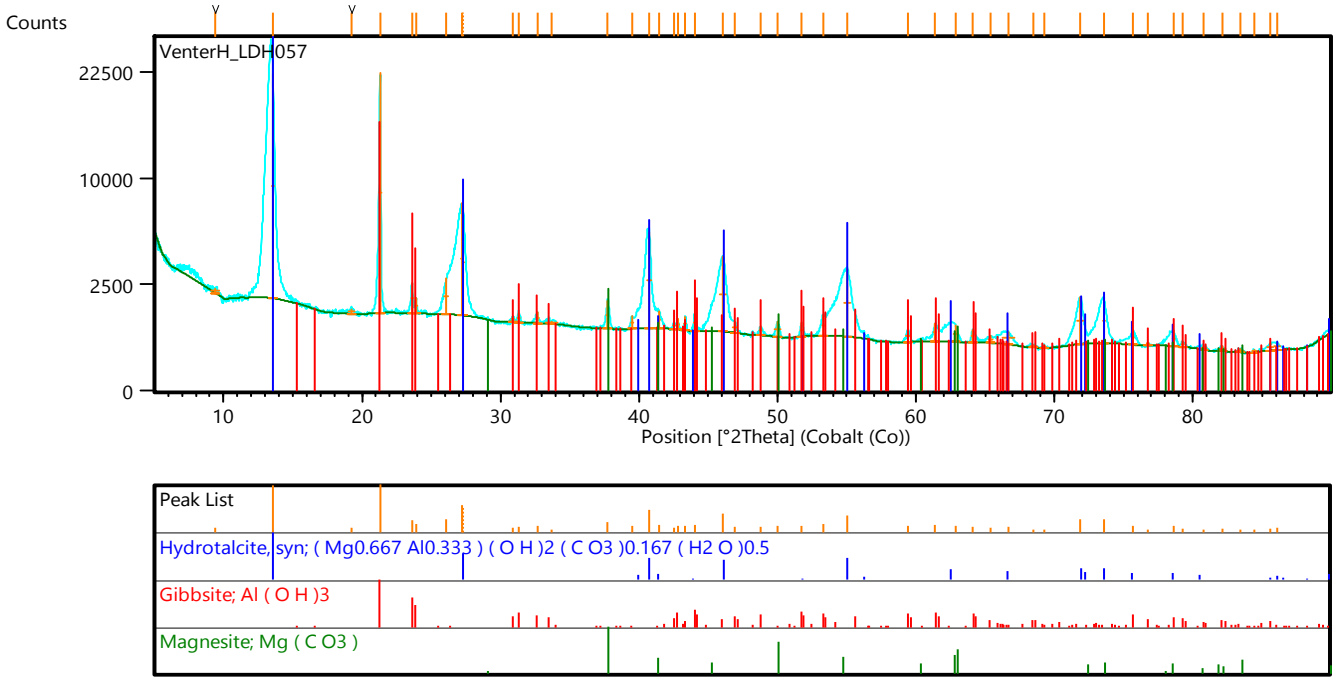

Figure 65: XRD Pattern - MgAl140-4

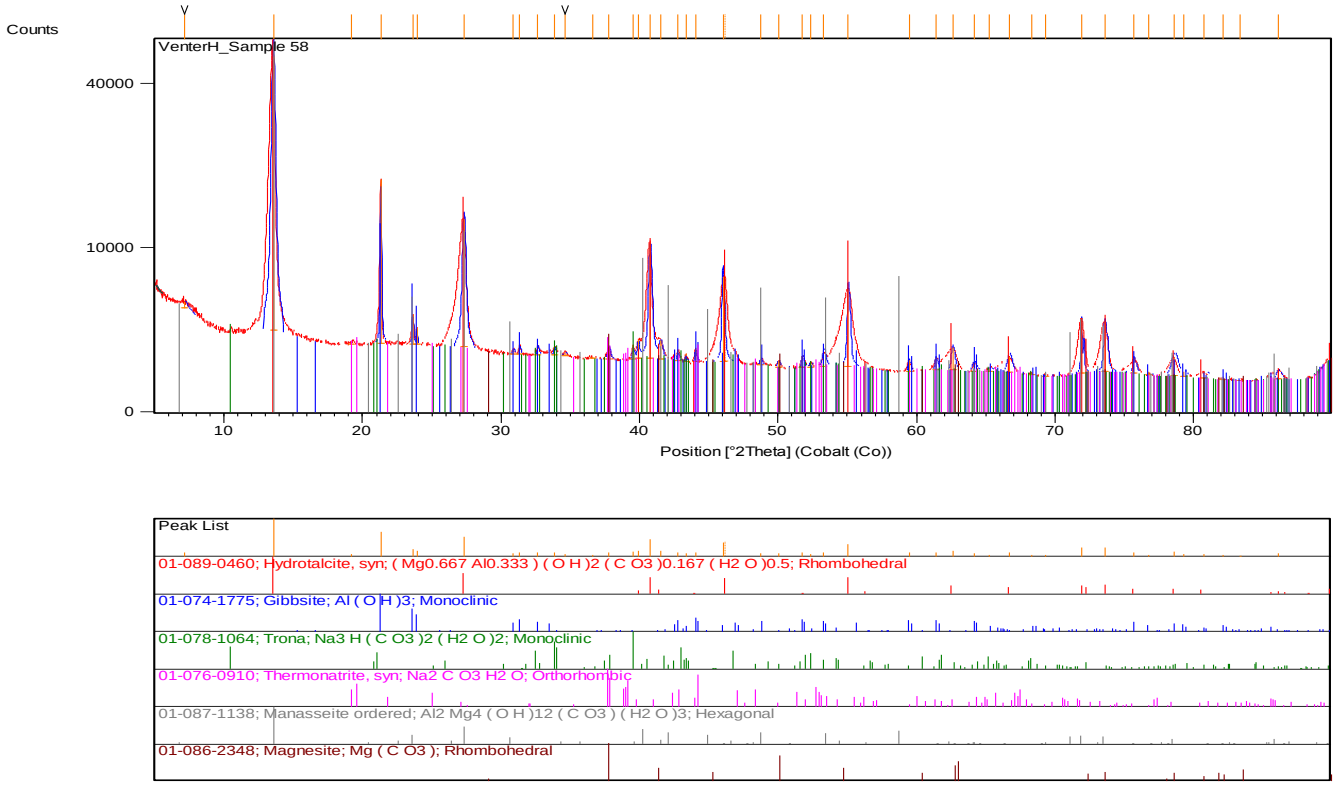

Figure 66: XRD Pattern - MgAl140-5

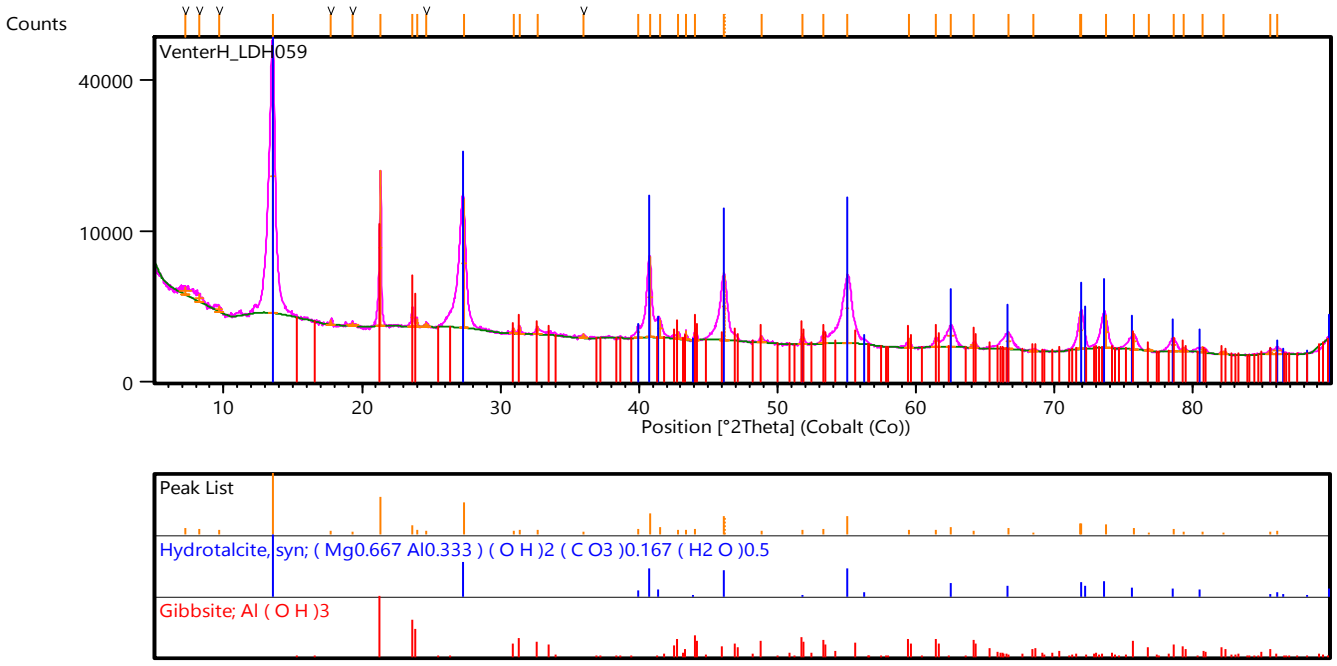

Figure 67: XRD Pattern - MgAl160-1

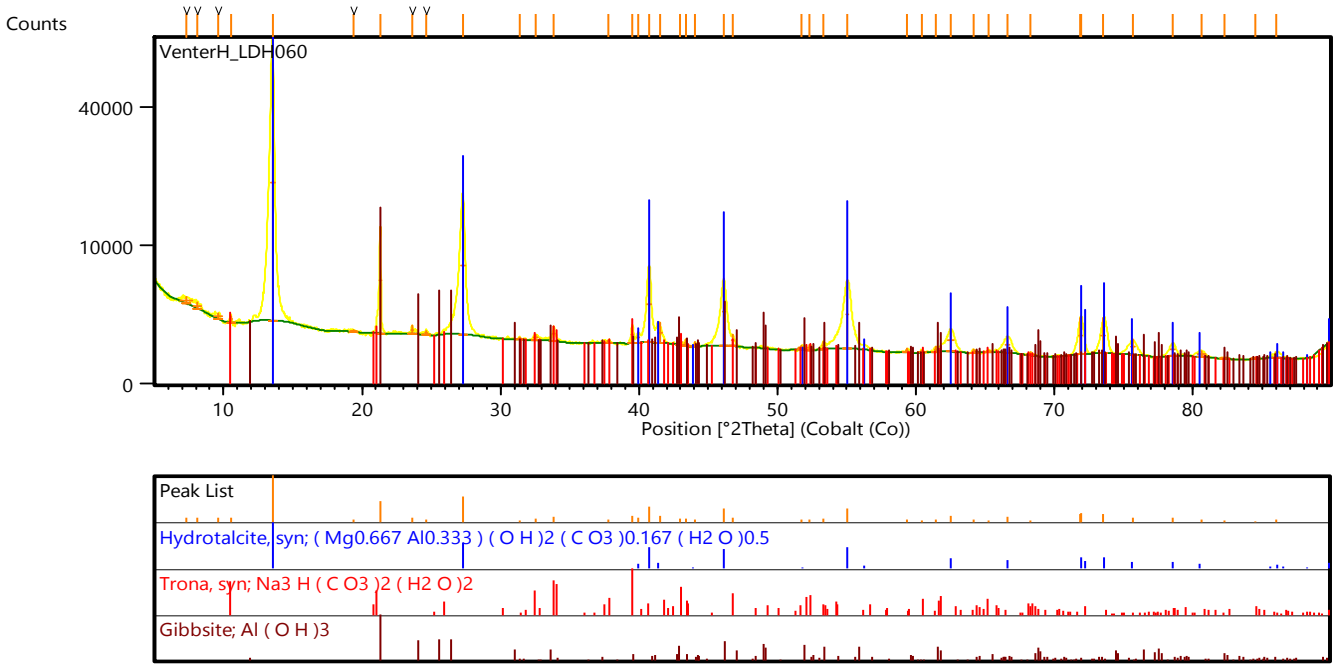

Figure 68: XRD Pattern - MgAl160-2

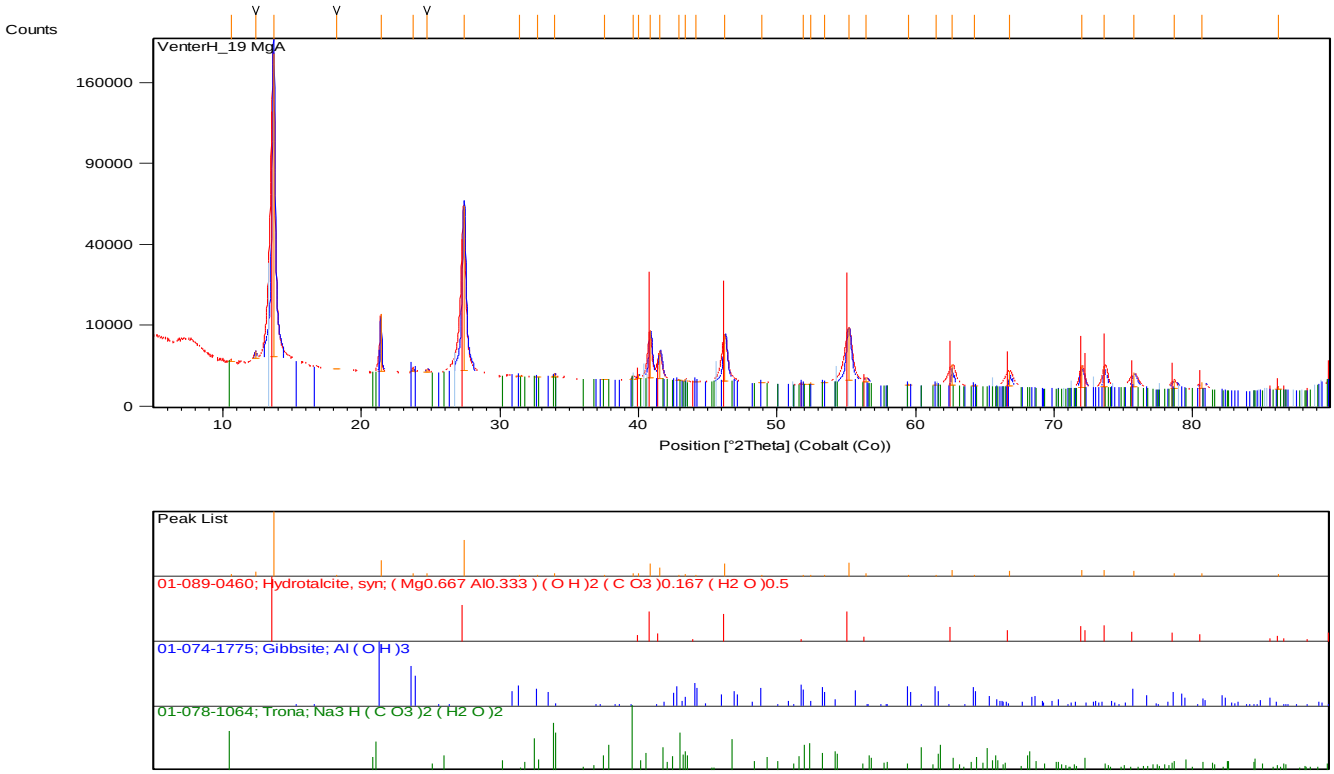

Figure 69: XRD Pattern - MgAl160-3

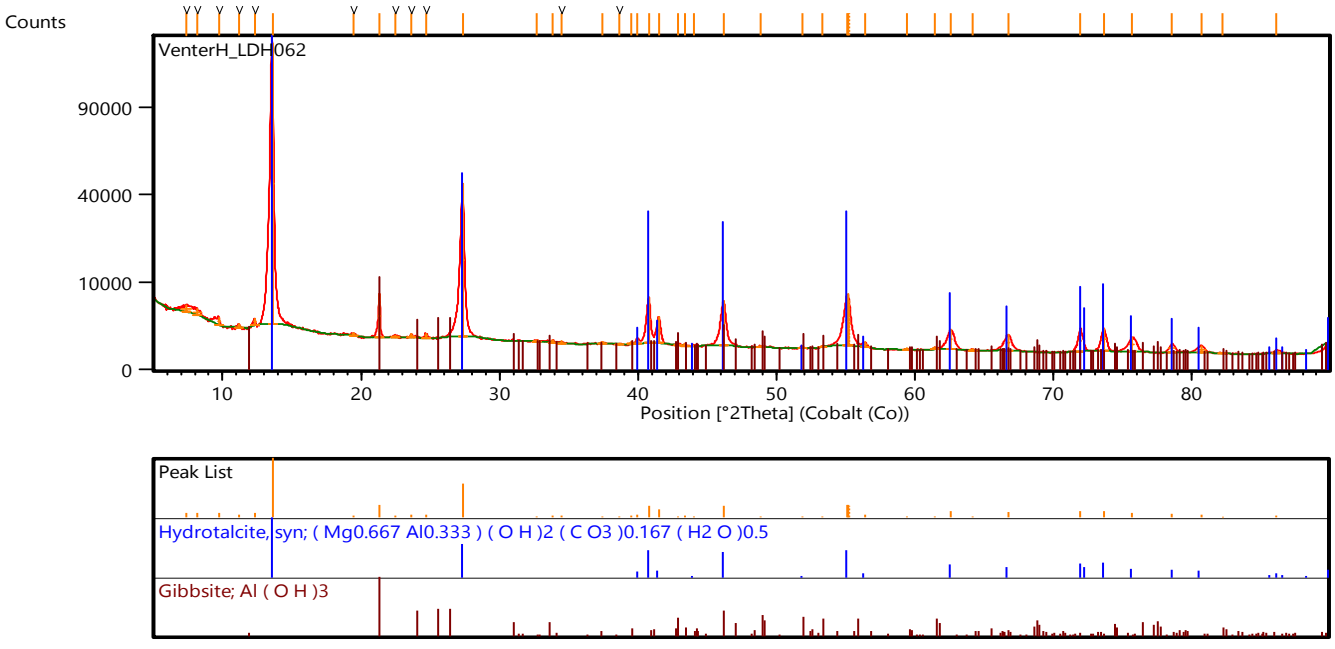

Figure 70: XRD Pattern - MgAl160-4

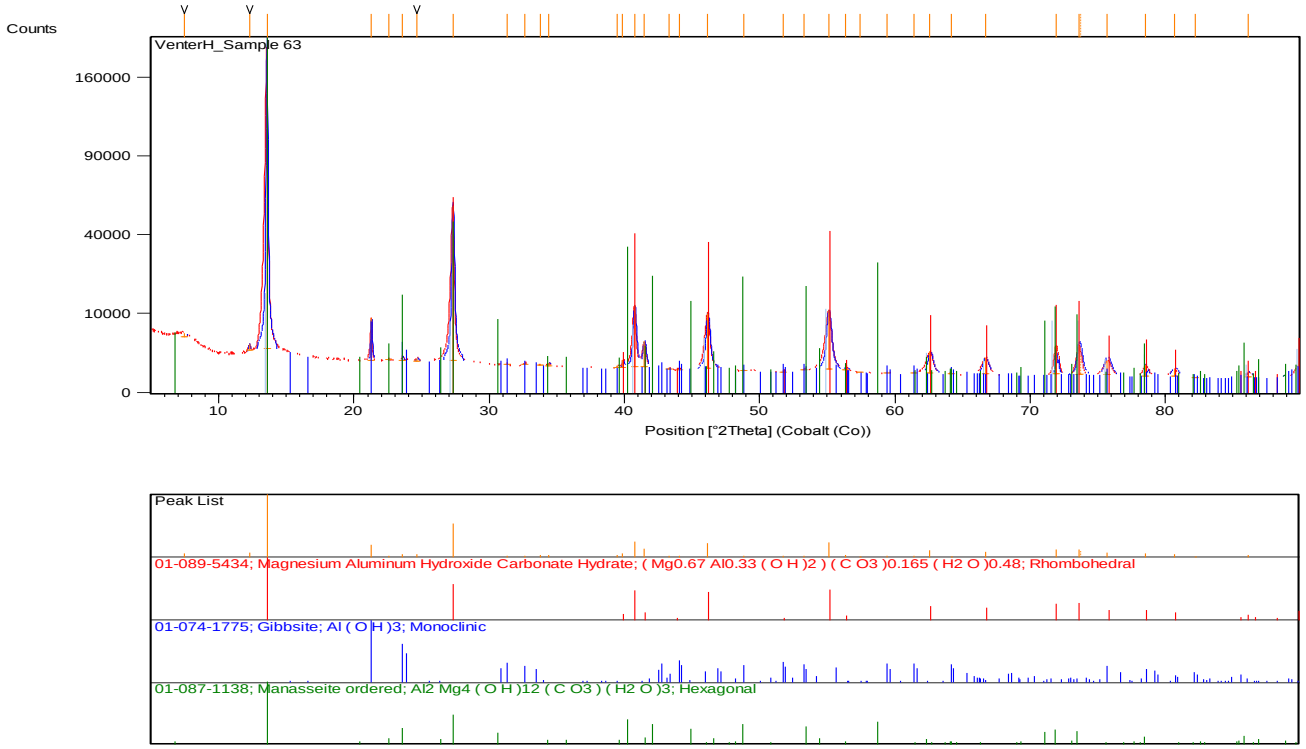

Figure 71: XRD Pattern - MgAl160-5

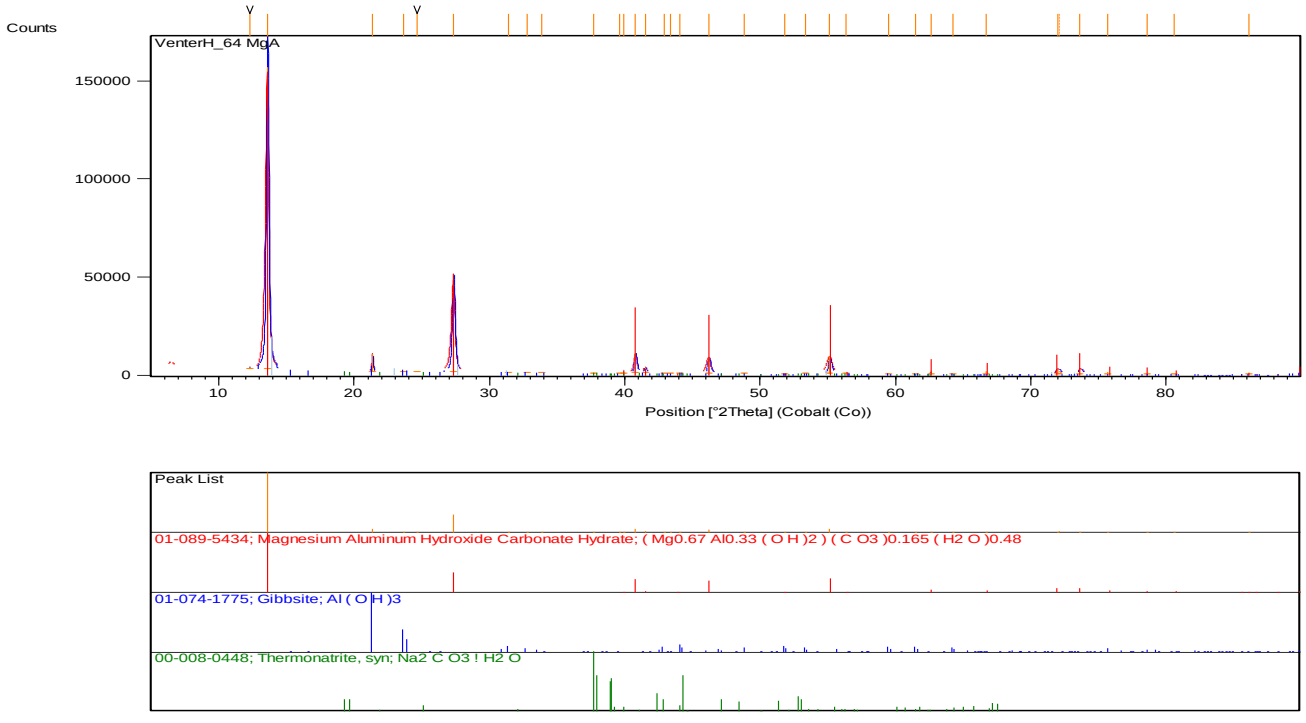

Figure 72: XRD Pattern - MgAl180-1

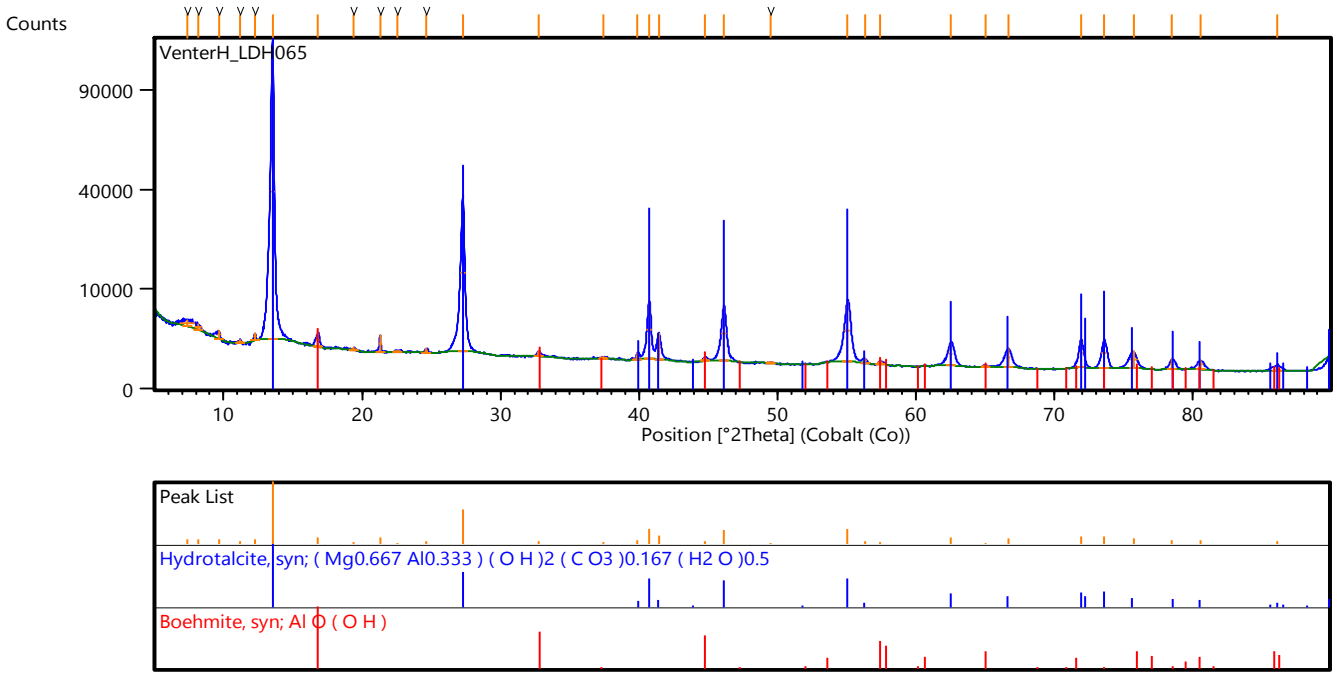

Figure 73: XRD Pattern - MgAl180-2

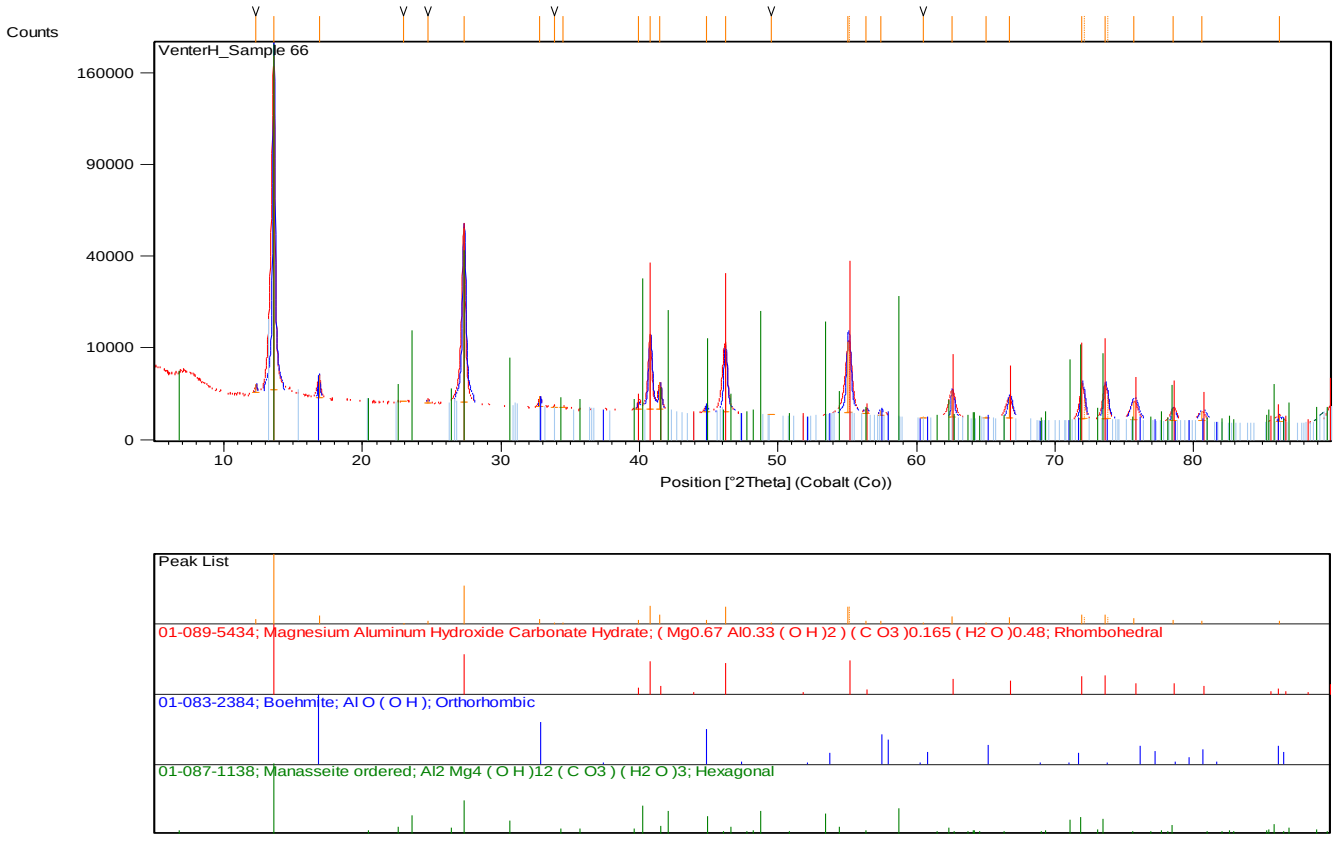

Figure 74: XRD Pattern - MgAl180-3

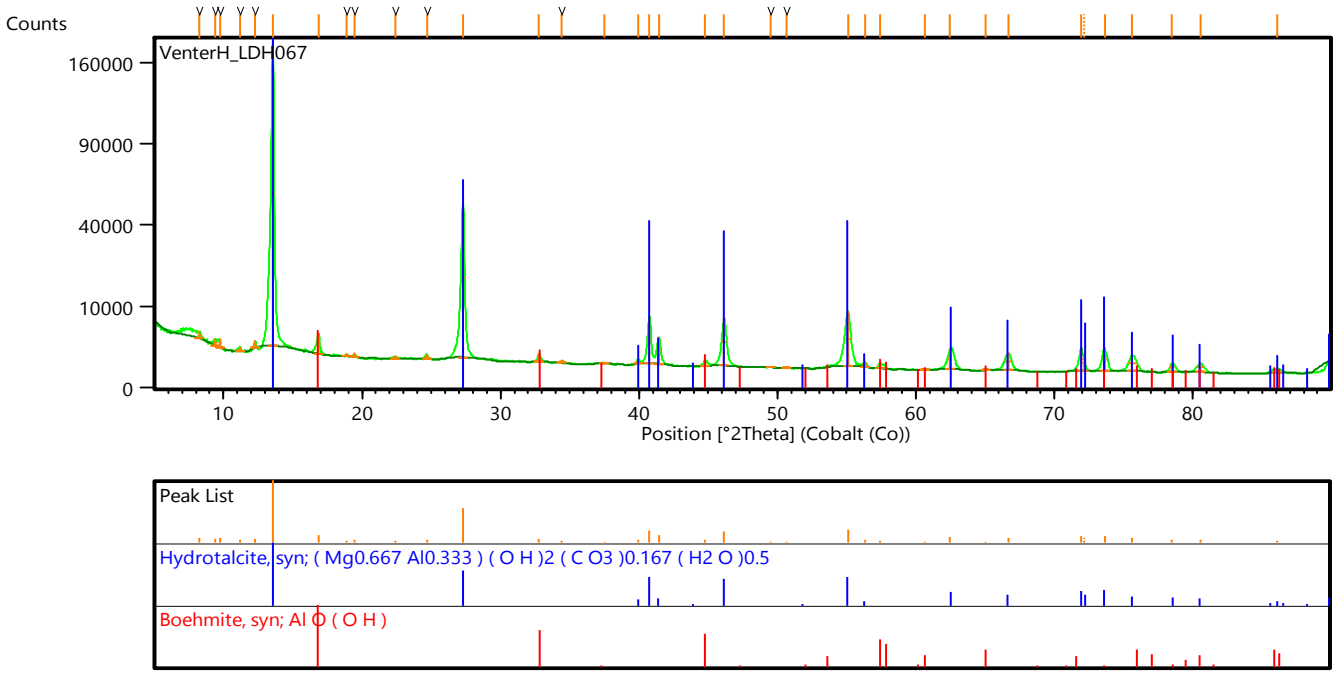

Figure 75: XRD Pattern - MgAl180-4

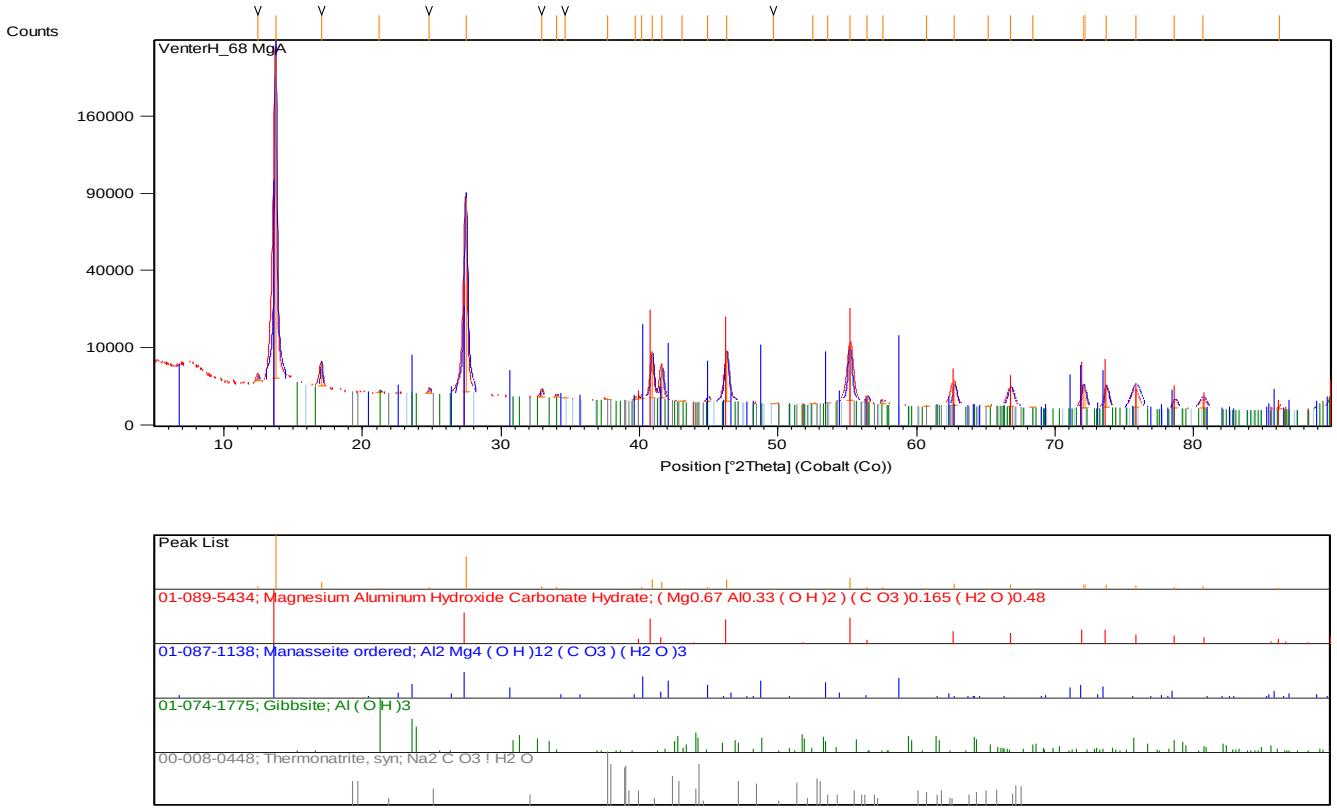

Figure 76: XRD Pattern - MgAl180-5

A.2. The effects of temperature or carbonate concentration on the formation of magnesite and hydromagnesite

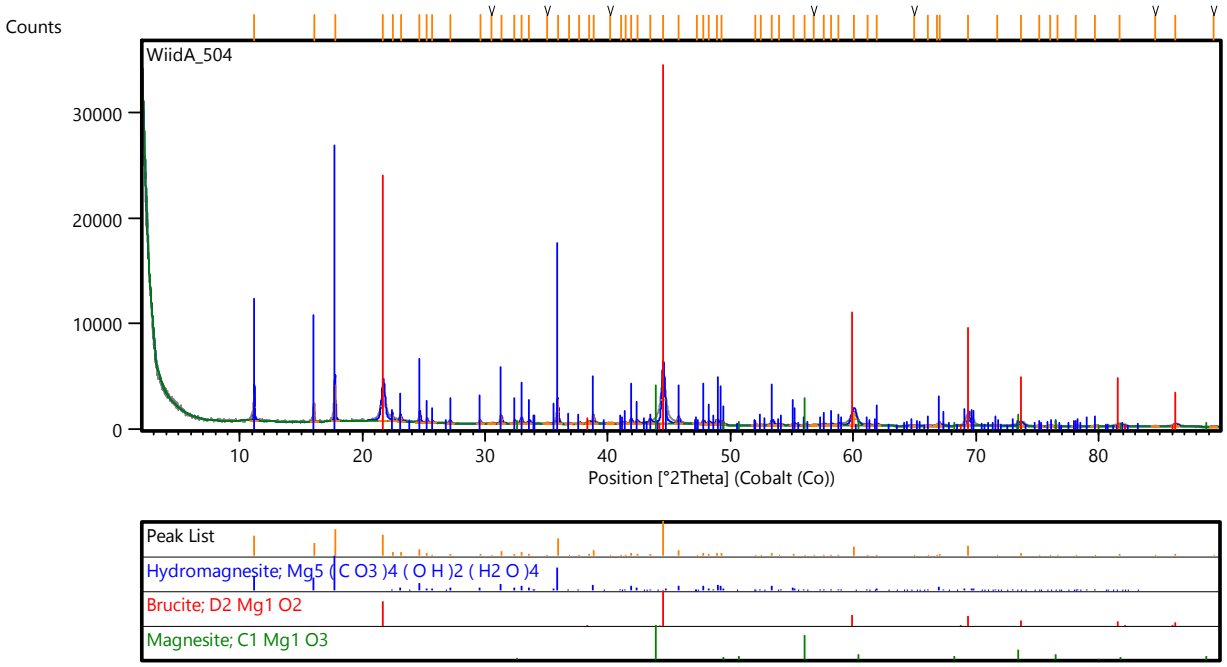

Figure 77: XRD pattern at 120 ^{o}C.

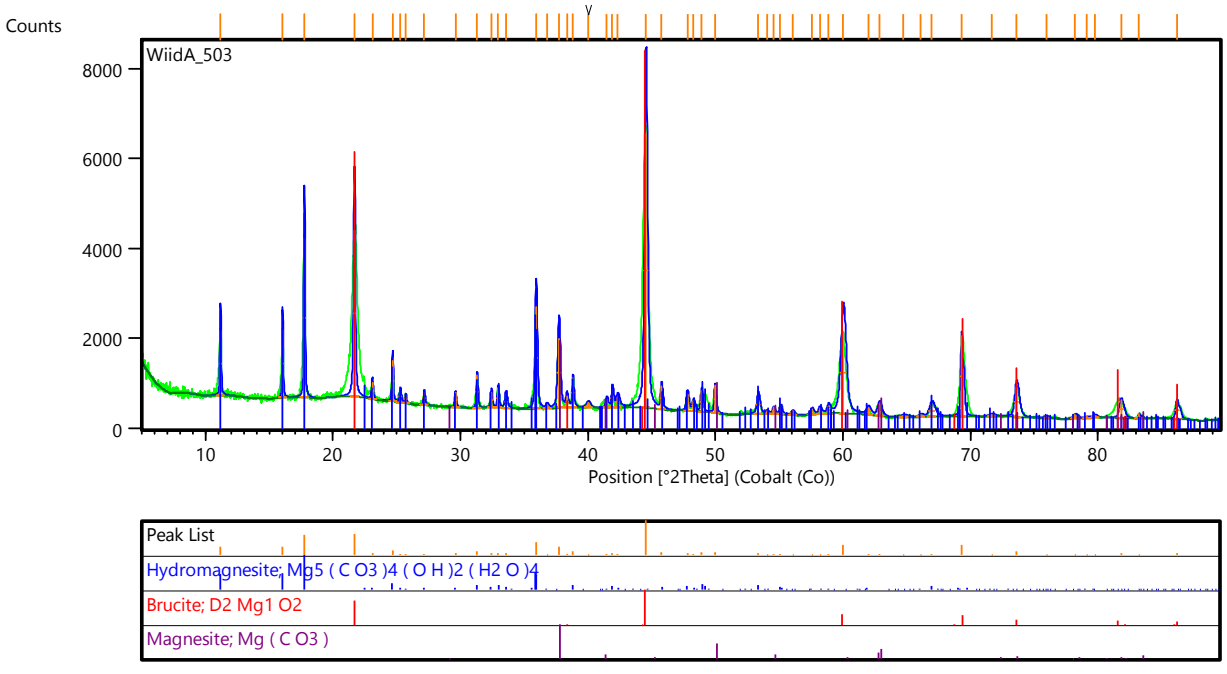

Figure 78: XRD pattern at 140 ^{o}C.

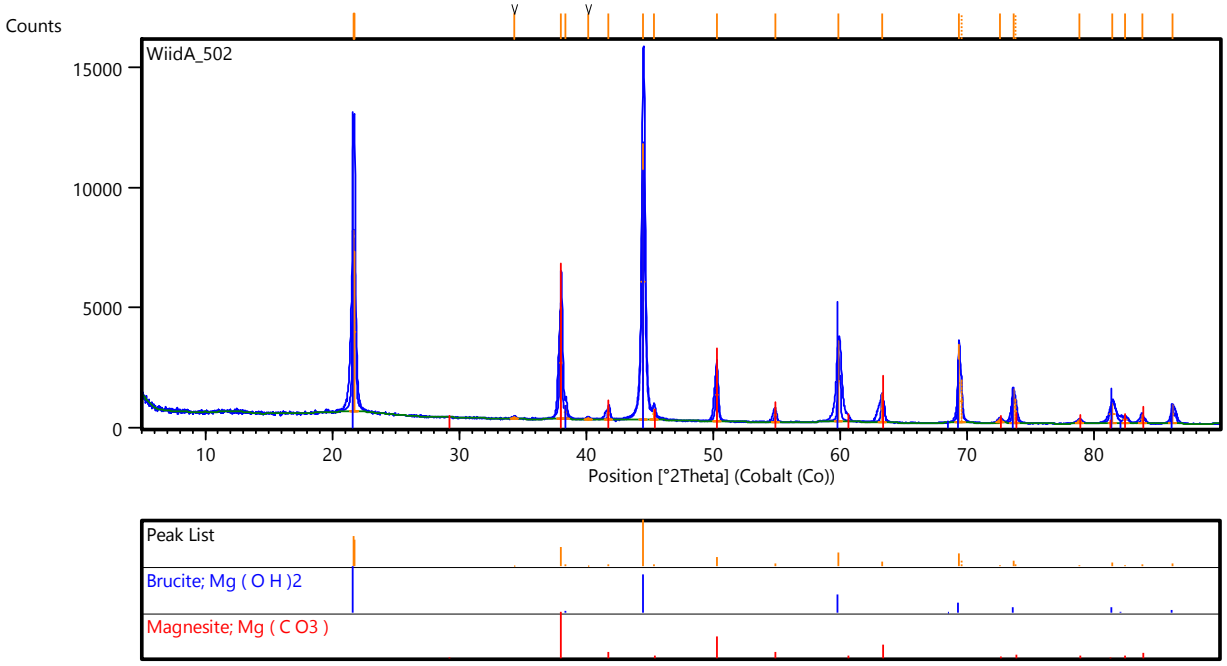

Figure 79: XRD pattern at 160 ^{o}C.

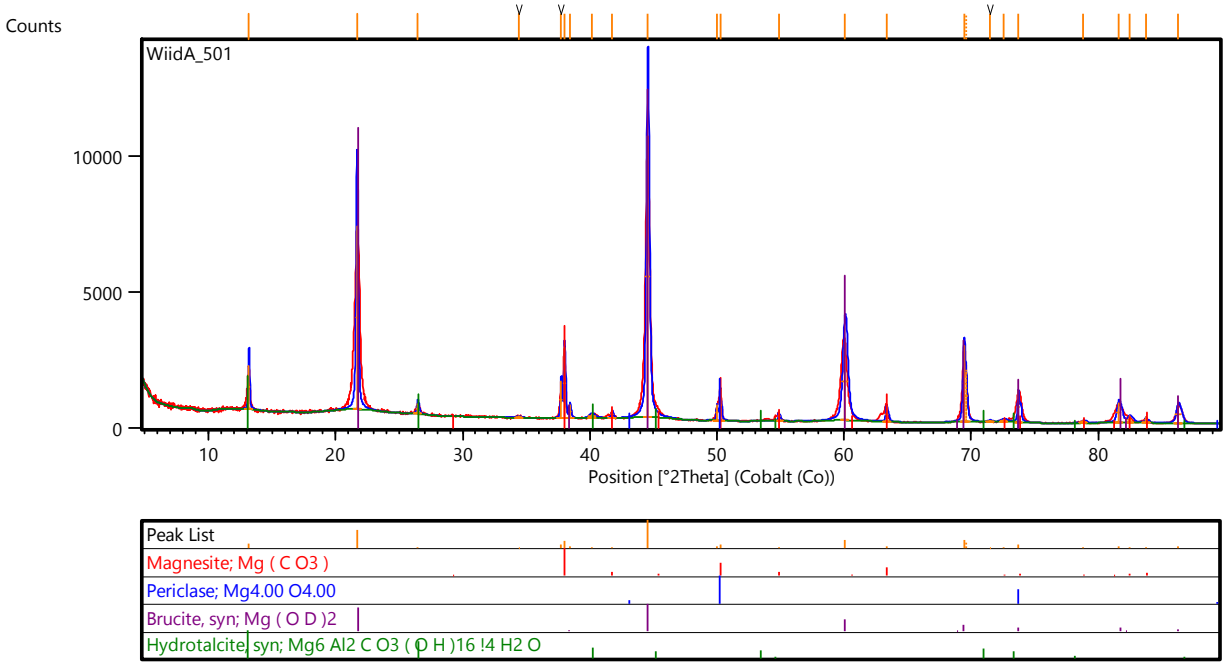

Figure 80: XRD pattern at 180 ^{o}C.

A.3. Mixed metal oxides/hydroxides method

Cobalt

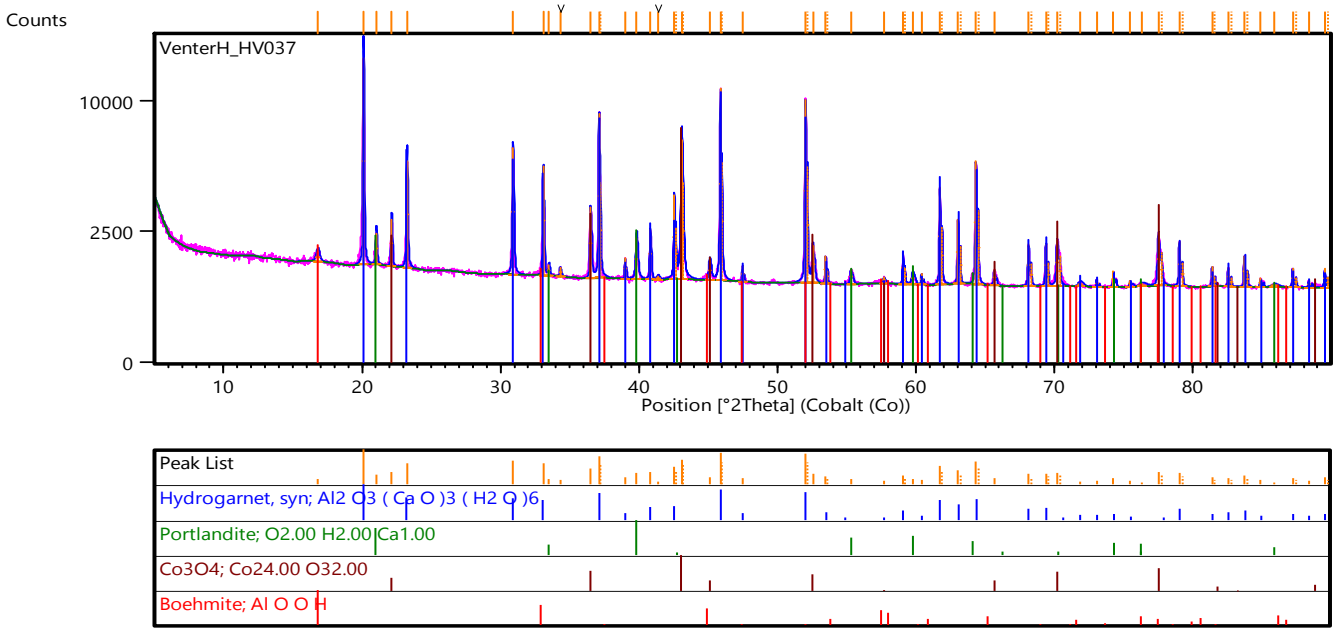

Figure 81: *Ca/Co(II)* 25 mole% - Inert

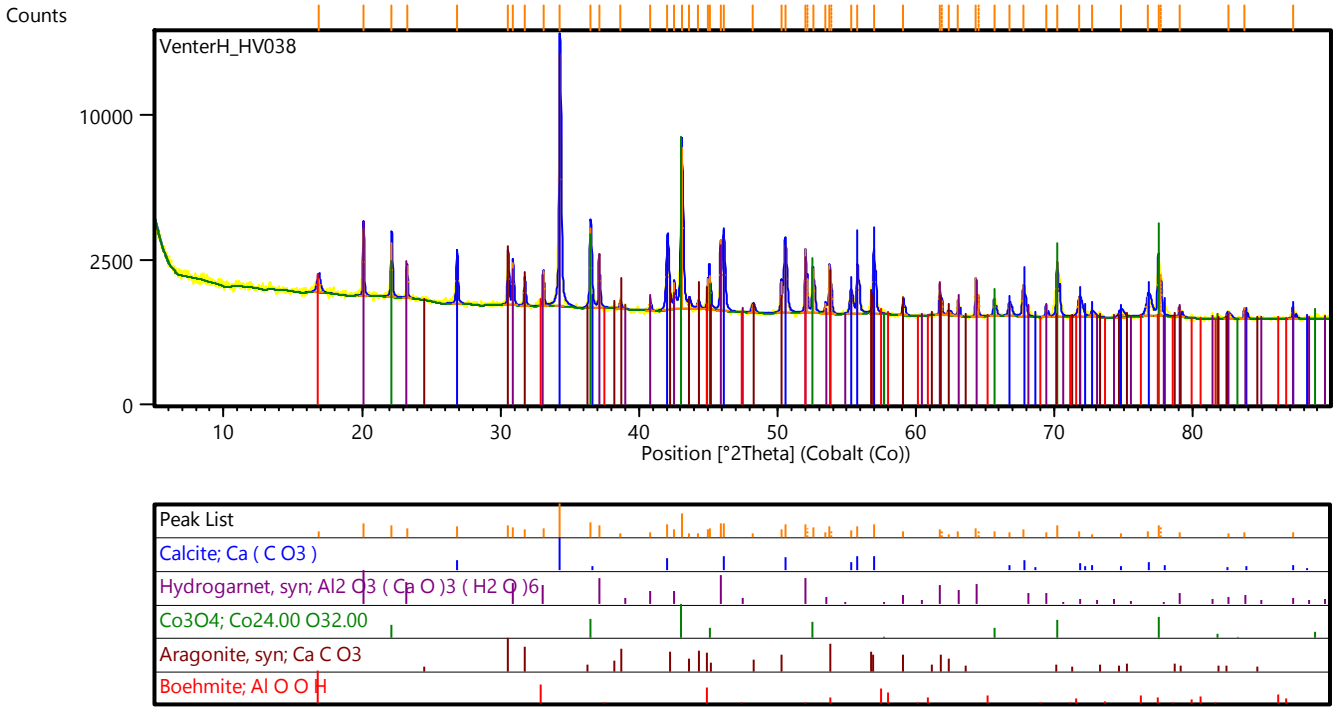

Figure 82: *Ca/Co(II)* 25 mole% - Carbonate

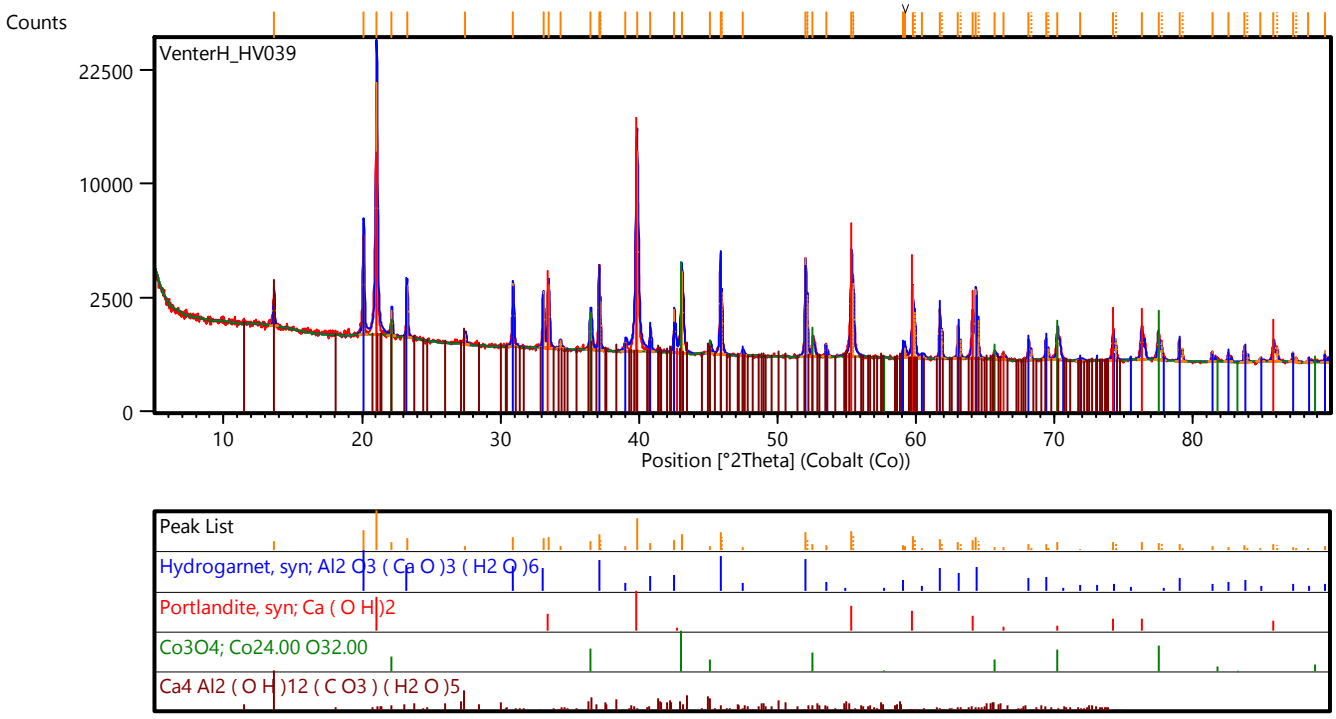

Figure 83: *Ca/Co(III)* 8.3 mole% - Inert

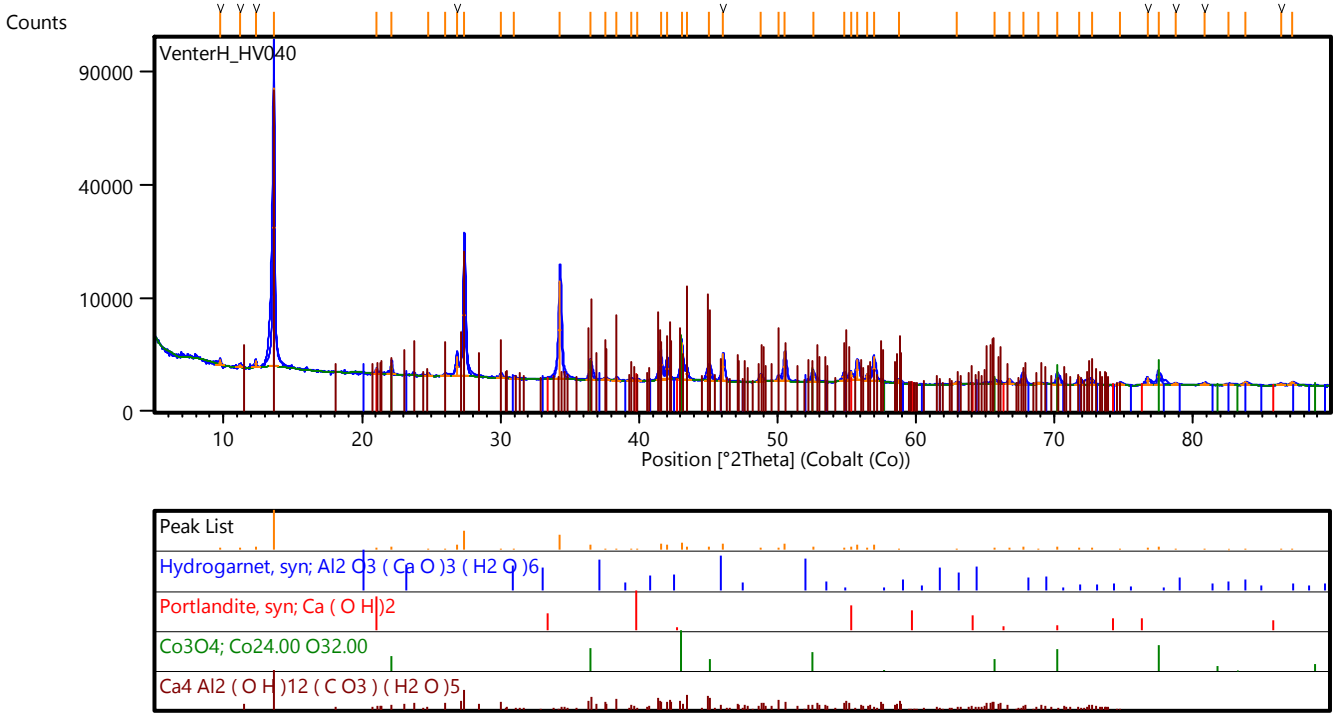

Figure 84: *Ca/Co(III)* 8.3 mole% - Carbonate

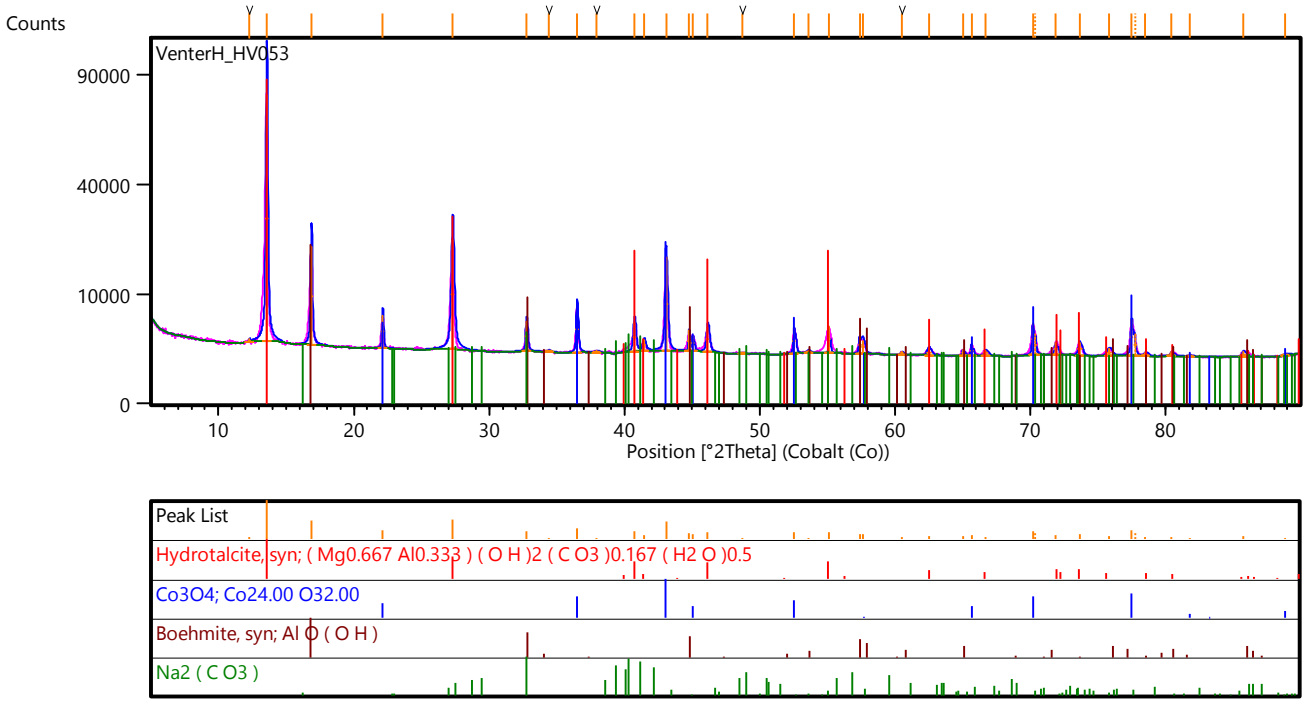

Figure 85: *Mg/Co(II)* 25 mole% - Carbonate

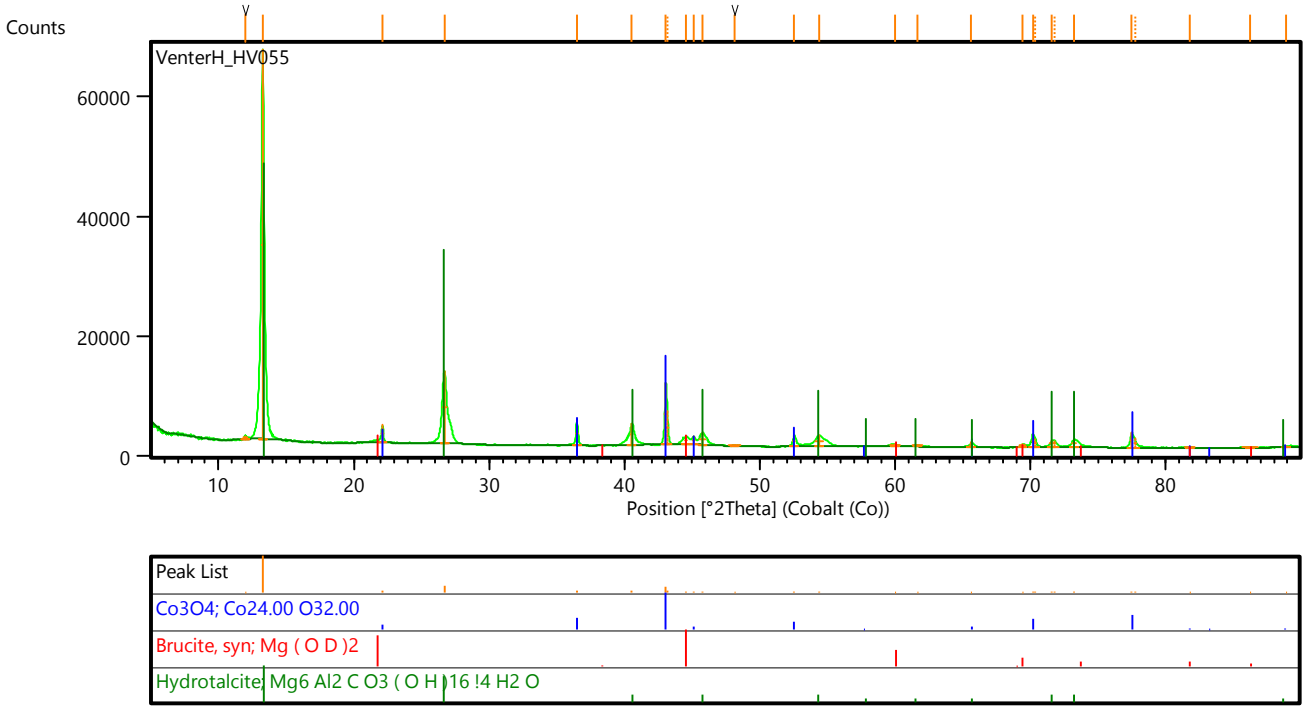

Figure 86: *Mg/Co(III)* 8.3 mole% - Carbonate

Copper

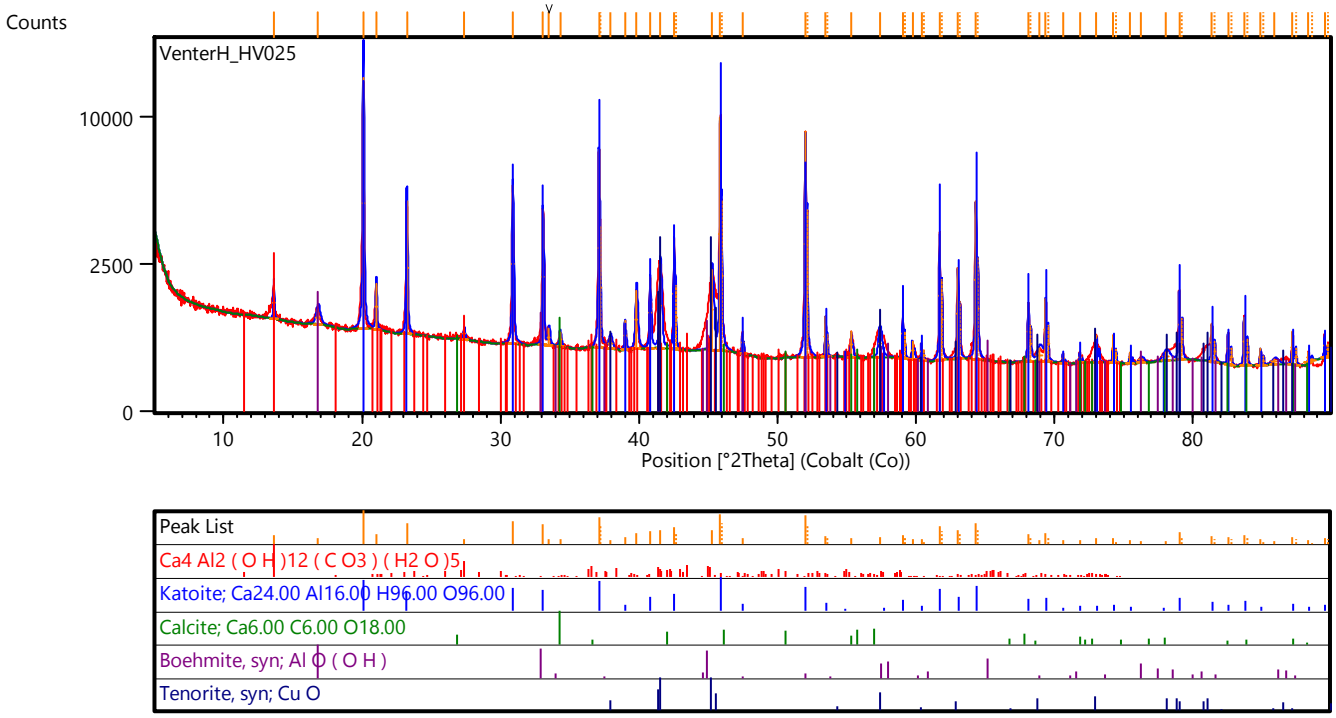

Figure 87: *Ca/Cu(II)* 25 mole% - Inert

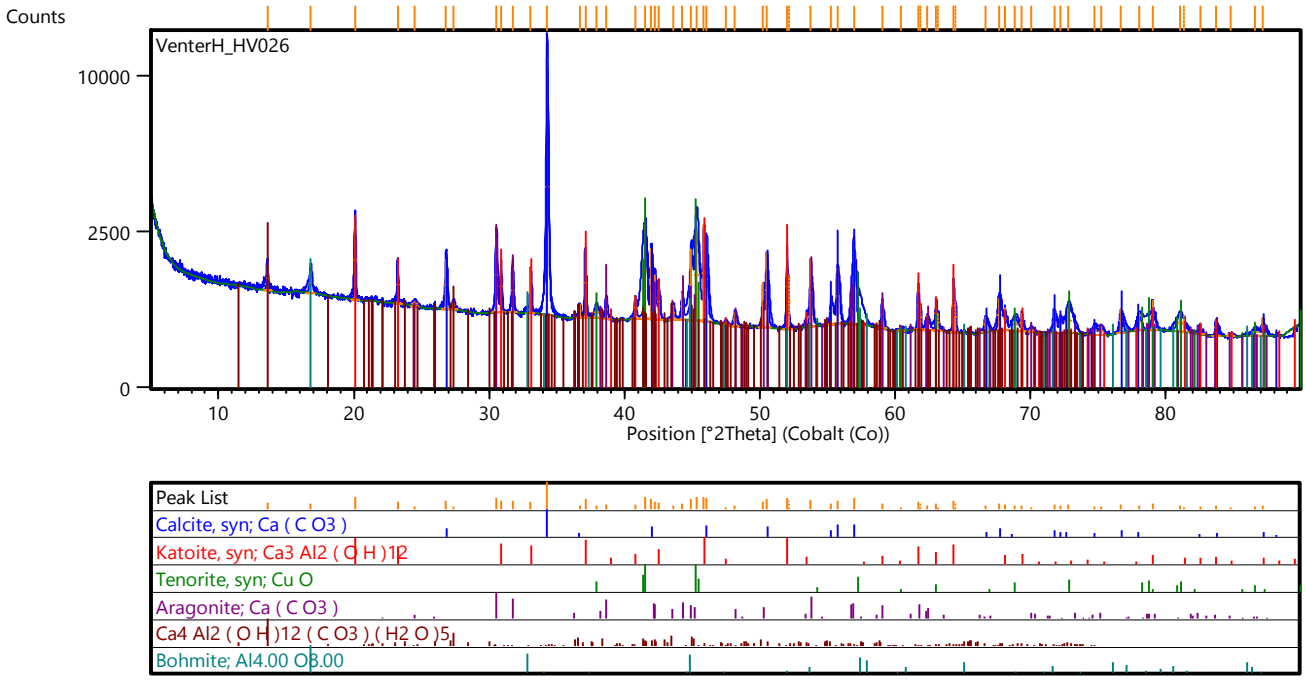

Figure 88: *Ca/Cu(II)* 25 mole% - Carbonate

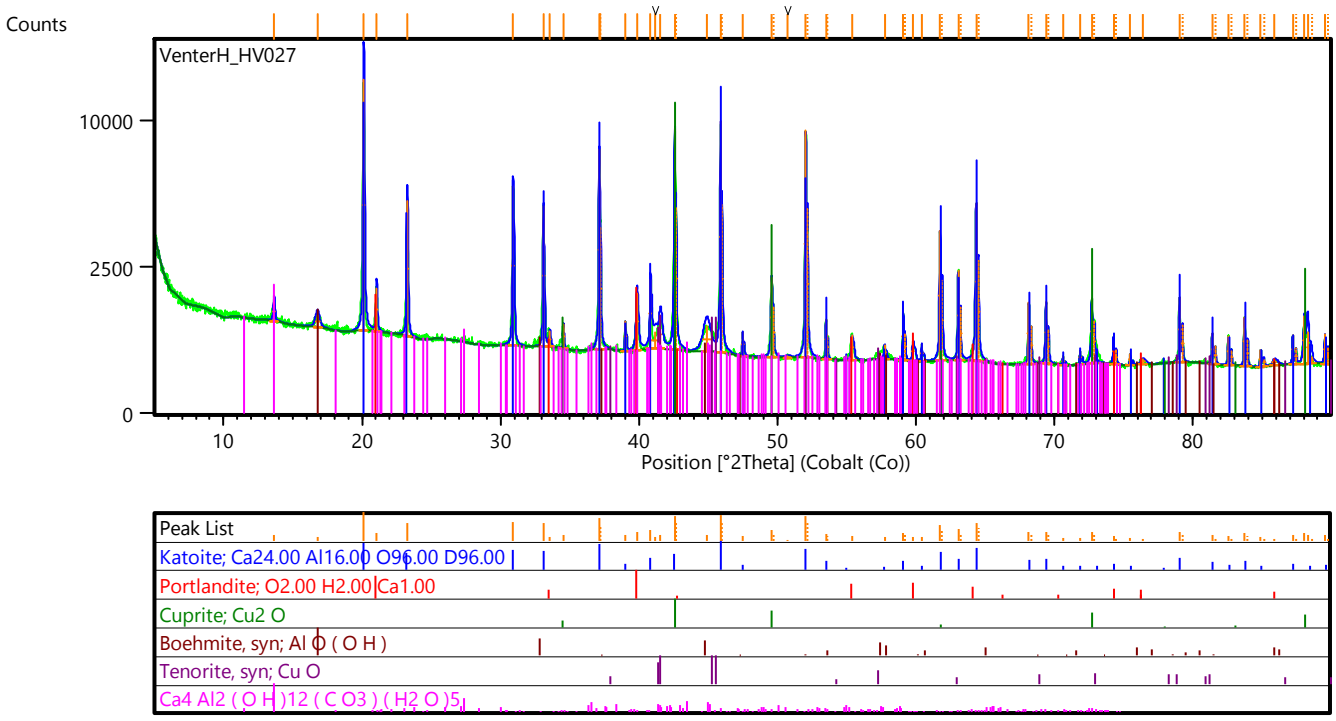

Figure 89: *Ca/Cu(I)* 25 mole% - Inert

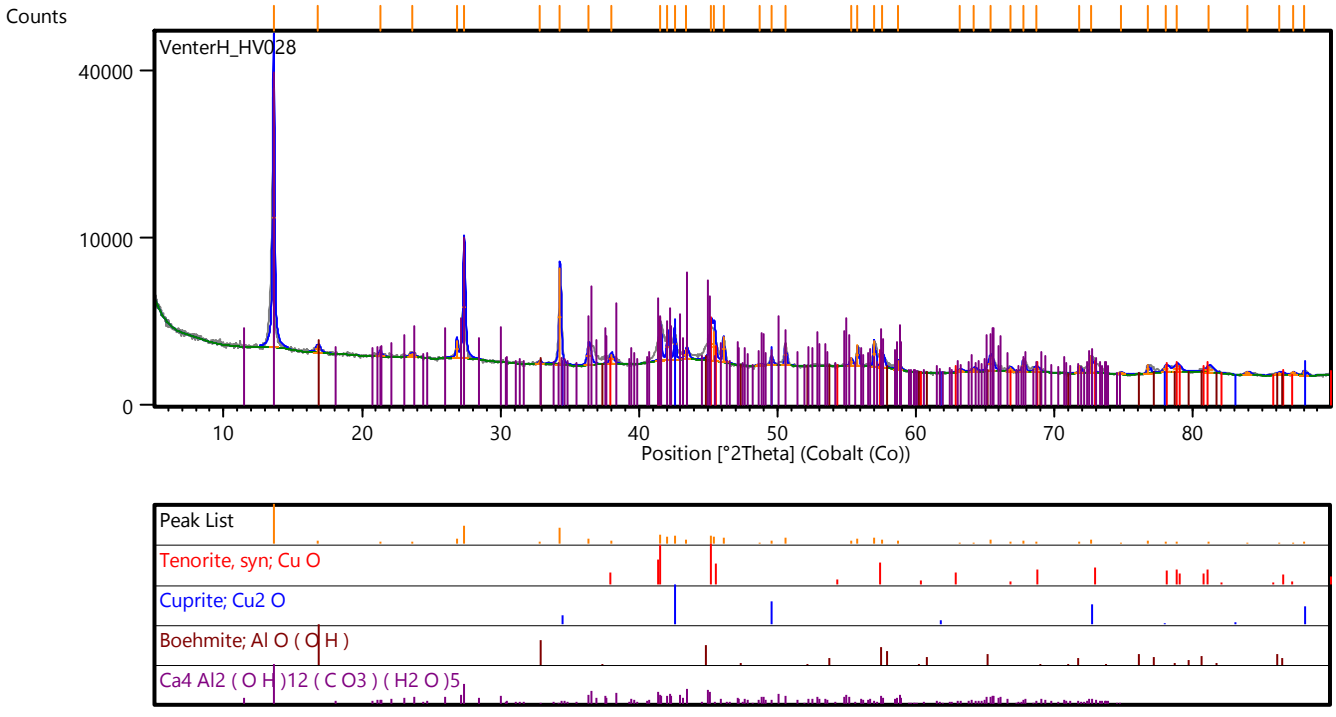

Figure 90: *Ca/Cu(I)* 25 mole% - Carbonate

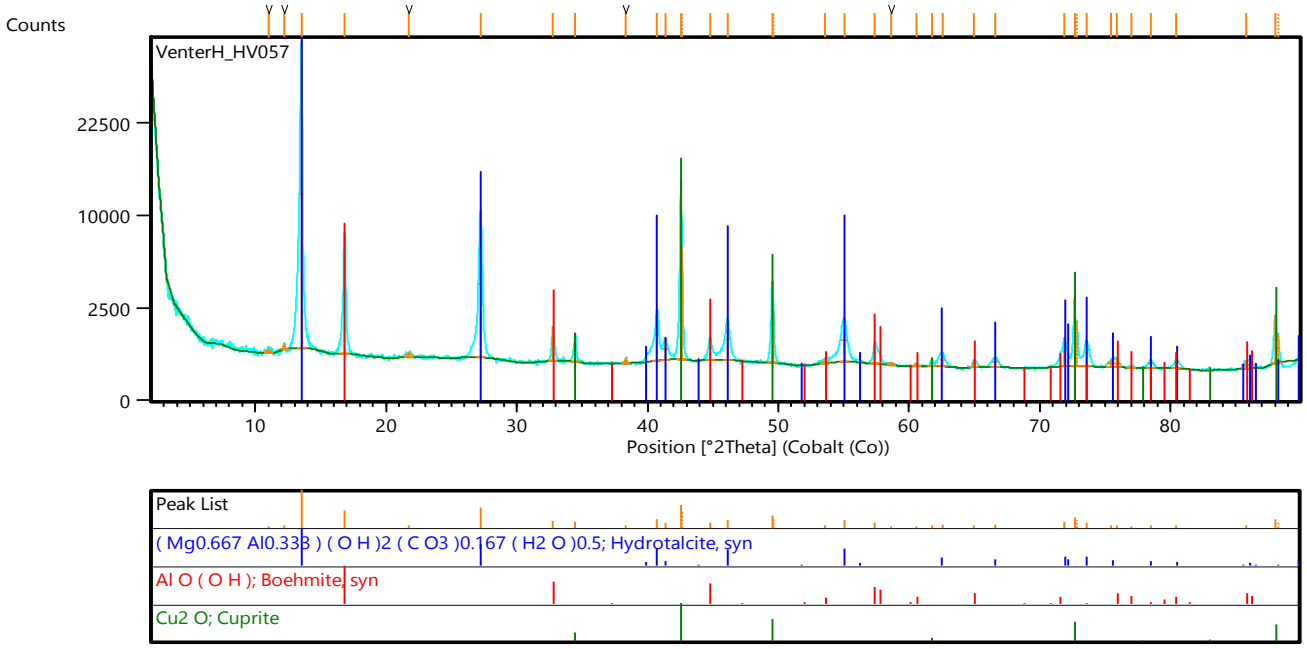

Figure 91: *Mg/Cu(I)* 25 mole% - Carbonate

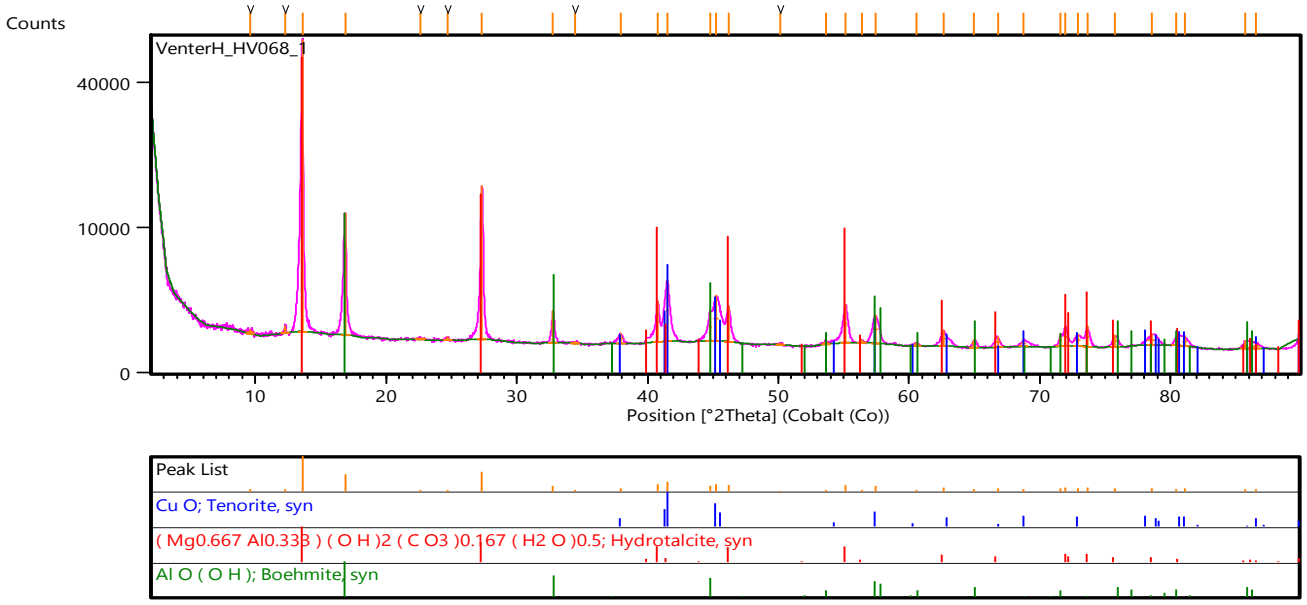

Figure 92: *Mg/Cu(II)* 25 mole% - Carbonate

Manganese

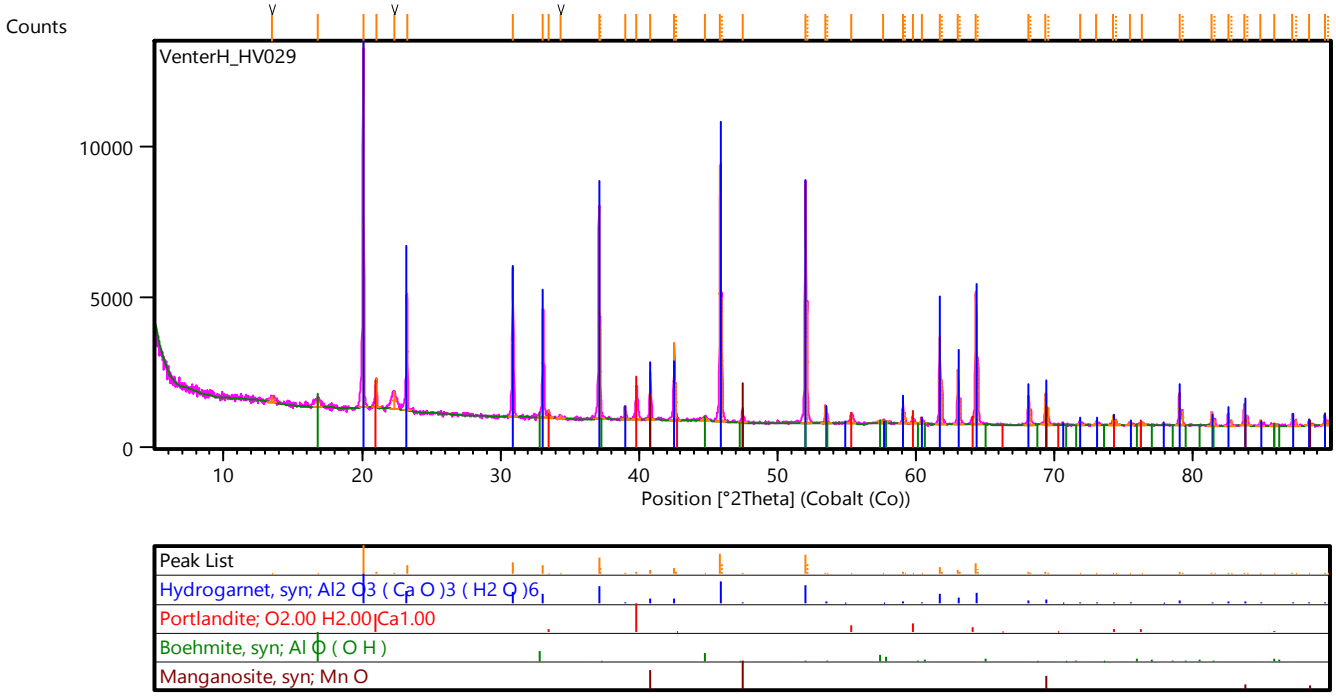

Figure 93: *Ca/Mn(II)* 25 mole% - Inert

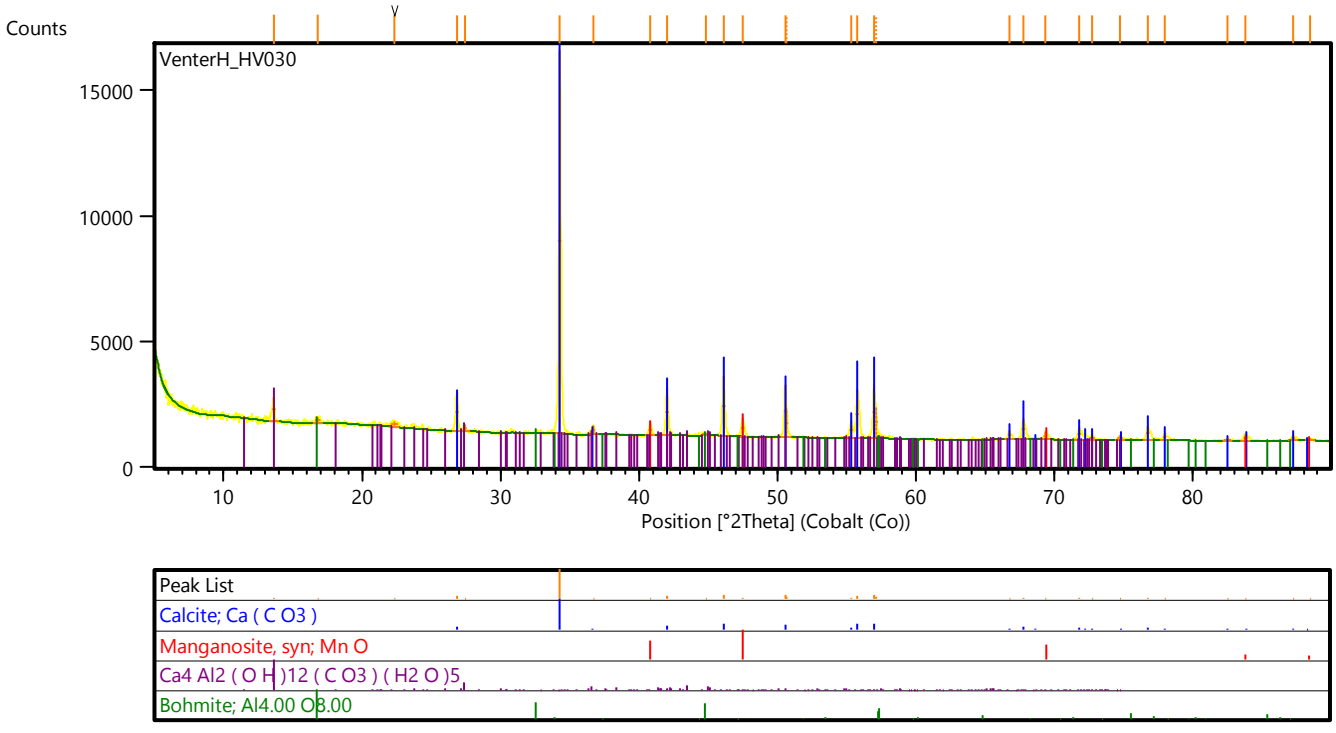

Figure 94: *Ca/Mn(II)* 25 mole% - Carbonate

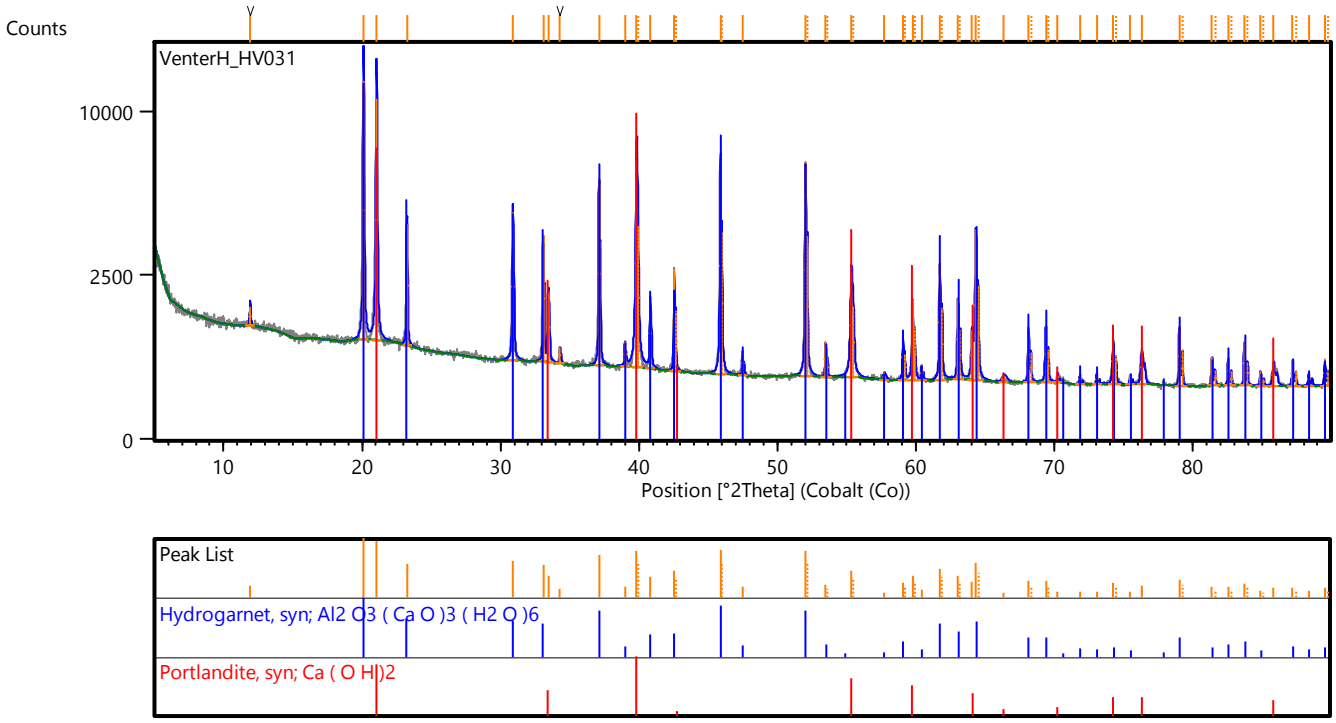

Figure 95: *Ca/Mn(II)* 8.3 mole% - Inert

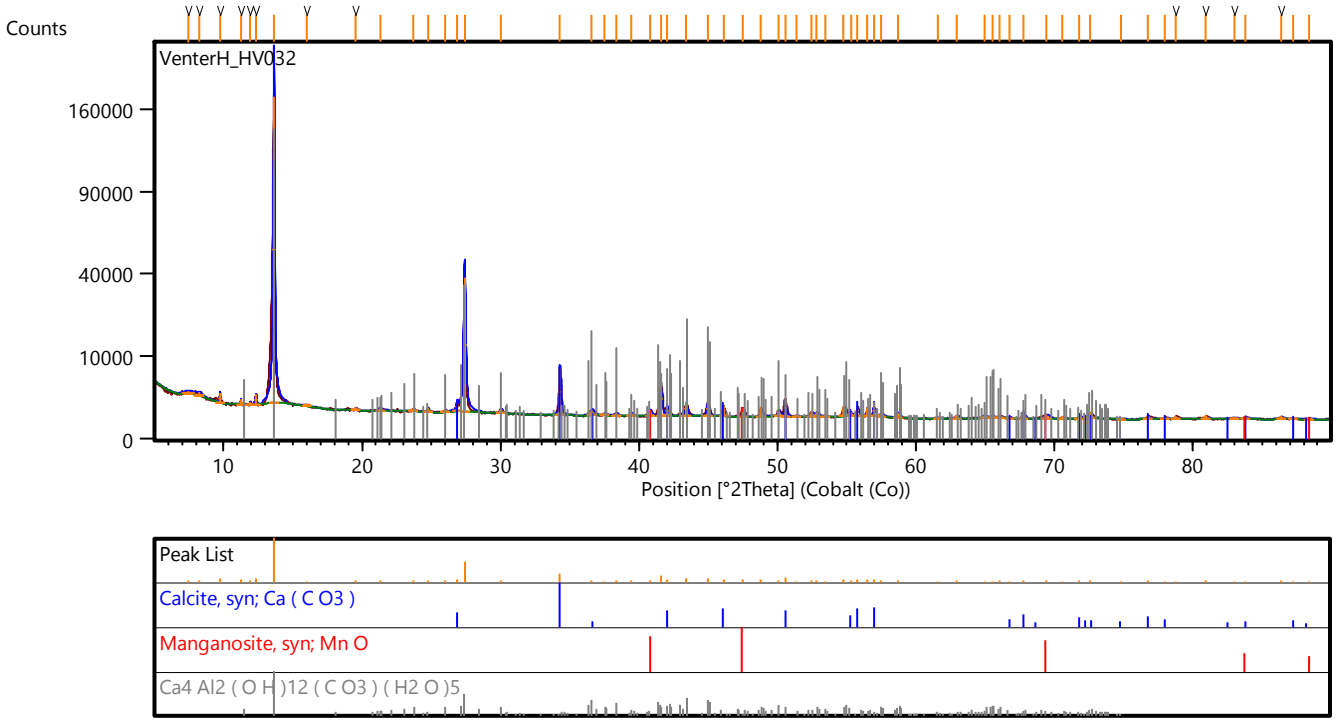

Figure 96: *Ca/Mn(II)* 8.3 mole% - Carbonate

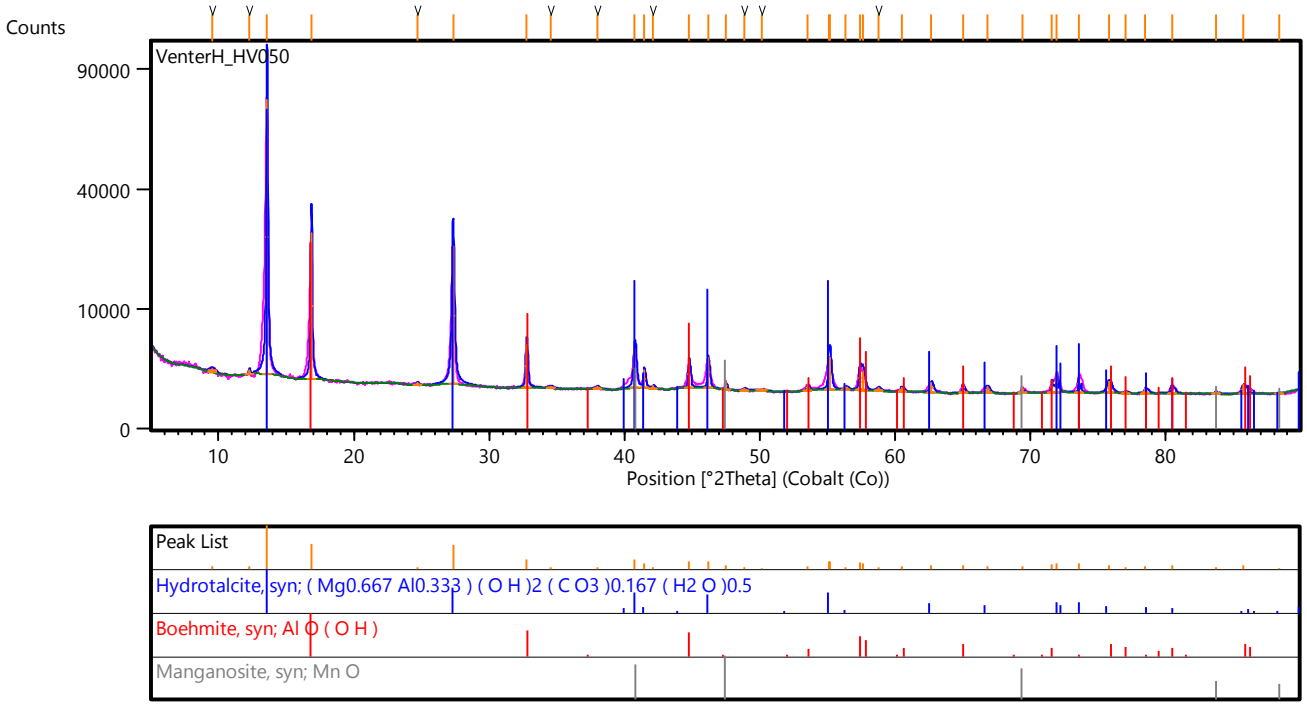

Figure 97: *Mg/Mn(II)* 25 mole% - Carbonate

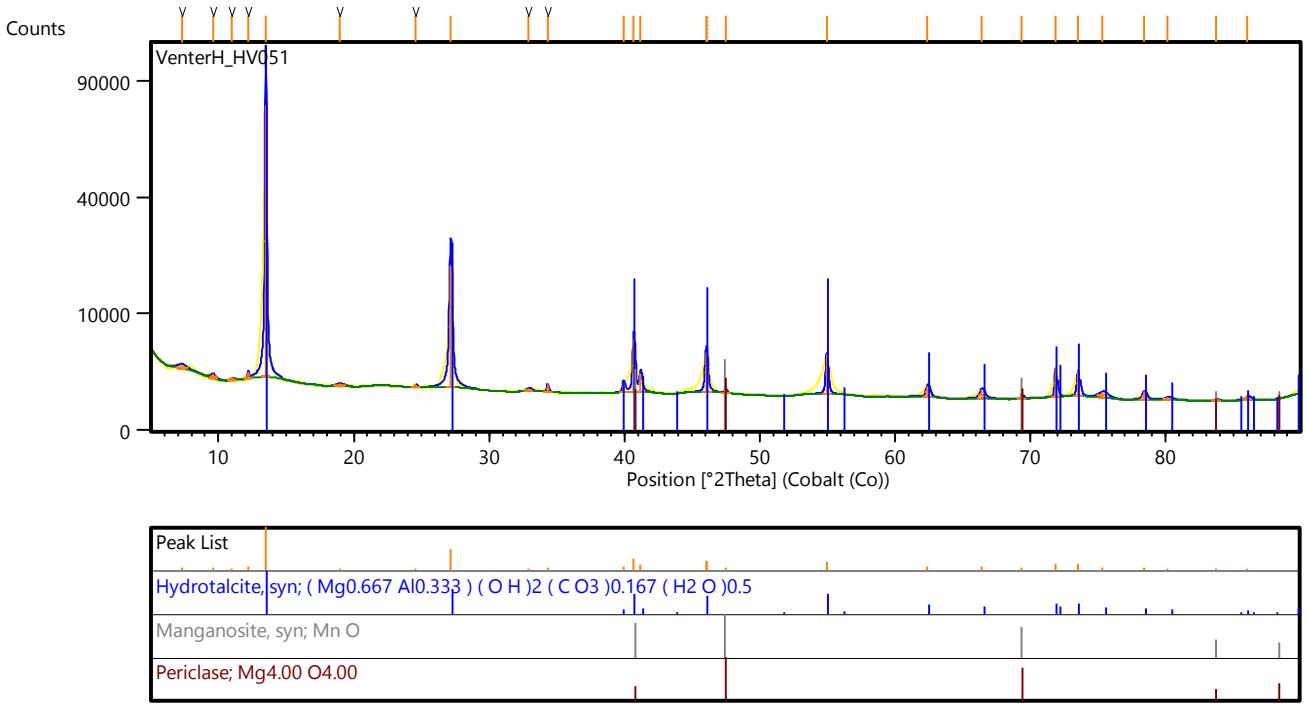

Figure 98: *Mg/Mn(II)* 8.3 mole% - Carbonate

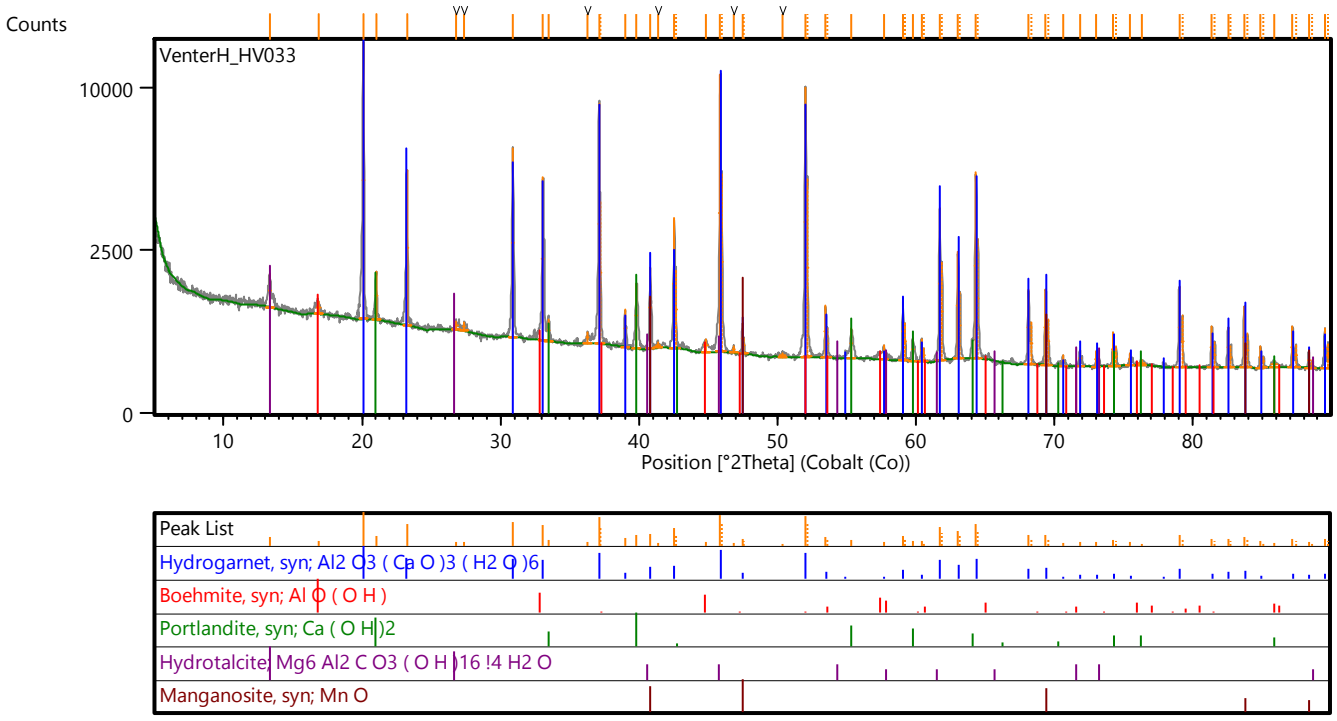

Figure 99: *Ca/Mn(IV)* 25 mole% - Inert

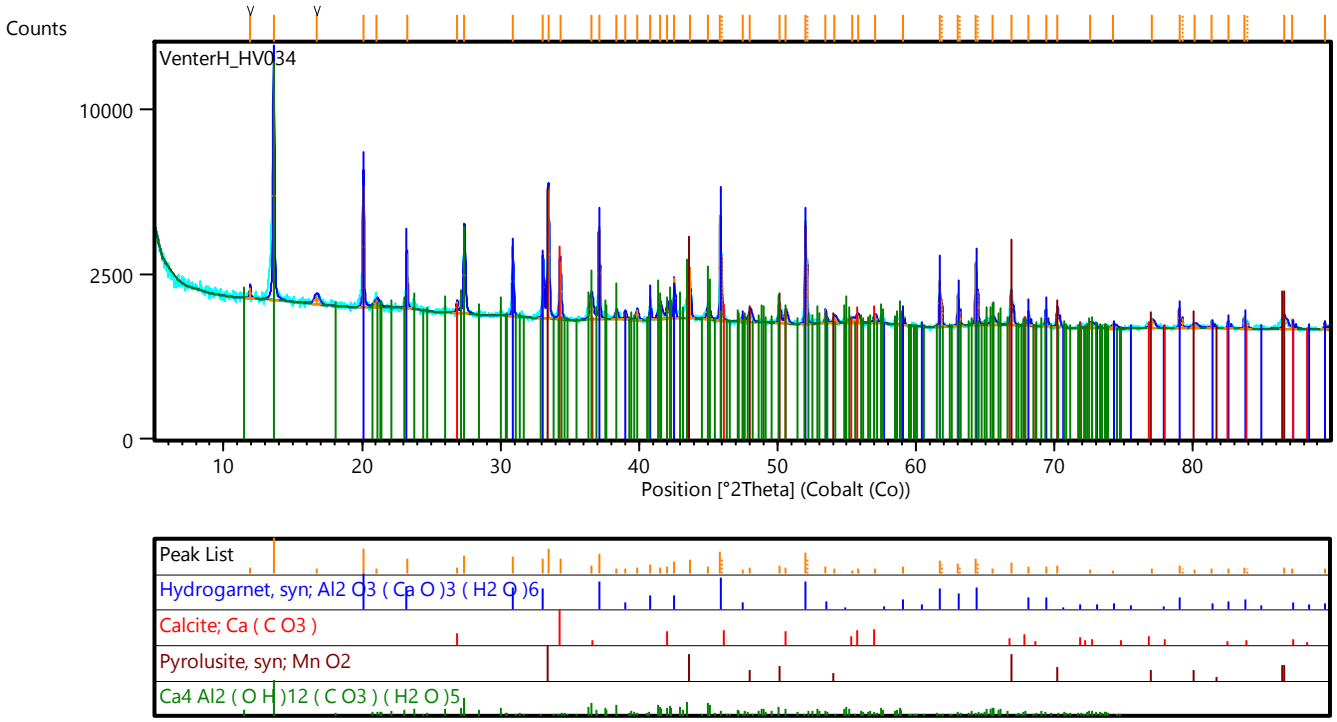

Figure 100: *Ca/Mn(IV)* 25 mole% - Carbonate

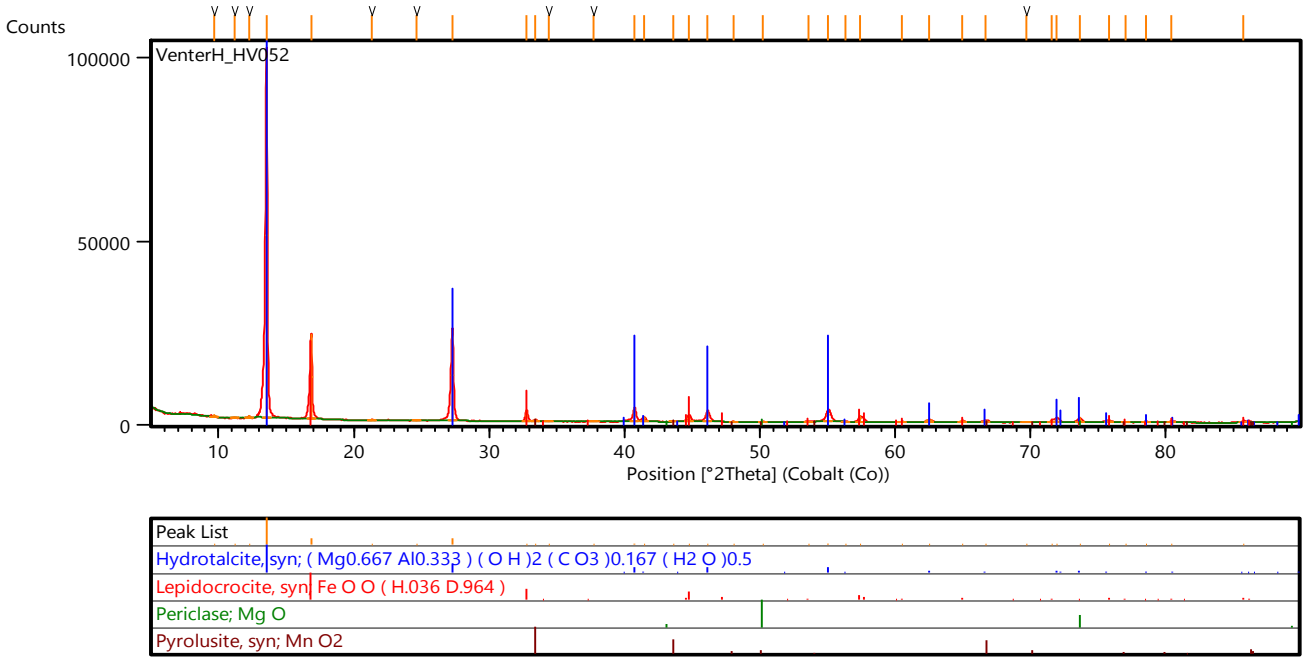

Figure 101: *Mg/Mn(IV)* 25 mole% - Carbonate

Molybdenum

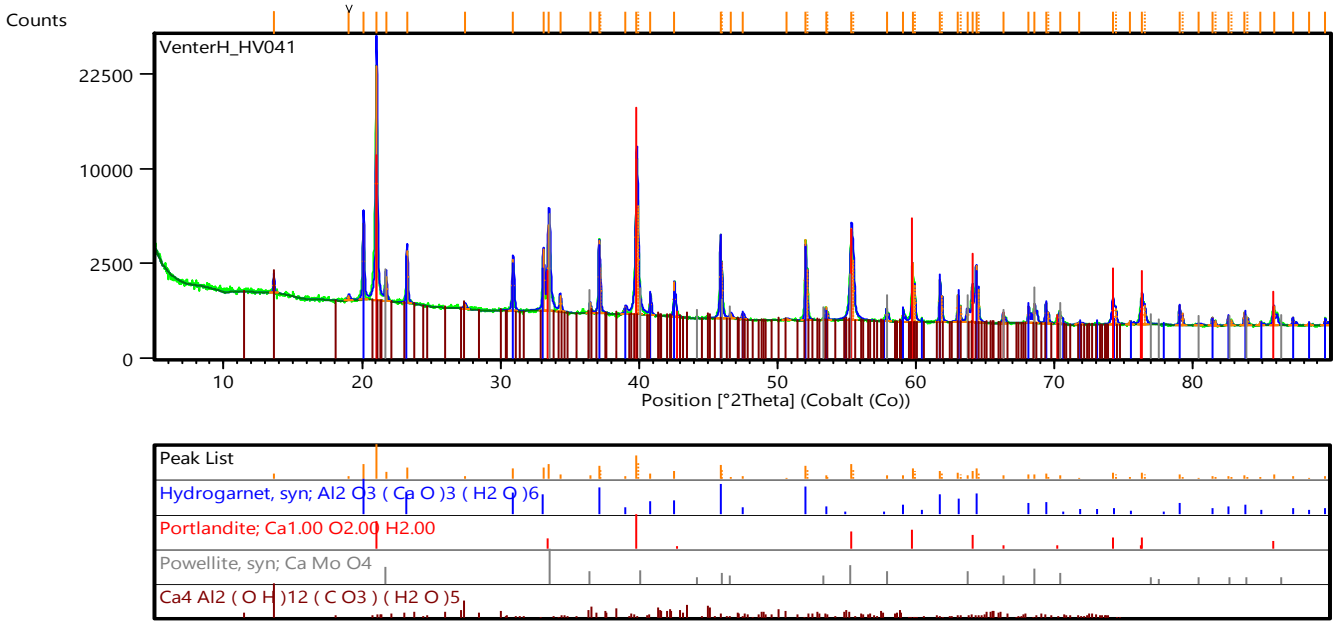

Figure 102: *Ca/Mo* 25 mole% - Inert

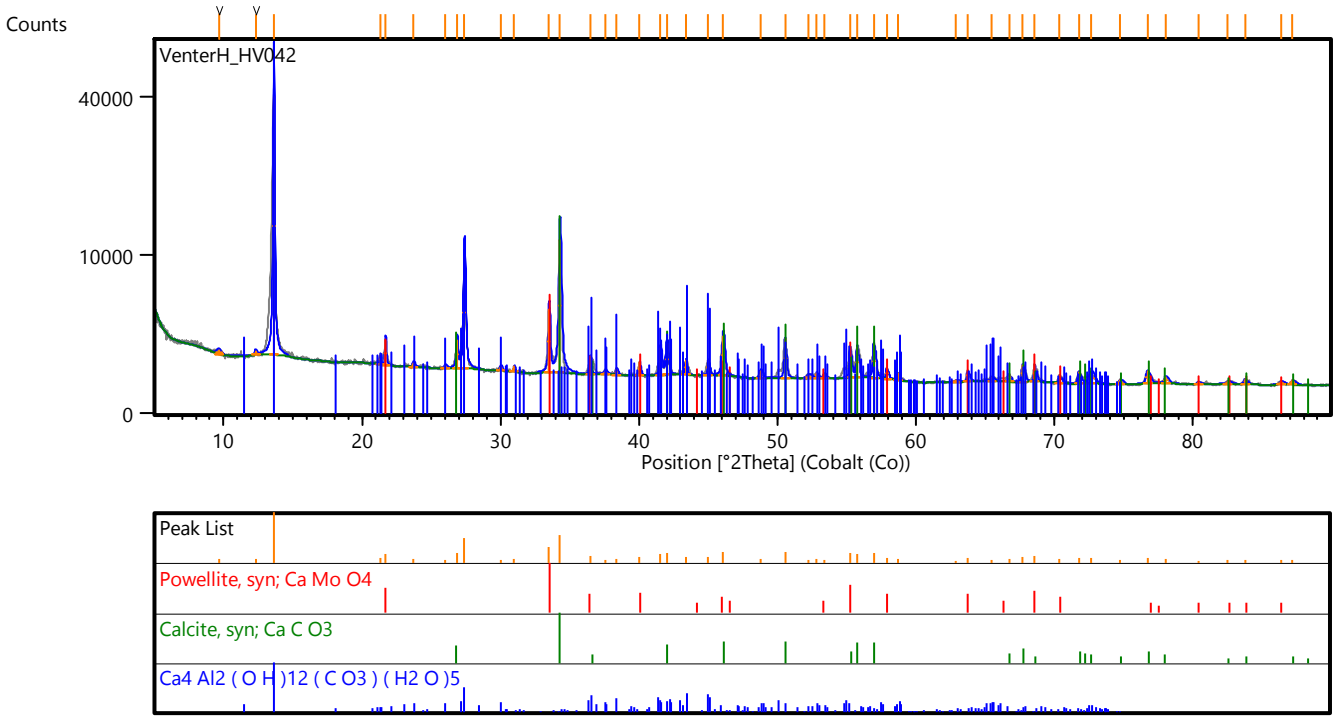

Figure 103: *Ca/Mo* 25 mole% - Carbonate

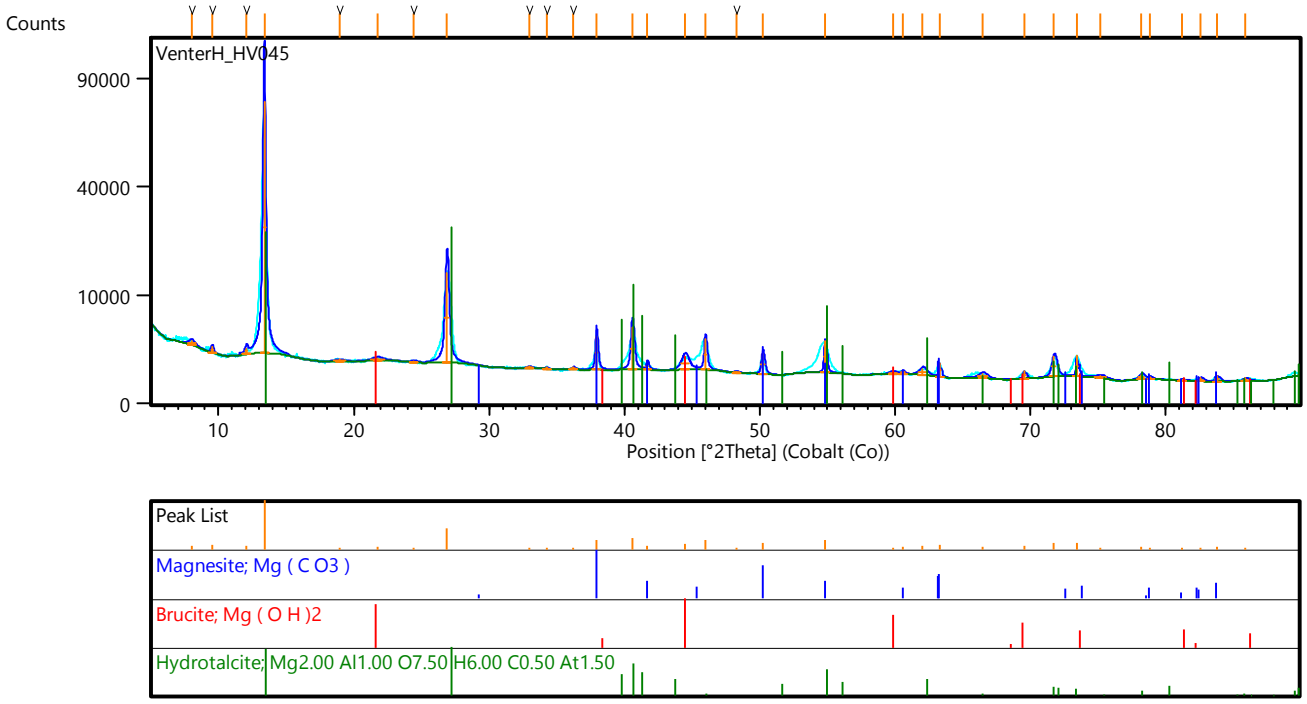

Figure 104: *Mg/Mo* 25 mole% - Carbonate

Nickel

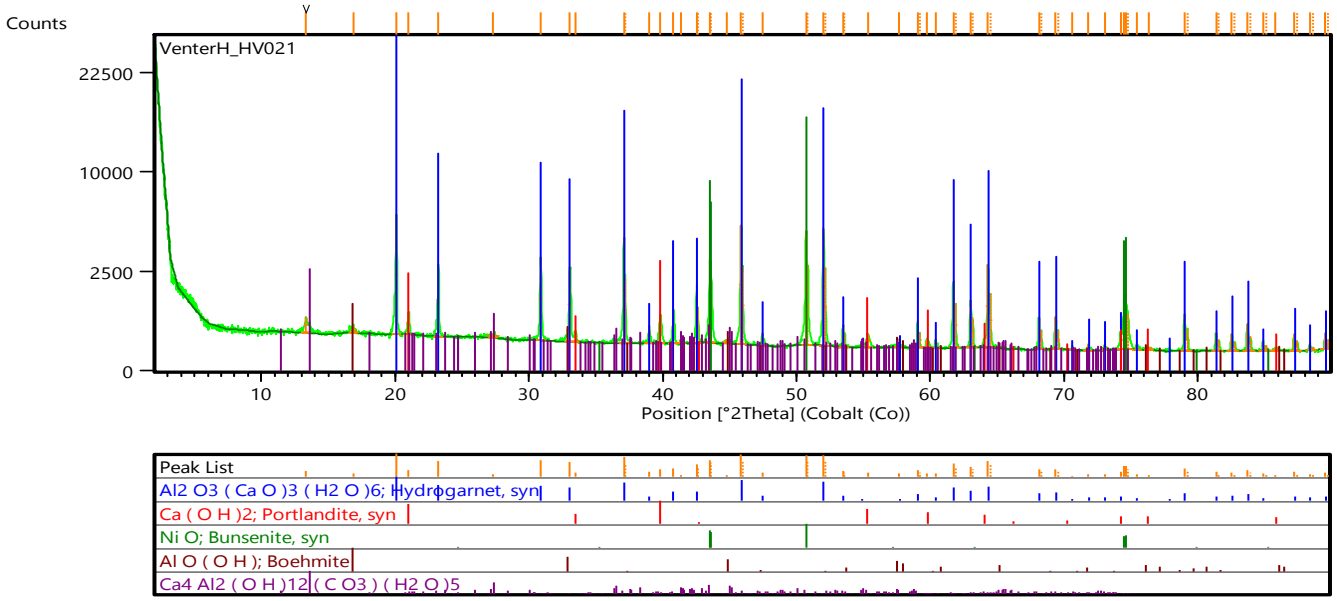

Figure 105: *Ca/Ni* 25 mole% - Inert

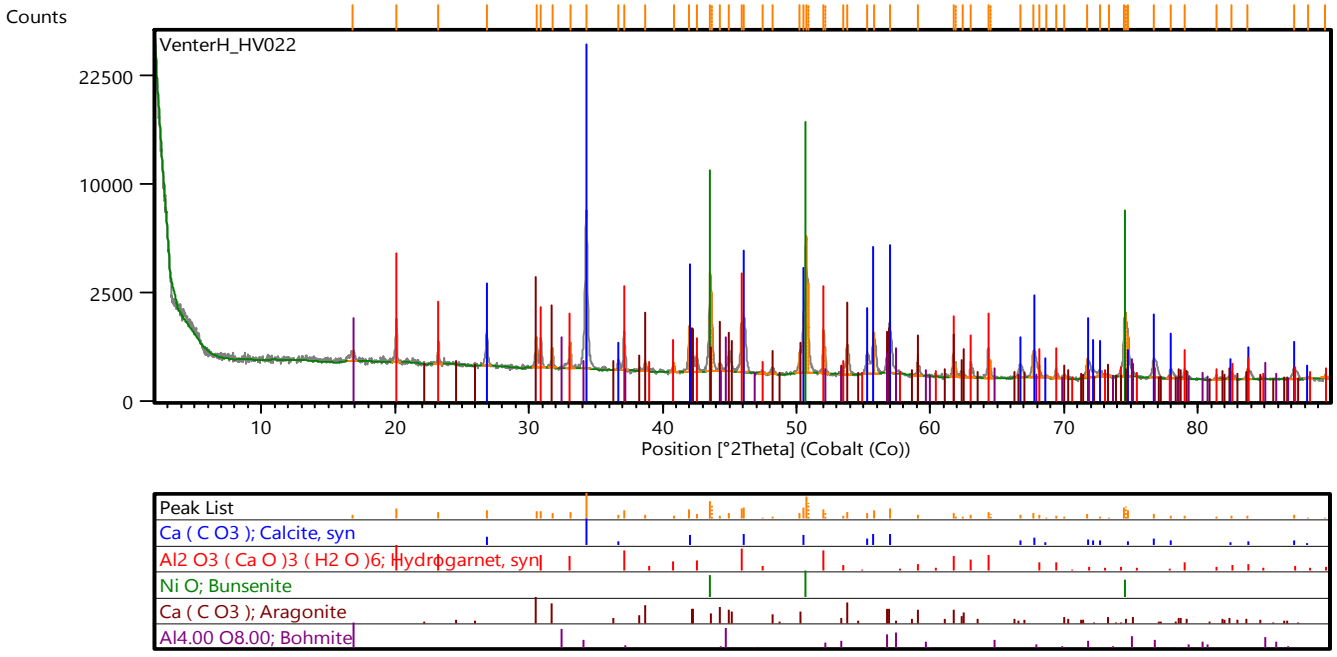

Figure 106: *Ca/Ni* 25 mole% - Carbonate

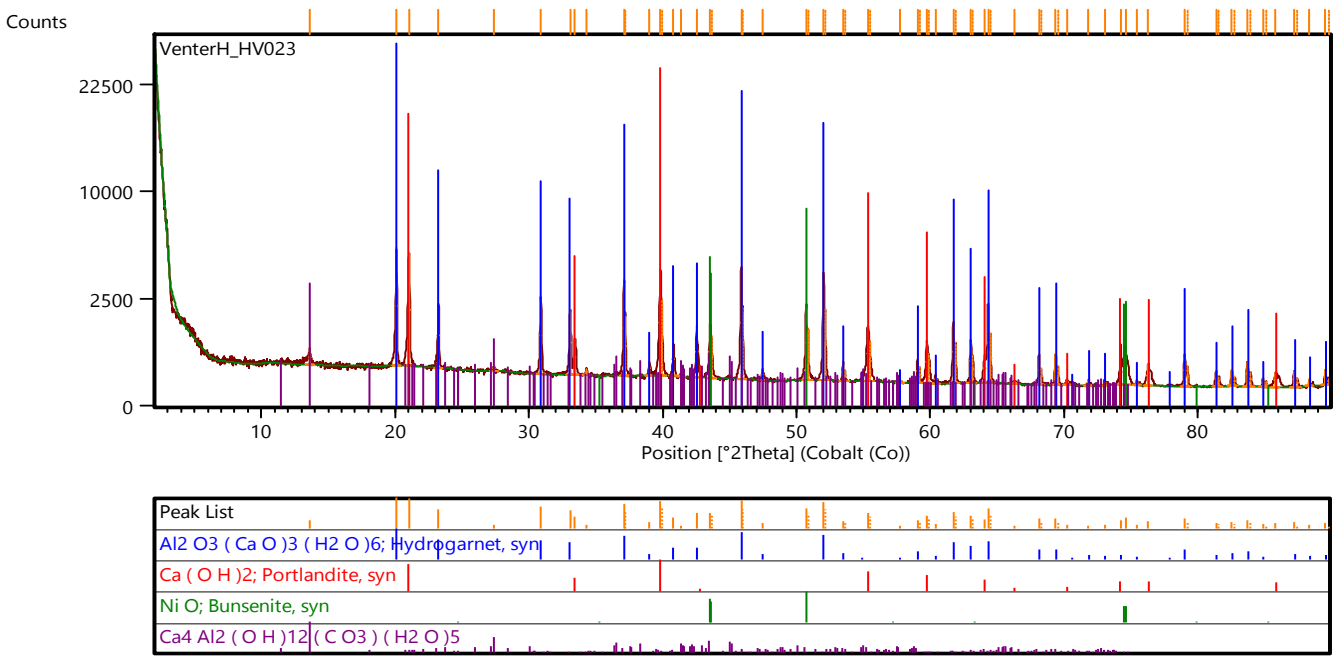

Figure 107: *Ca/Ni* 8.3 mole% - Inert

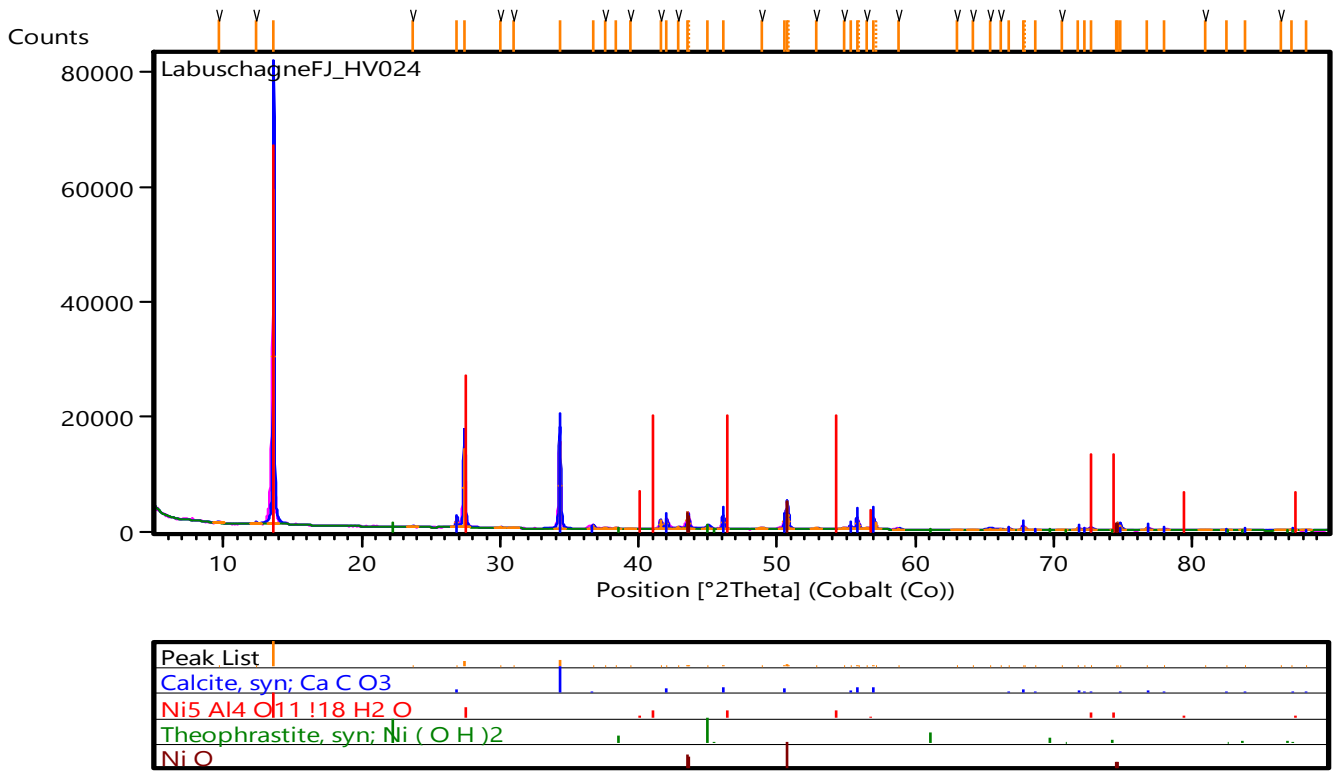

Figure 108: *Ca/Ni* 8.3 mole% - Carbonate

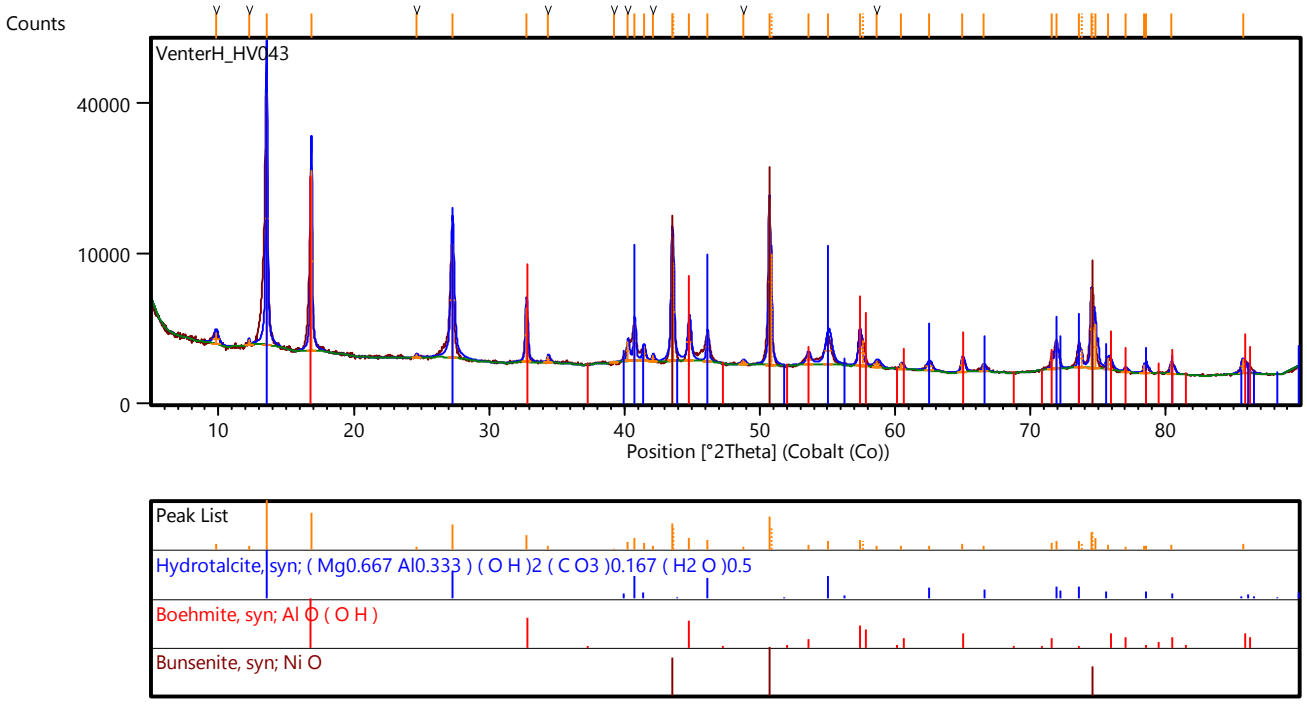

Figure 109: *Mg/Ni* 25 mole% - Carbonate

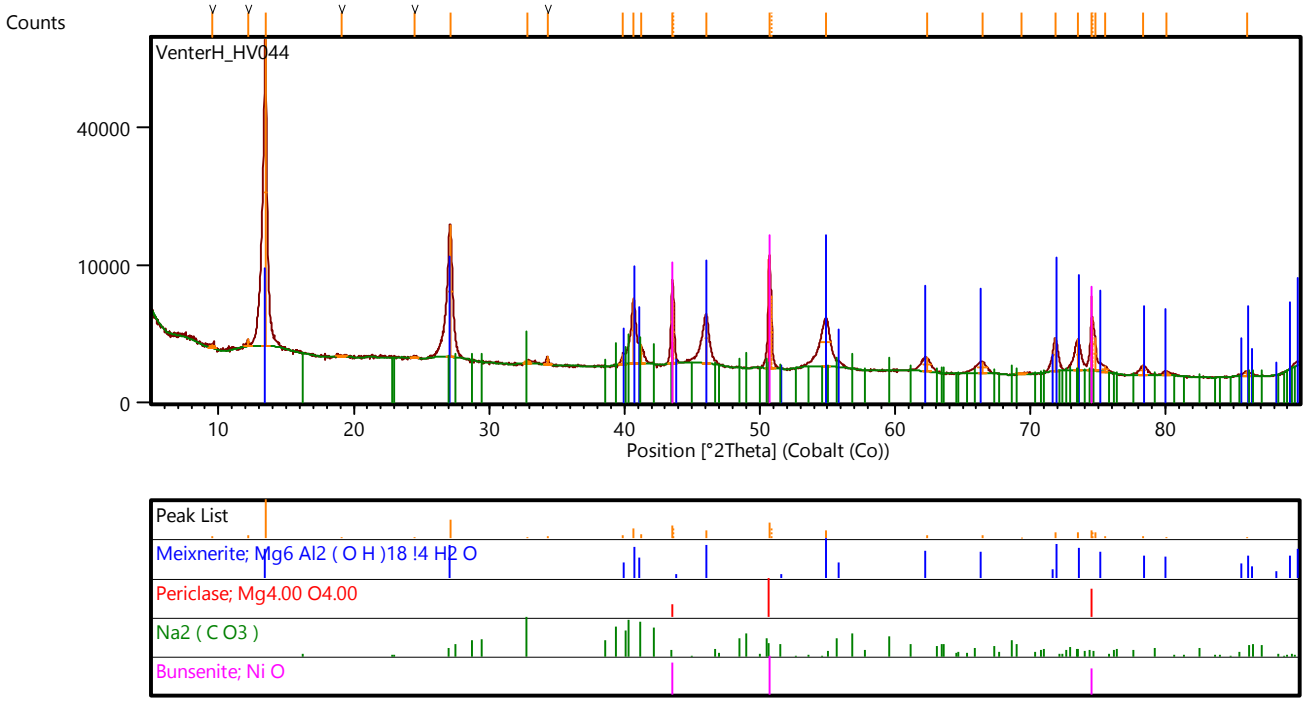

Figure 110: *Mg/Ni* 8.3 mole% - Carbonate

Tin

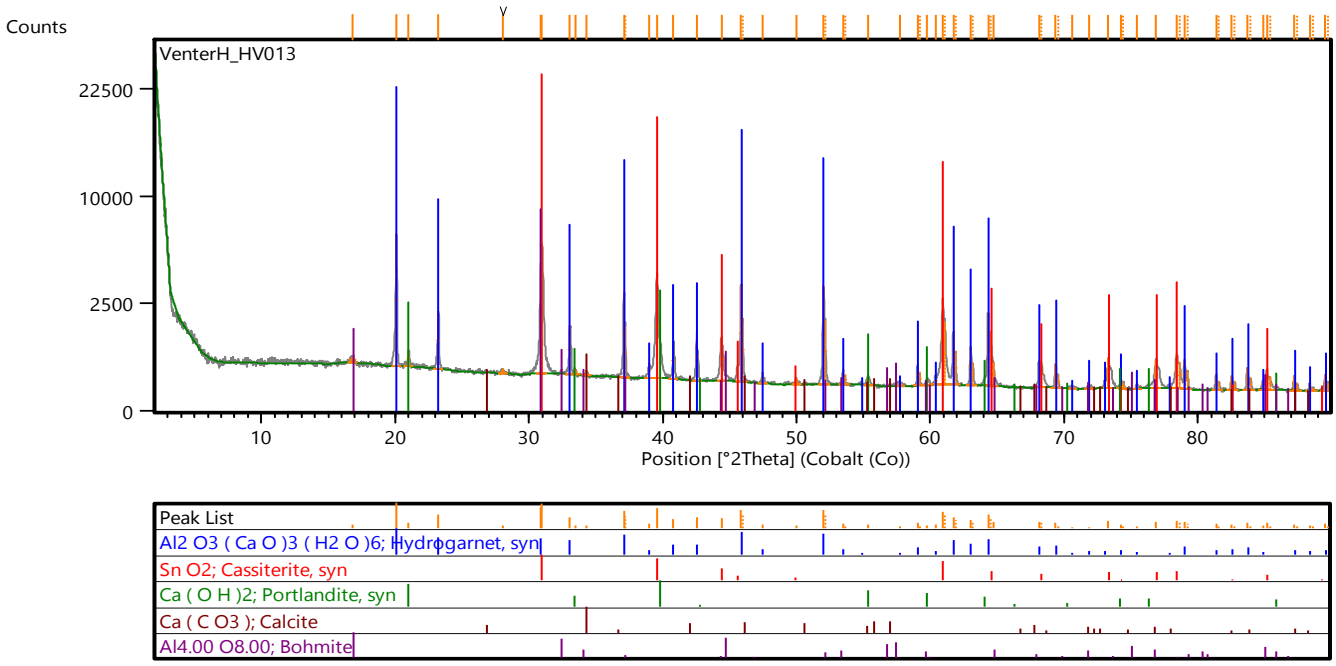

Figure 111: *Ca/Sn* 25 mole% - Inert

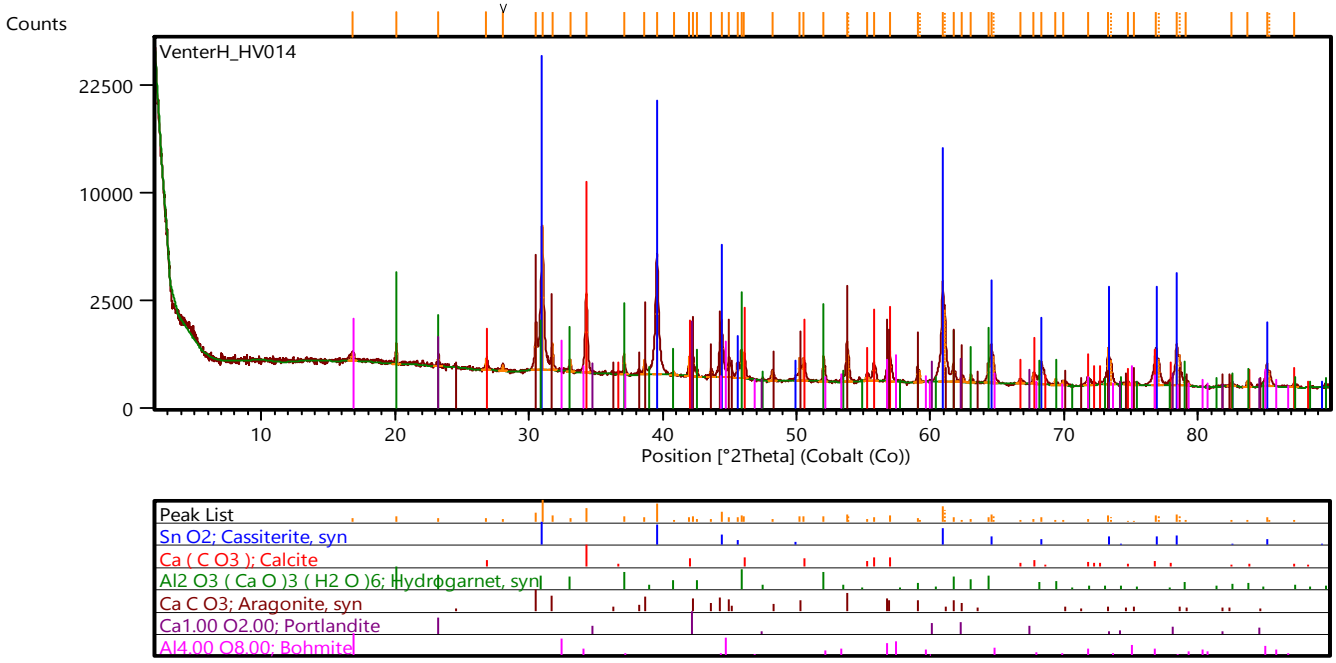

Figure 112: *Ca/Sn* 25 mole% - Carbonate

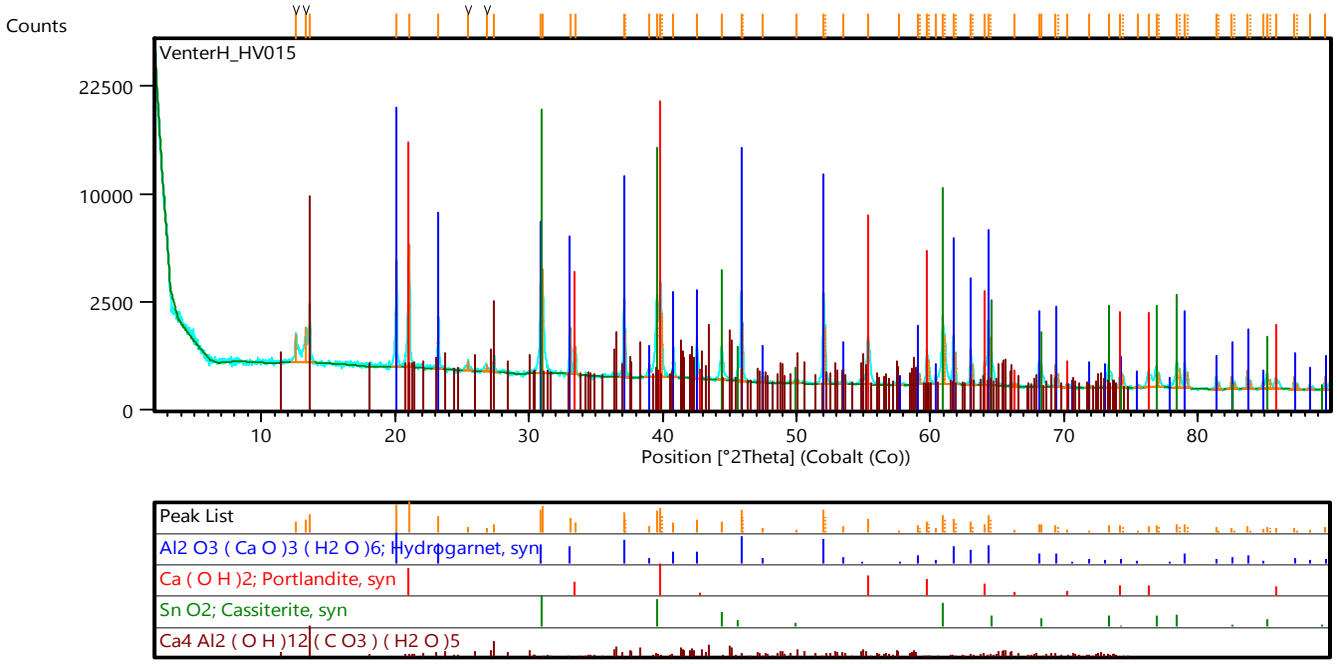

Figure 113: *Ca/Sn* 8.3 mole% - inert

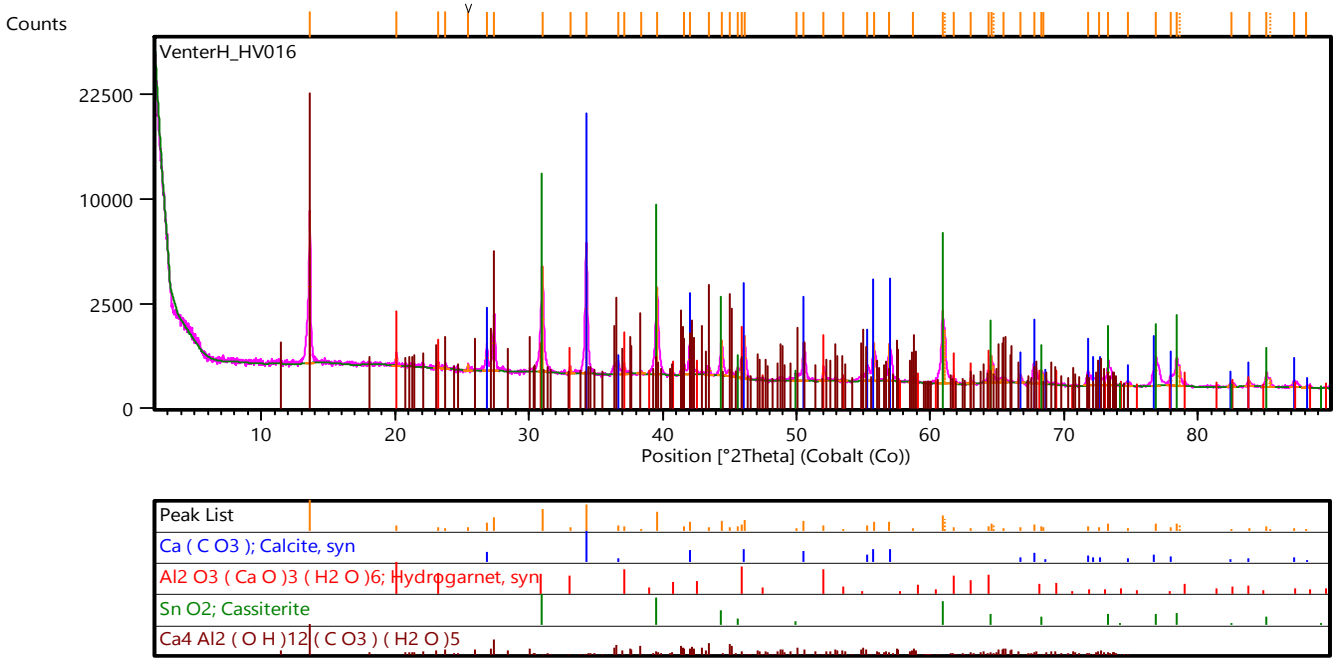

Figure 114: *Ca/Sn* 8.3 mole% - Carbonate

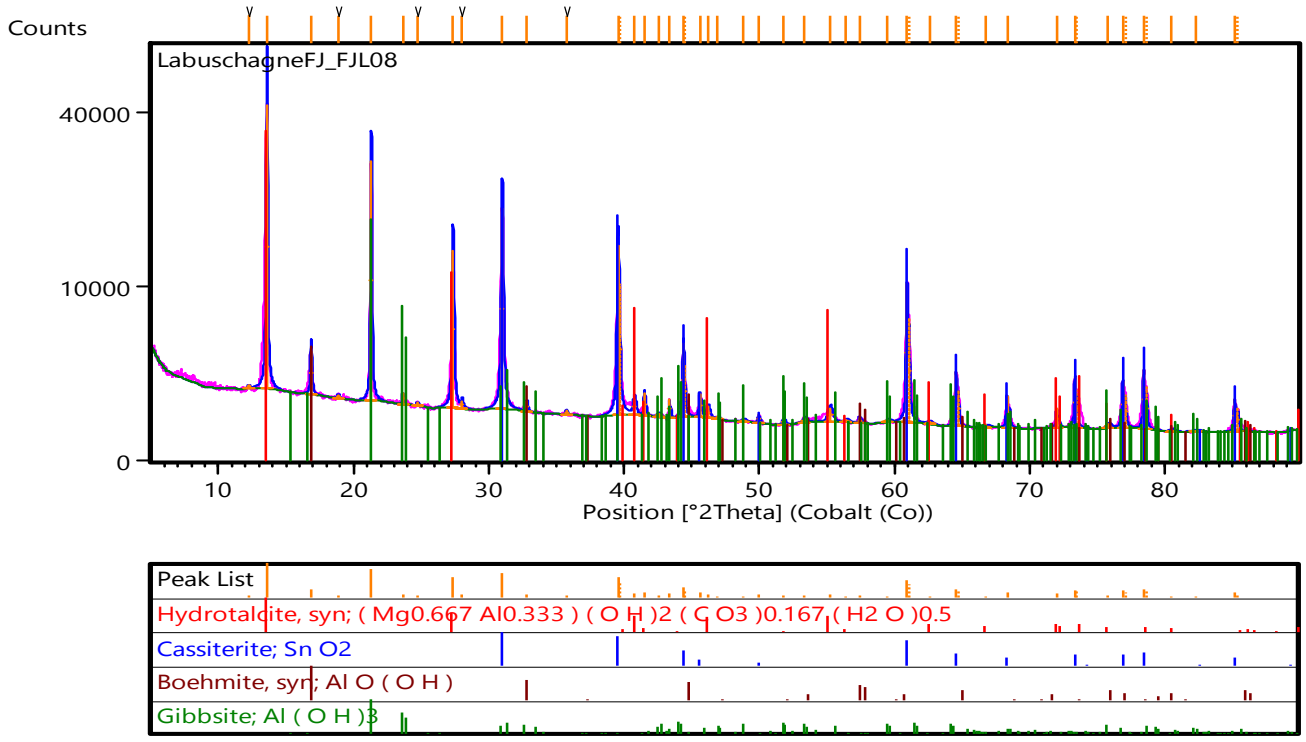

Figure 115: *Mg/Sn* 25 mole% - Carbonate

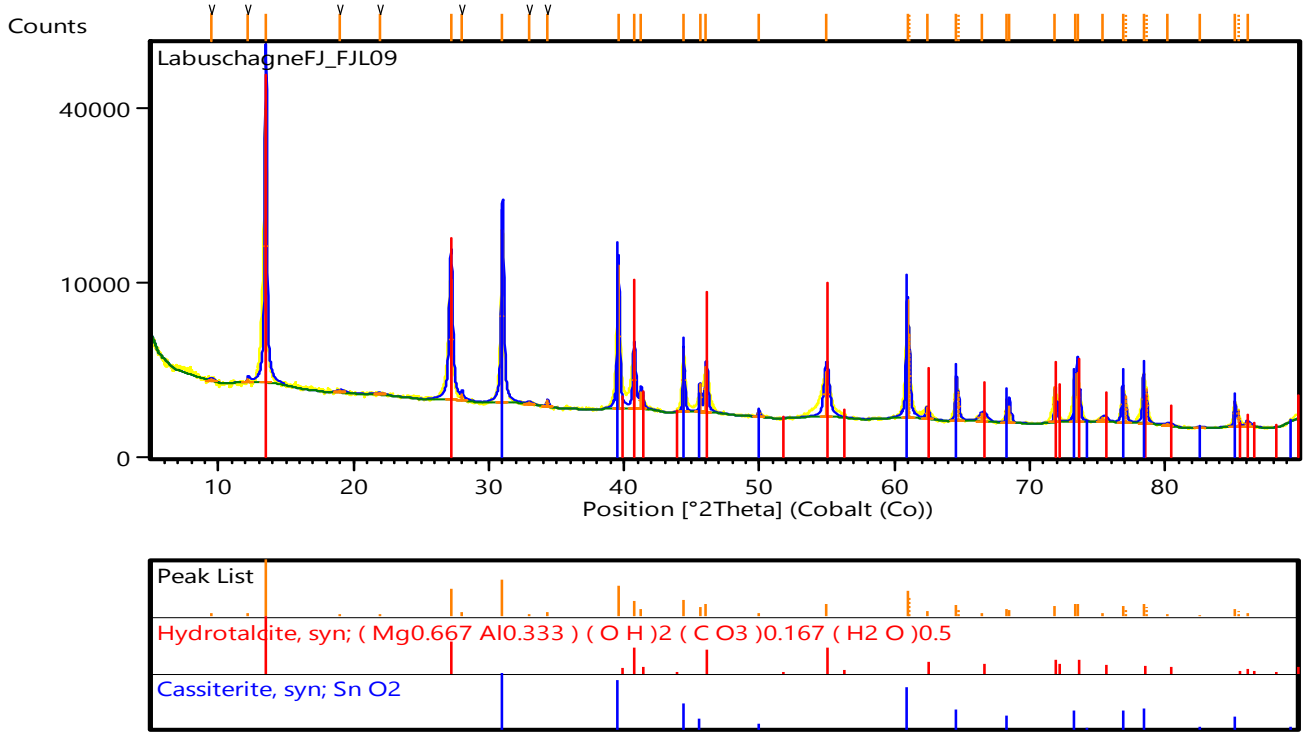

Figure 116: *Mg/Sn* 8.3 mole% - Carbonate

Titanium

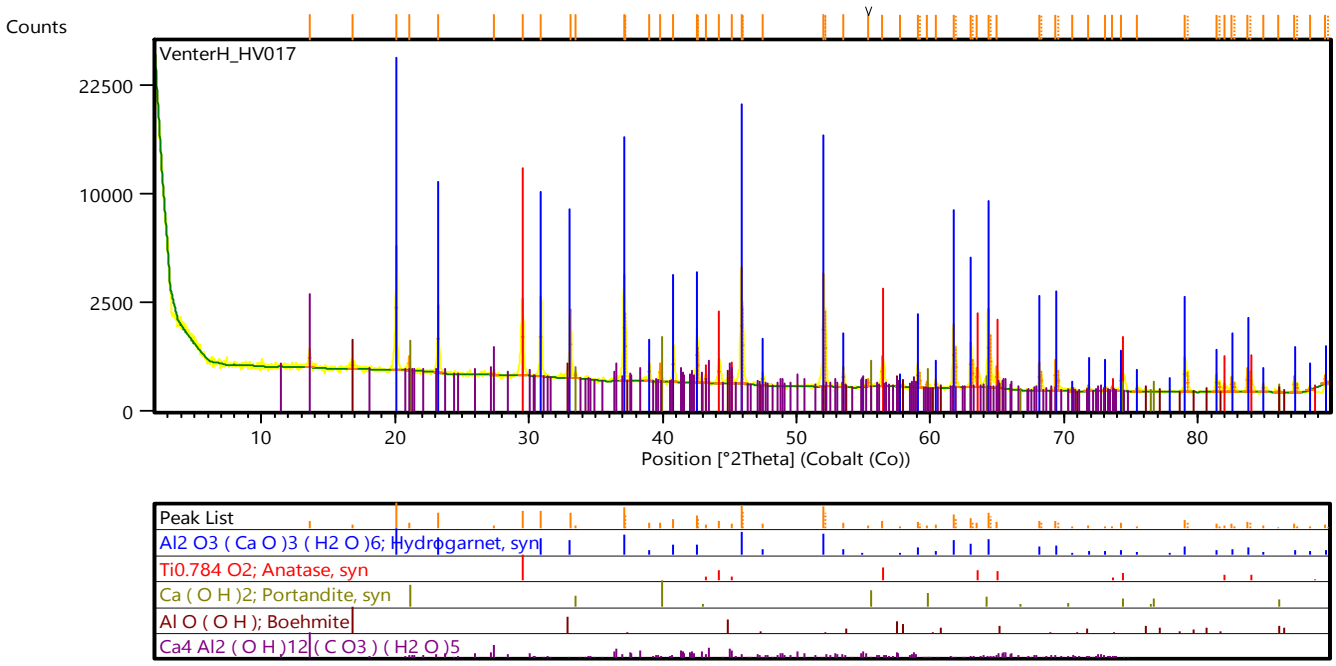

Figure 117: *Ca/Ti* 25 mole% - Inert

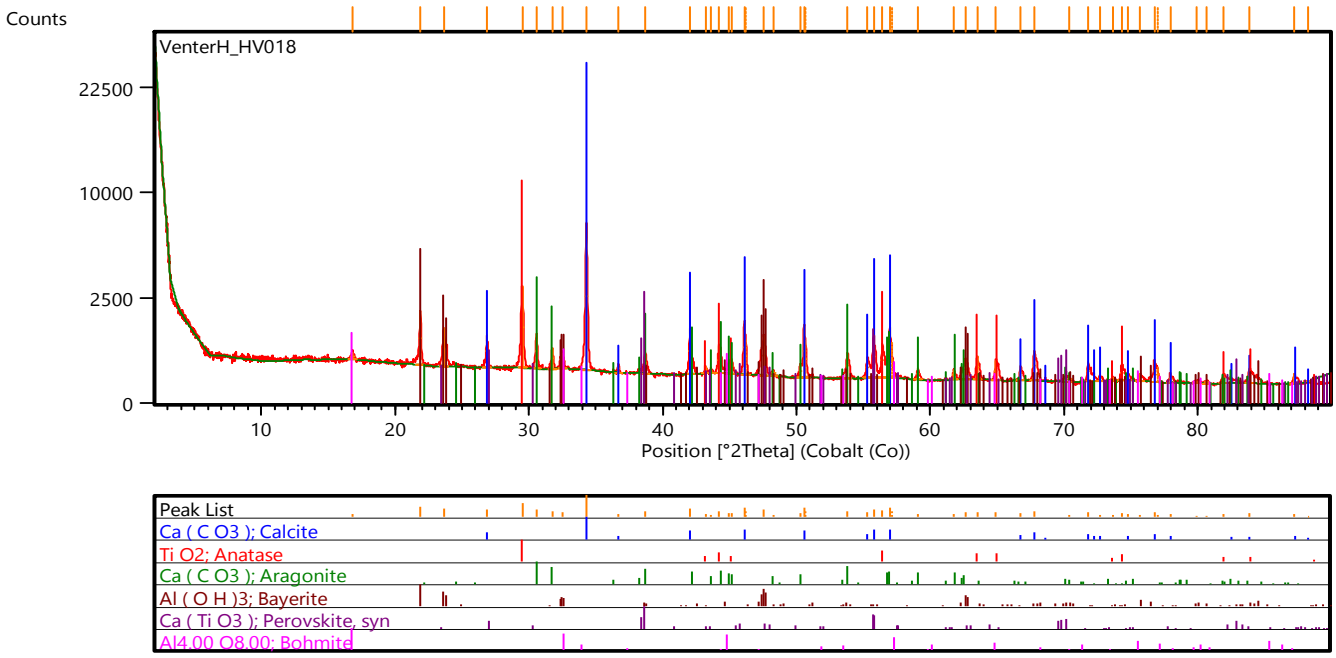

Figure 118: *Ca/Ti* 25 mole% - Carbonate

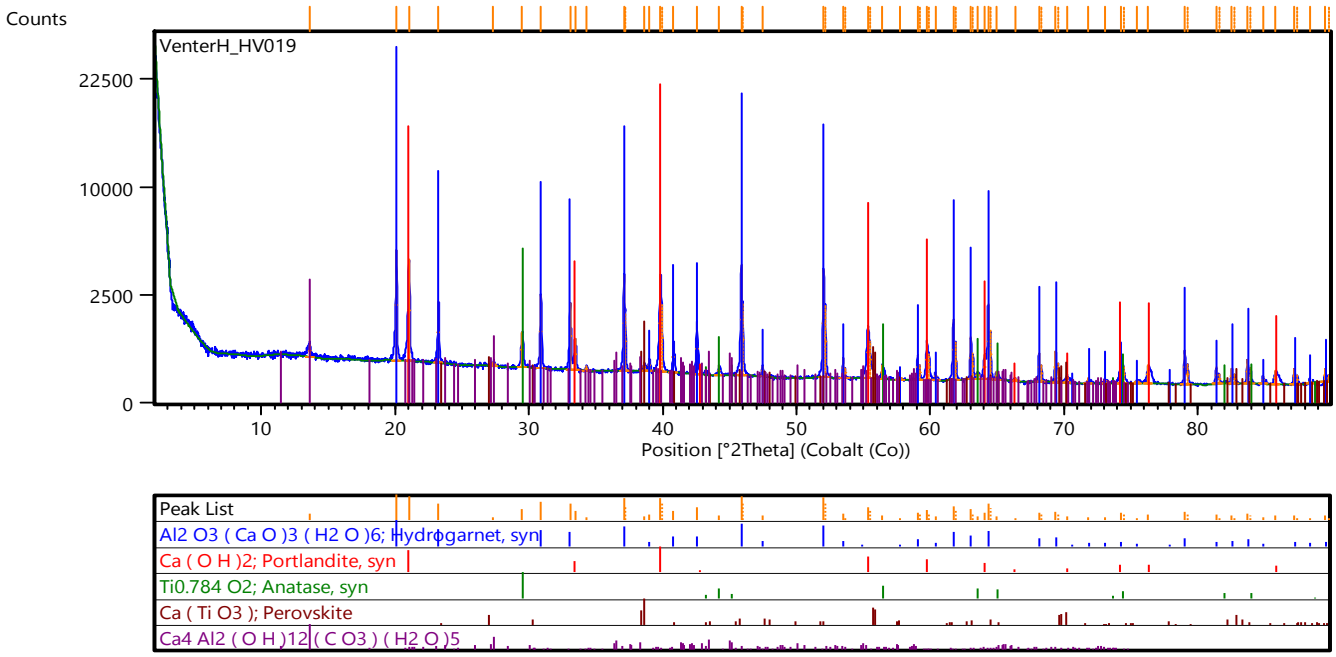

Figure 119: *Ca/Ti* 8.3 mole% - Inert

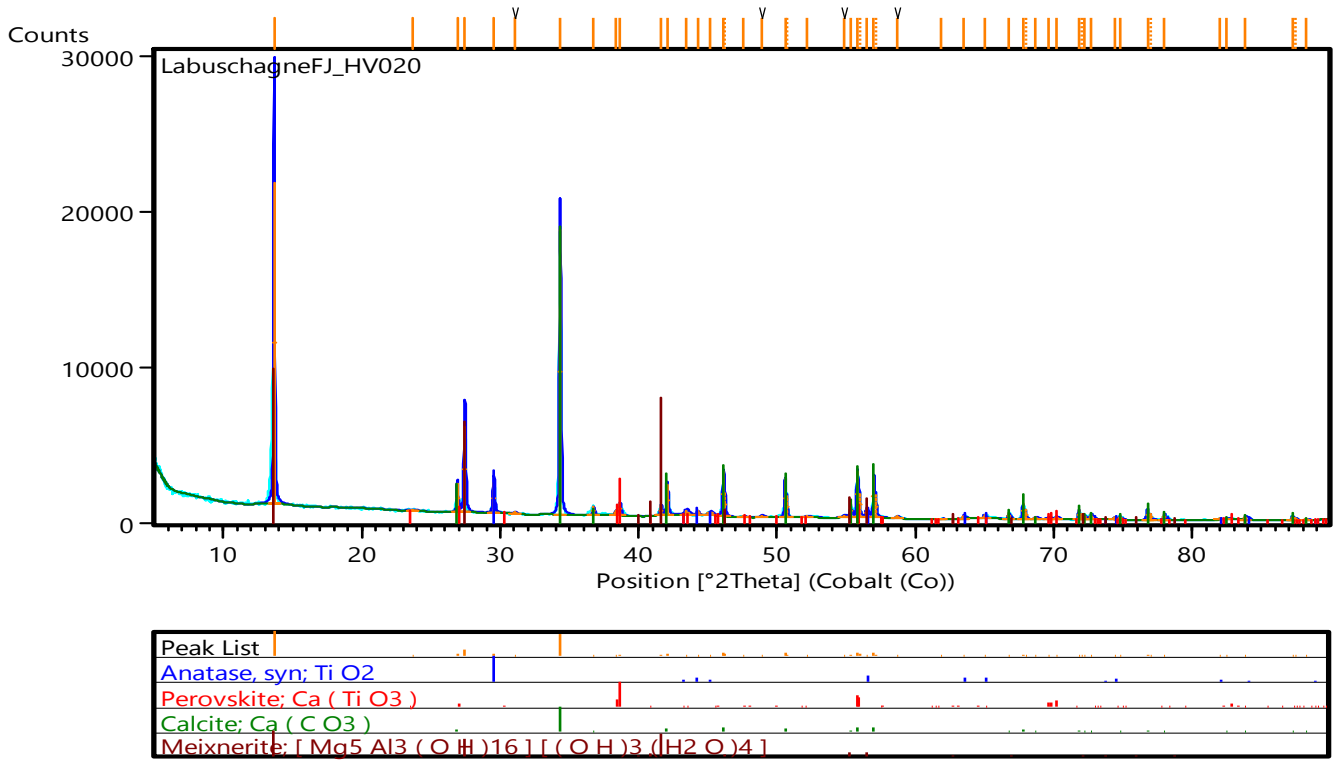

Figure 120: *Ca/Ti* 8.3 mole% - Carbonate

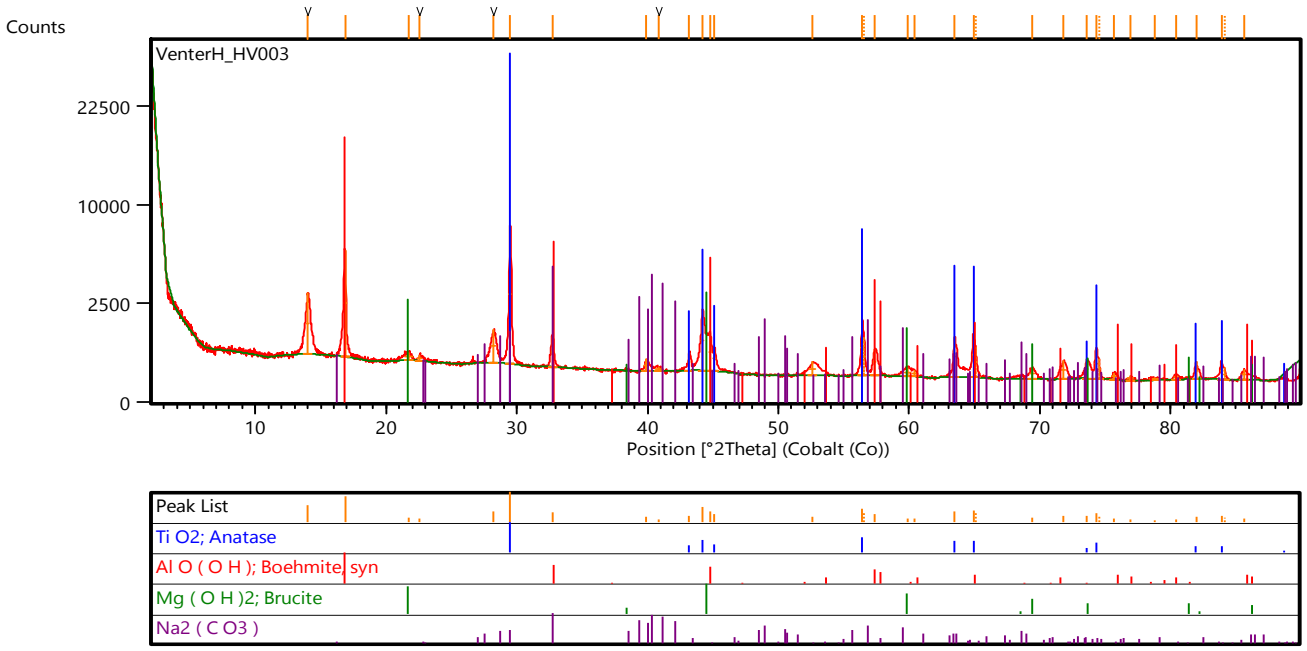

Figure 121: *Mg/Ti* 25 mole% - Inert

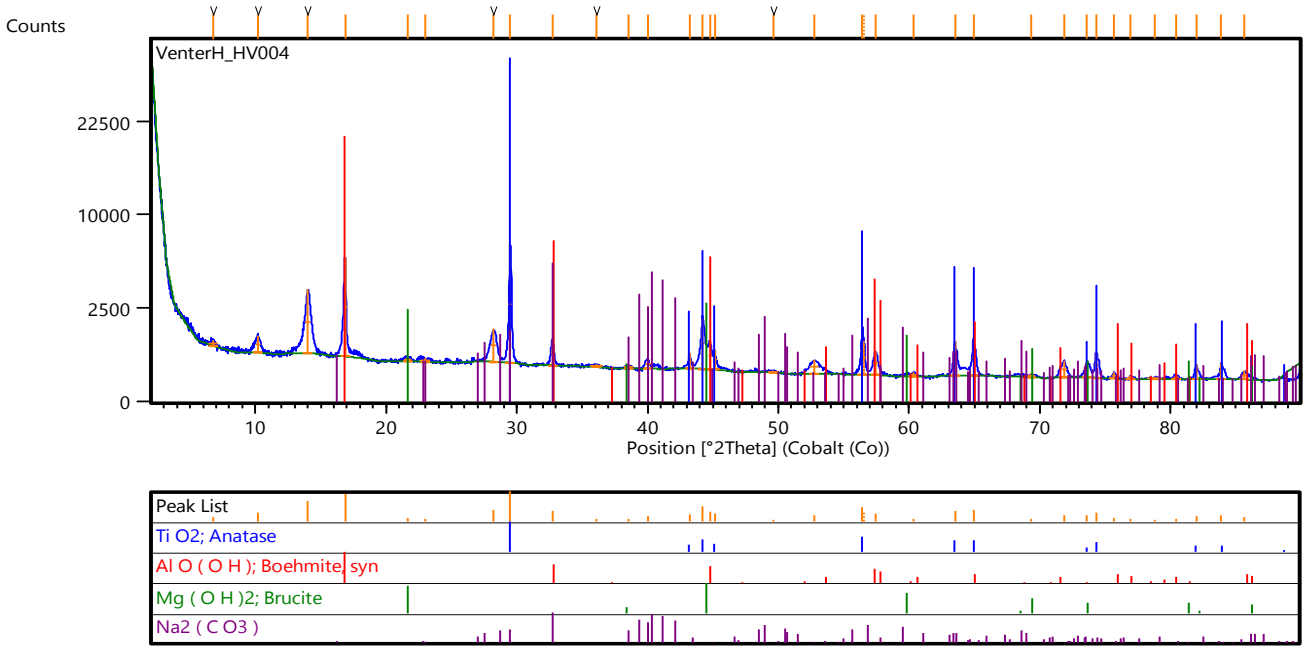

Figure 122: *Mg/Ti* 25 mole% - Carbonate

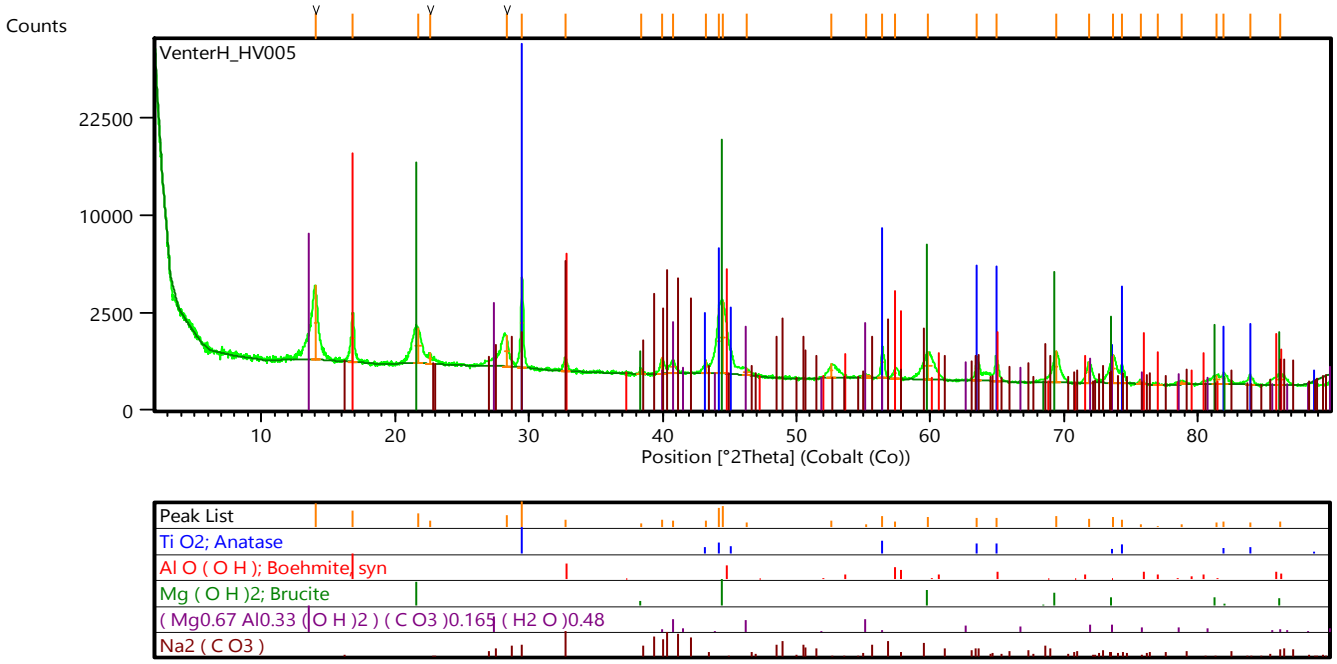

Figure 123: *Mg/Ti* 8.3 mole% - Inert

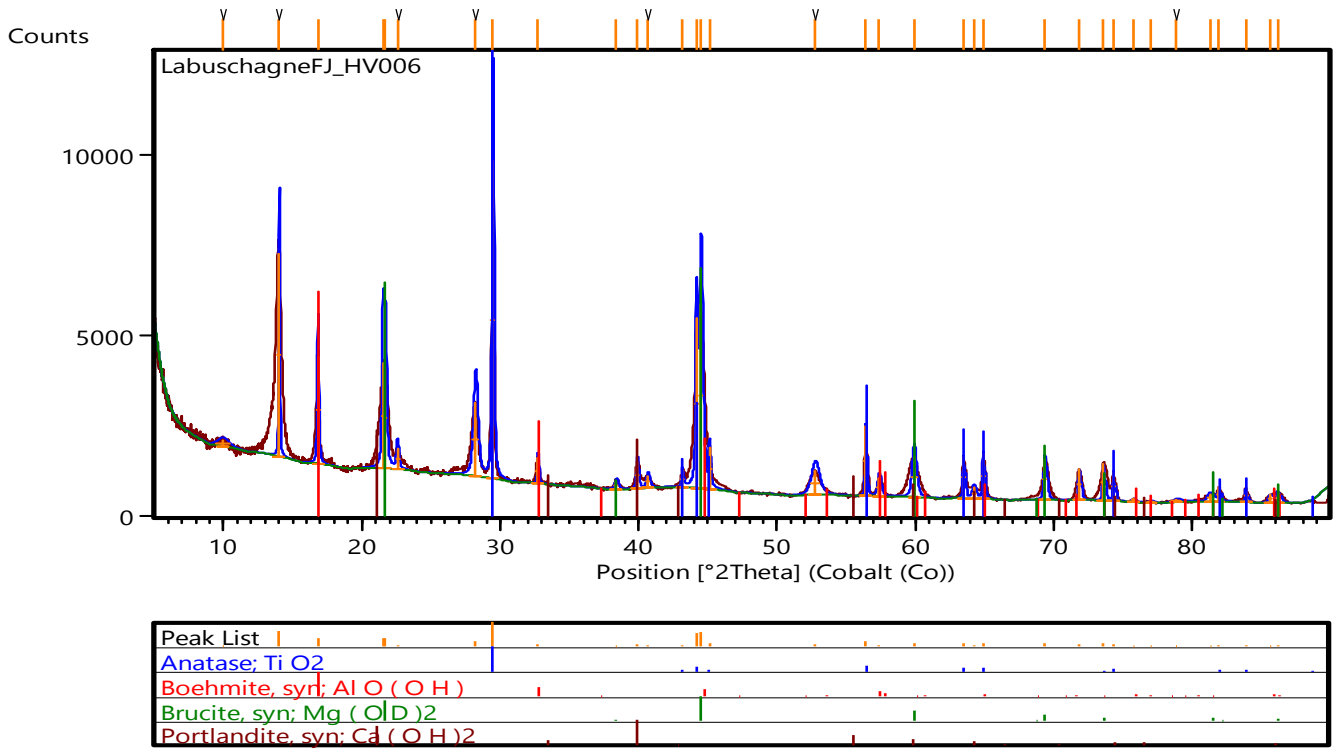

Figure 124: *Mg/Ti* 8.3 mole% - Carbonate

Zinc

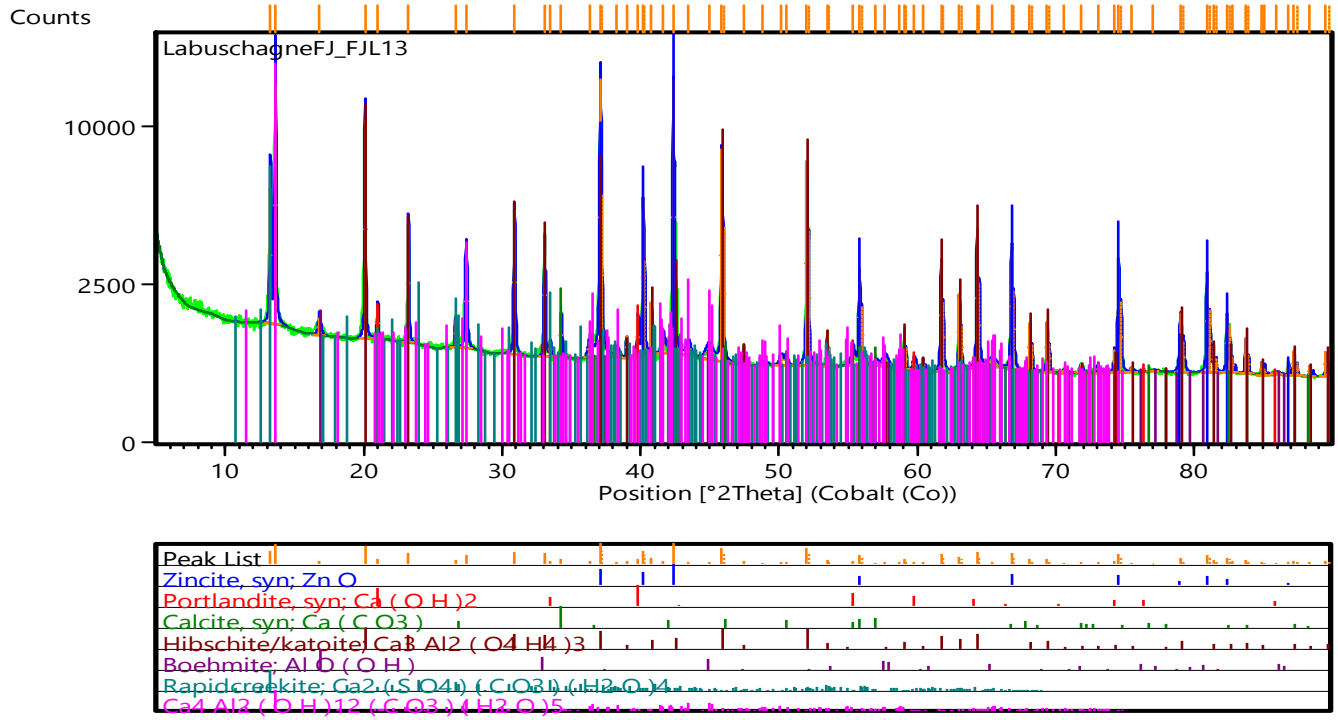

Figure 125: *Ca/Zn* 25 mole% - Inert

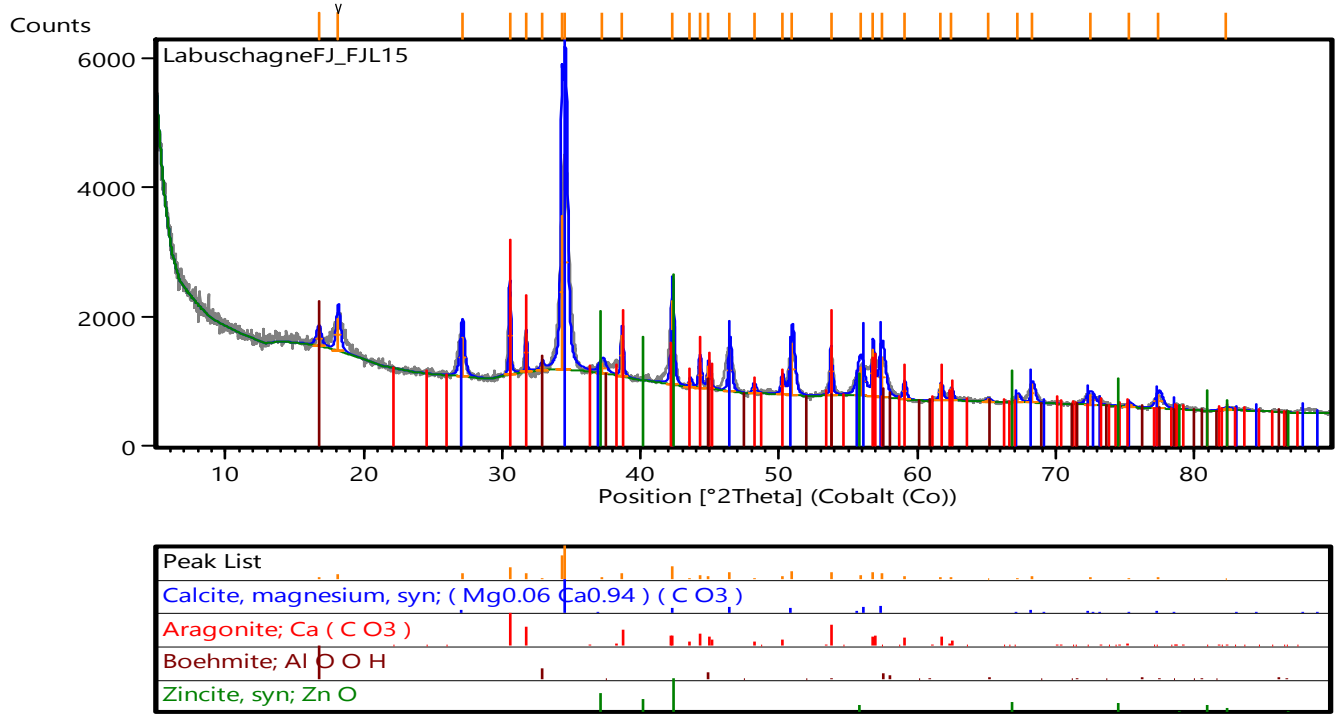

Figure 126: *Ca/Zn* 25 mole% - Carbonate

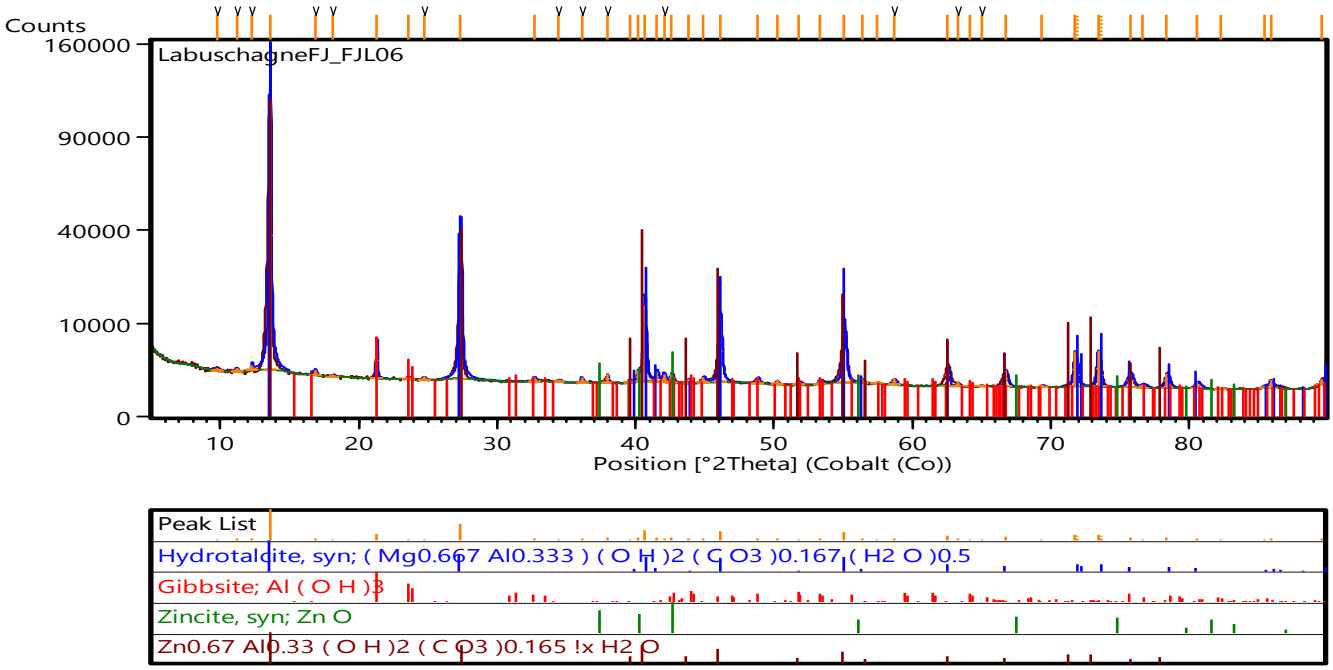

Figure 127: *Mg/Zn* 25 mole% - Carbonate

Appendix B: ICP Analysis

	Metal Species		
	Mg	Al	Metal Ratio
Sample Name	(mg/l)	(mg/l)	(Mg:Al)
MgAl120-1	17.62	9.35	2.09
MgAl120-2	20.48	11.06	2.06
MgAl120-3	18.97	11.13	1.89
MgAl120-4	19.85	11.49	1.92
MgAl120-5	21.12	12.38	1.89
MgAl140-1	19.95	11.13	1.99
MgAl140-2	18.95	10.98	1.92
MgAl140-3	20.44	11.23	2.02
MgAl140-4	19.93	11.51	1.92
MgAl140-5	21.05	11.62	2.01
MgAl160-1	22.61	14.22	1.76
MgAl160-2	20.89	12.20	1.90
MgAl160-3	22.14	12.64	1.94
MgAl160-4	22.06	12.33	1.99
MgAl160-5	22.69	12.84	1.96
MgAl180-1	21.58	12.15	1.97
MgAl180-2	23.44	13.03	2.00
MgAl180-3	23.37	12.66	2.05
MgAl180-4	22.11	11.65	2.11
MgAl180-5	22.29	12.03	2.06

Appendix C: BET Analsysis

Sample	BET Analysis (m^2/g)
MgAl120-1	9.99
MgAl120-2	11.88
MgAl120-3	11.55
MgAl120-4	15.65
MgAl120-5	13.54
MgAl140-1	19.24
MgAl140-2	42.76
MgAl140-3	54.10
MgAl140-4	33.33
MgAl140-5	29.82
MgAl160-1	27.89
MgAl160-2	27.74
MgAl160-3	21.85
MgAl160-4	16.50
MgAl160-5	14.63
MgAl180-1	25.62
MgAl180-2	20.09
MgAl180-3	13.30
MgAl180-4	10.36
MgAl180-5	9.19

Appendix D: PSA analysis results

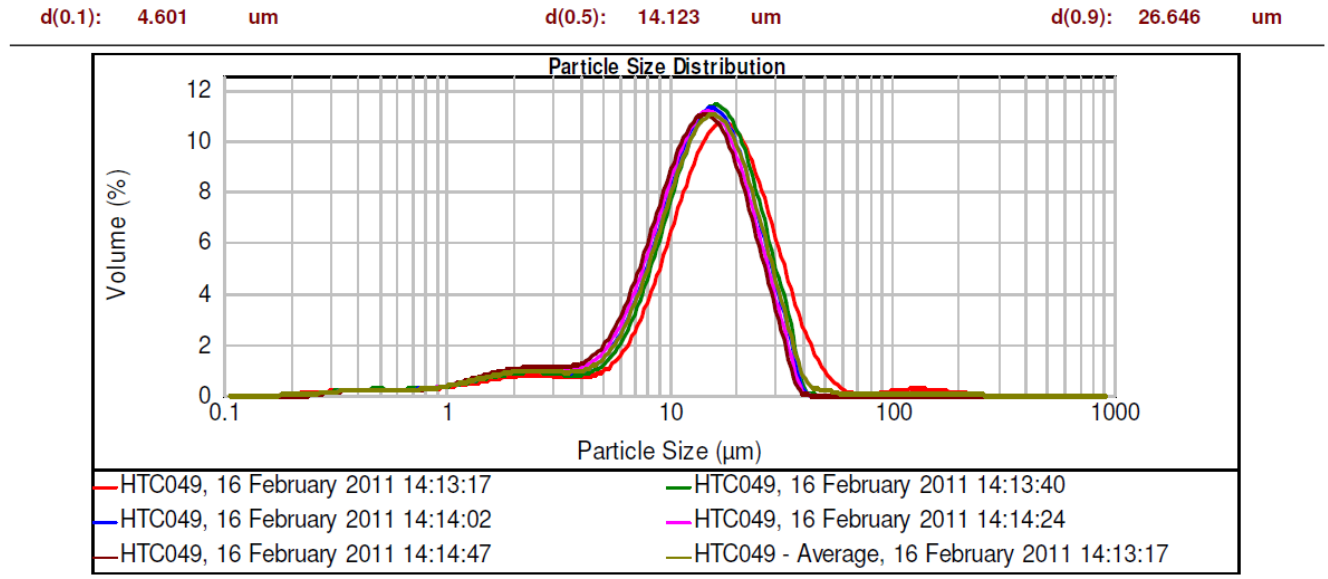

Figure 128: PSA - MgAl120-1

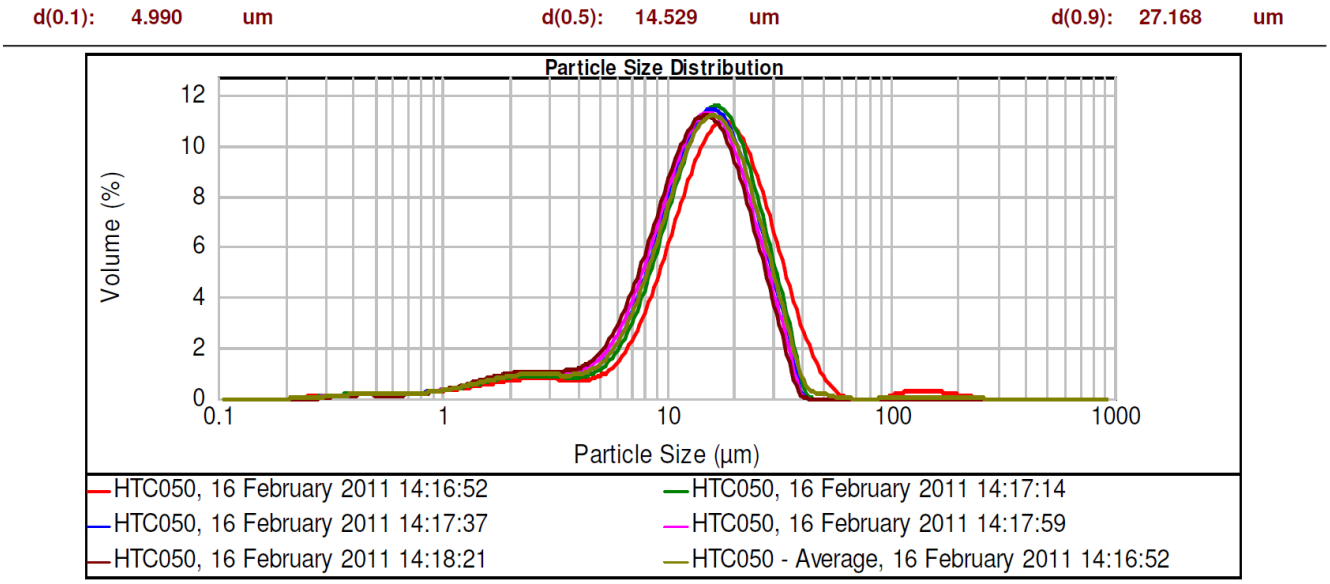

Figure 129: PSA - MgAl120-2

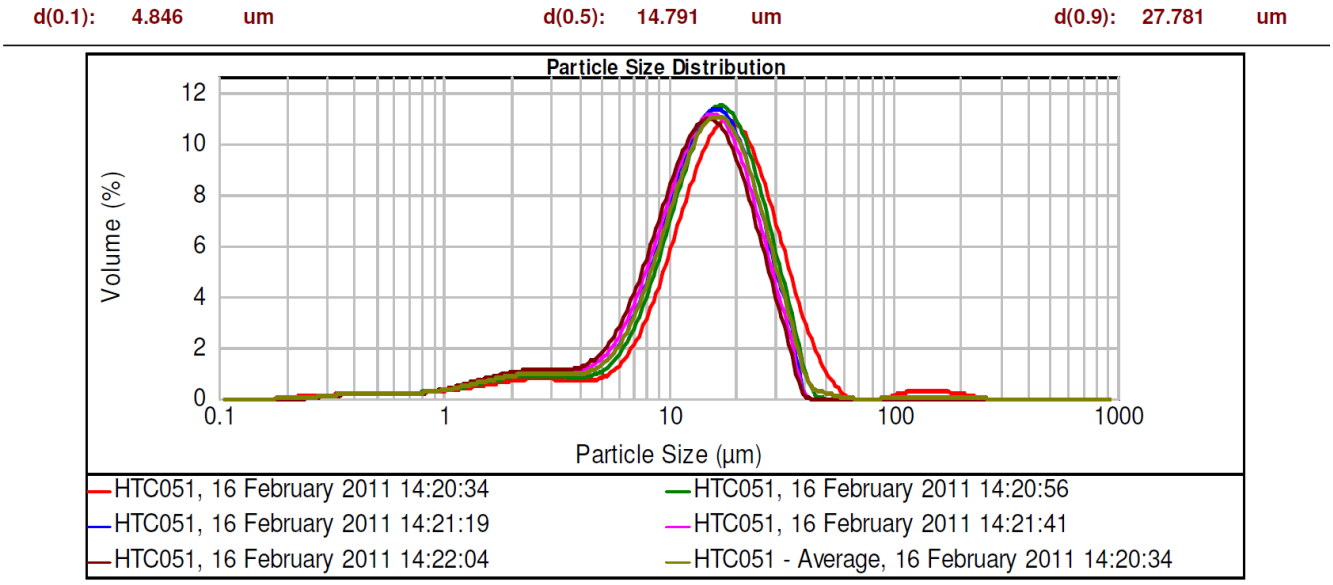

Figure 130: PSA - MgAl120-3

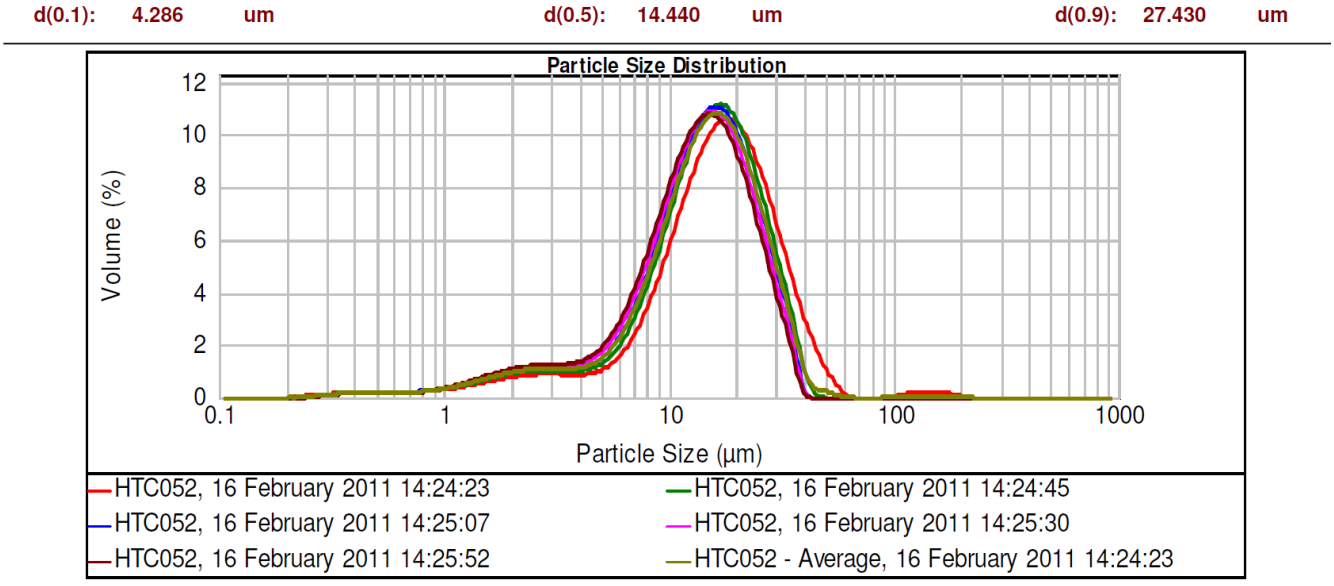

Figure 131: PSA - MgAl120-4

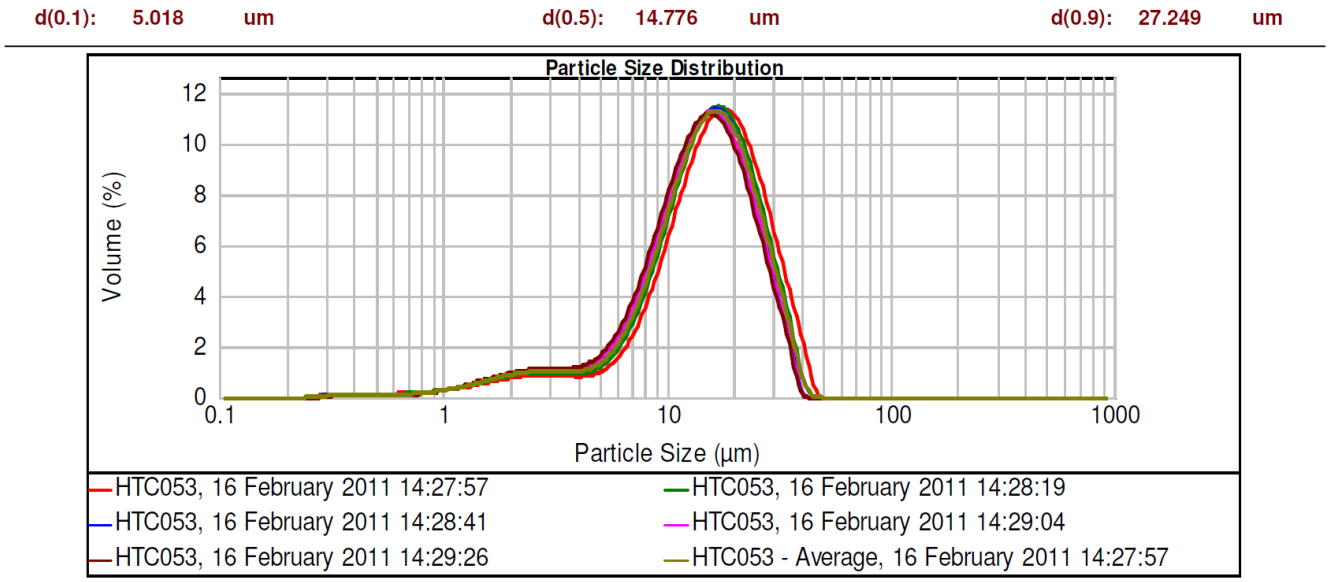

Figure 132: PSA - MgAl120-5

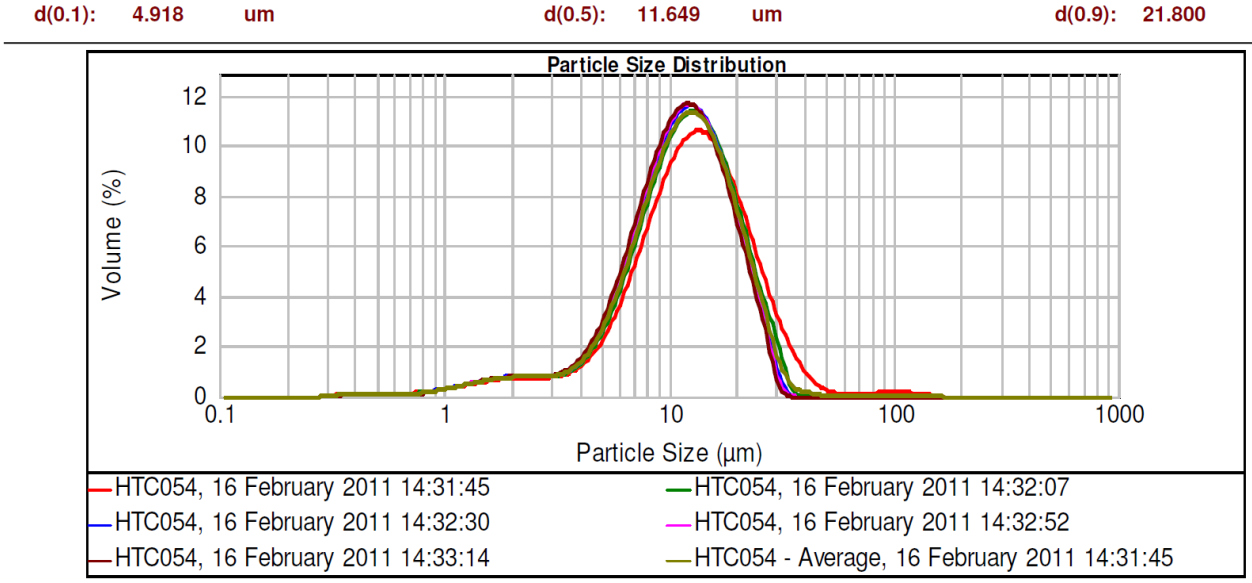

Figure 133: PSA - MgAl140-1

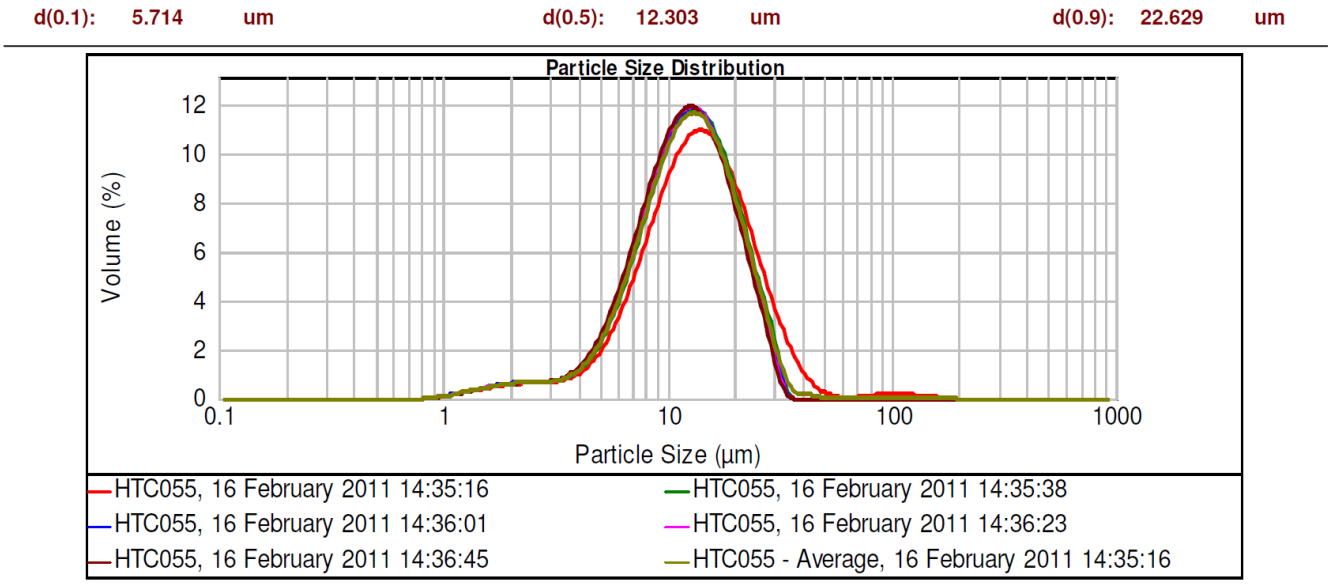

Figure 134: PSA - MgAl140-2

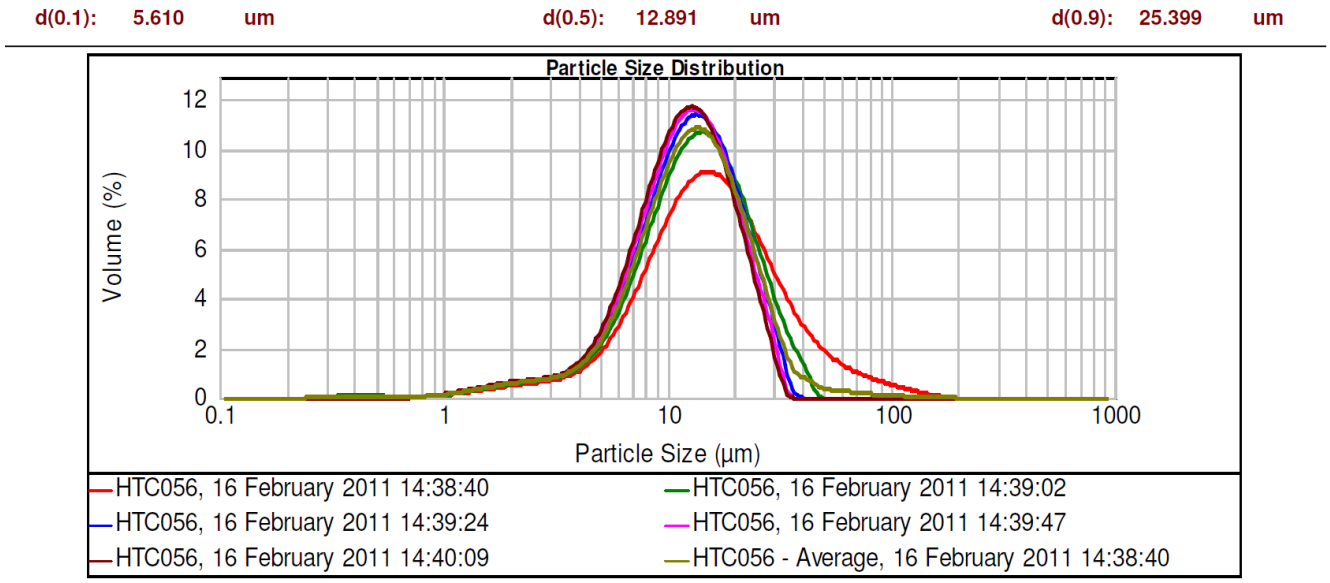

Figure 135: PSA - MgAl140-3

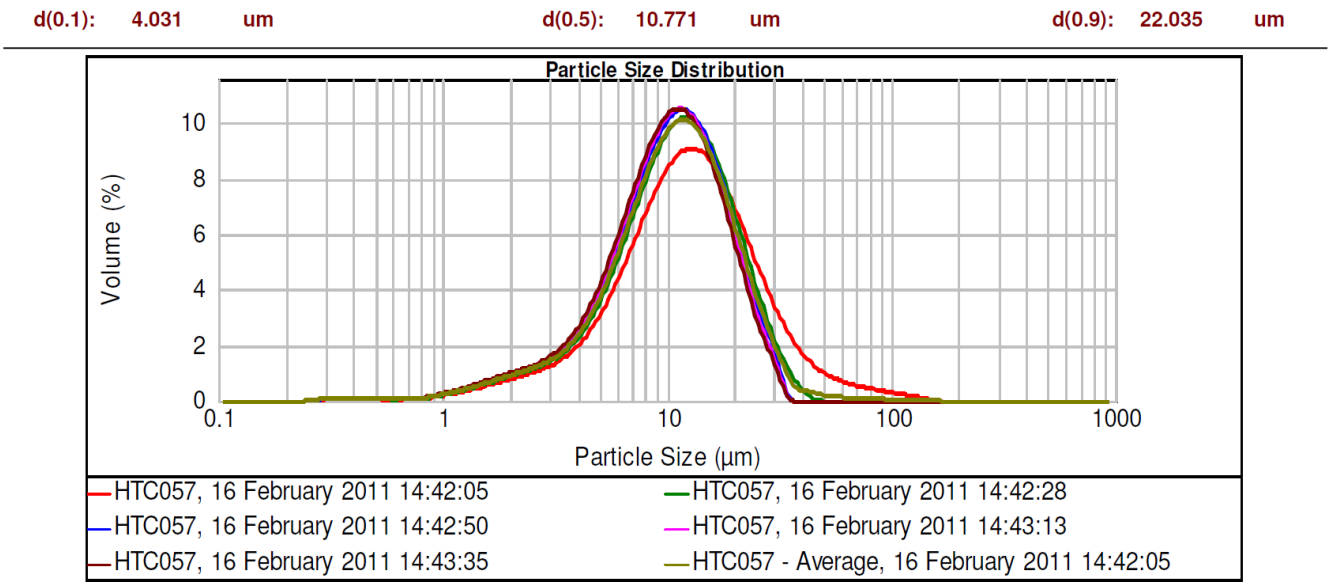

Figure 136: PSA - MgAl140-4

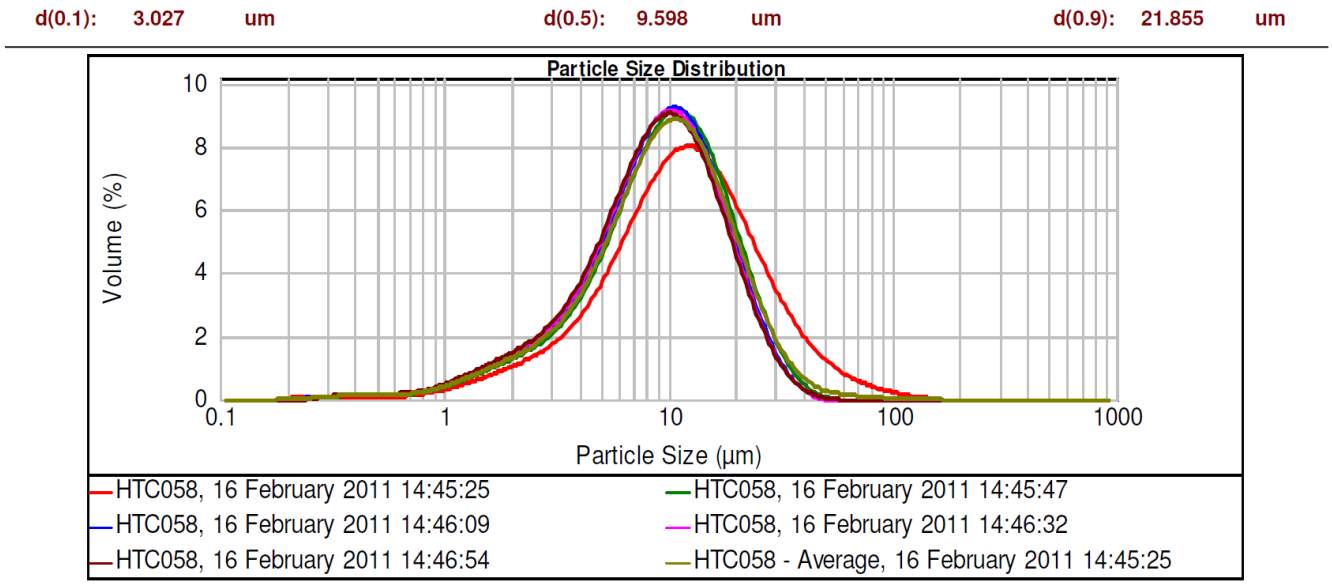

Figure 137: PSA - MgAl140-5

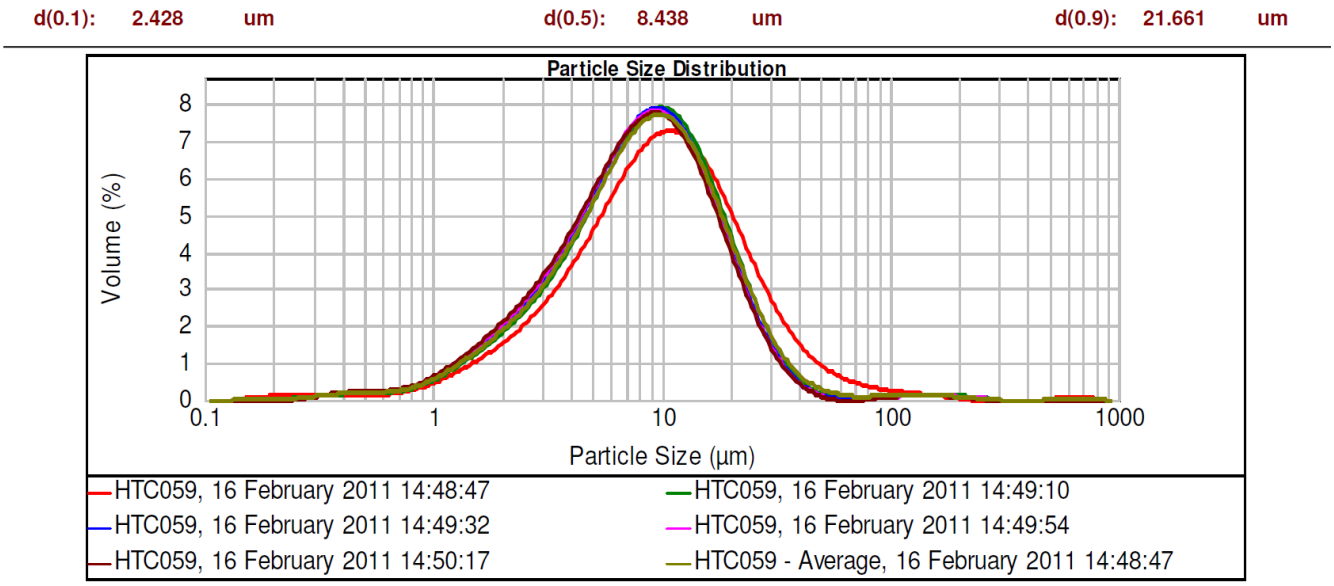

Figure 138: PSA - MgAl160-1

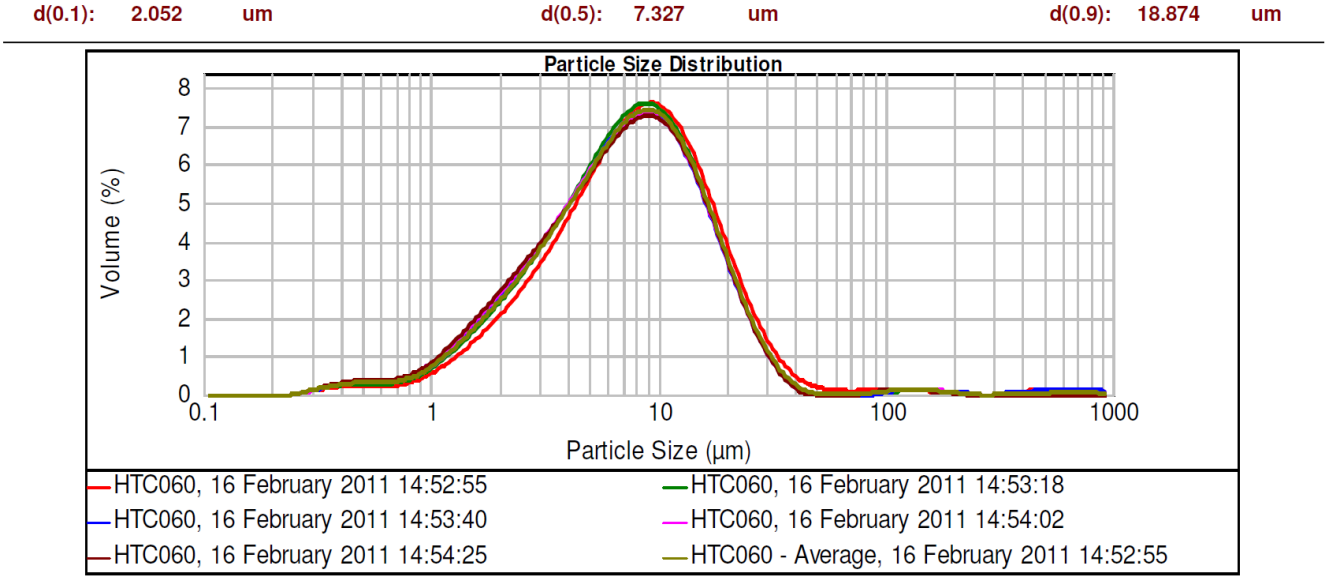

Figure 139: PSA - MgAl160-2

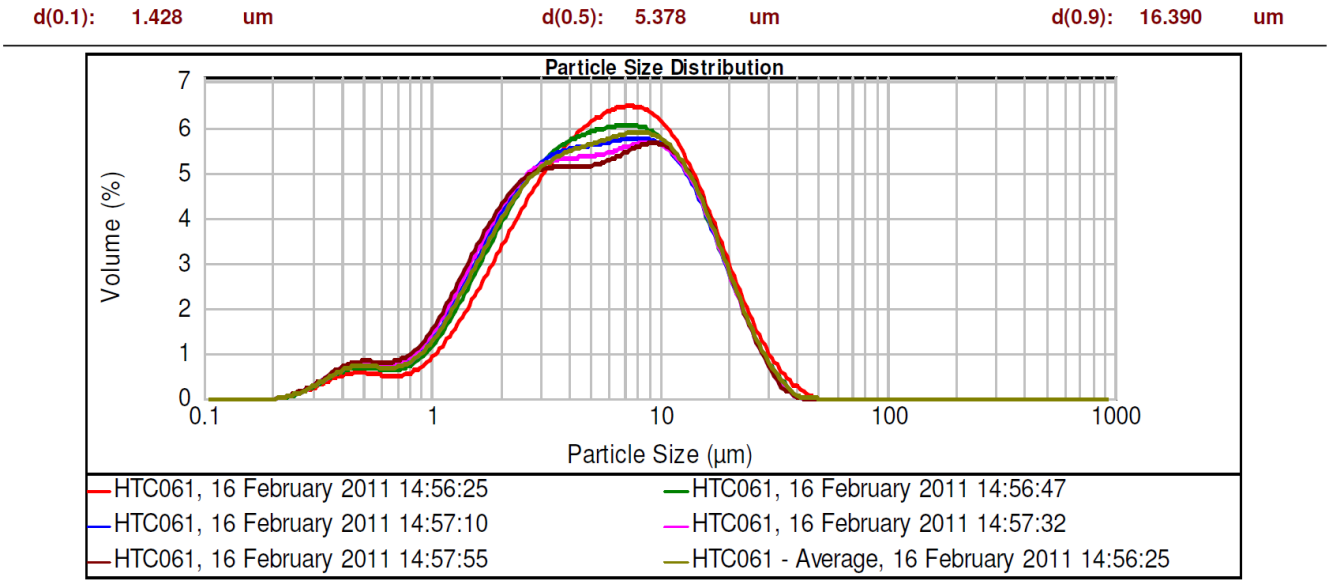

Figure 140: PSA - MgAl160-3

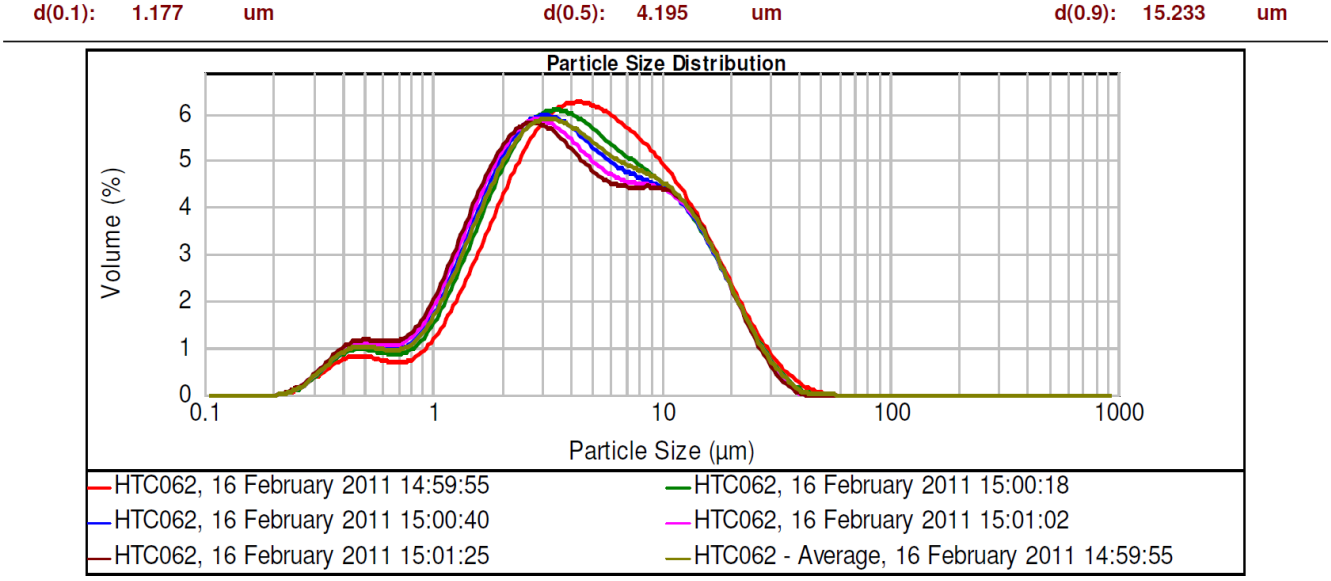

Figure 141: PSA - MgAl160-4

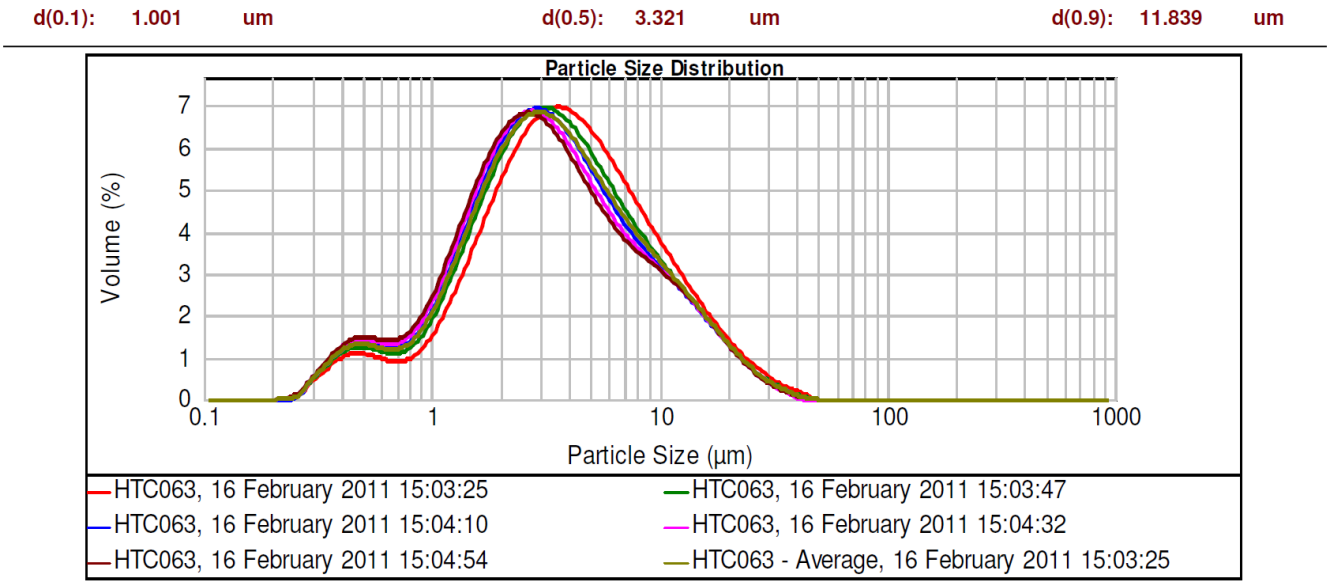

Figure 142: PSA - MgAl160-5

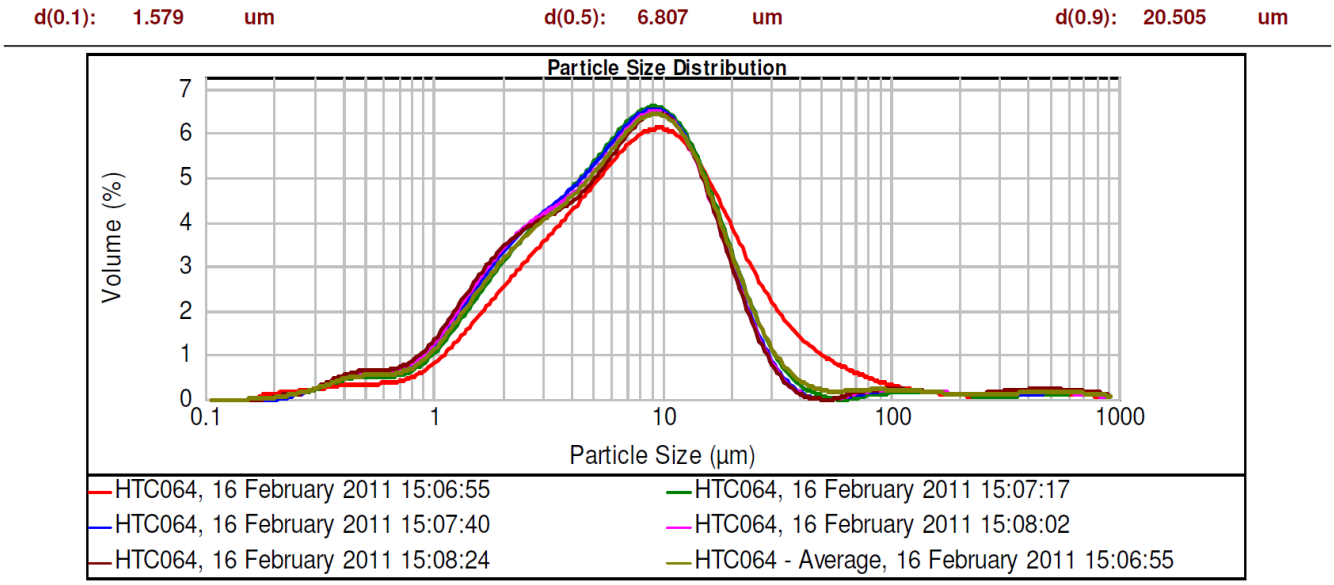

Figure 143: PSA - MgAl180-1

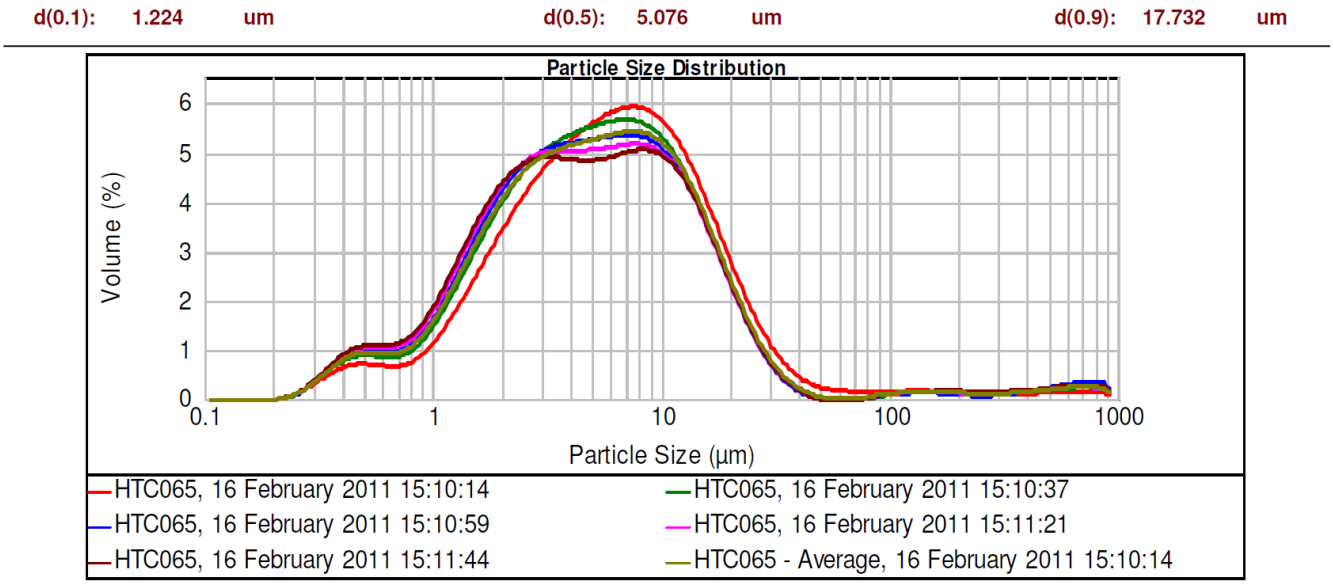

Figure 144: PSA - MgAl180-2

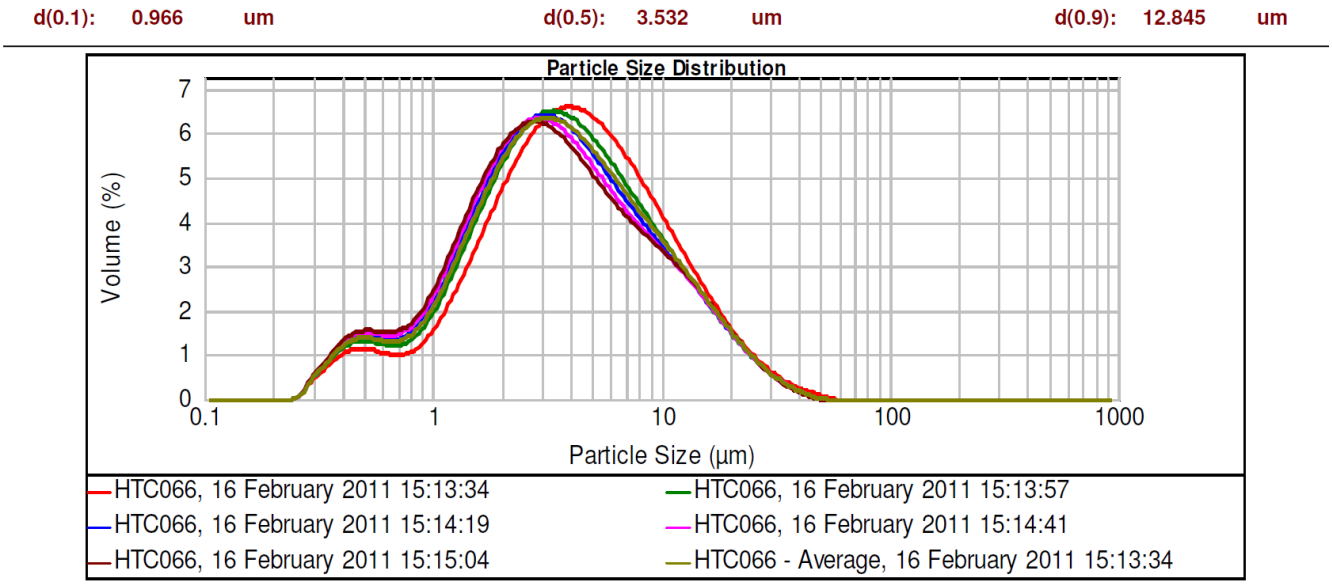

Figure 145: PSA - MgAl180-3

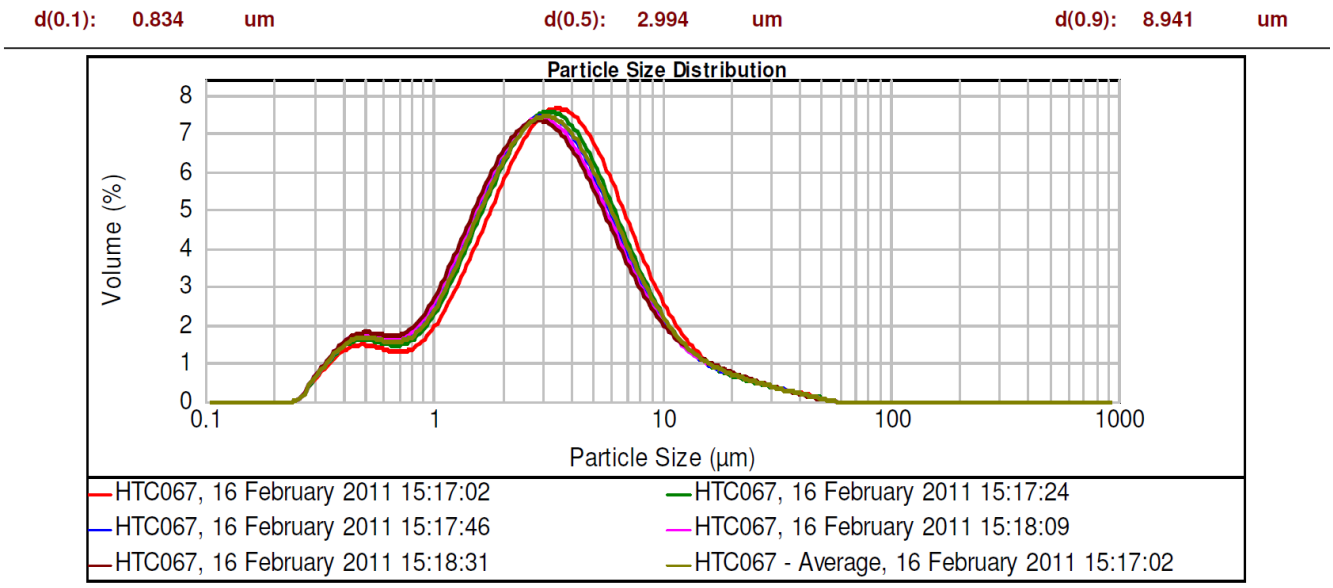

Figure 146: PSA - MgAl180-4

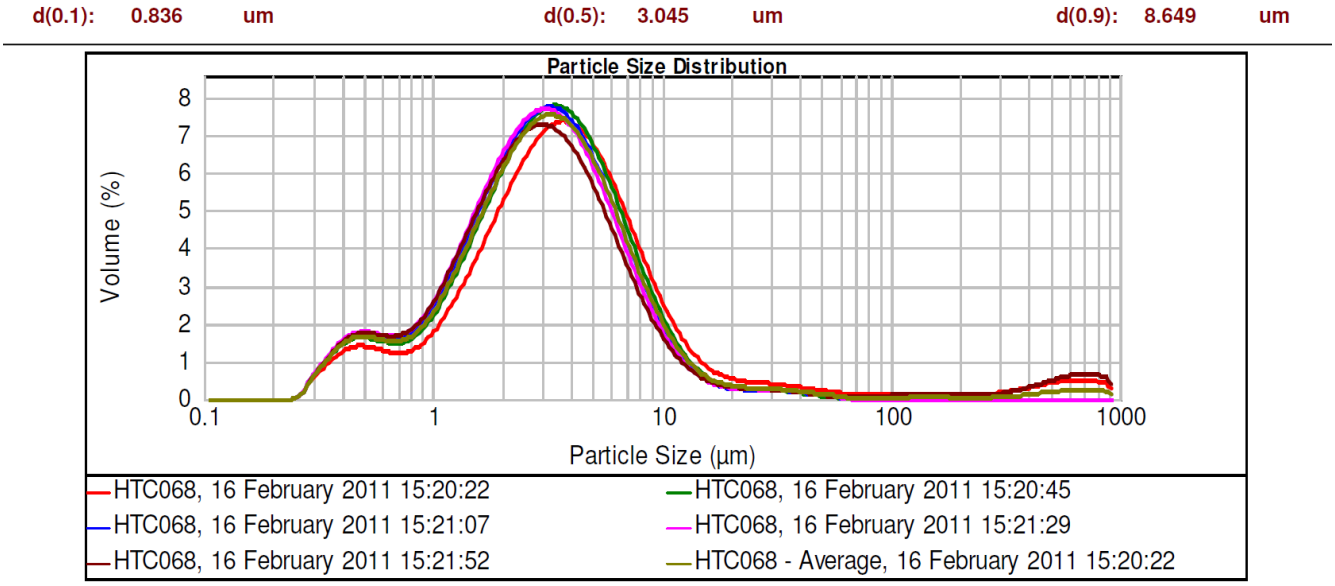

Figure 147: PSA - MgAl180-5

Appendix E: SEM Images

E.1. Mg-Al-CO_3 LDH synthesis

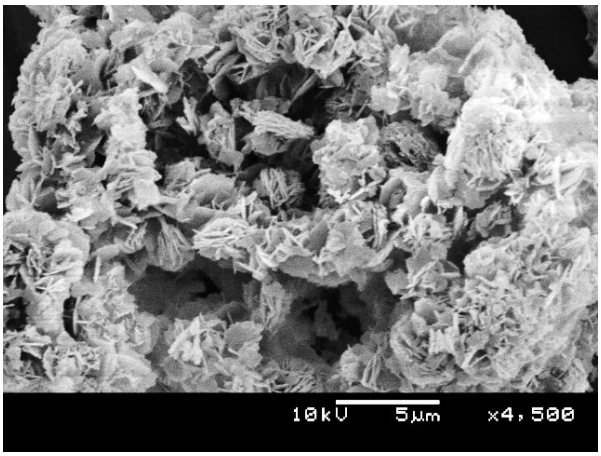

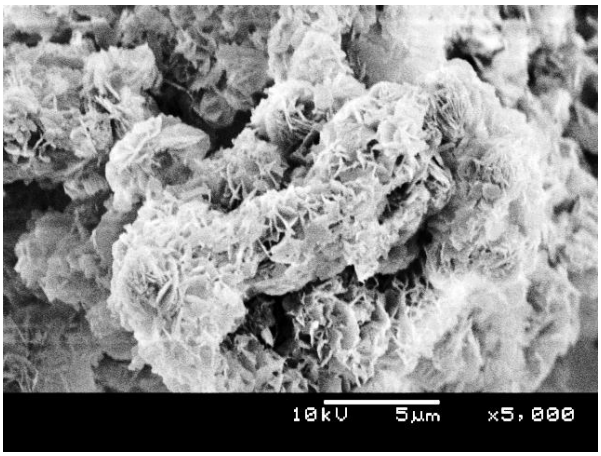

Figure 148: SEM - MgAl120-1

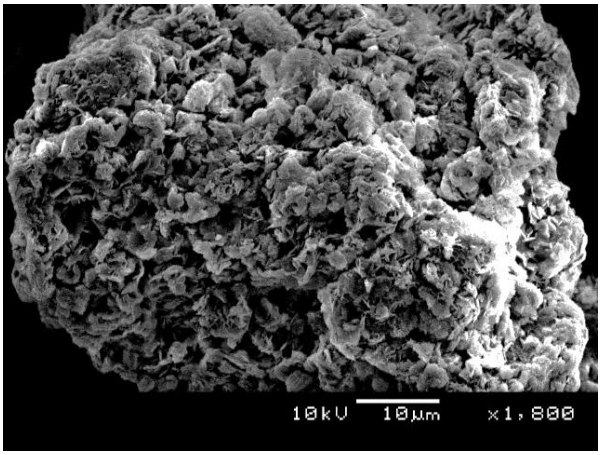

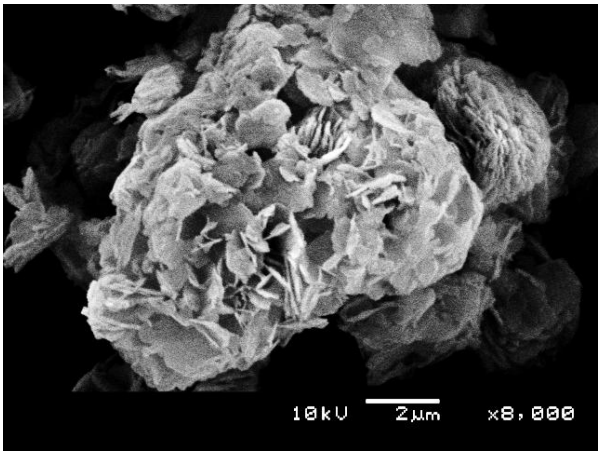

Figure 149: SEM - MgAl120-5

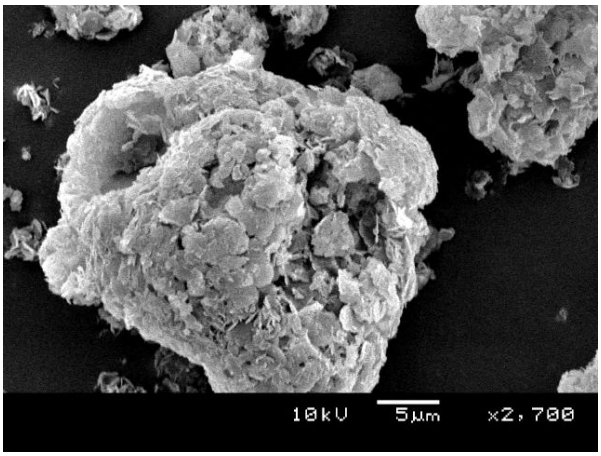

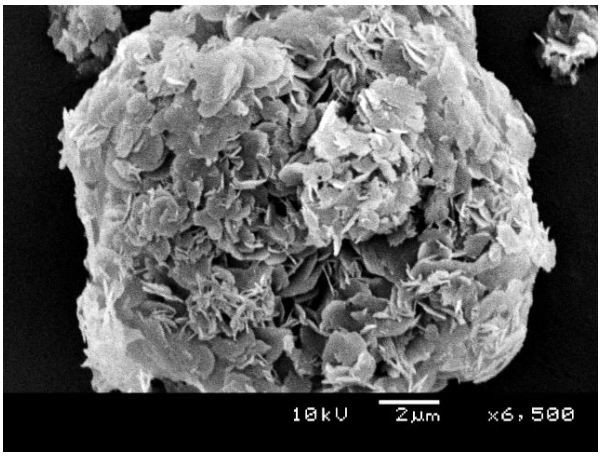

Figure 150: SEM - MgAl140-3

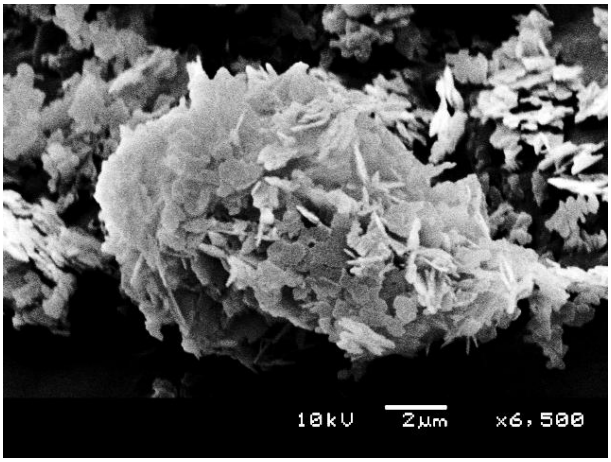

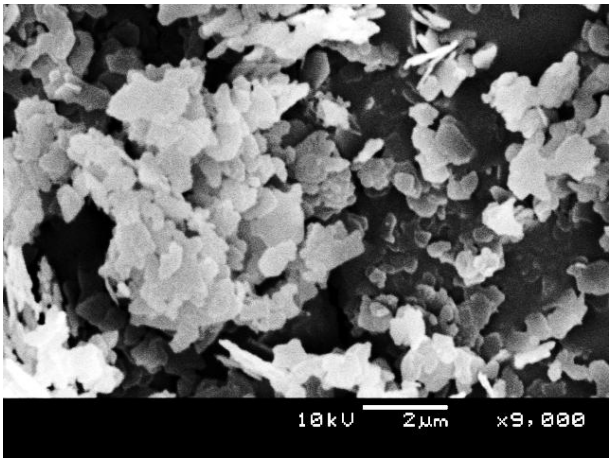

Figure 151: SEM - MgAl160-3

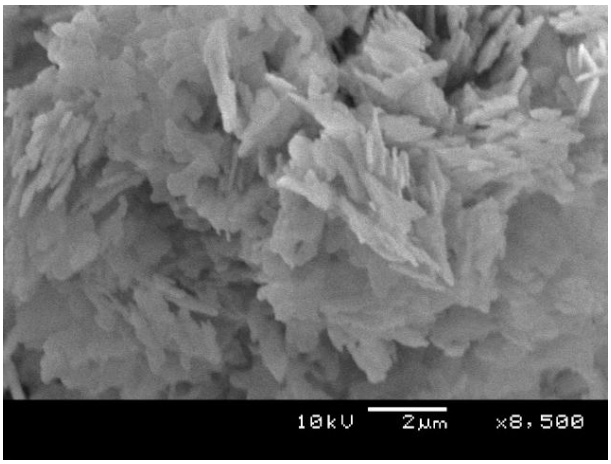

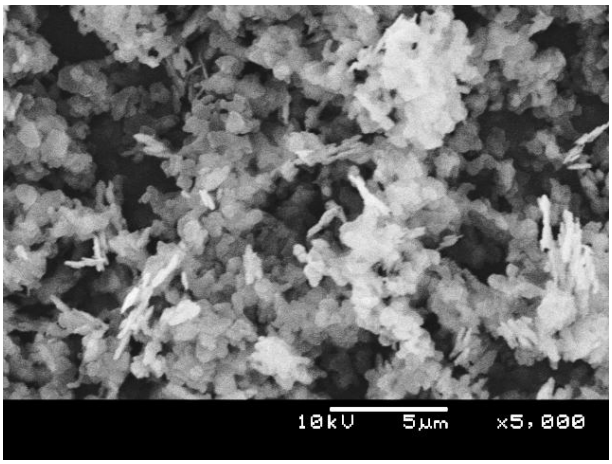

Figure 152: SEM - MgAl160-5

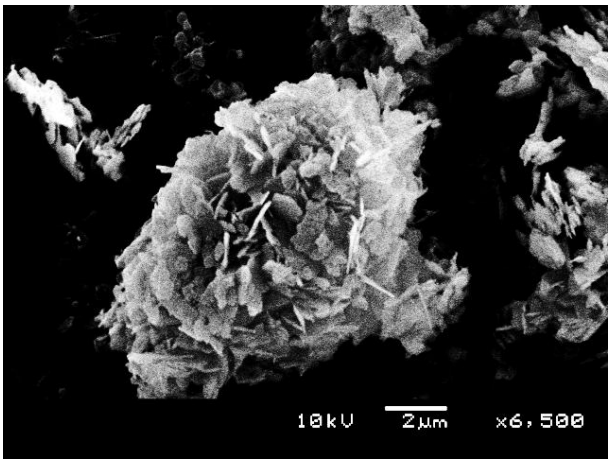

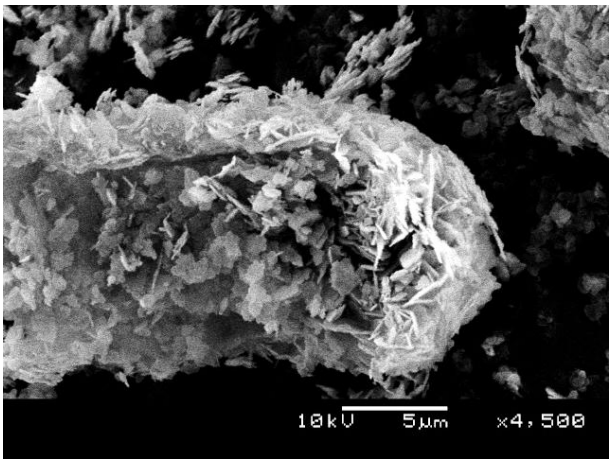

Figure 153: SEM - MgAl180-1

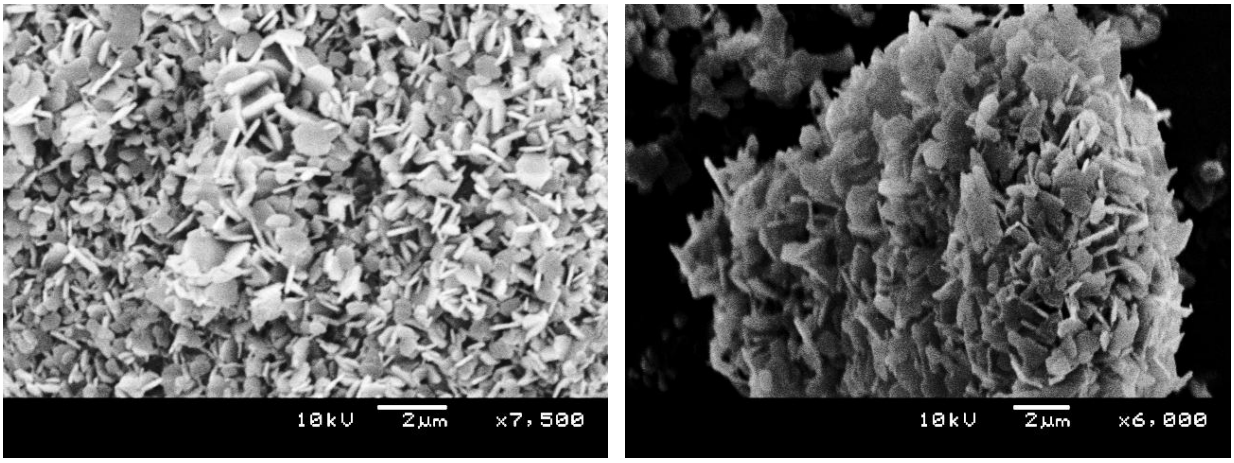

Figure 154: SEM - MgAl180-4

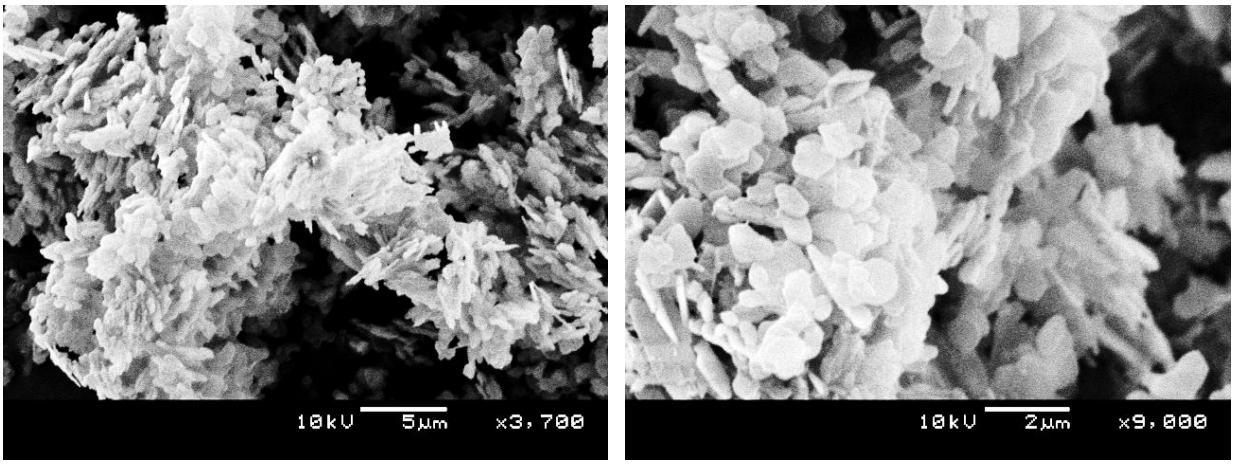

Figure 155: SEM - MgAl180-5

E.2. Mixed metal oxides/hydroxides method

Cobalt

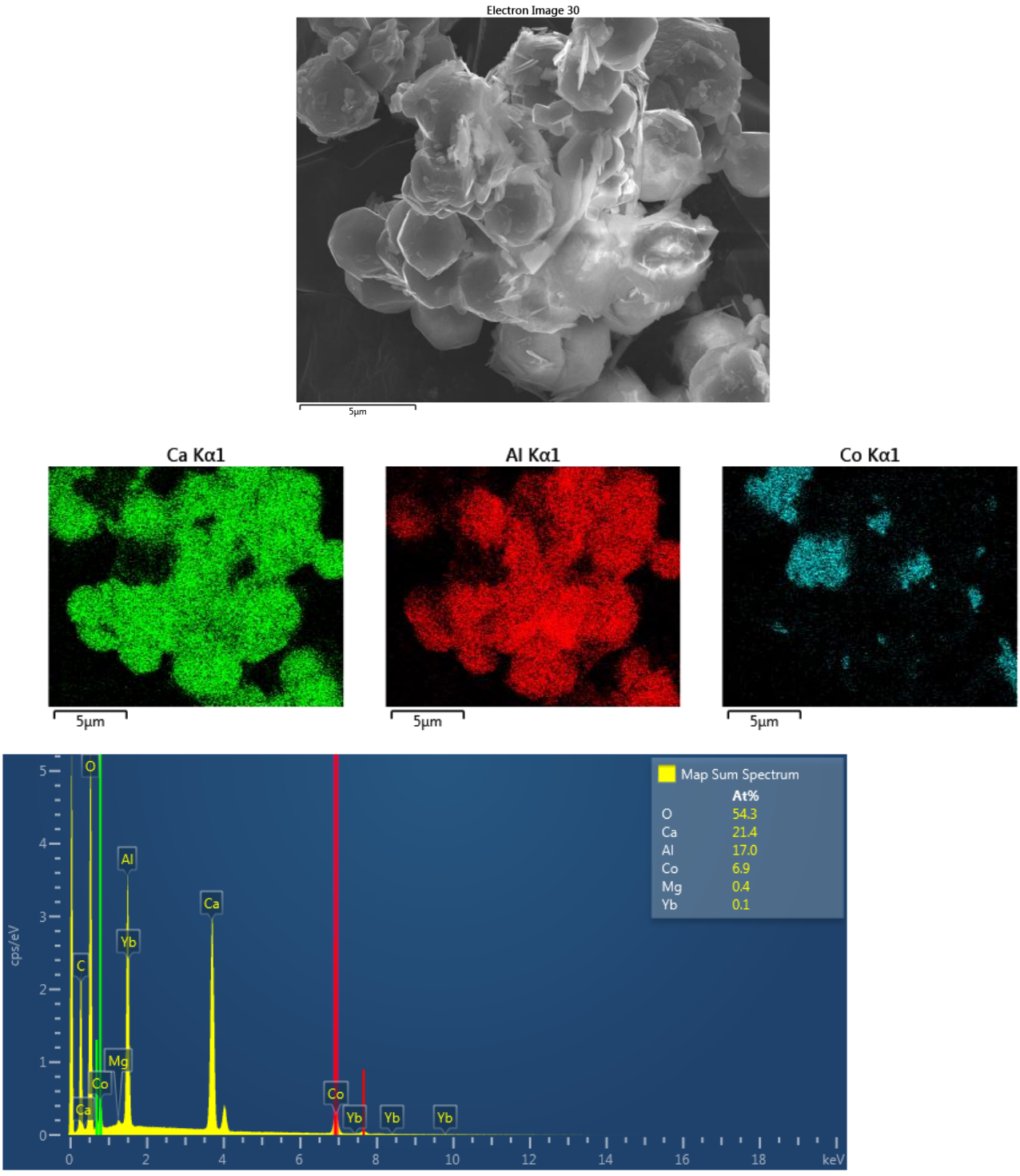

Figure 156: *Ca/Co(II)* 25 mole% - Inert

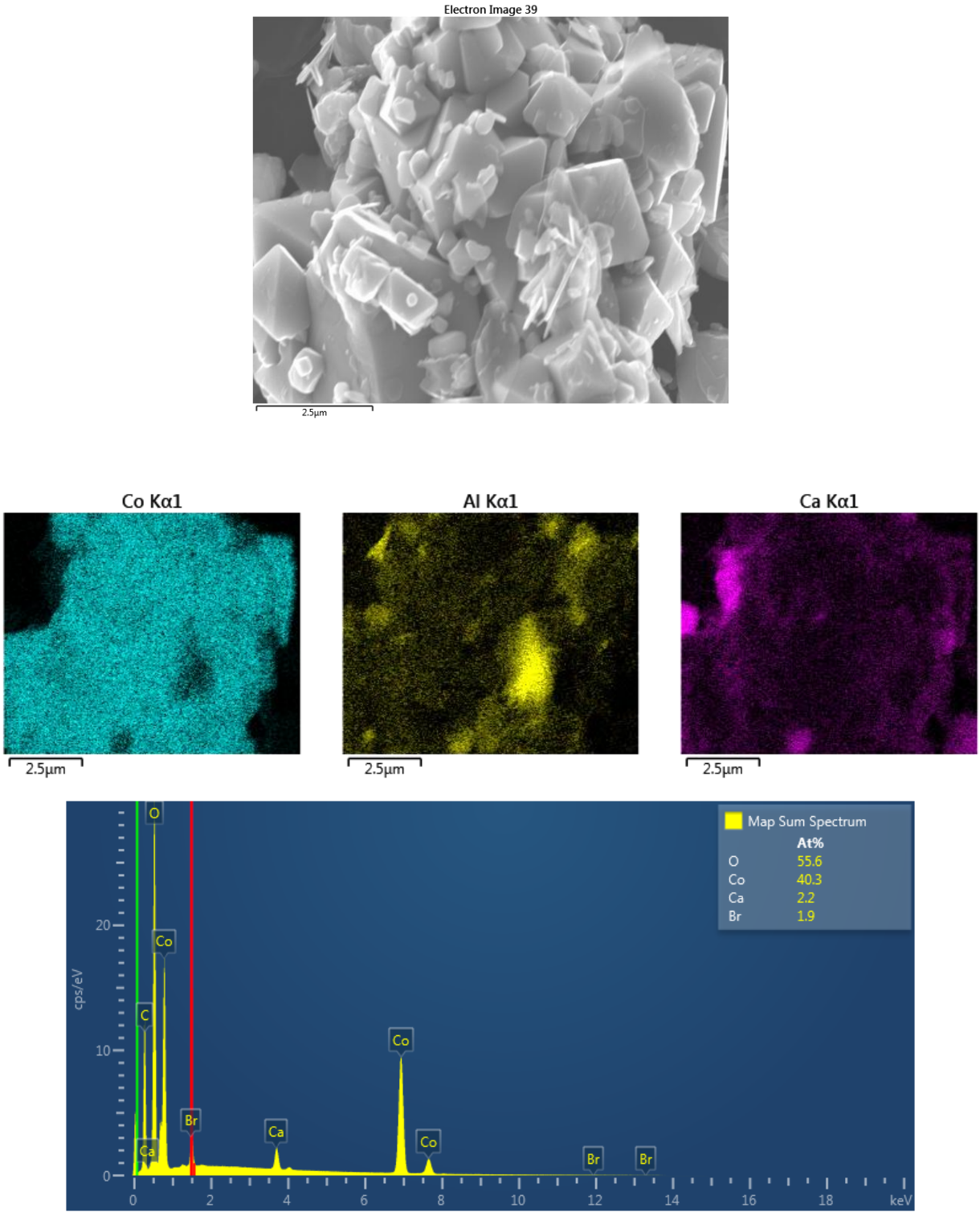

Figure 157: *Ca/Co(II)* 25 mole% - Carbonate

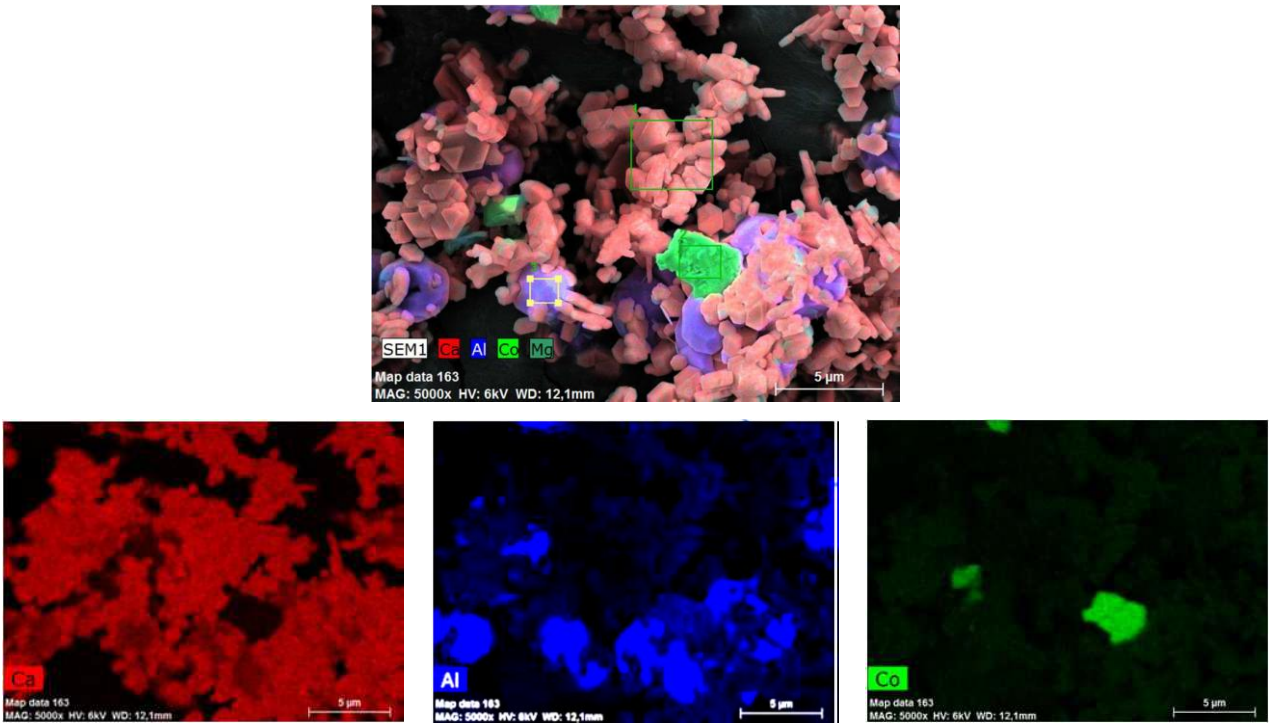

1.

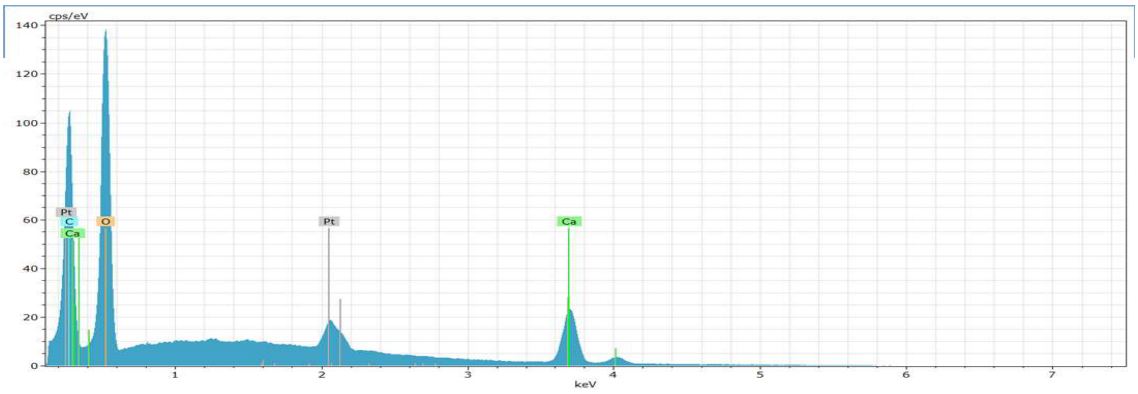

2.

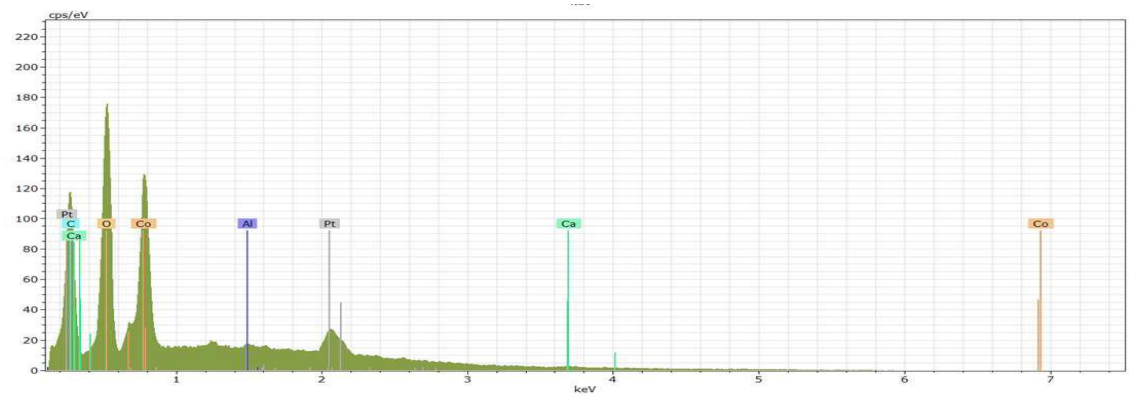

Figure 158: *Ca/Co(II)* 8.3 mole% - Inert

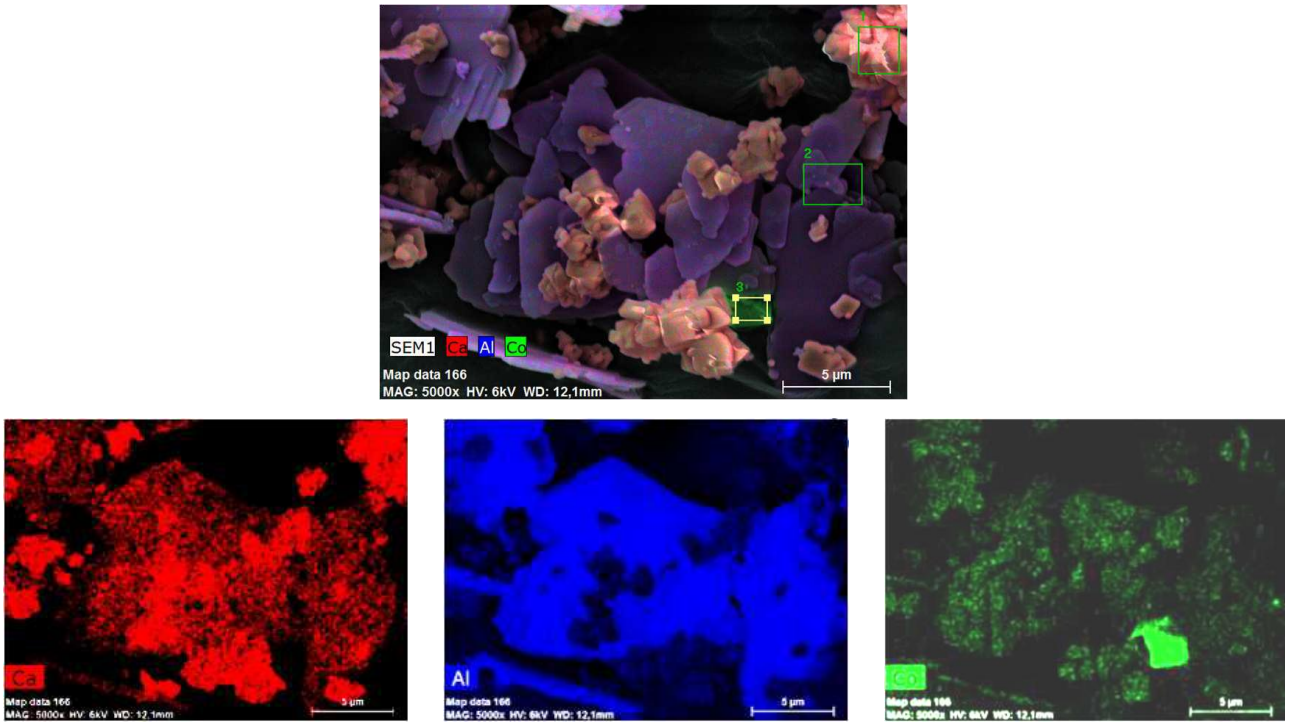

1.

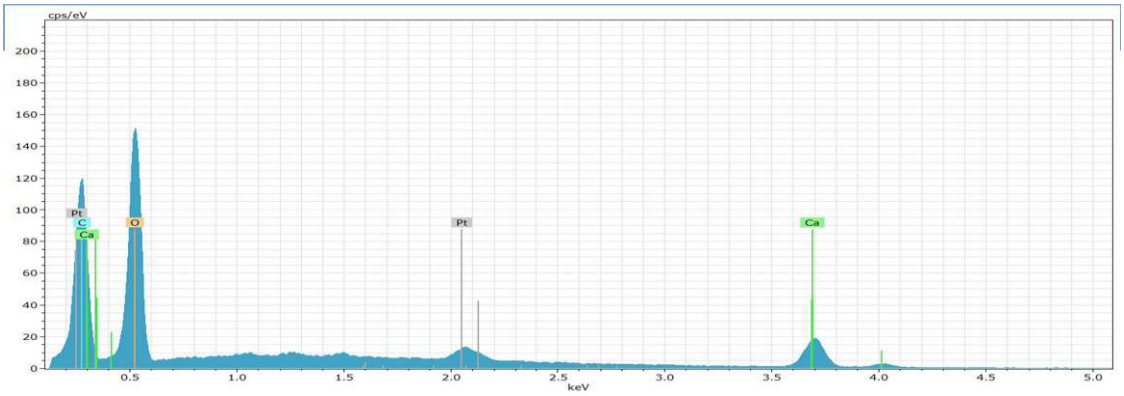

2.

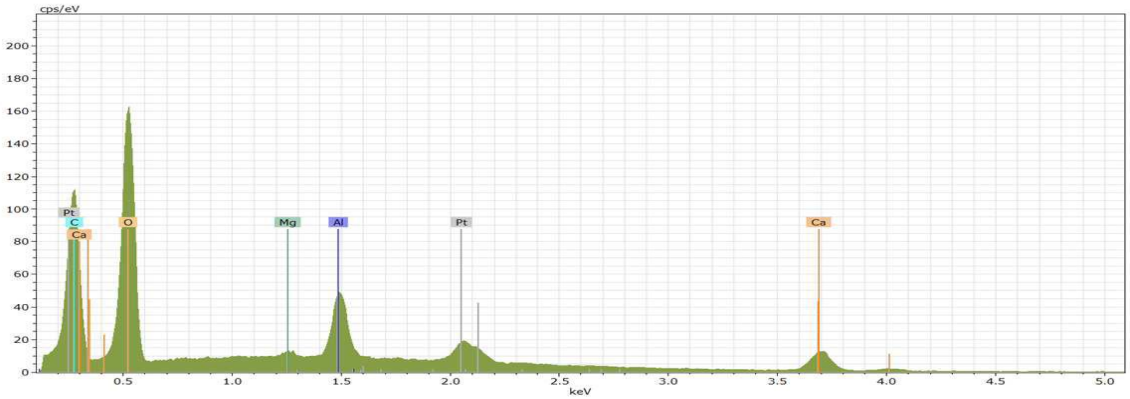

Figure 159: *Ca/Co(II)* 8.3 mole% - Carbonate

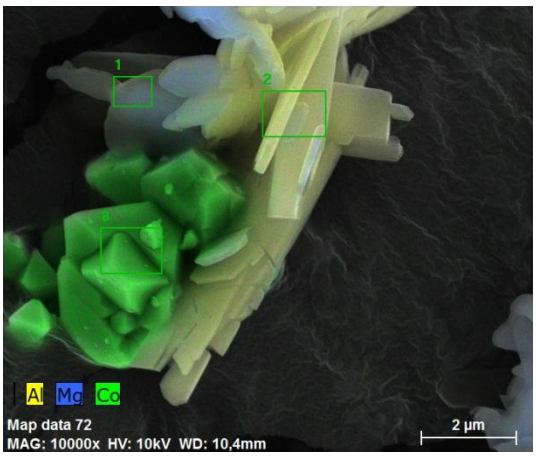

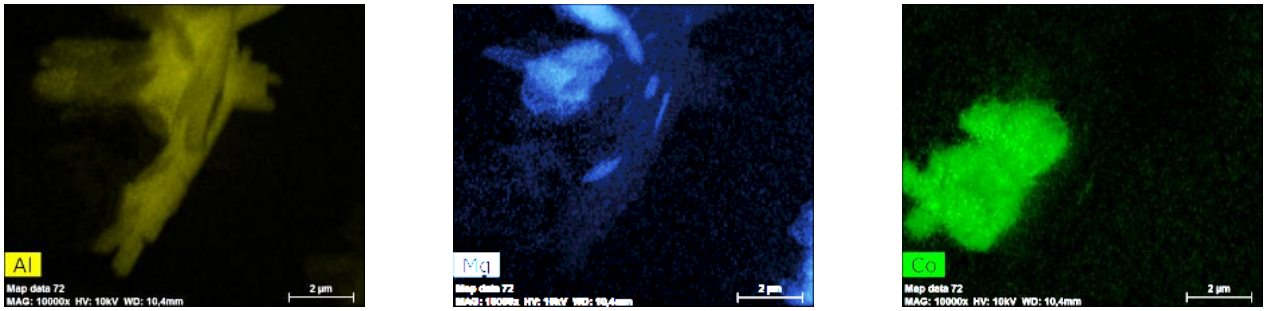

2.

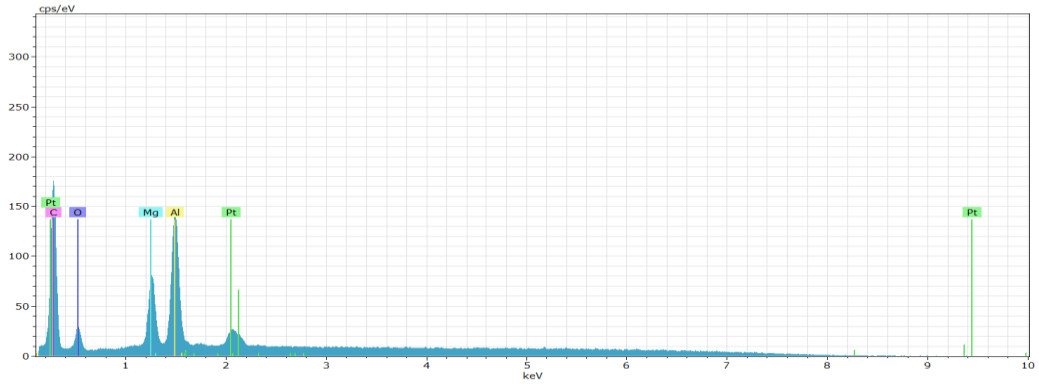

3.

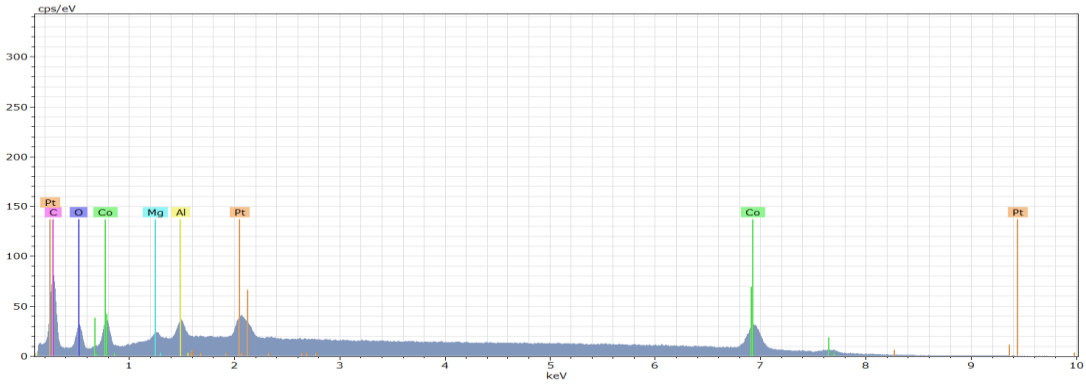

Figure 160: *Mg/Co(II)* 25 mole% - Carbonate

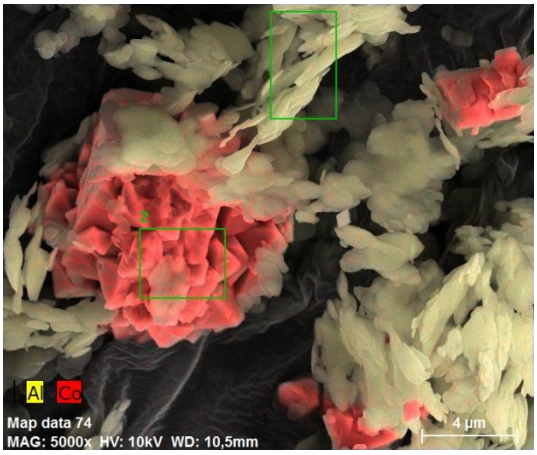

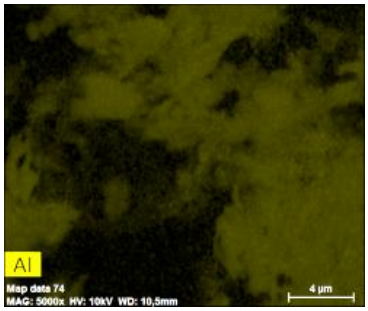

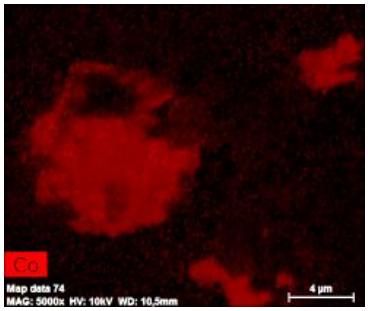

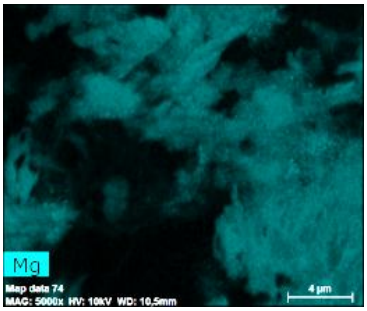

1.

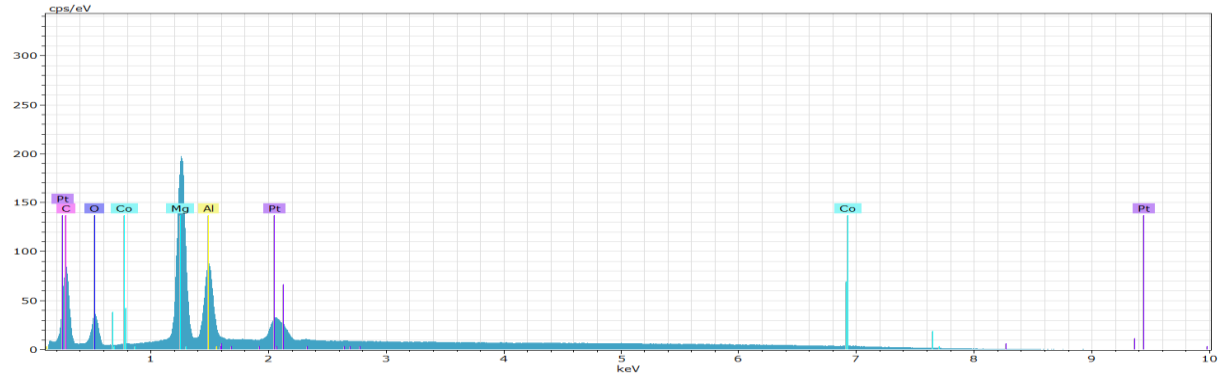

2.

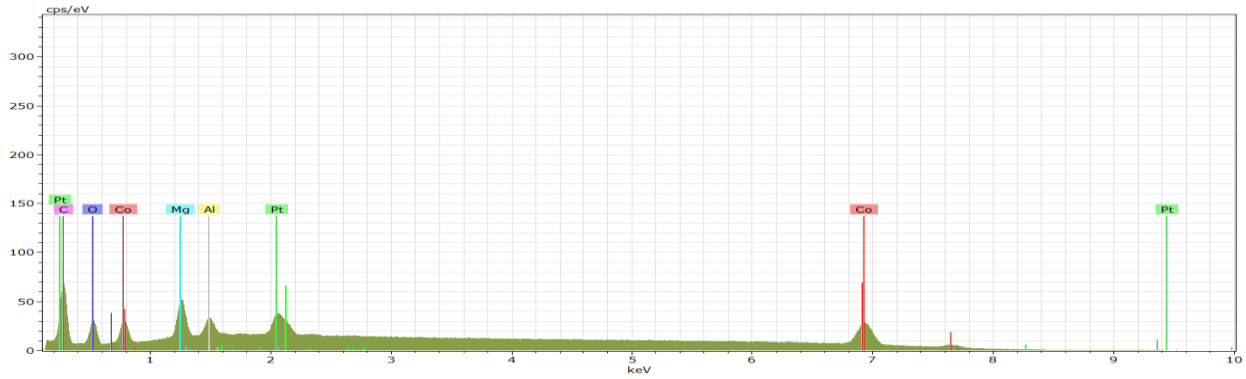

Figure 161: *Mg/Co(II)* 8.3 mole% - Carbonate

Copper

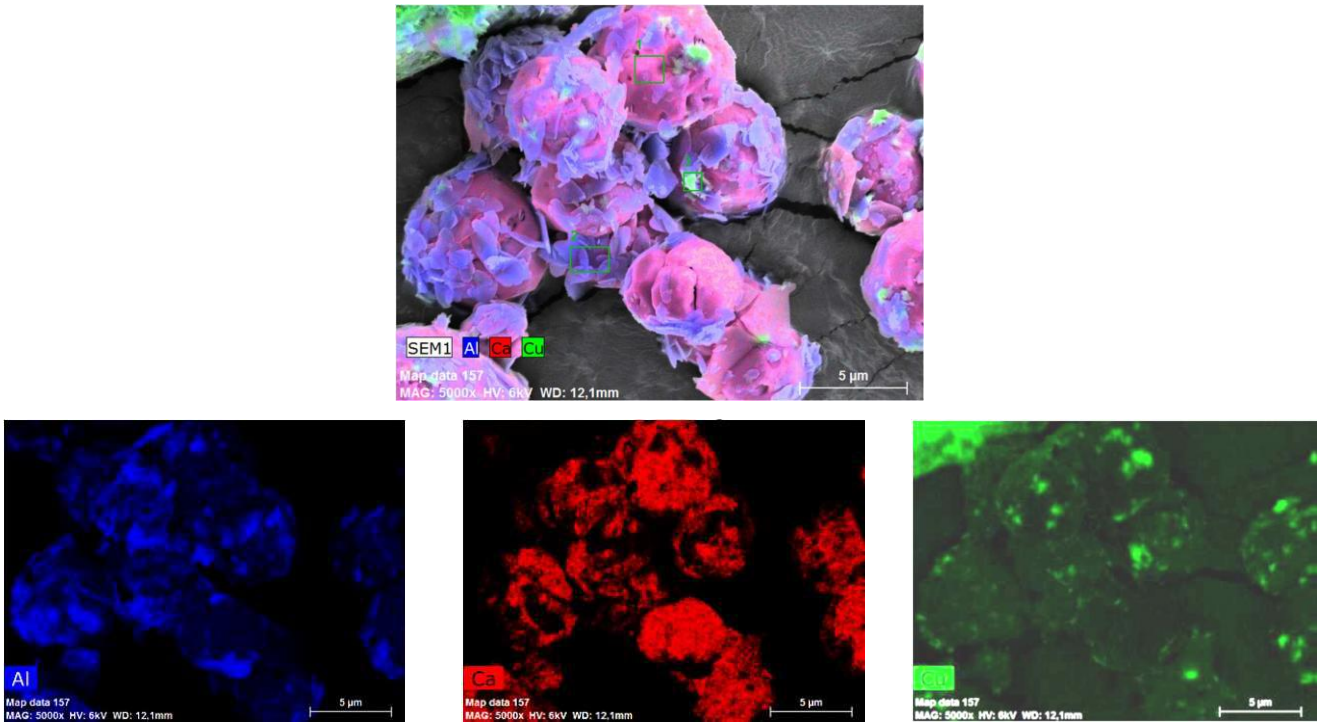

1.

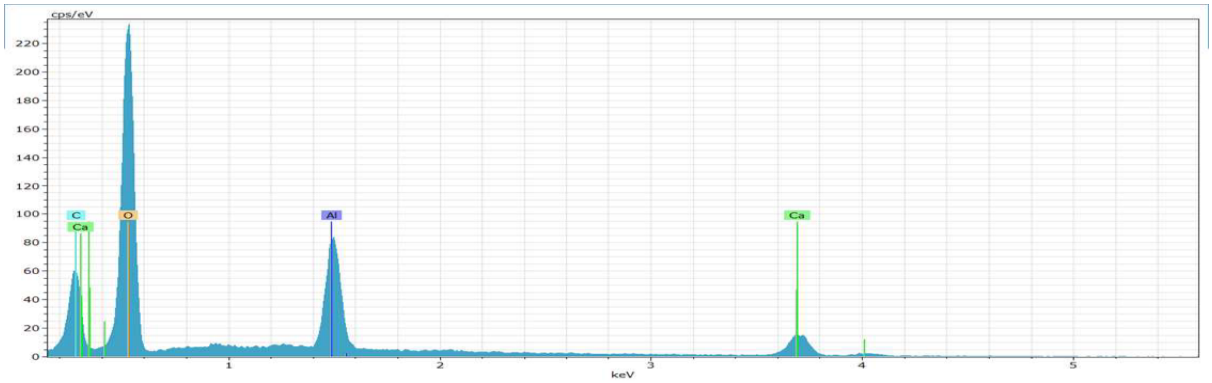

2.

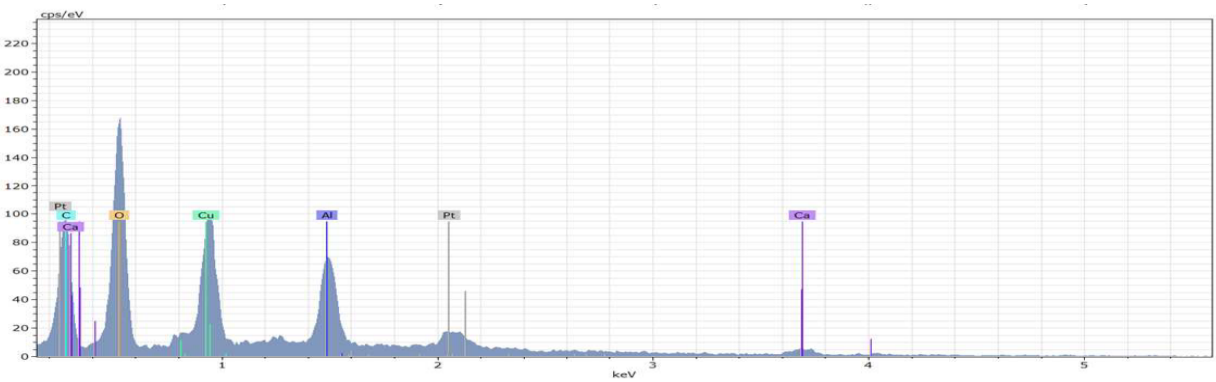

Figure 162: *Ca/Cu(I)* 25 mole% - Inert

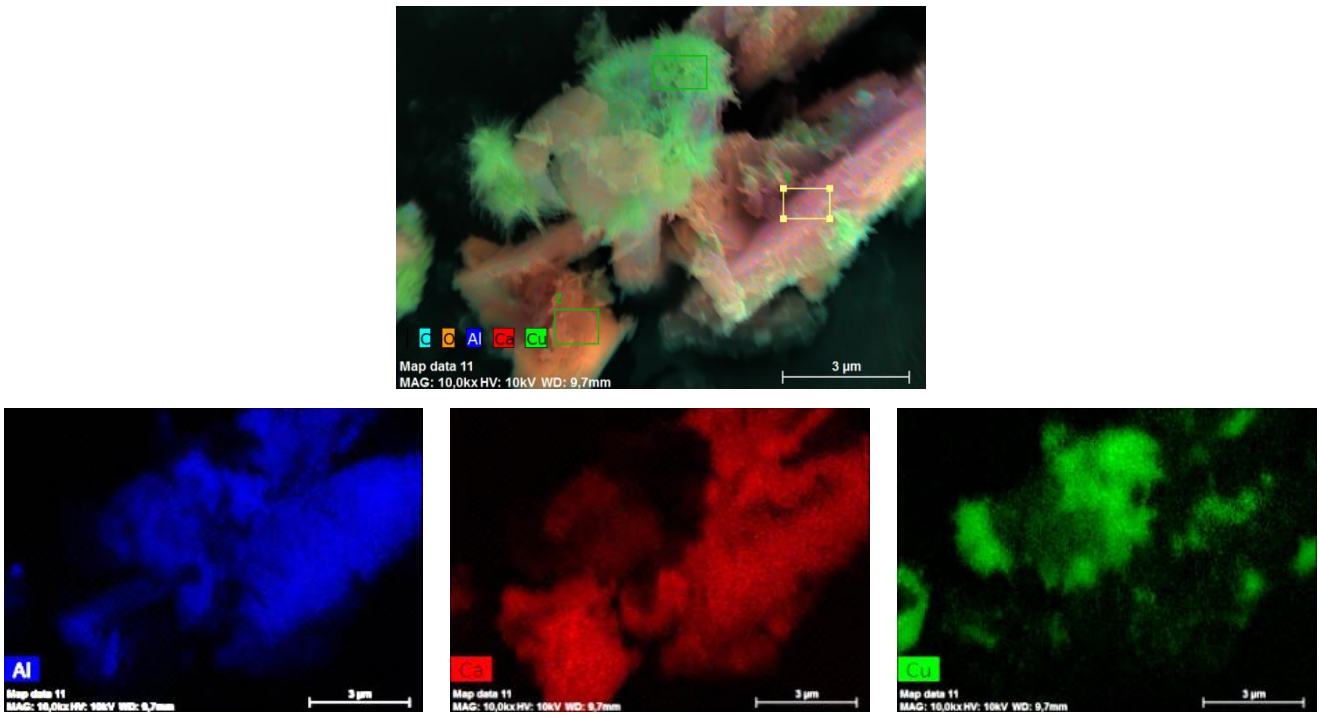

1.

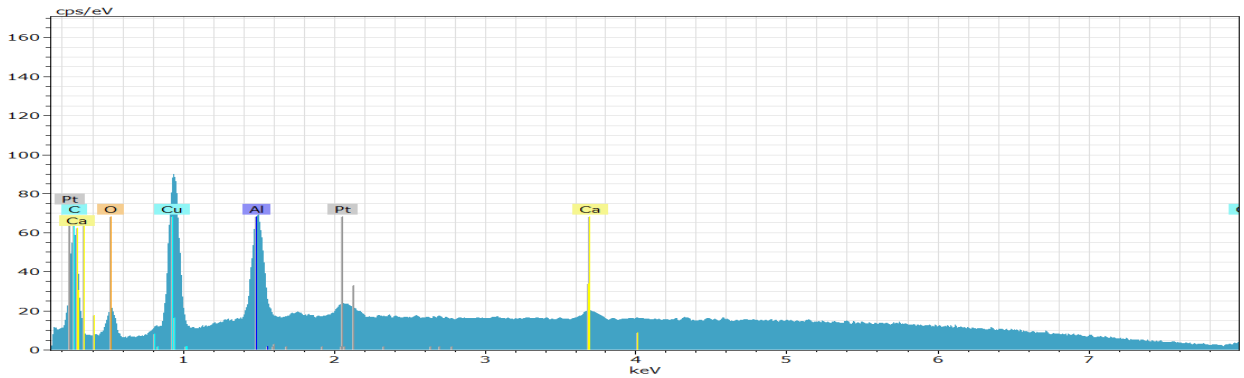

2.

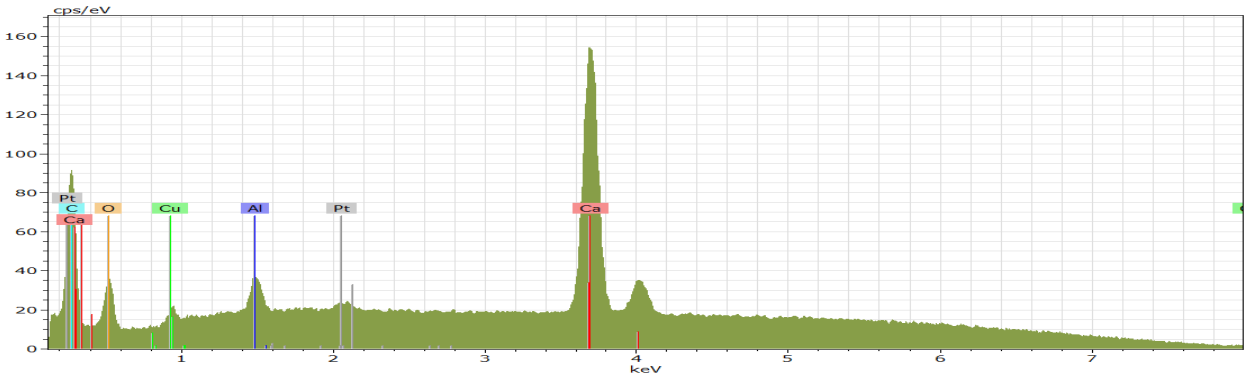

Figure 163: *Ca/Cu(I)* 25 mole% - Carbonate

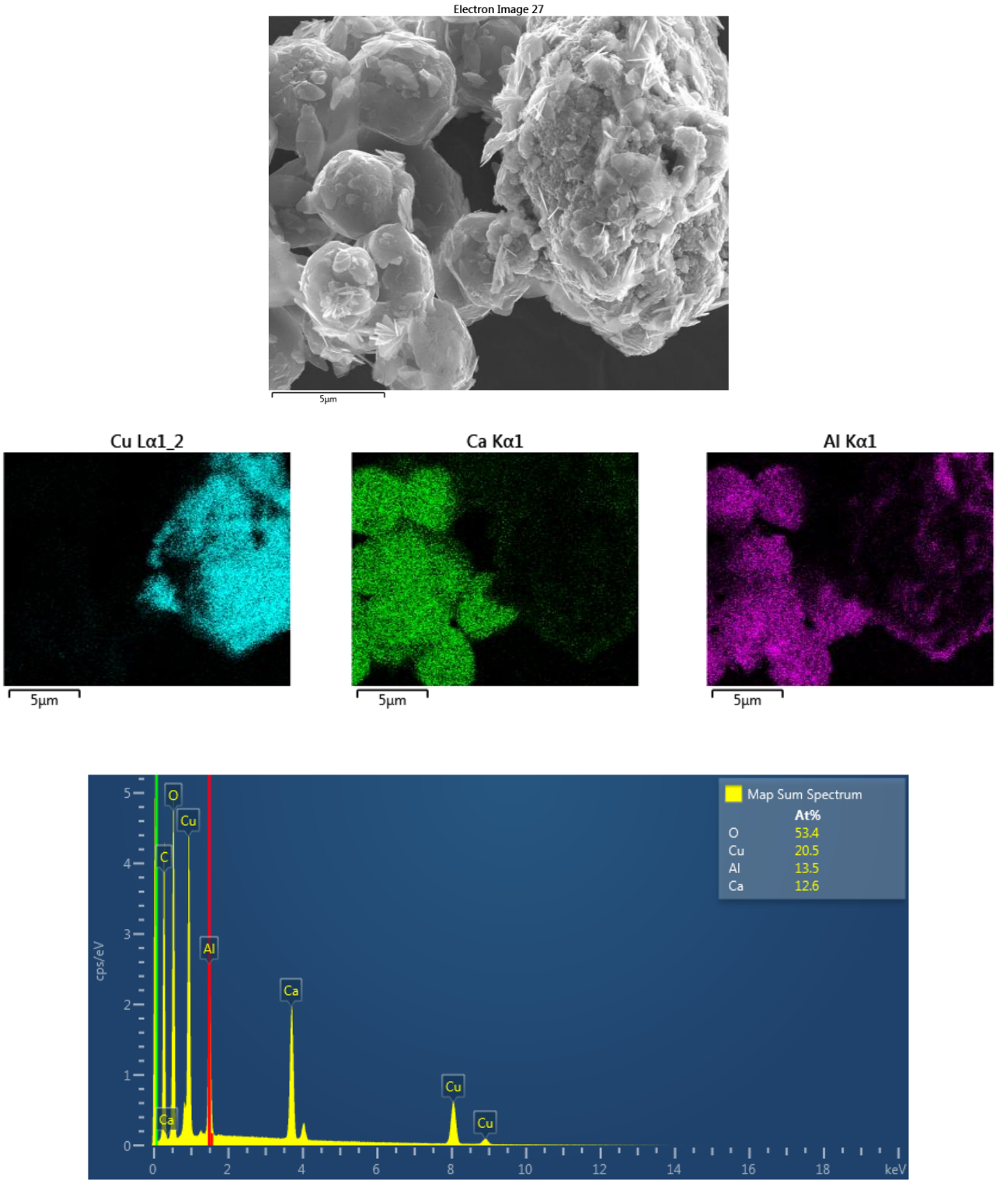

Figure 164: *Ca/Cu(II)* 25 mole% - Inert

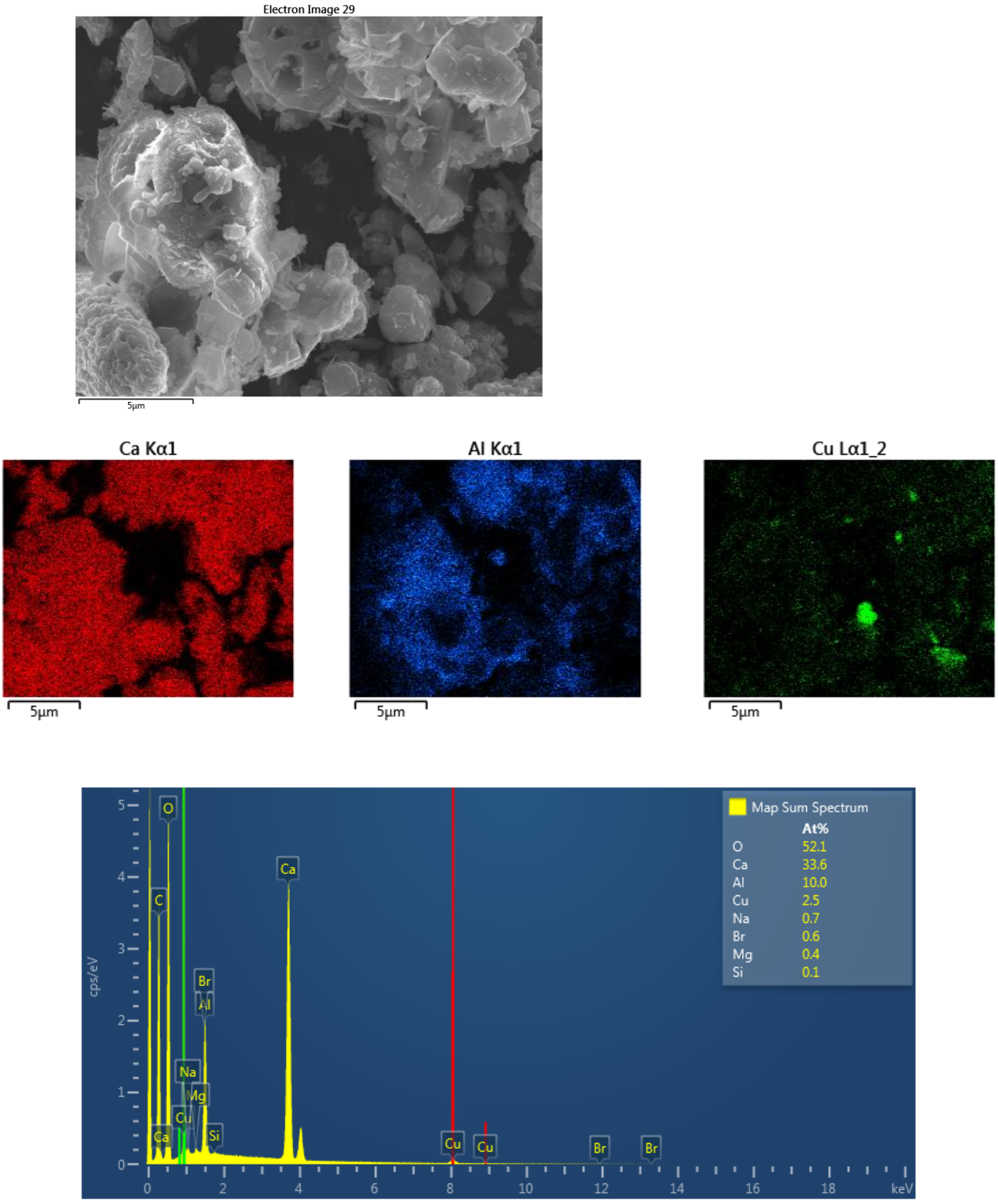

Figure 165: *Ca/Cu(II)* 25 mole% - Carbonate

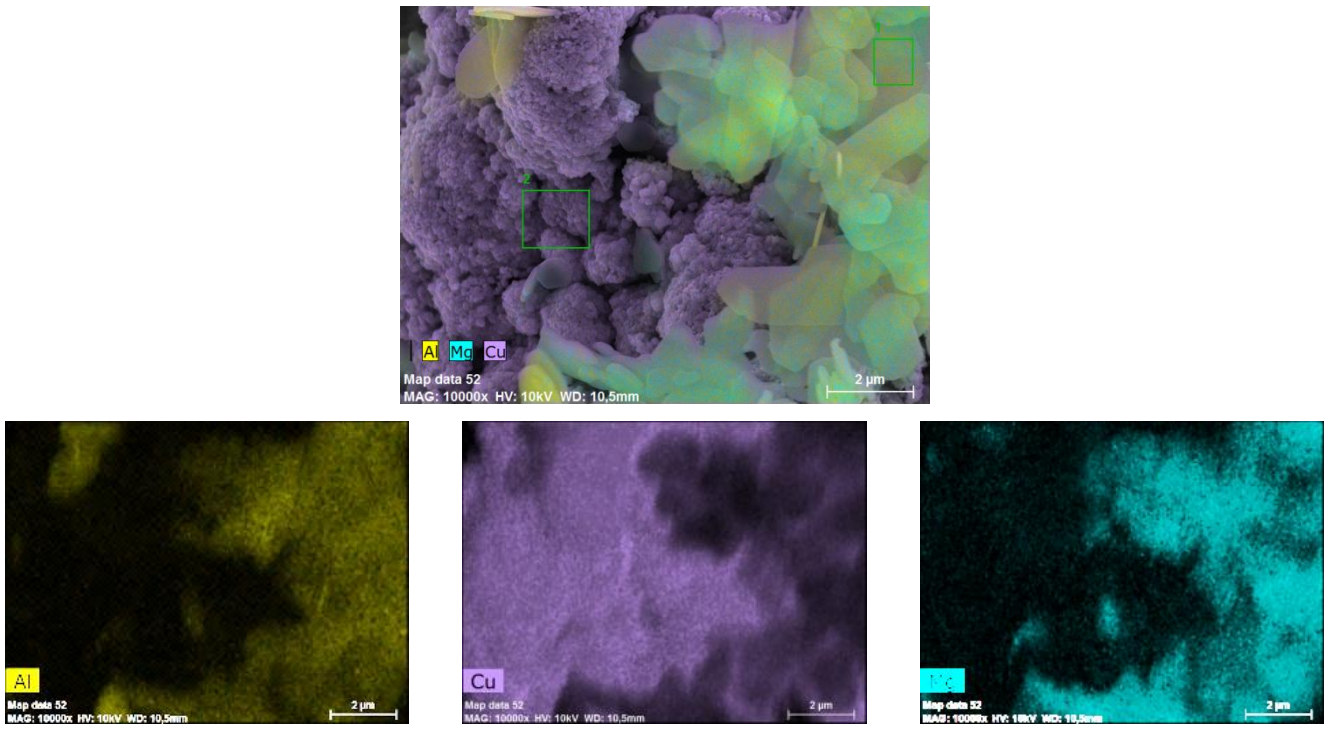

1.

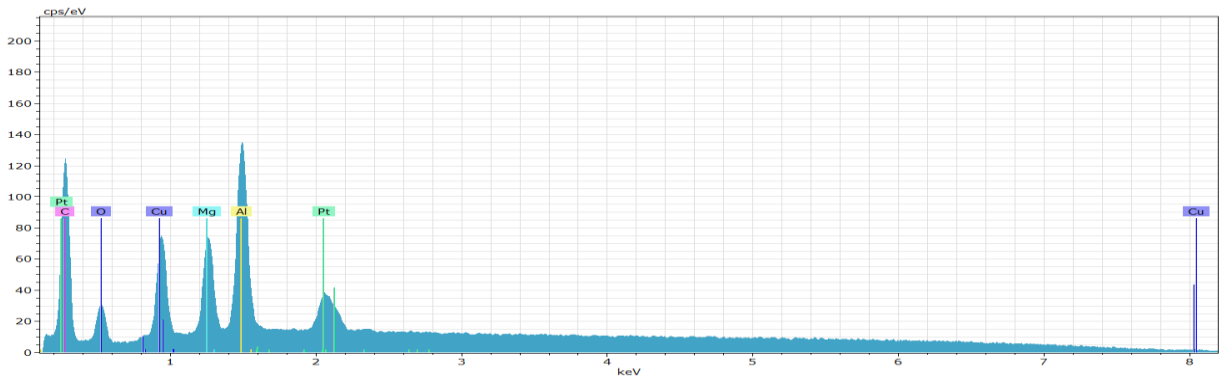

2.

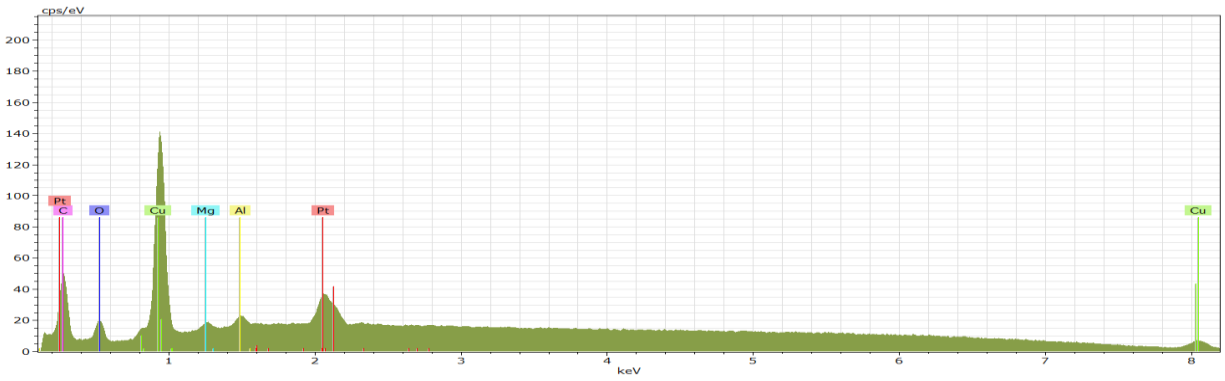

Figure 166: *Mg/Cu(II)* 25 mole% - Carbonate

Manganese

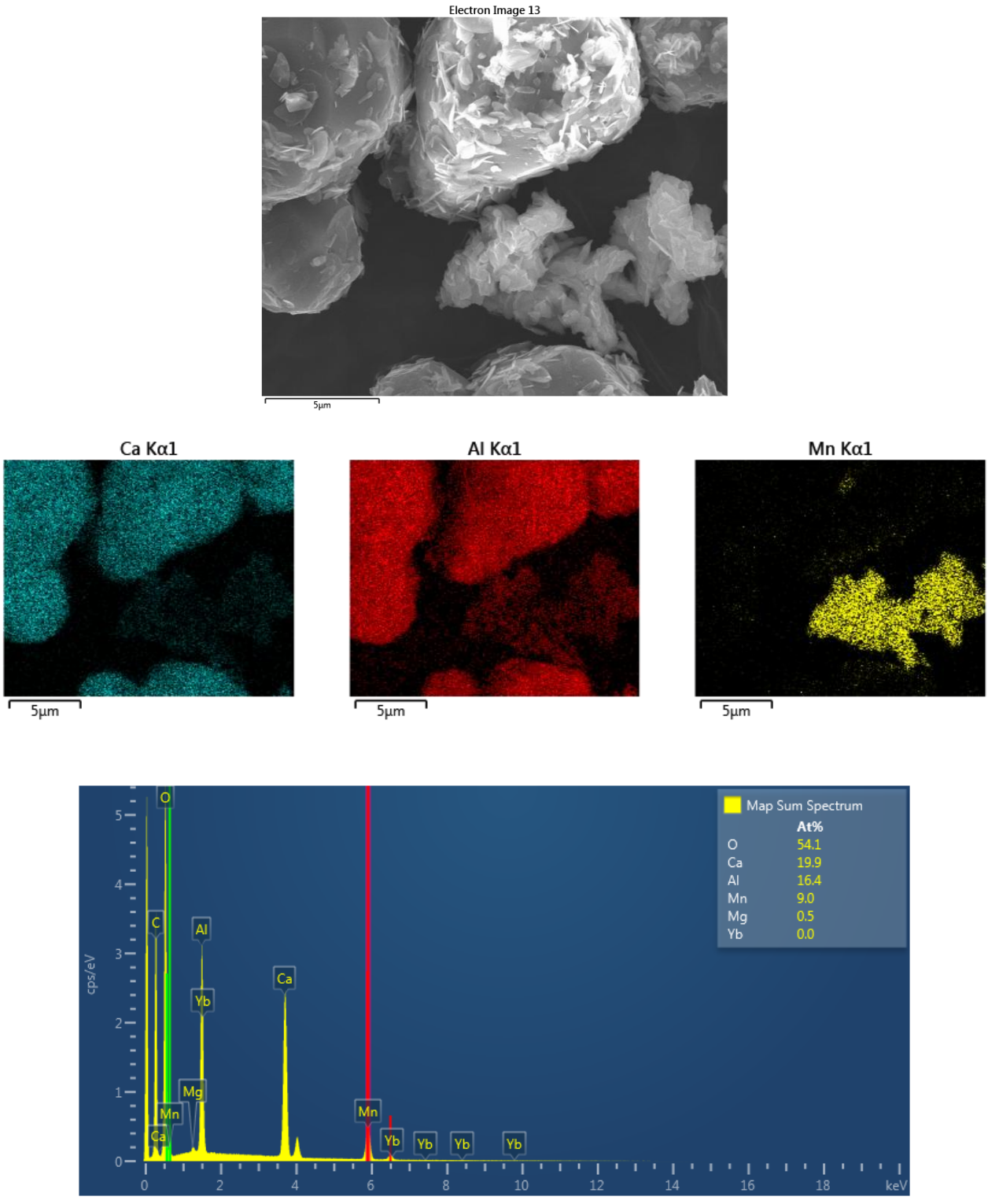

Figure 167: *Ca/Mn(II)* 25 mole% - Inert

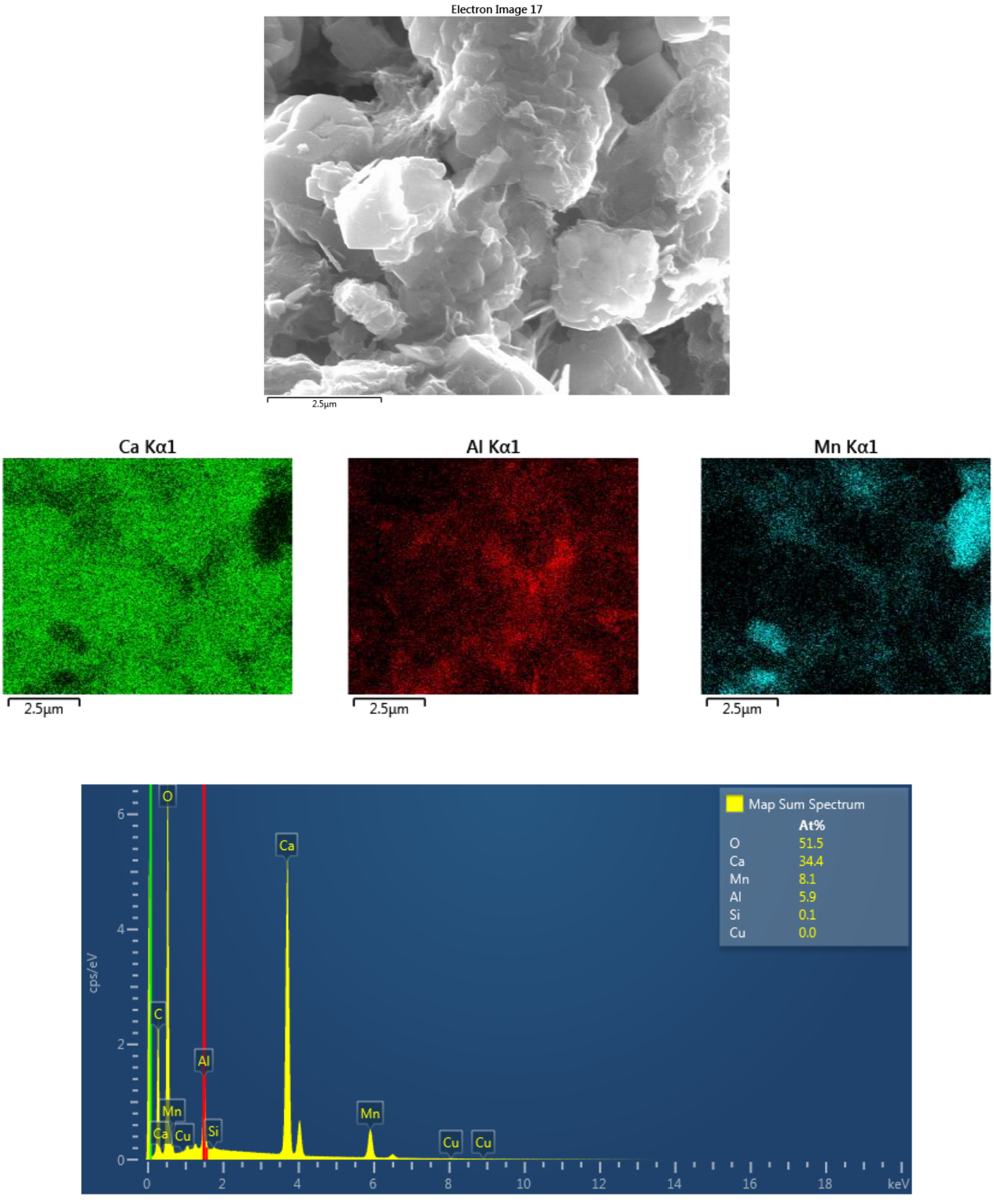

Figure 168: *Ca/Mn(II)* 25 mole% - Carbonate

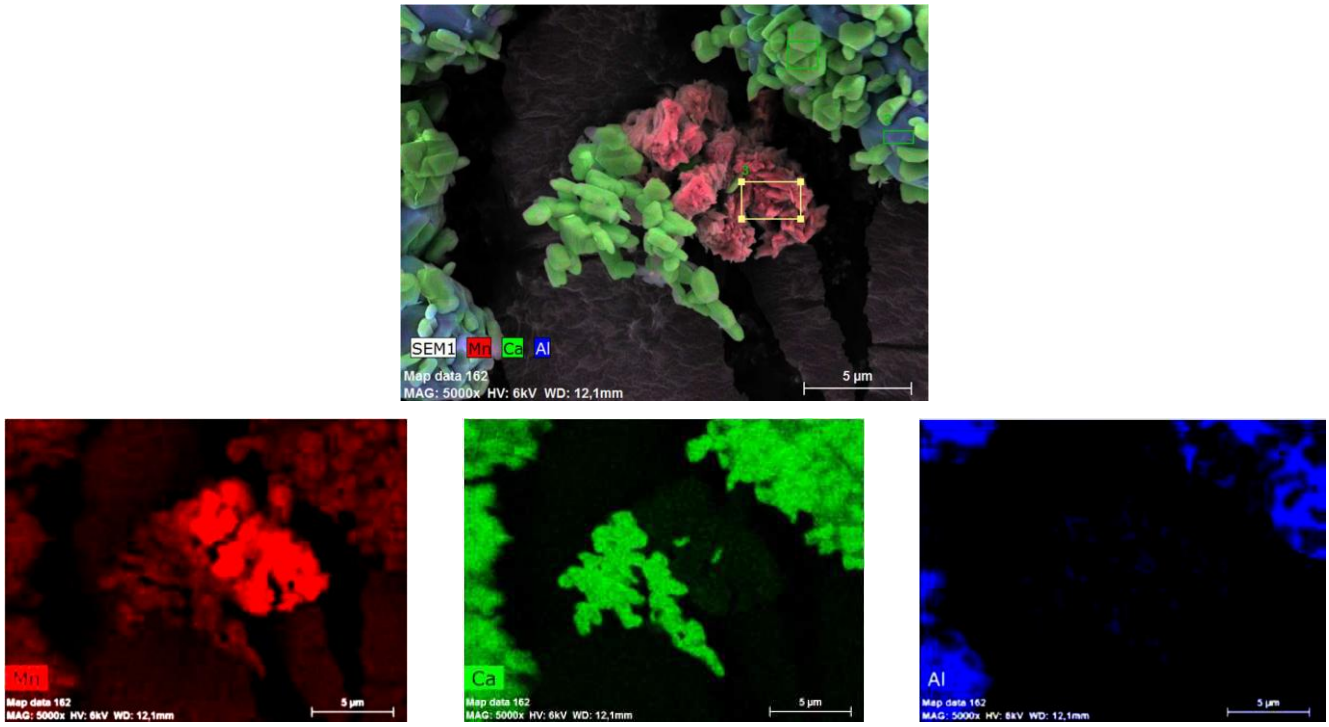

1.

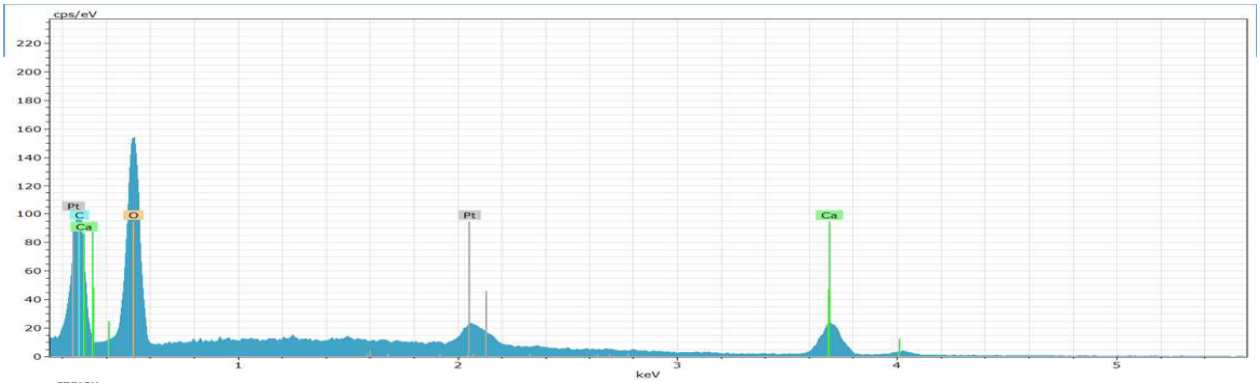

3.

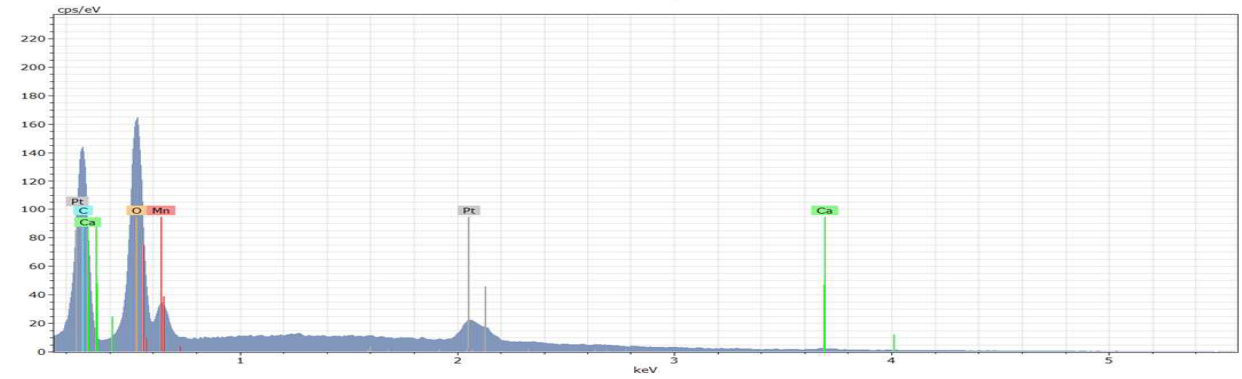

Figure 169: *Ca/Mn(II)* 8.3 mole% - Inert

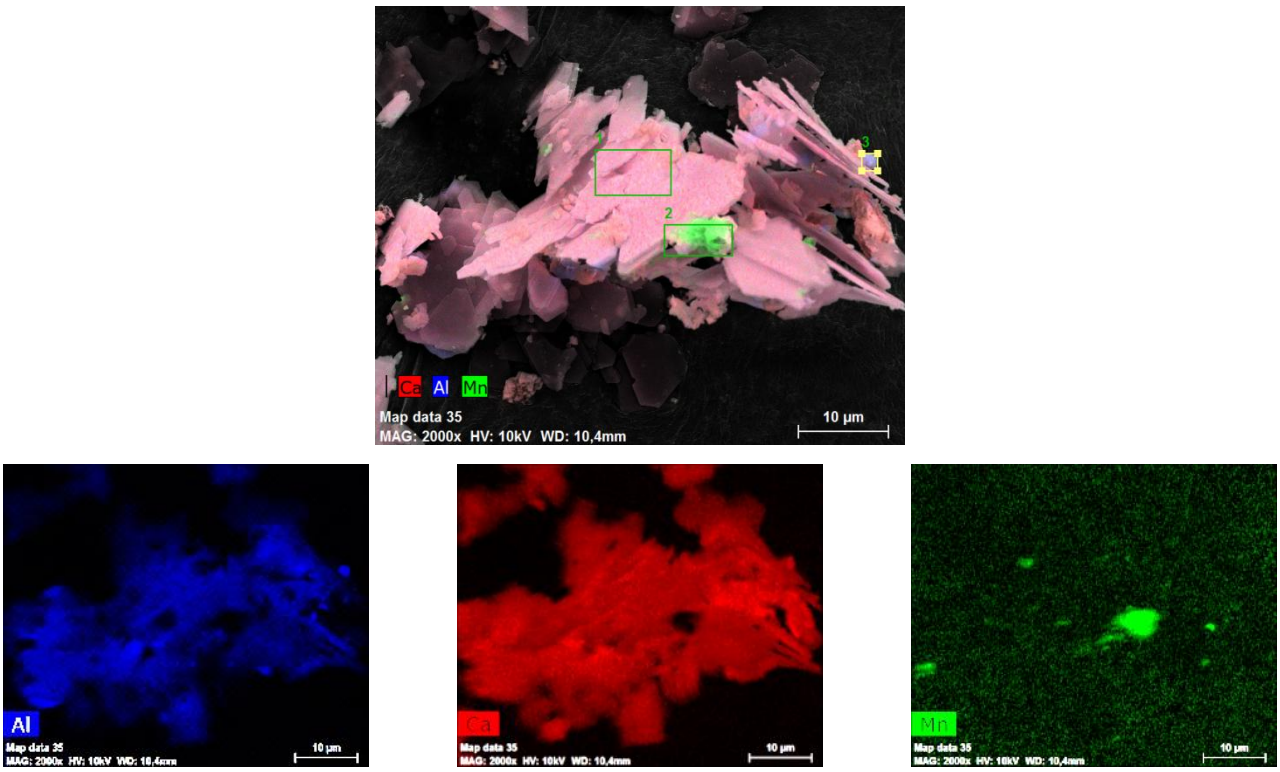

1.

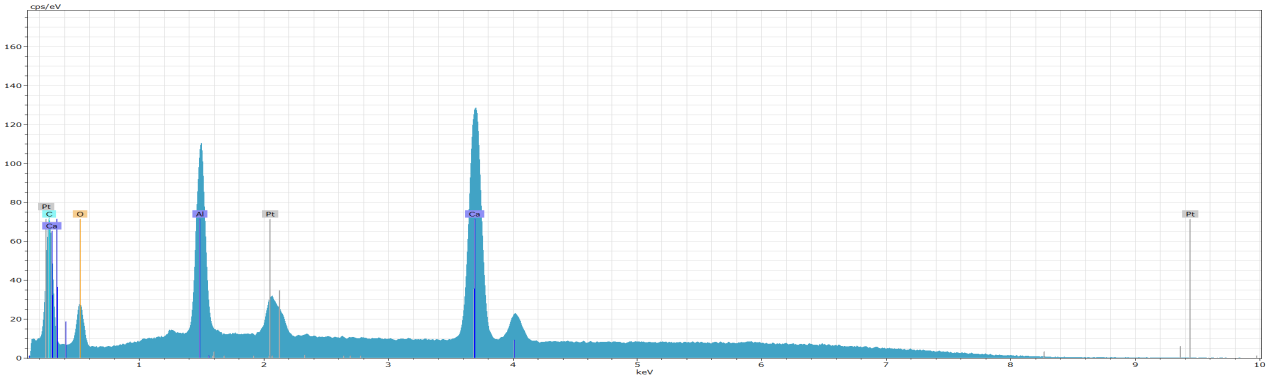

2.

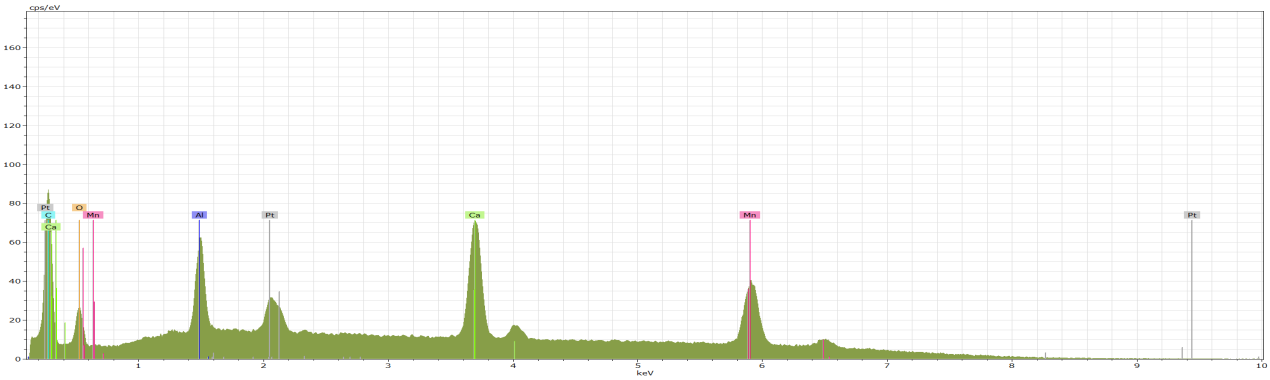

Figure 170: *Ca/Mn(II)* 8.3 mole% - Carbonate

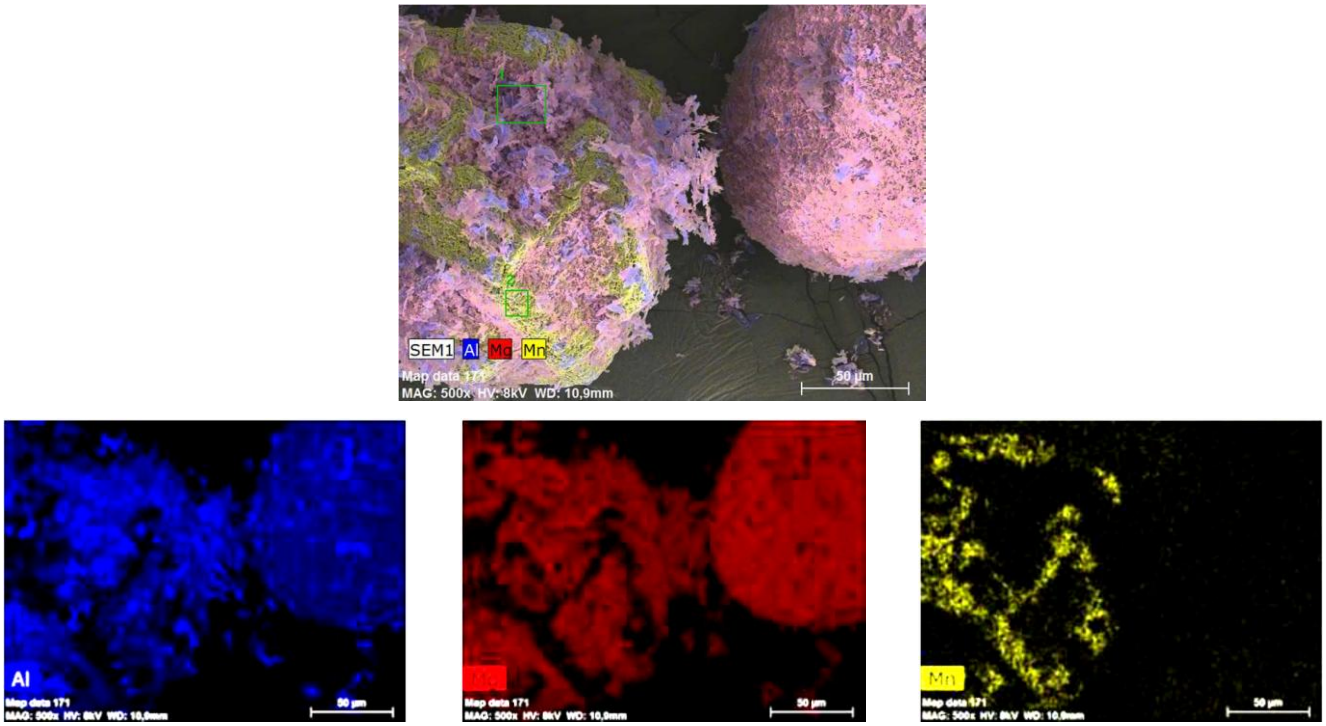

1.

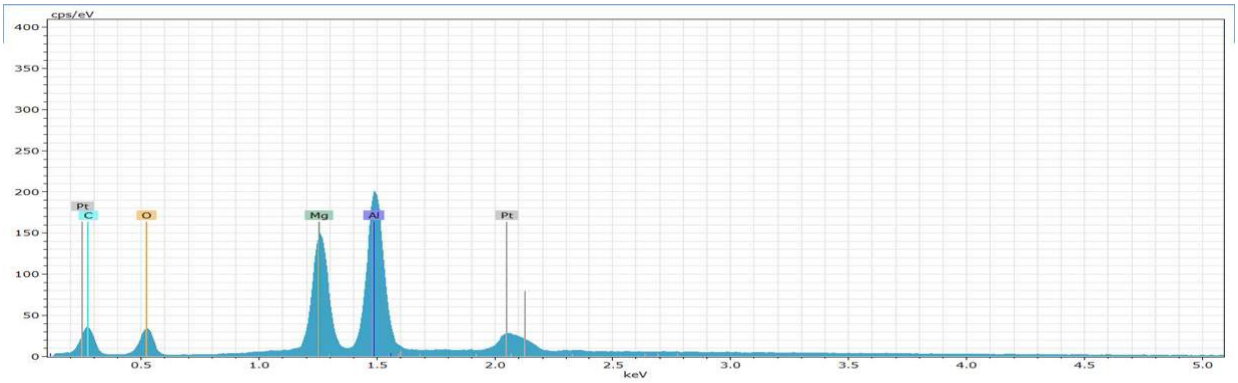

2.

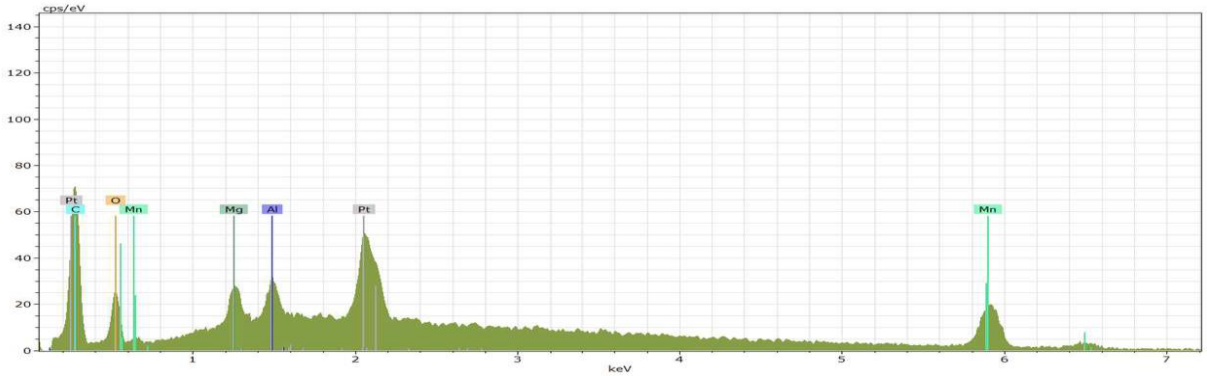

Figure 171: *Mg/Mn(II)* 25 mole% - Carbonate

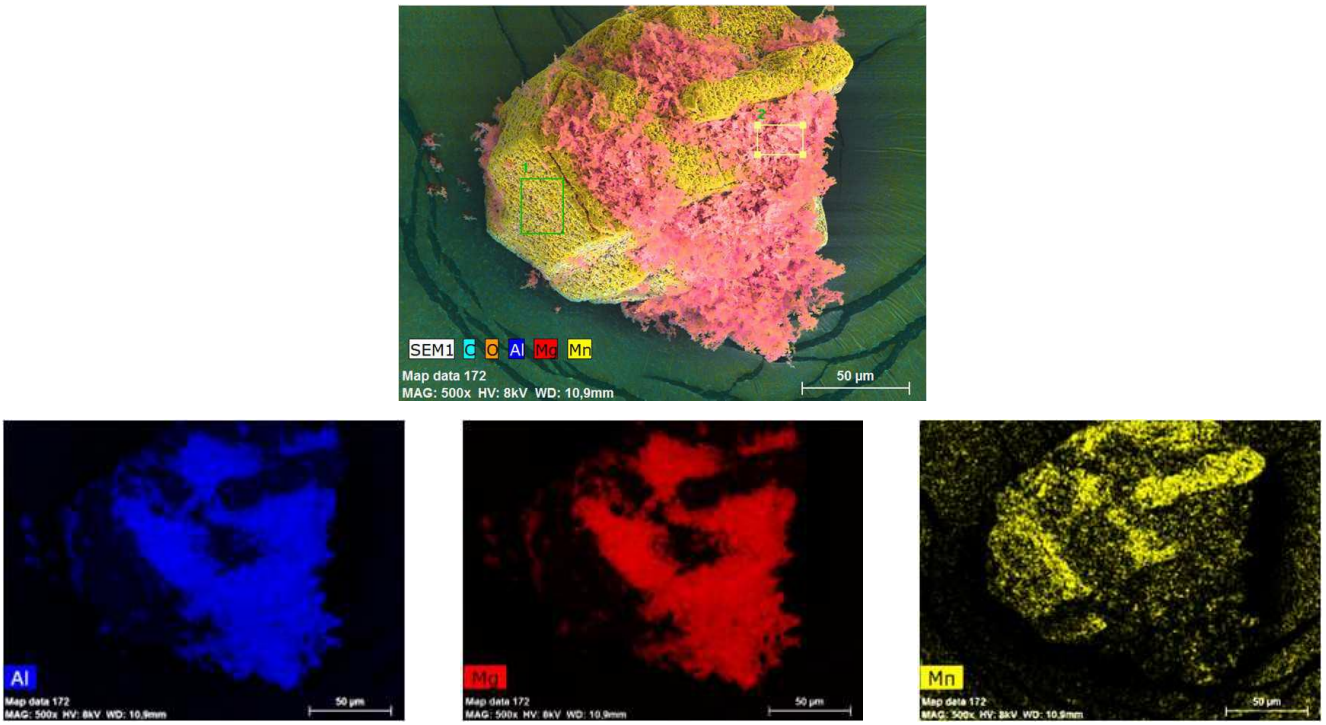

1.

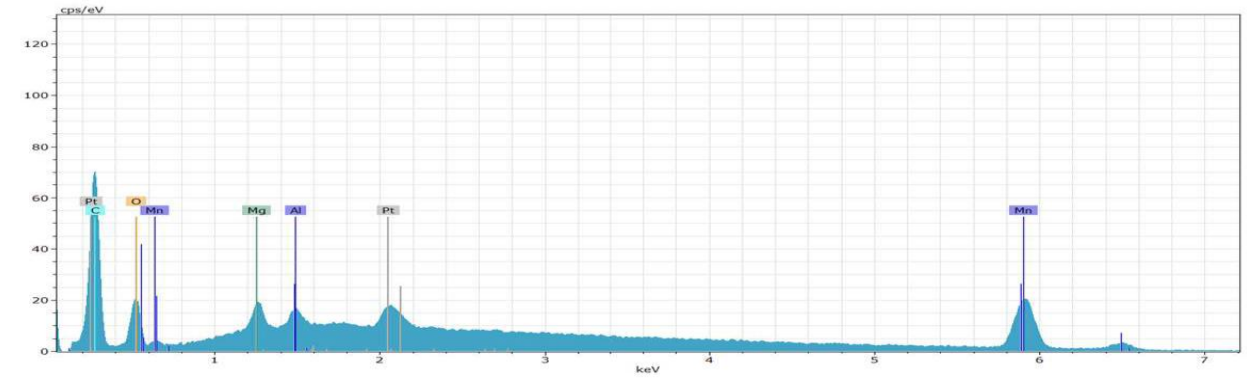

2.

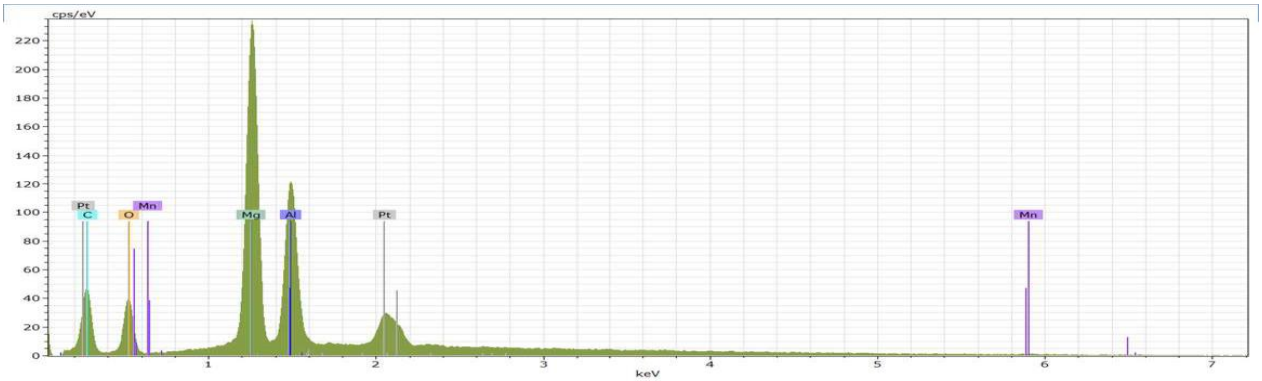

Figure 172: *Mg/Mn(II)* 8.3 mole% - Carbonate

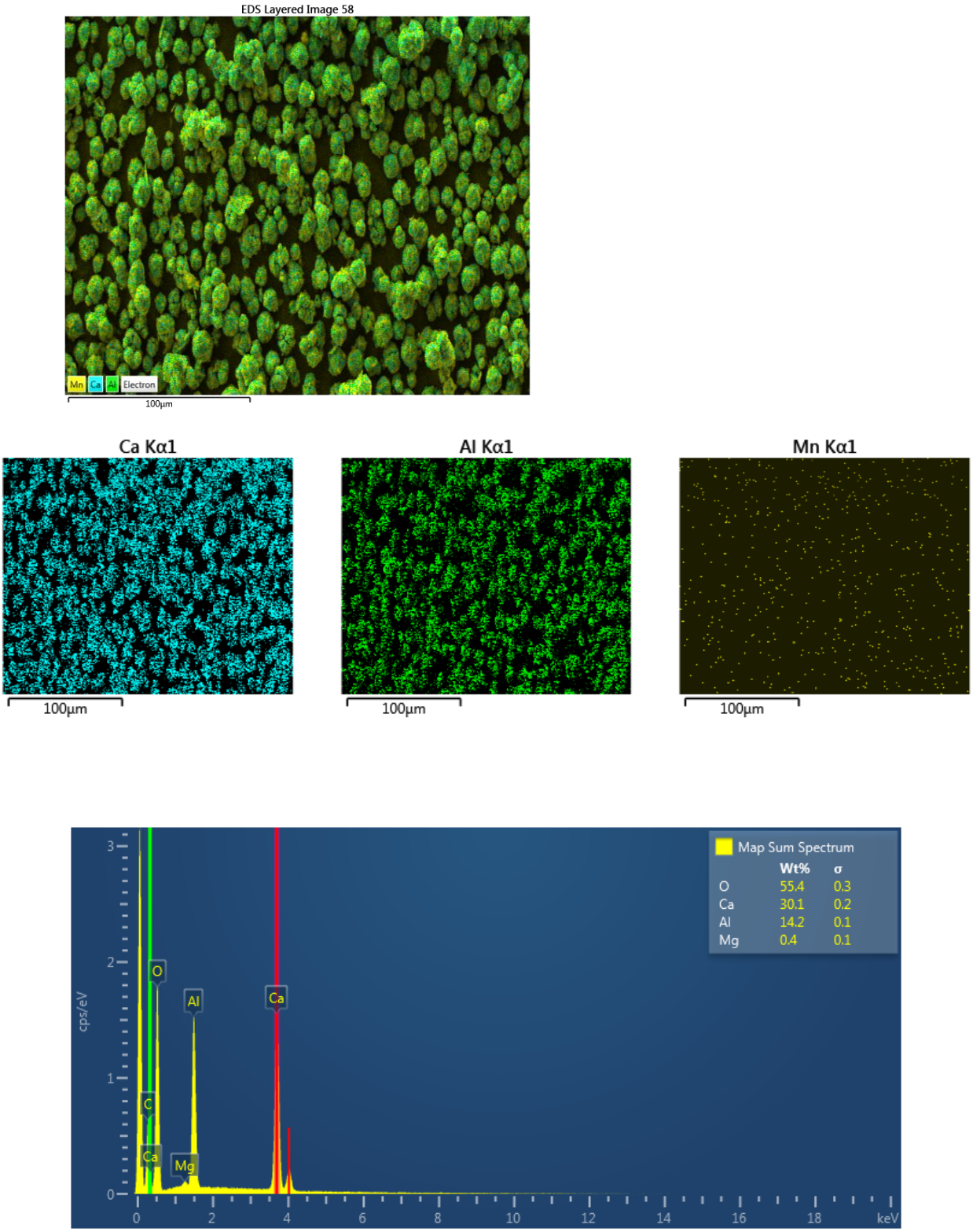

Figure 173: *Ca/Mn(IV)* 25 mole% - Inert

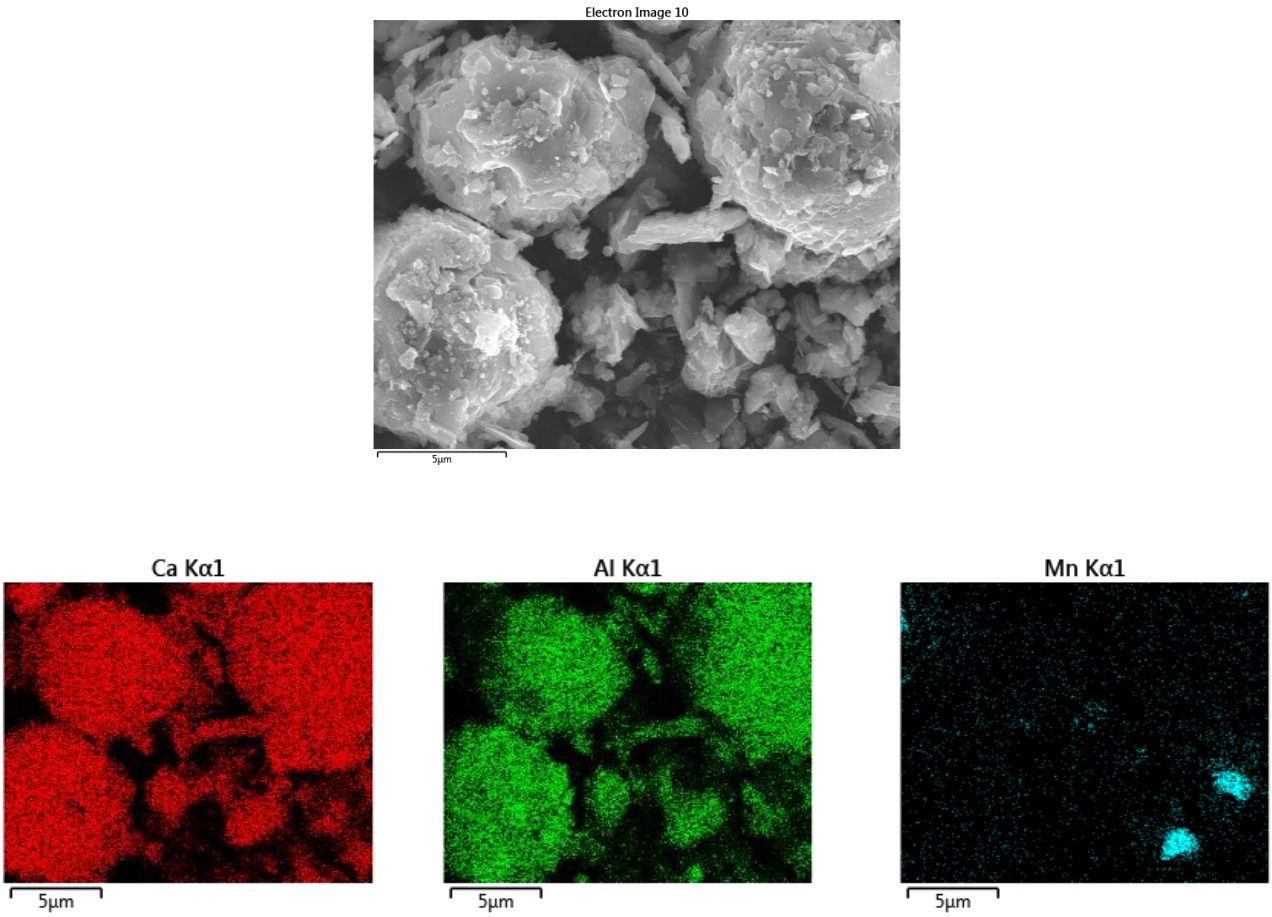

Figure 174: *Ca/Mn(IV)* 25 mole% - Carbonate

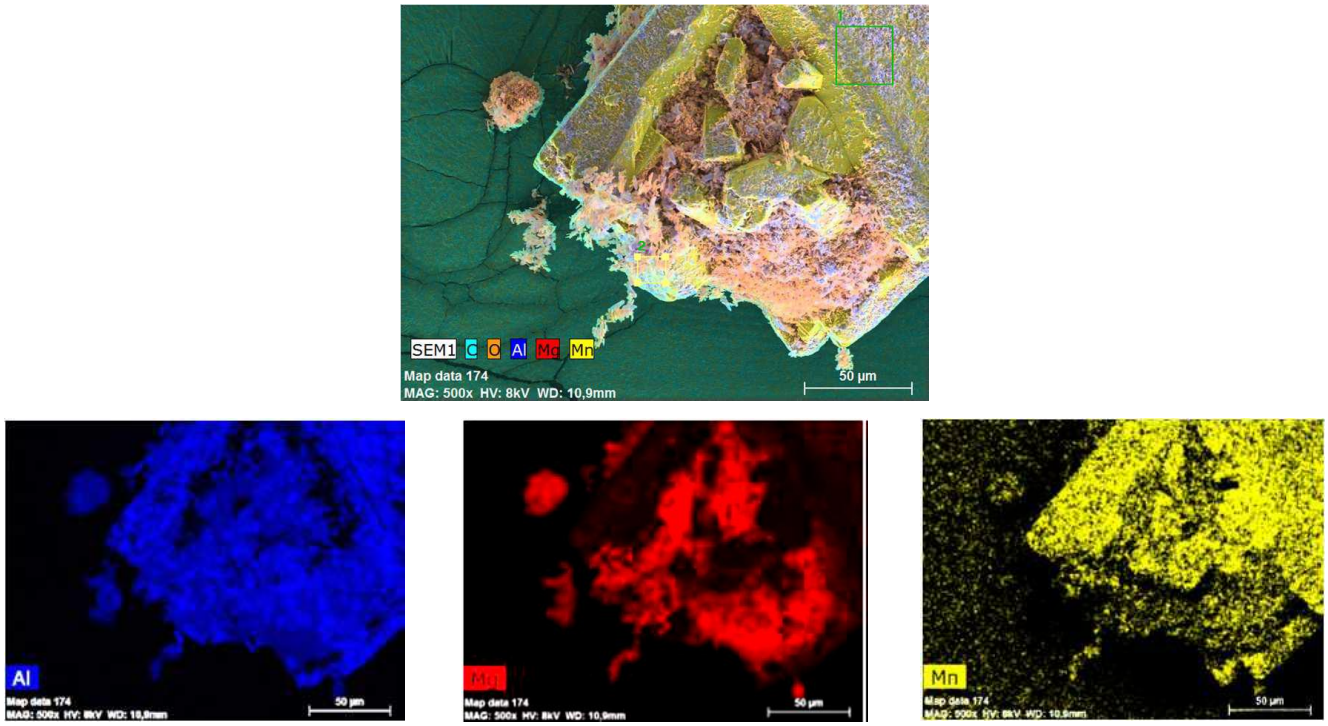

1.

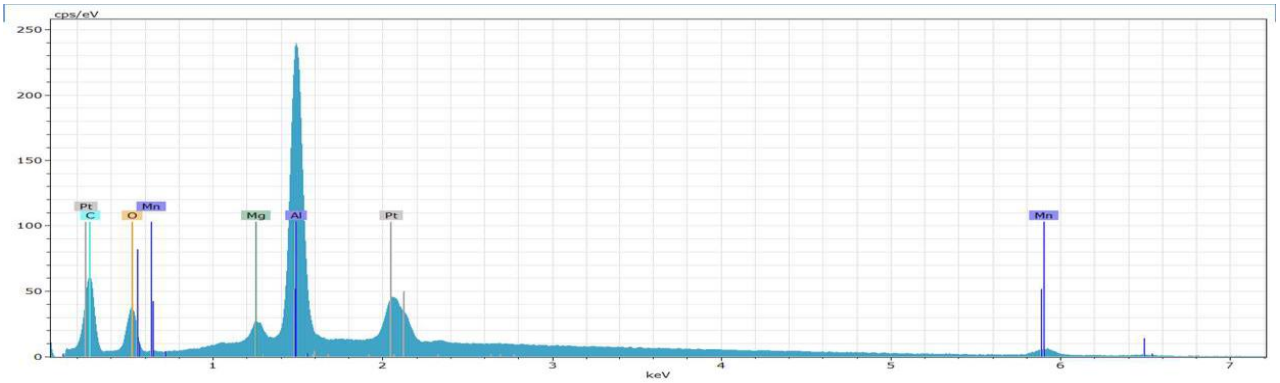

2.

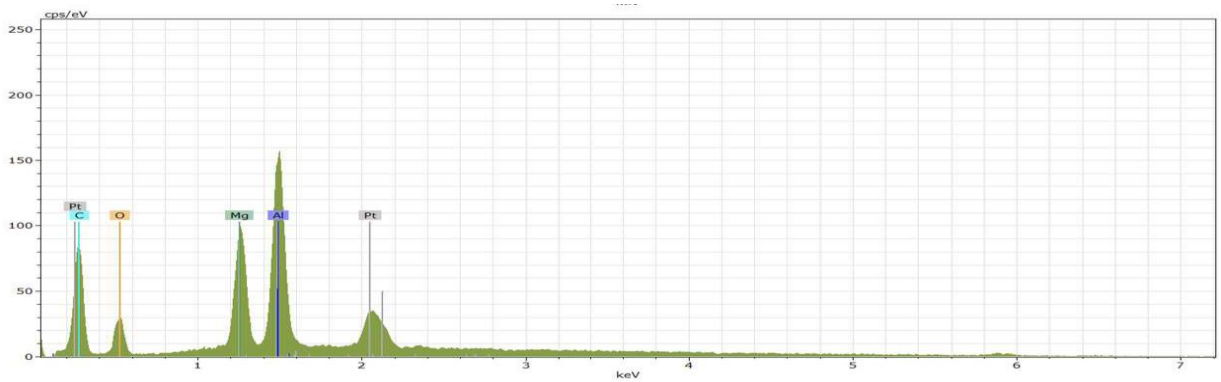

Figure 175: *Mg/Mn(IV)* 25 mole% - Carbonate

Molybdenum

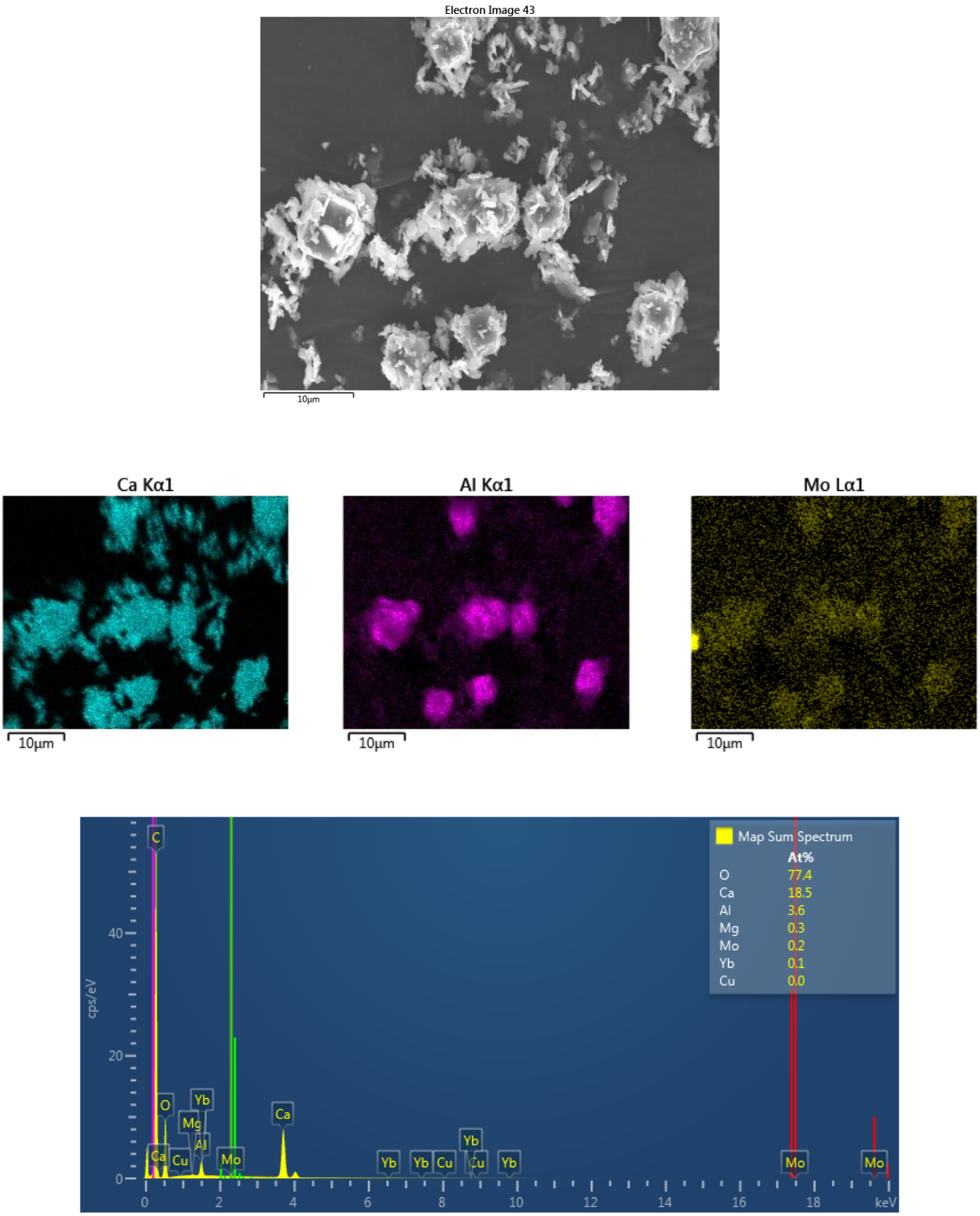

Figure 176: *Ca/Mo* 25 mole% - Inert

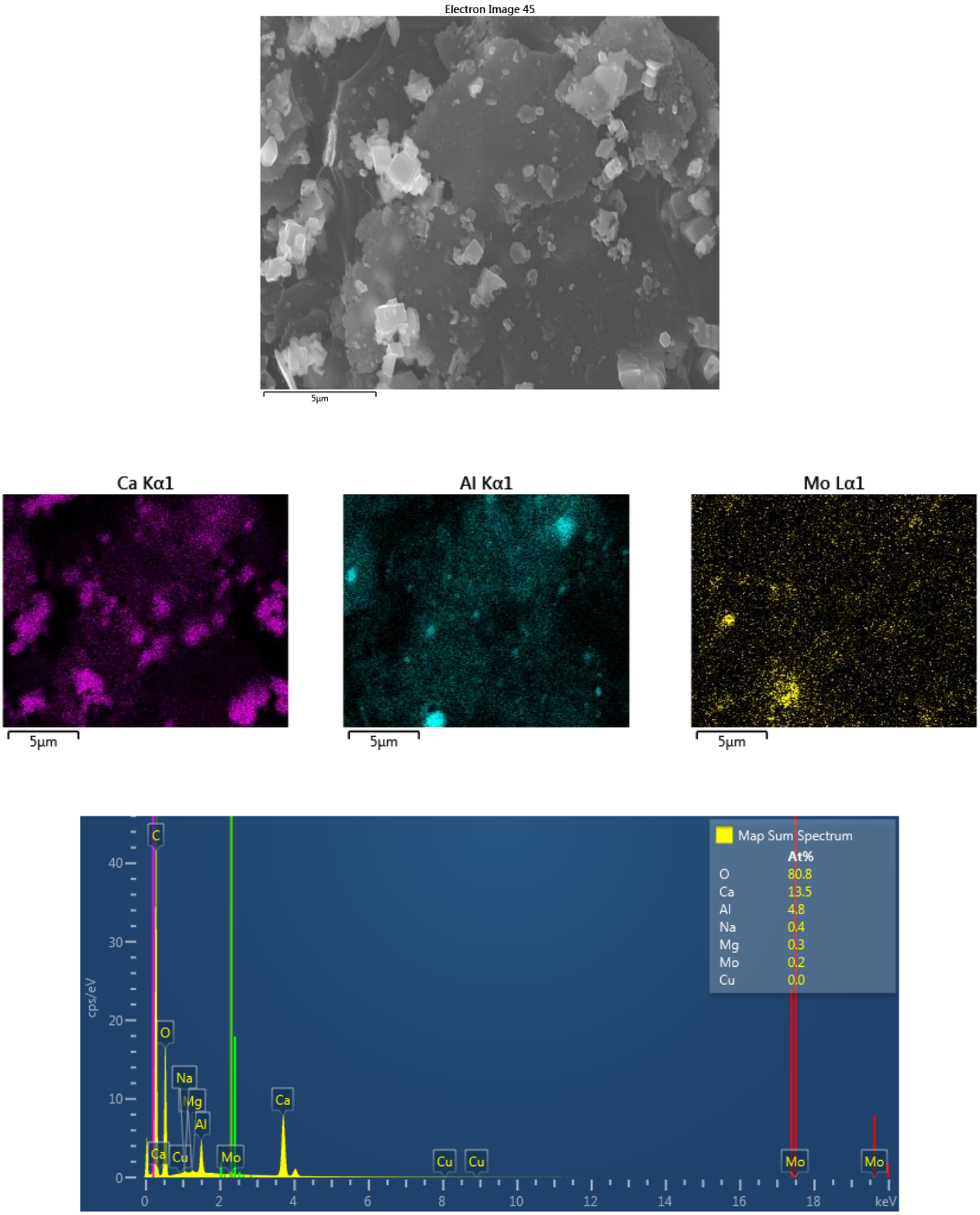

Figure 177: *Ca/Mo* 25 mole% - Carbonate

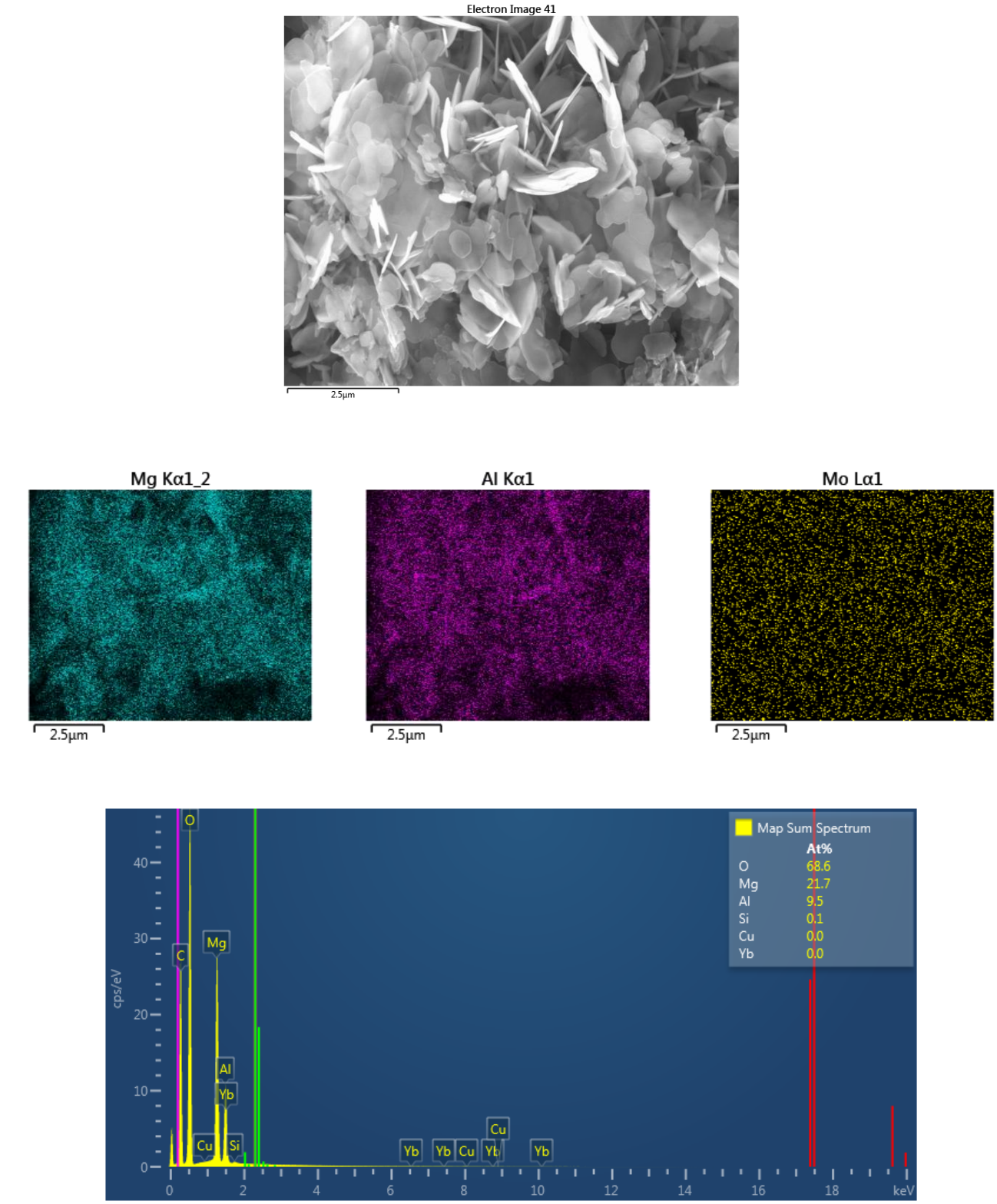

Figure 178: *Mg/Mo* 25 mole% - Carbonate

Nickel

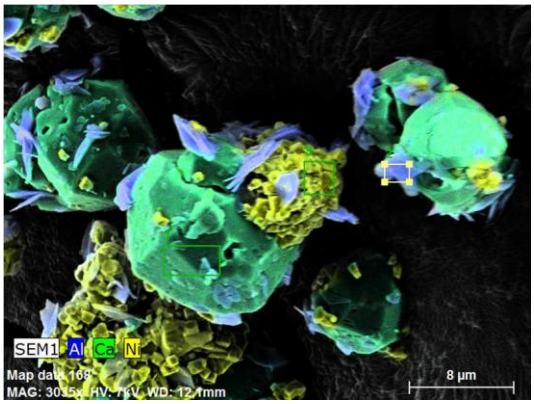

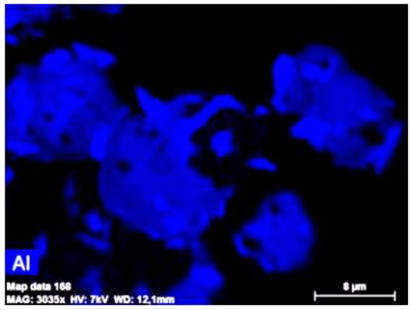

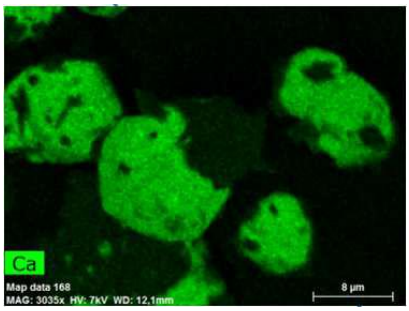

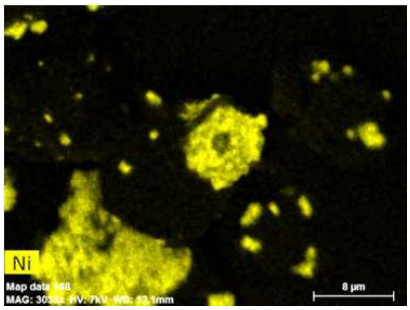

1.

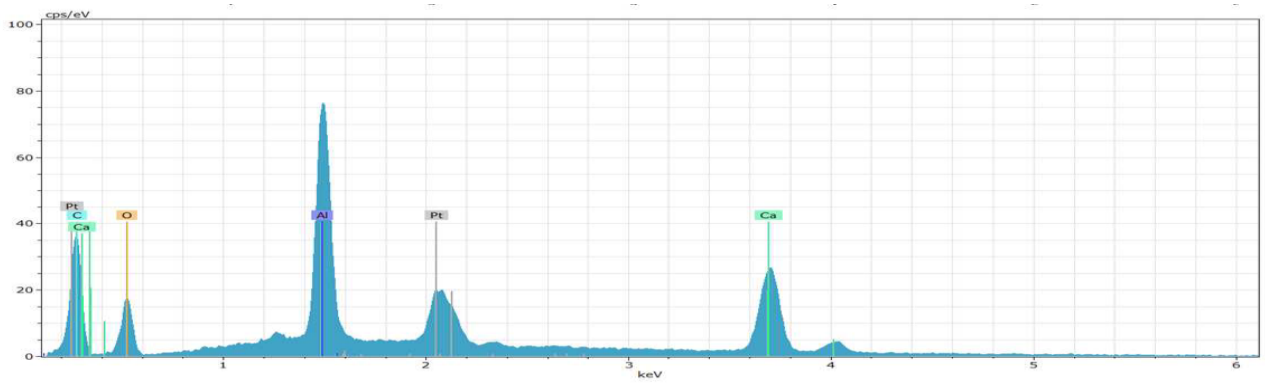

3.

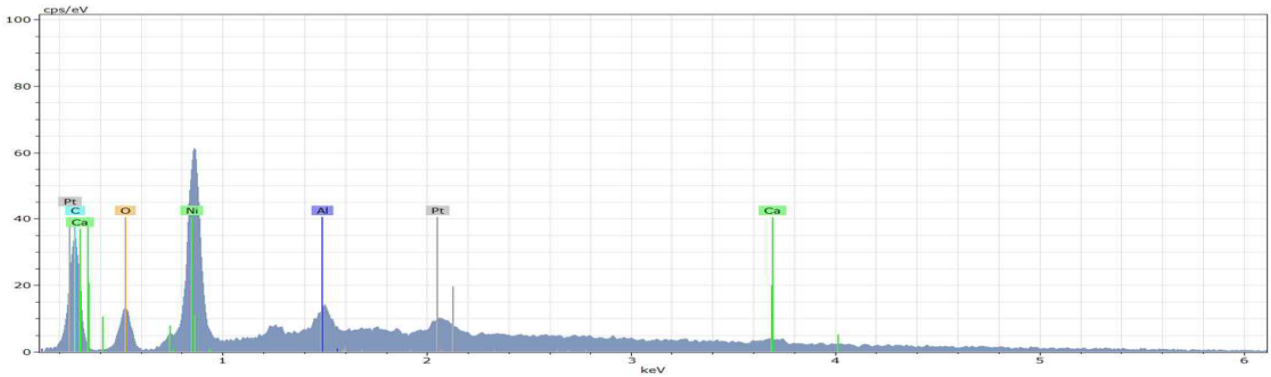

Figure 179: *Ca/Ni* 25 mole% - Inert

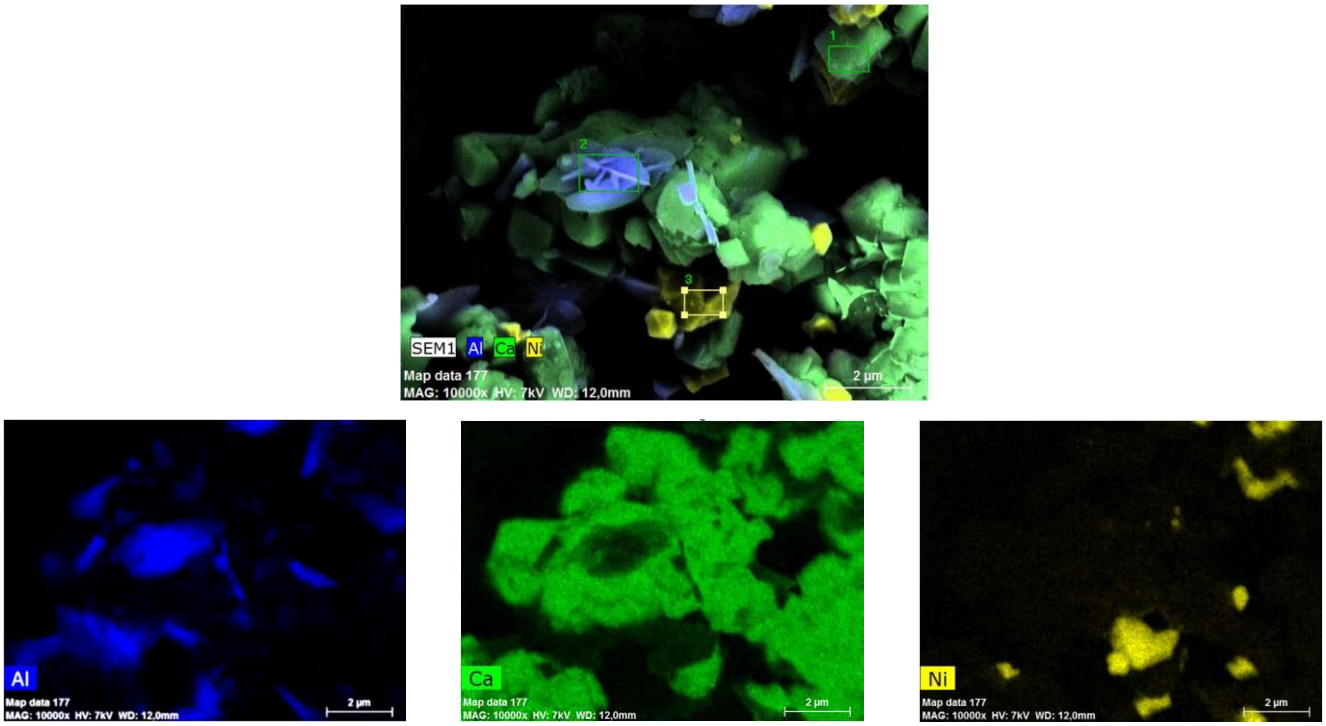

1.

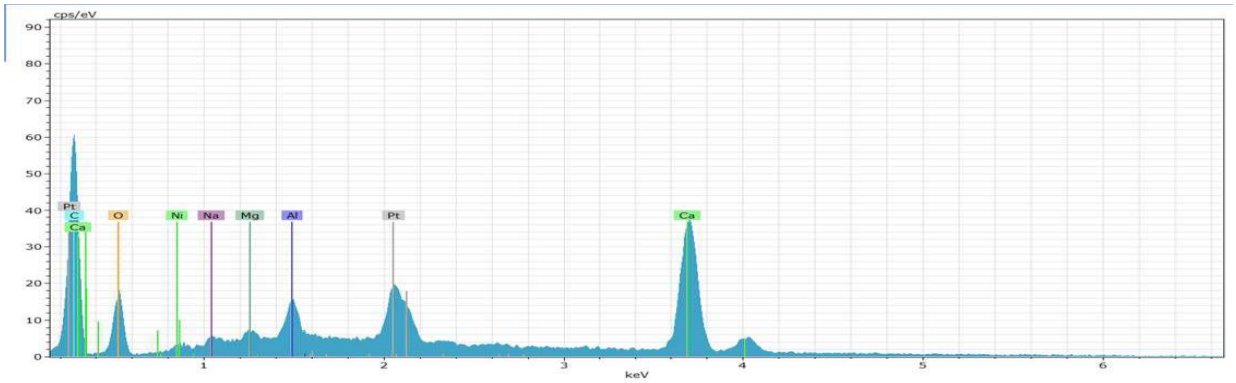

2.

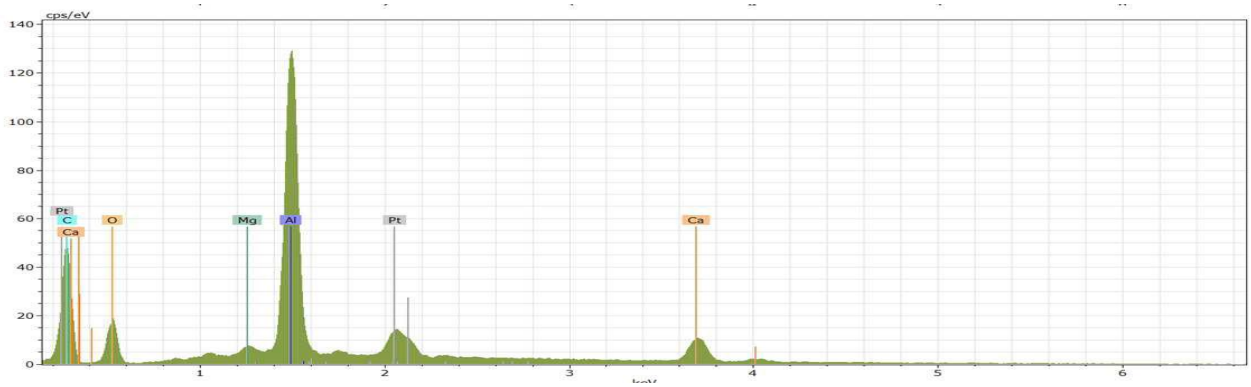

Figure 180: *Ca/Ni* 25 mole% - Carbonate

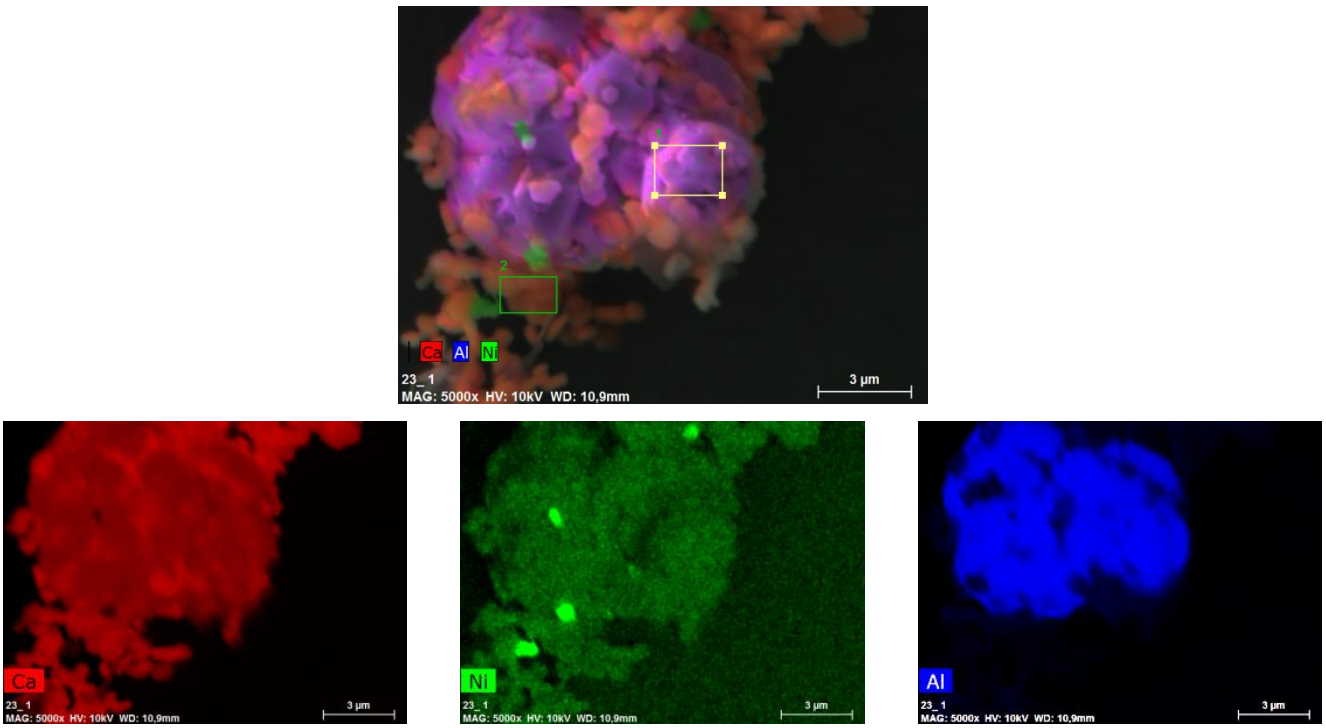

1.

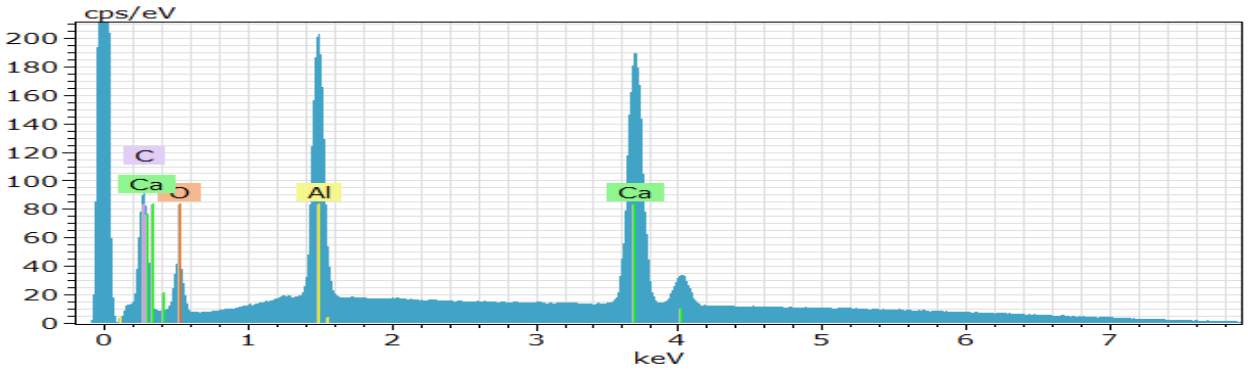

2.

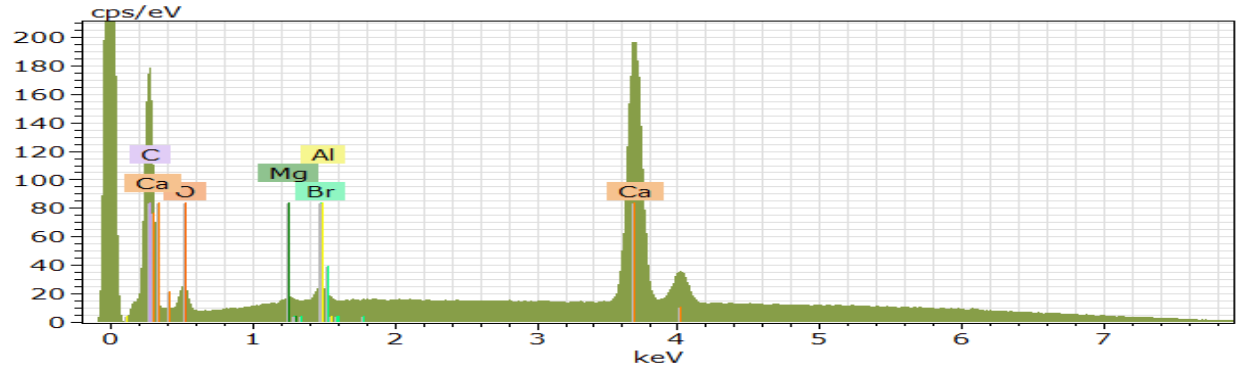

Figure 181: *Ca/Ni* 8.3 mole% - Inert

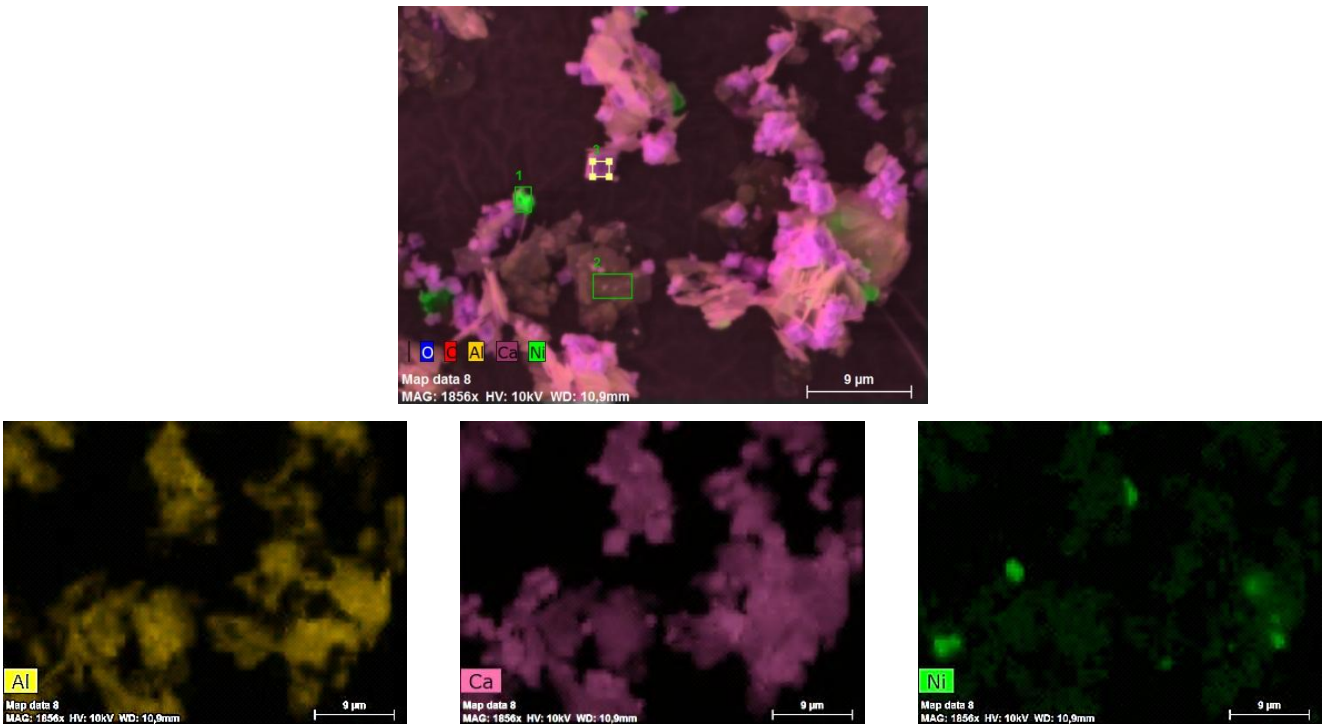

1.

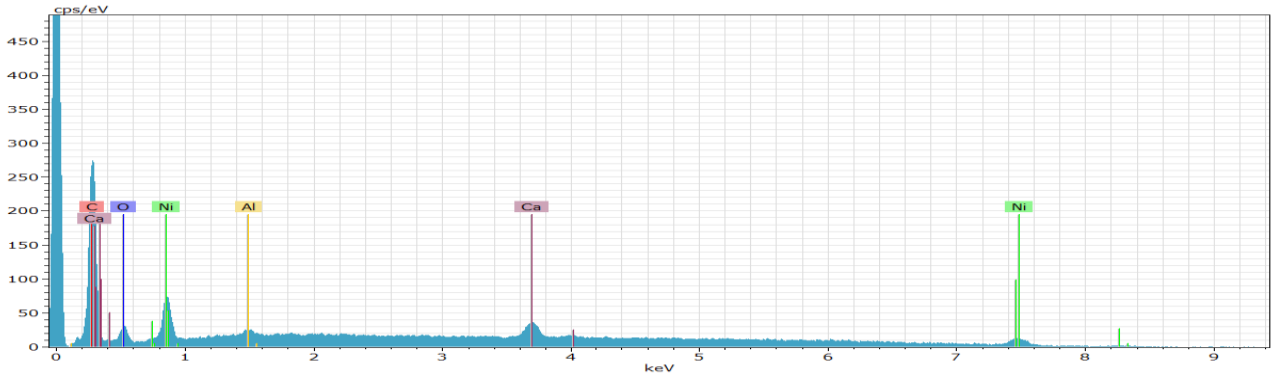

2.

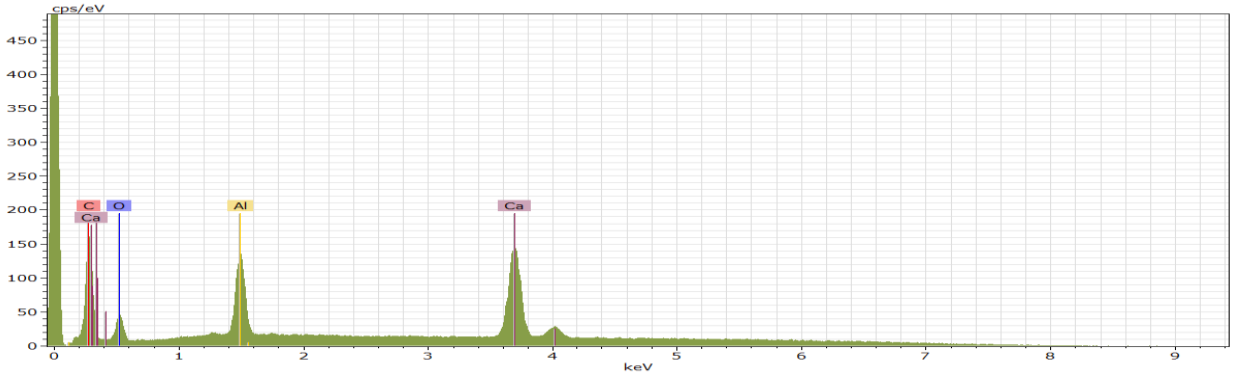

Figure 182: *Ca/Ni* 8.3 mole% - Carbonate

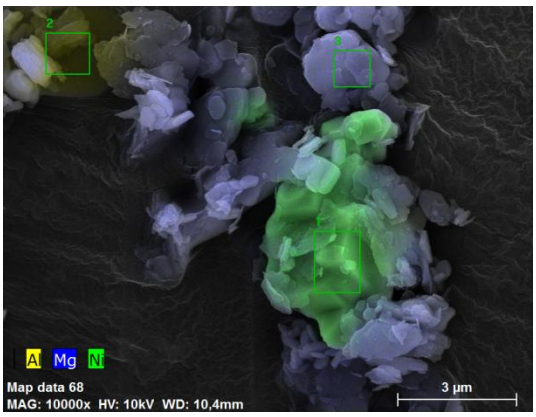

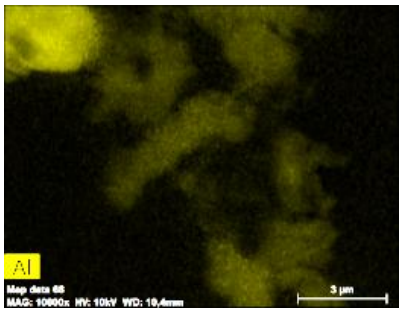

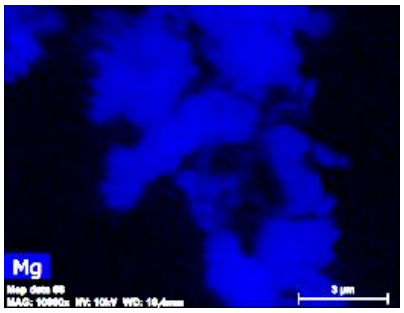

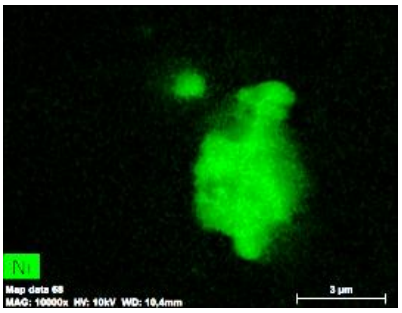

1.

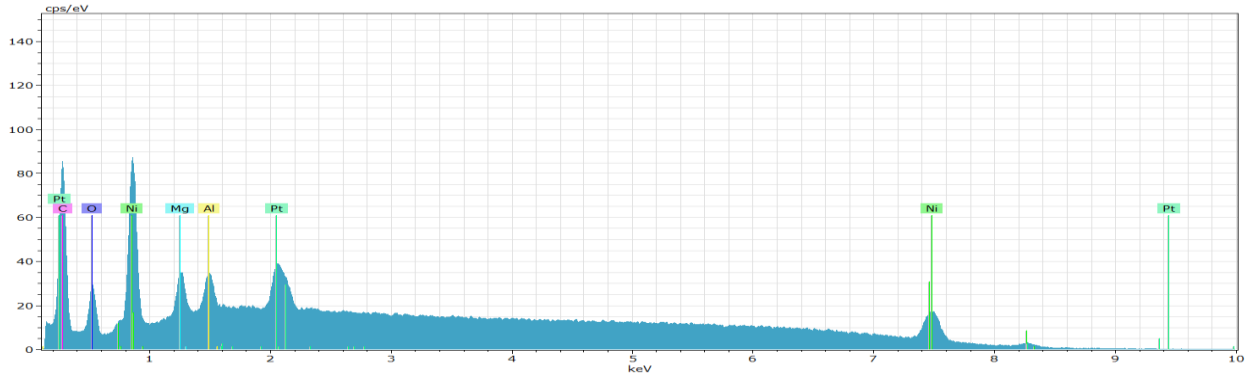

3.

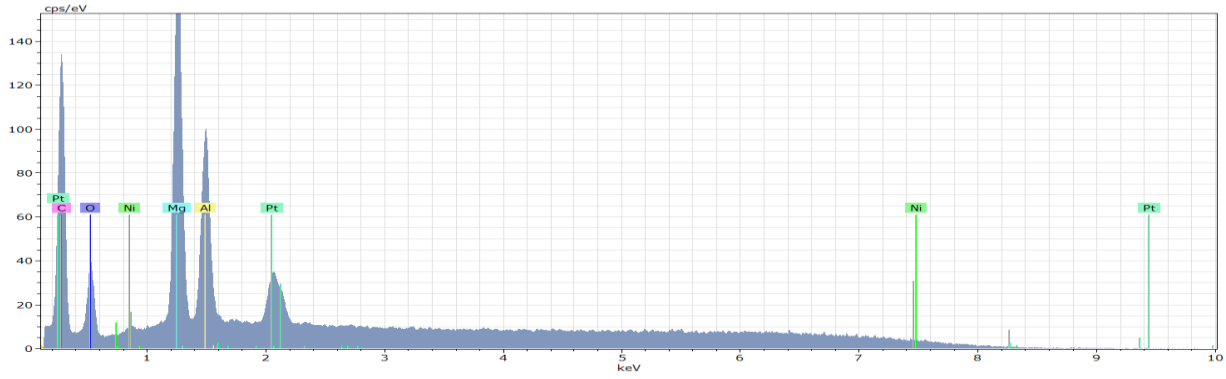

Figure 183: *Mg/Ni* 25 mole% - Carbonate

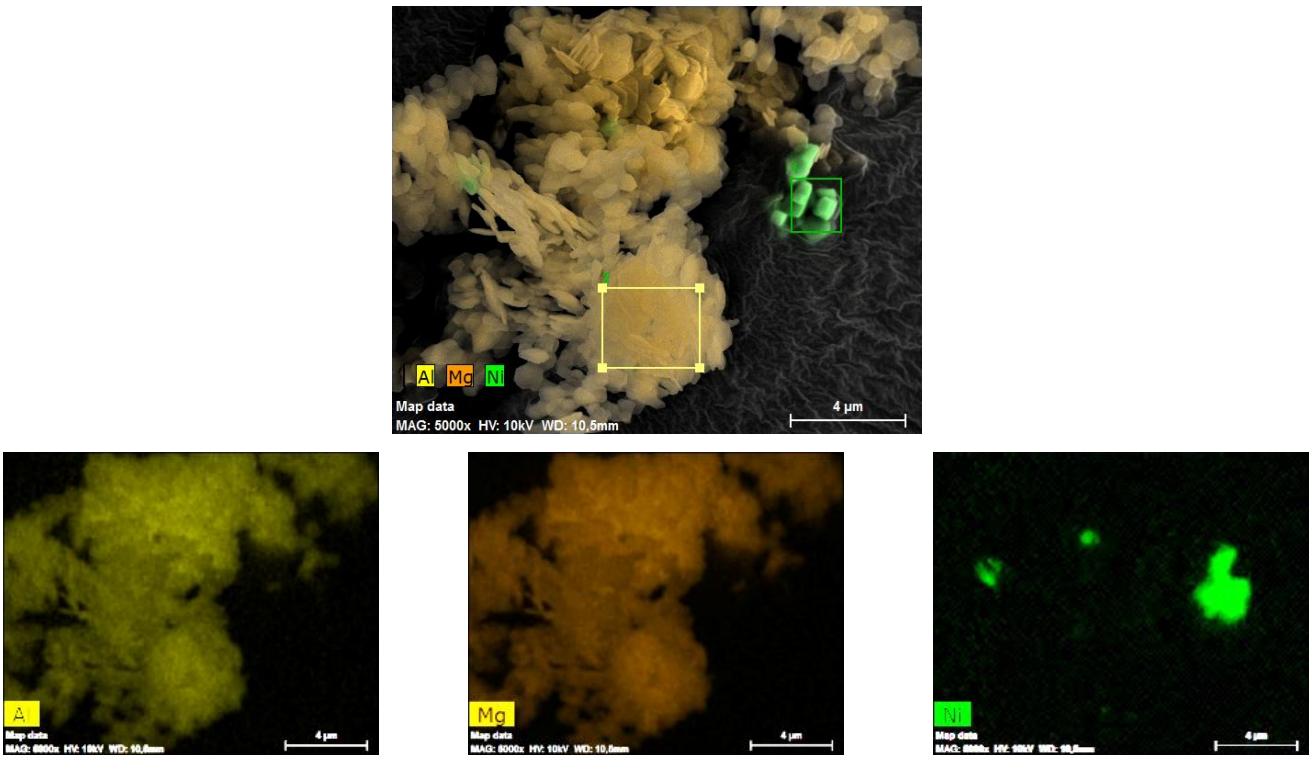

1.

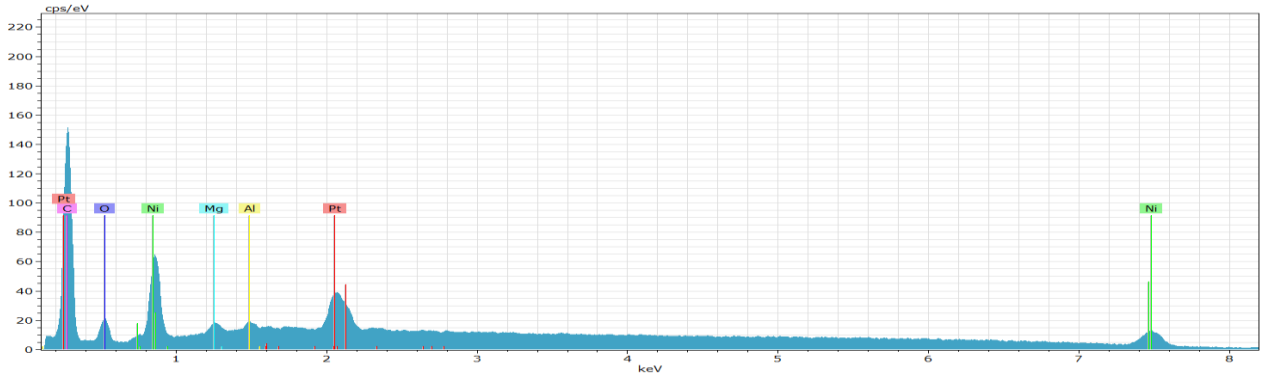

2.

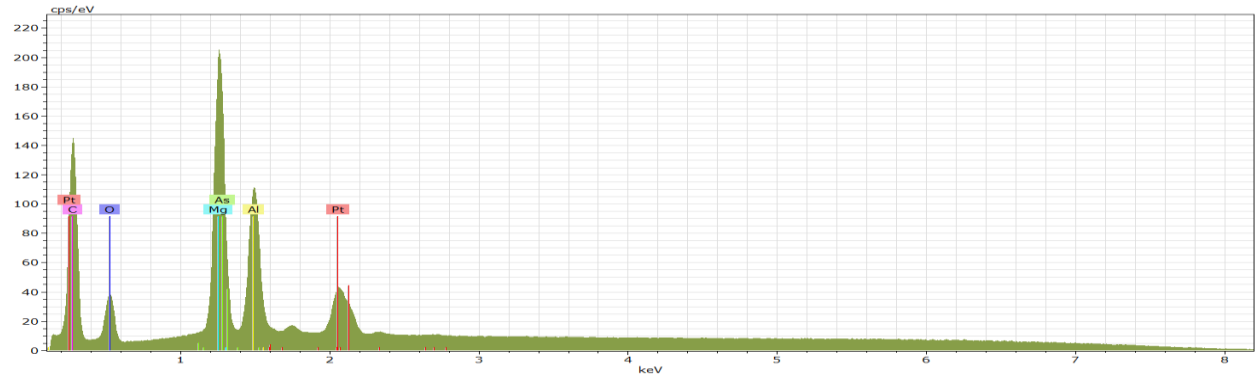

Figure 184: *Mg/Ni* 8.3 mole% - Carbonate

Tin

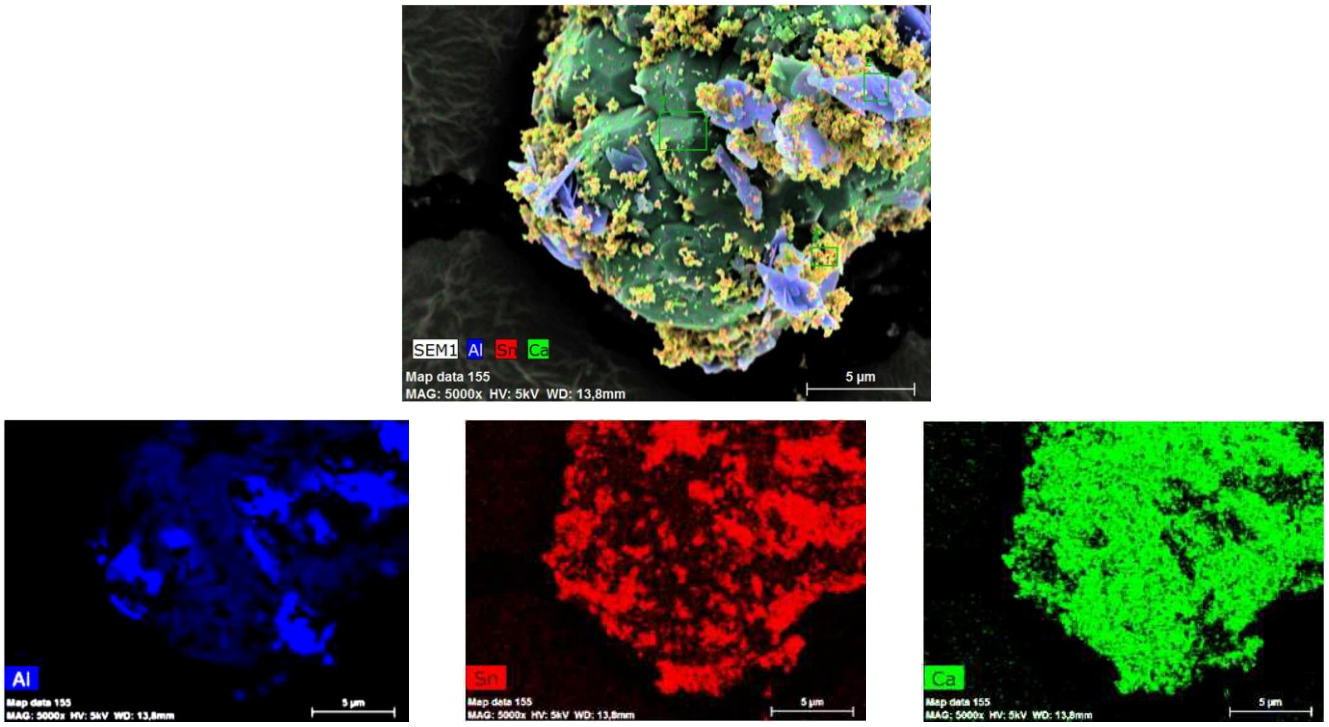

1.

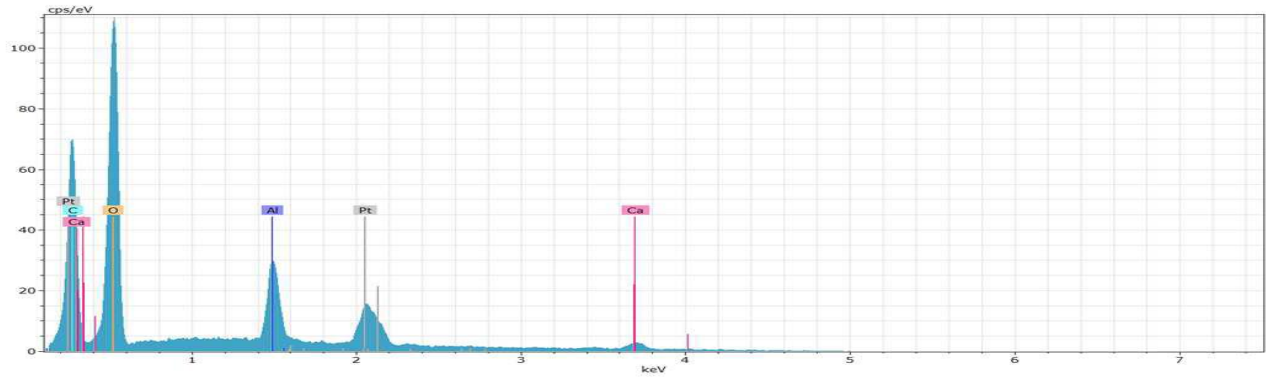

3.

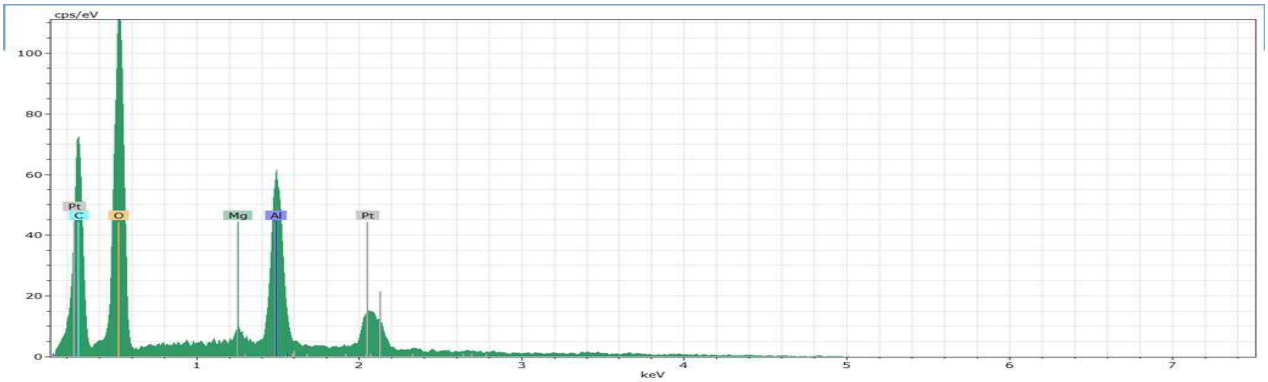

Figure 185: *Ca/Sn* 25 mole% - Inert

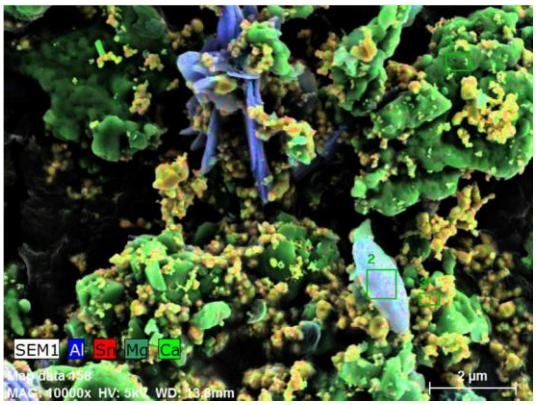

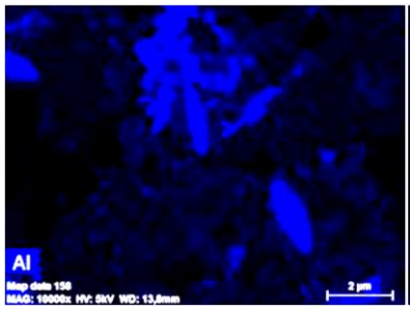

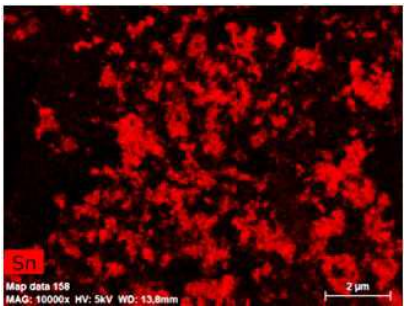

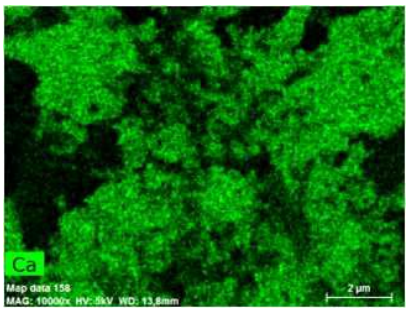

1.

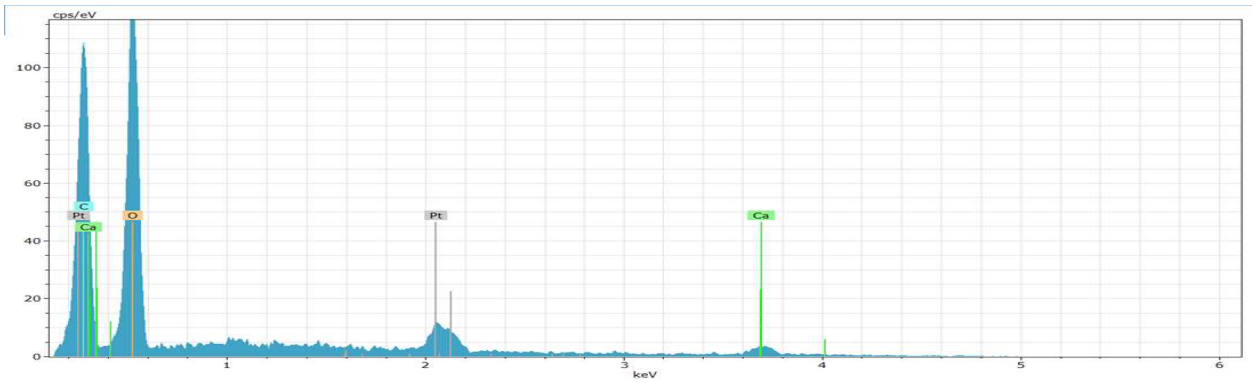

2.

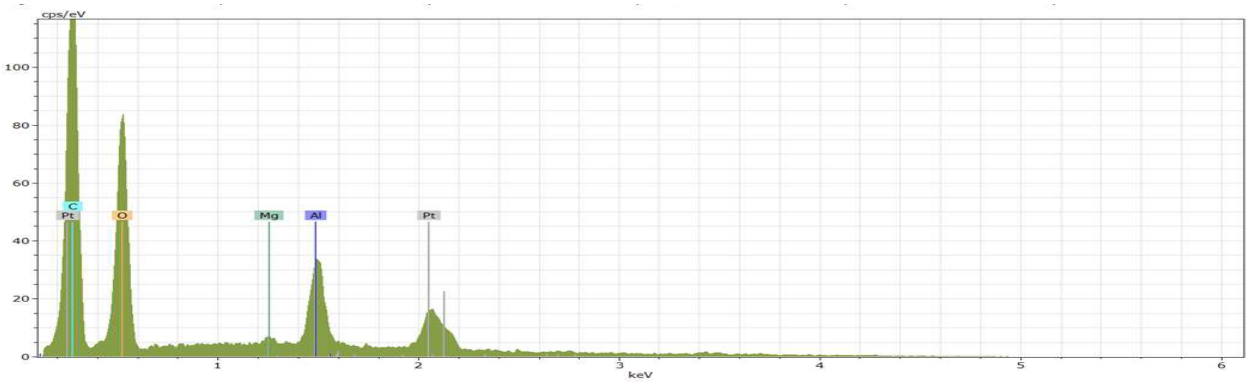

Figure 186: *Ca/Sn* 25 mole% - Carbonate

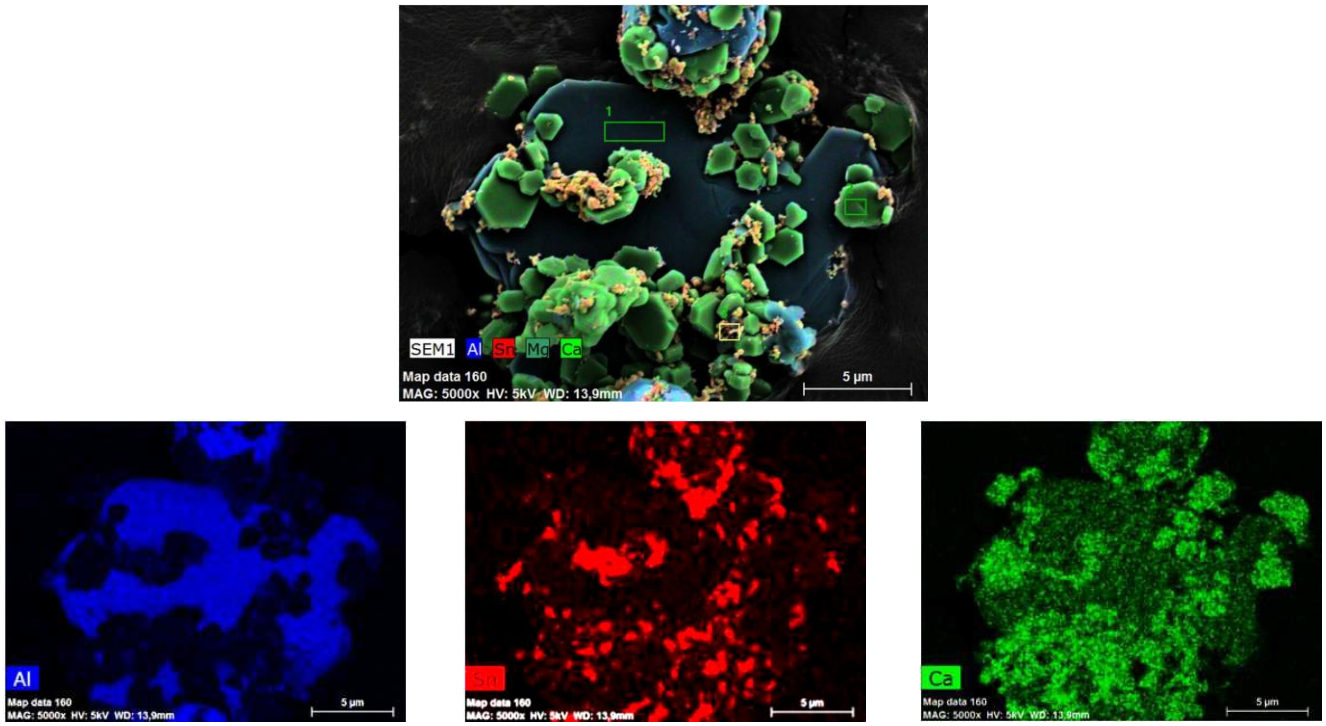

1.

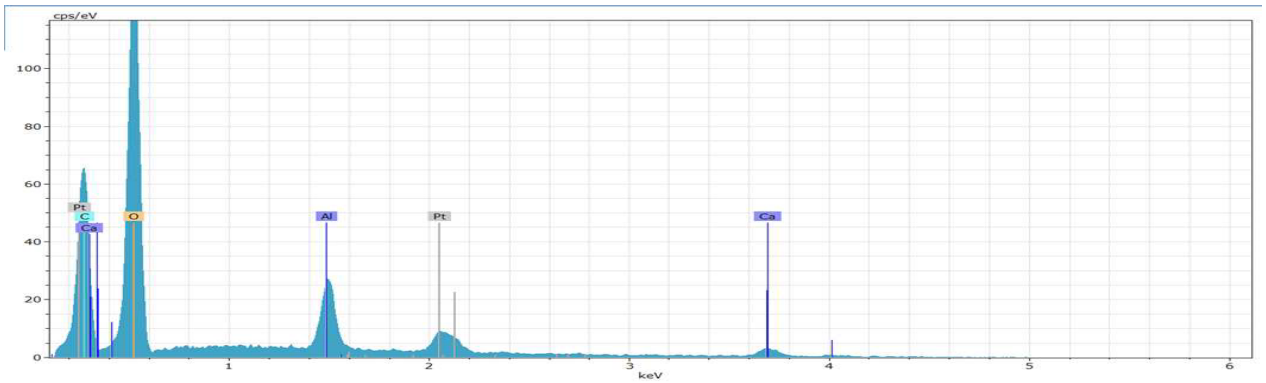

2.

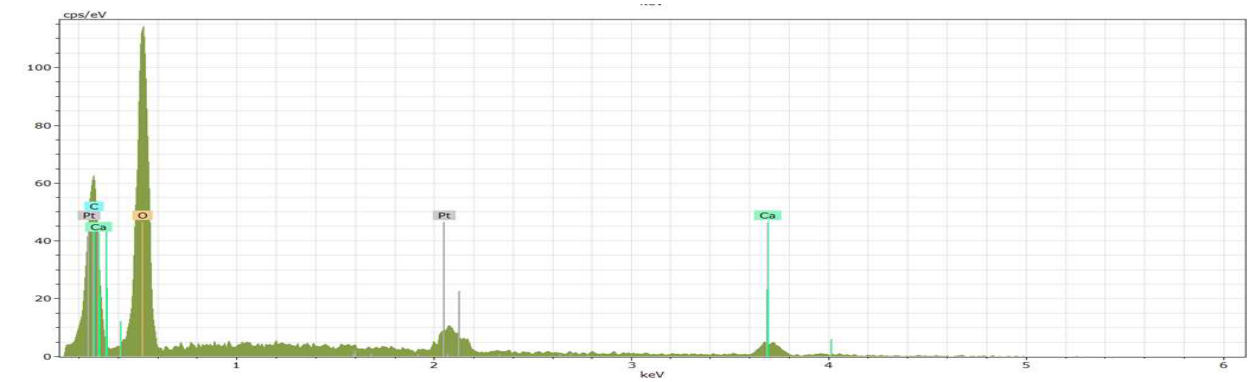

Figure 187: *Ca/Sn* 8.3 mole% - Inert

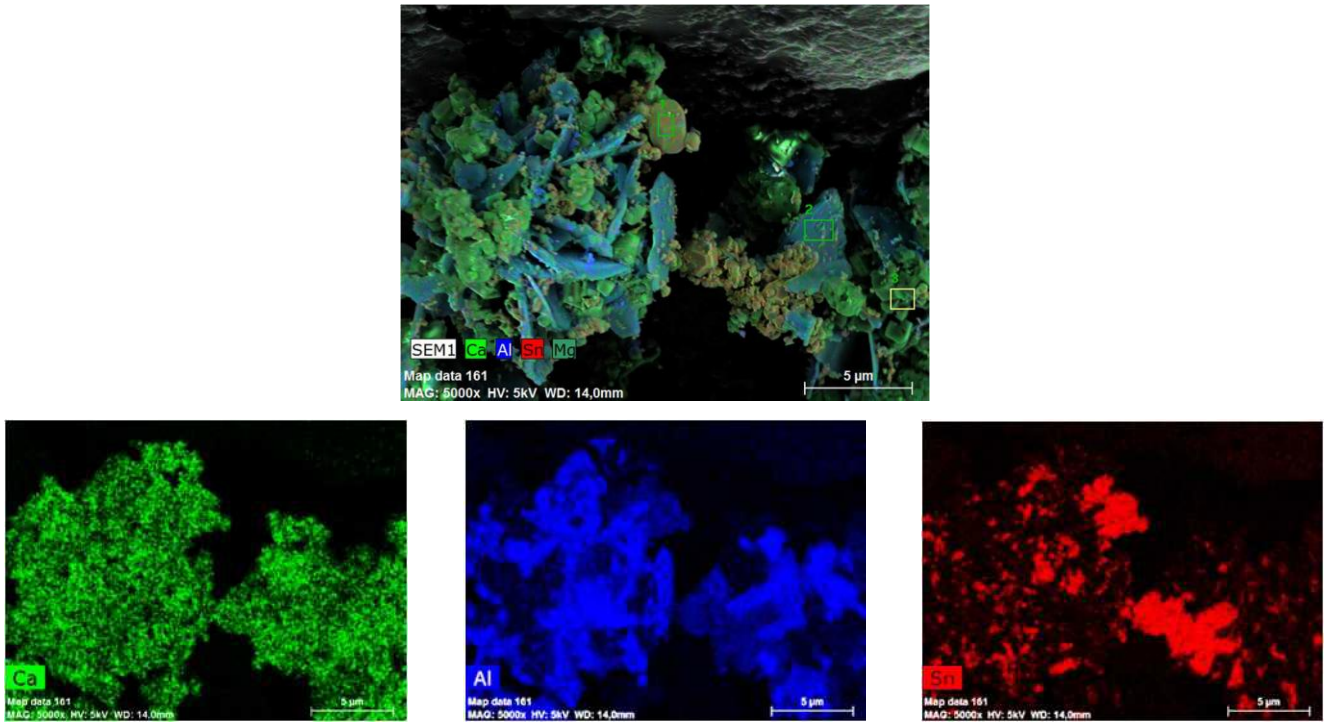

1.

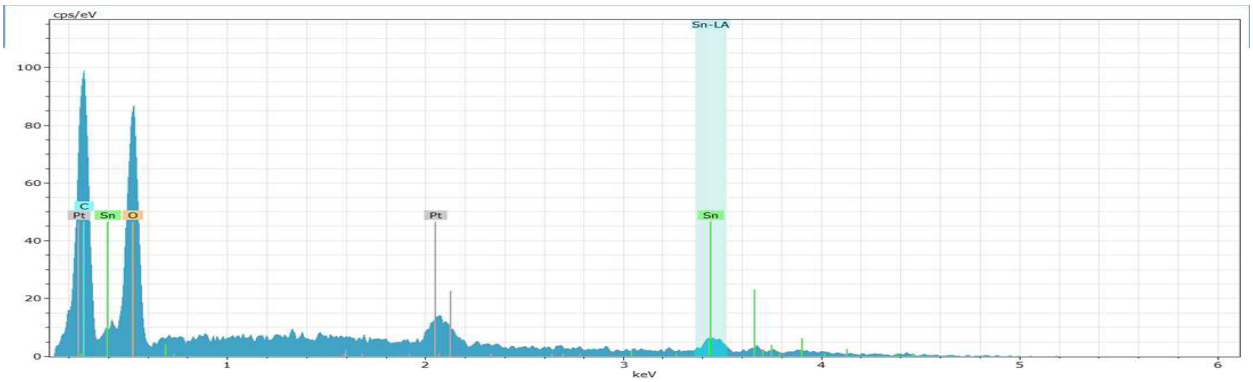

2.

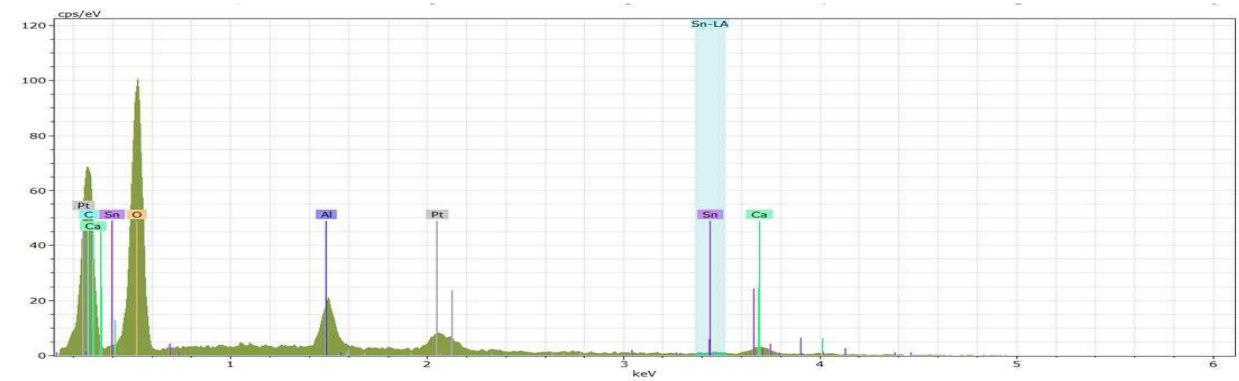

Figure 188: *Ca/Sn* 8.3 mole% - Carbonate

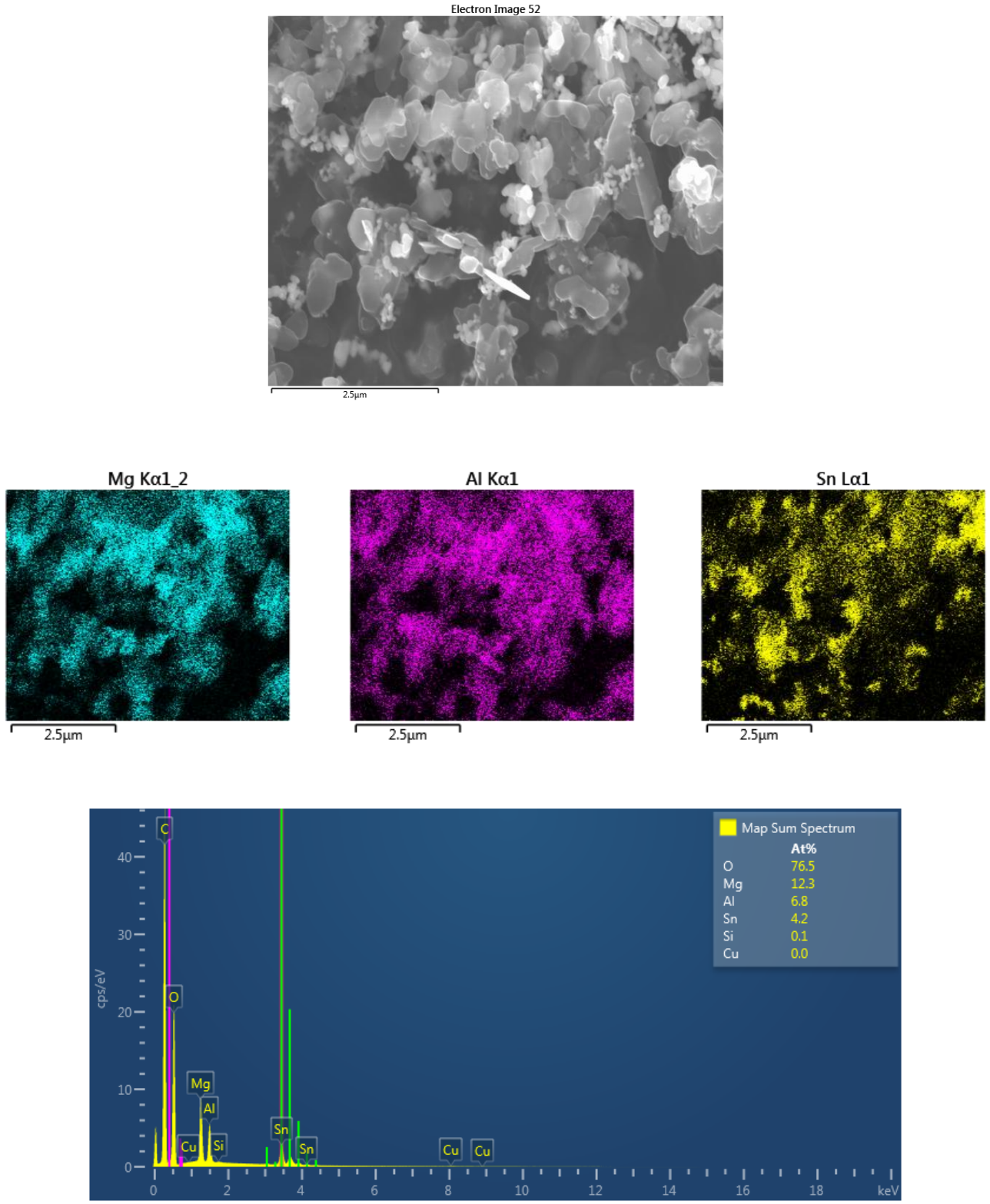

Figure 189: *Mg/Sn* 25 mole% - Inert

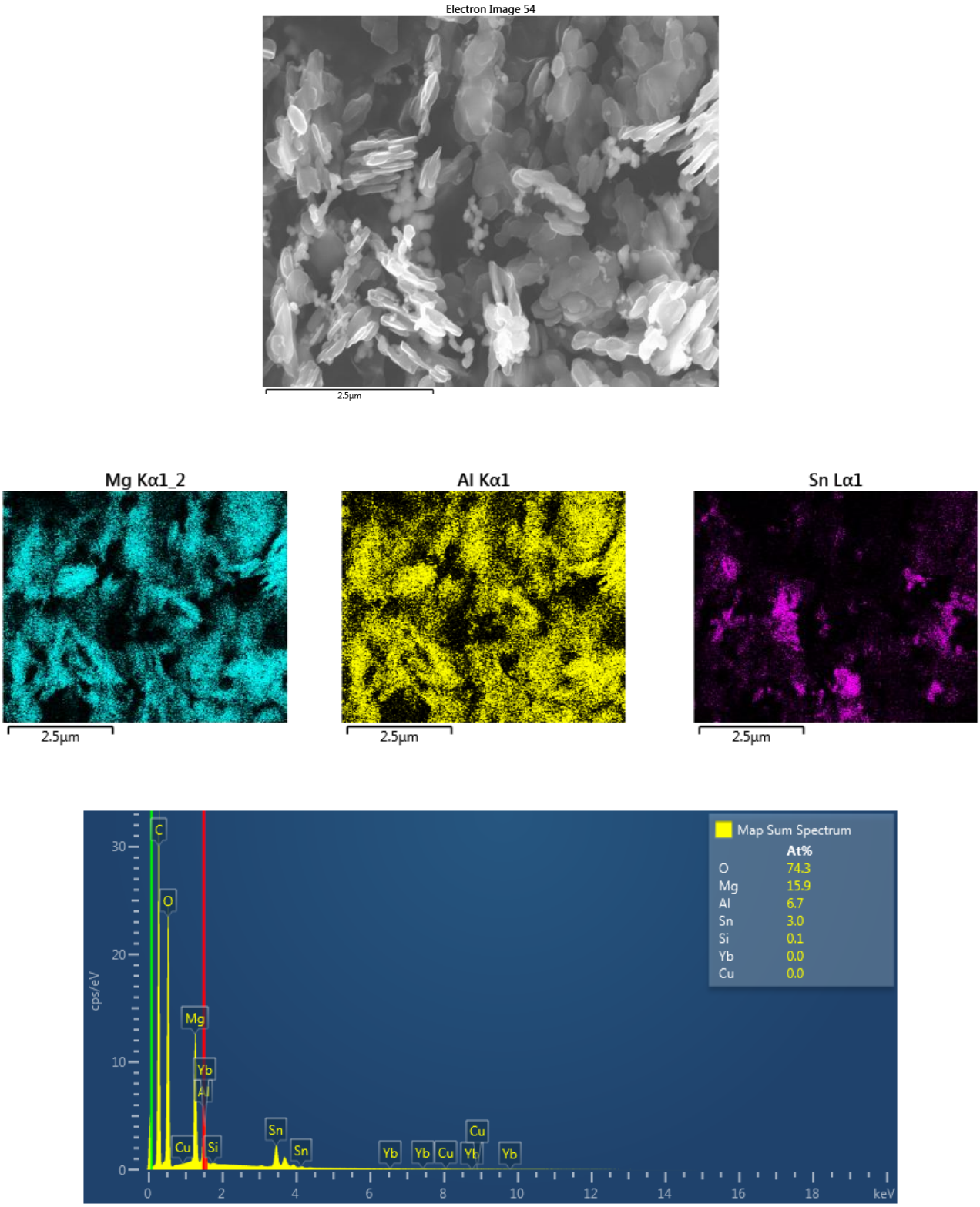

Figure 190: *Mg/Sn* 25 mole% - Carbonate

Titanium

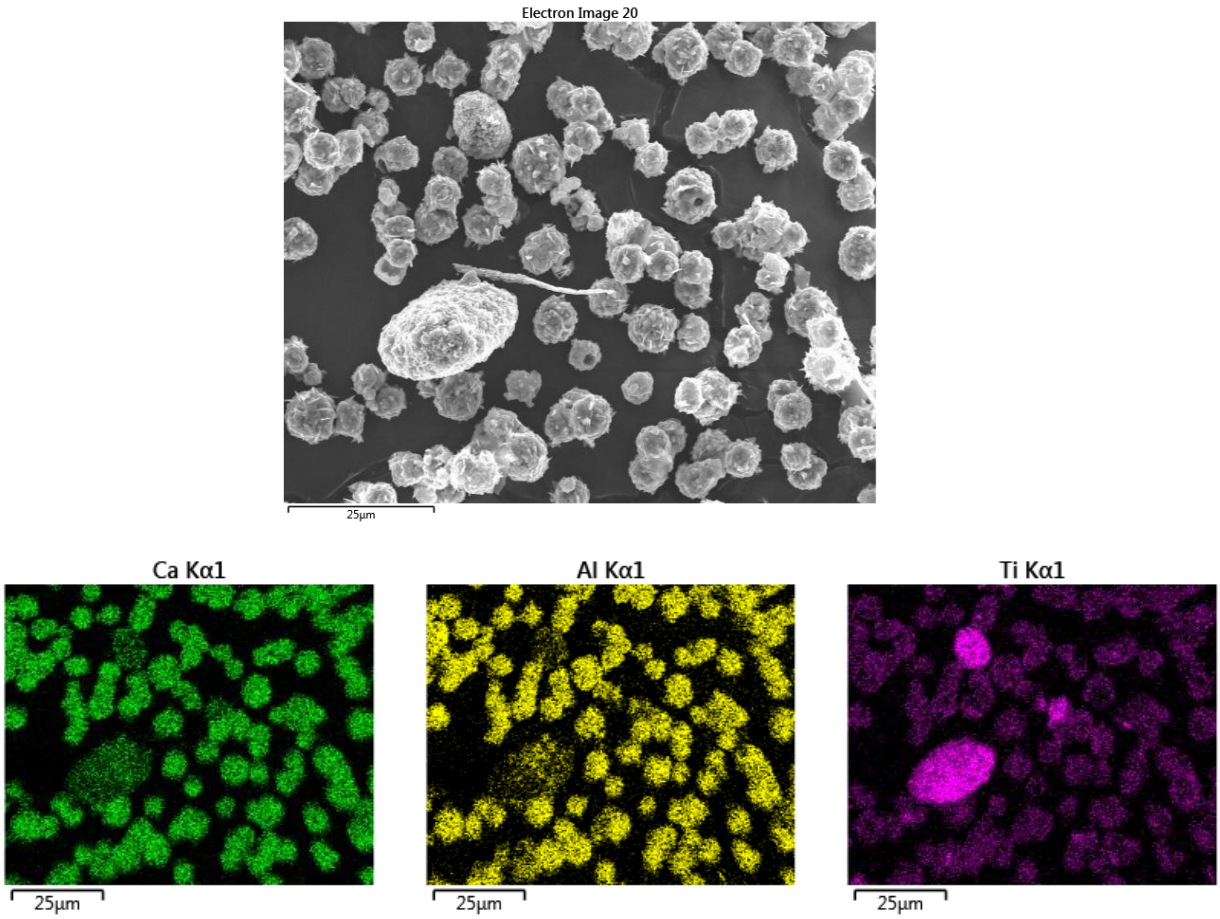

Figure 191: *Ca/Ti* 25 mole% - Inert

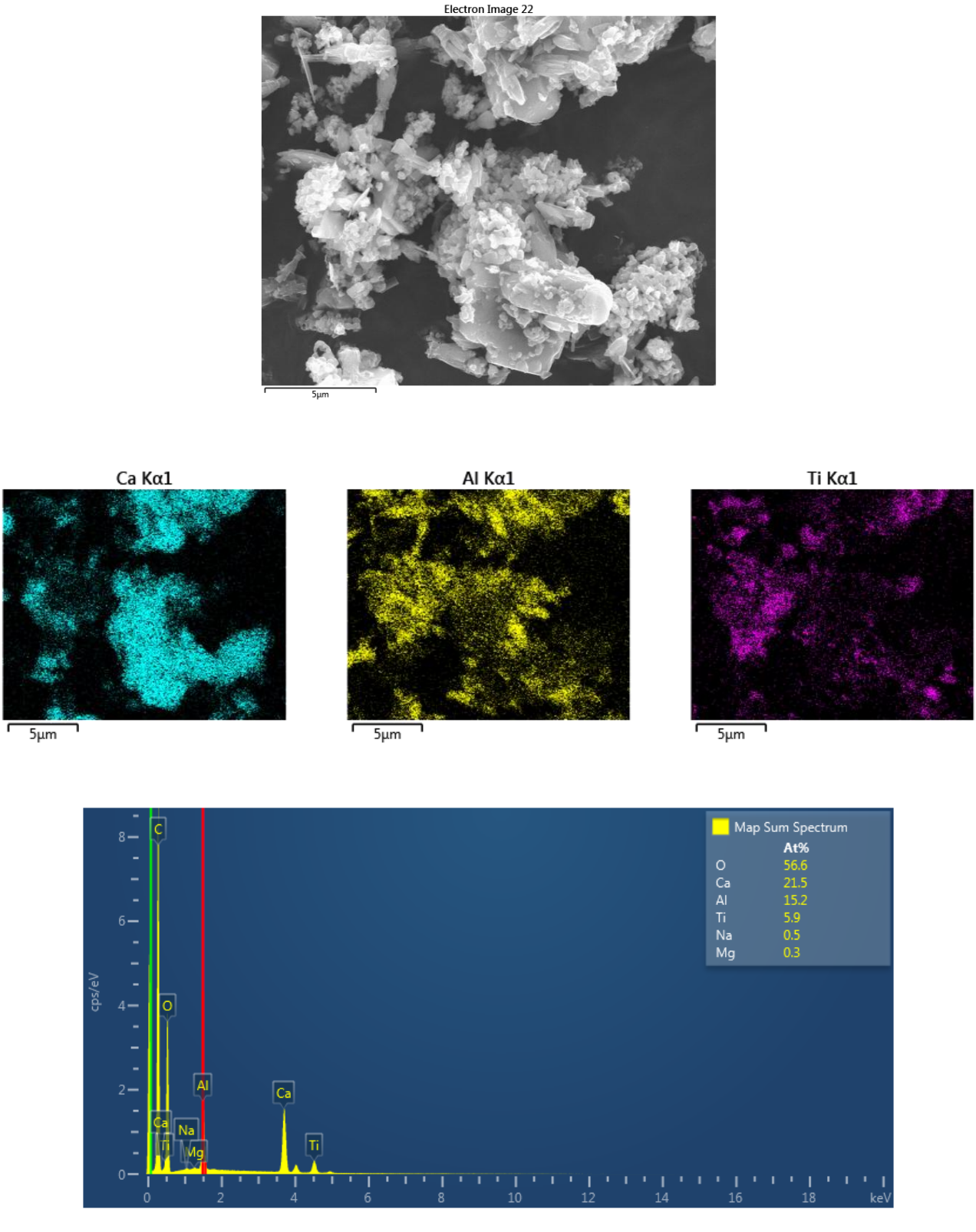

Figure 192: *Ca/Ti* 25 mole% - Carbonate

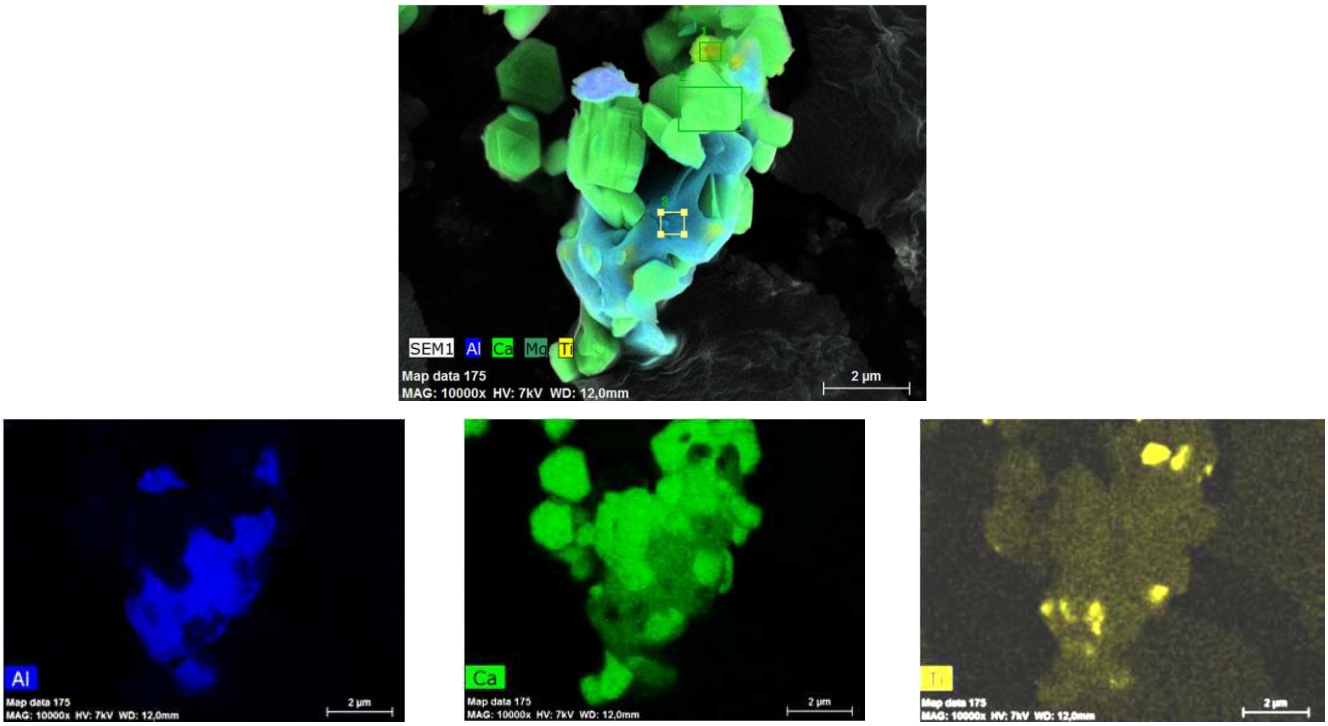

1.

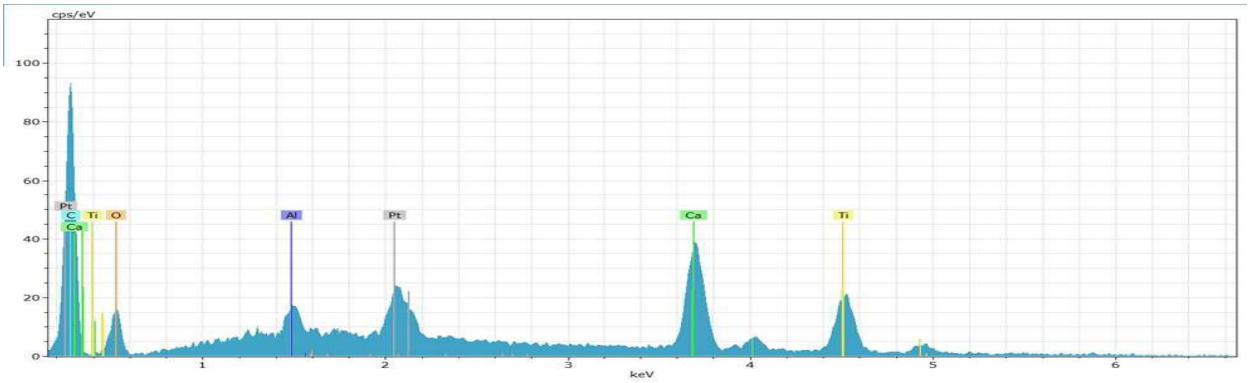

2.

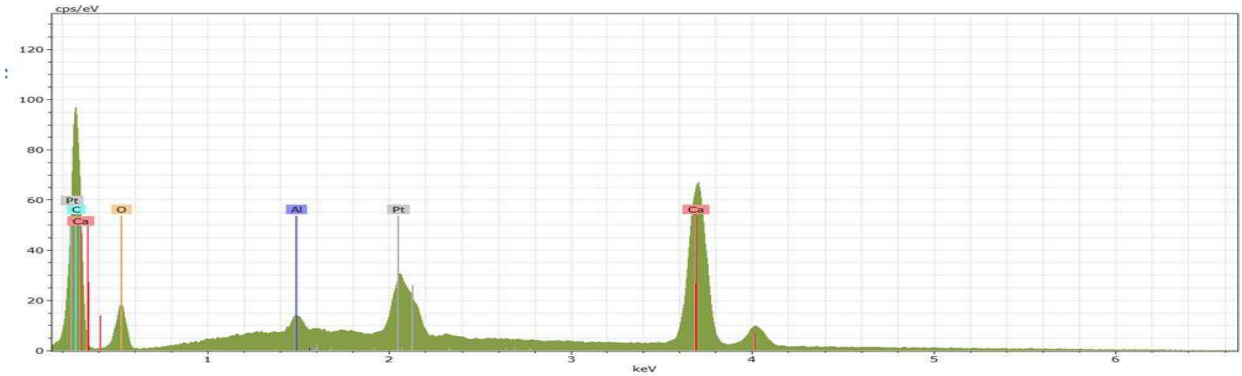

Figure 193: *Ca/Ti* 8.3 mole% - Inert

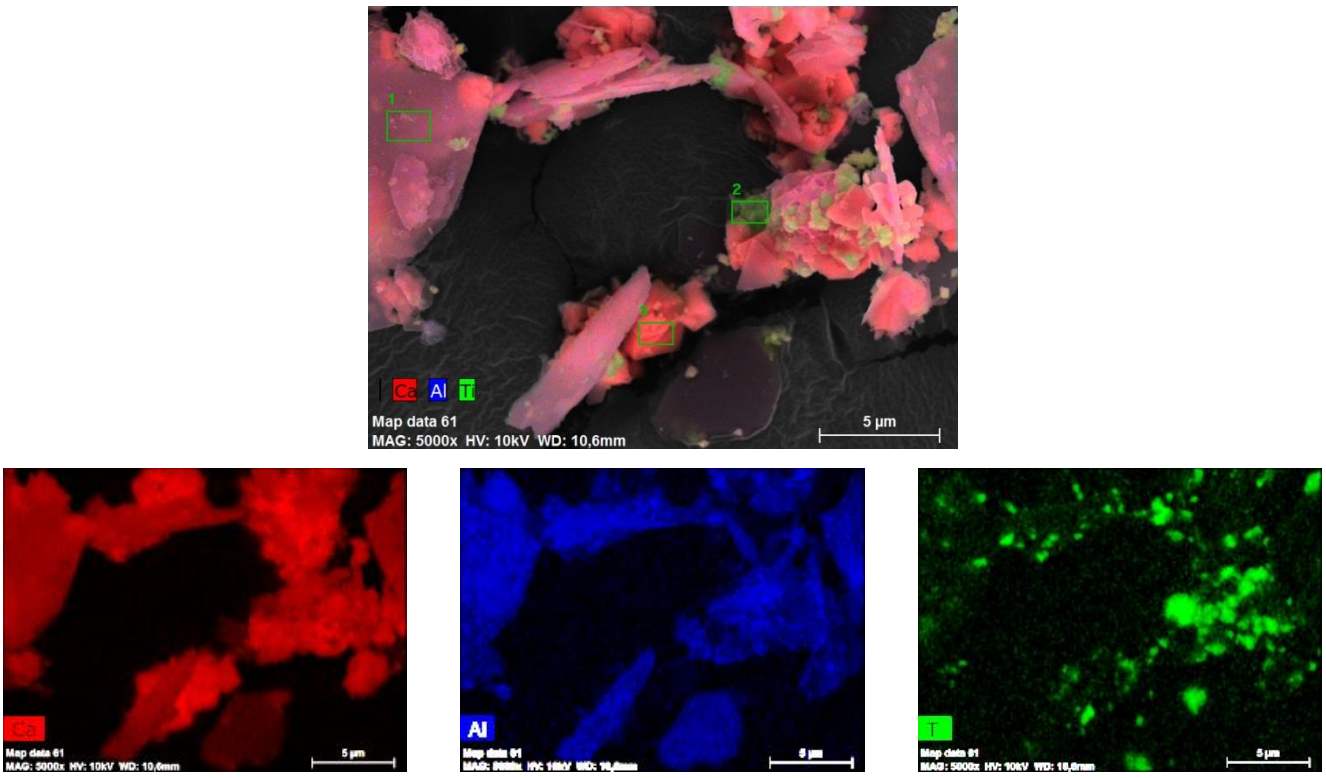

1.

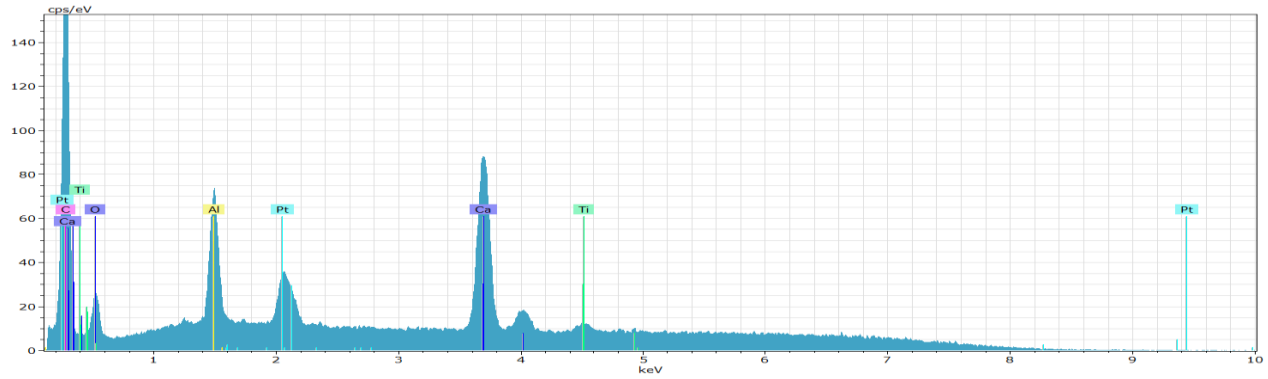

2.

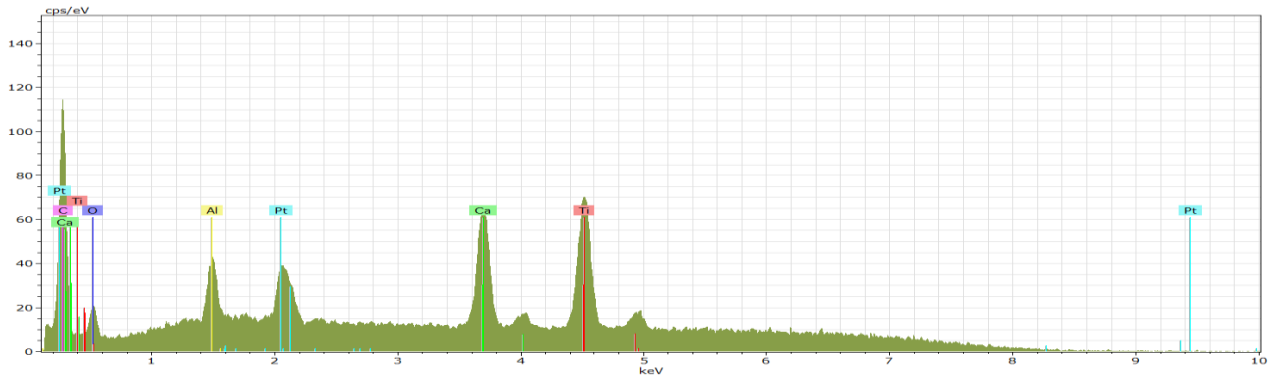

Figure 194: *Ca/Ti* 8.3 mole% - Carbonate

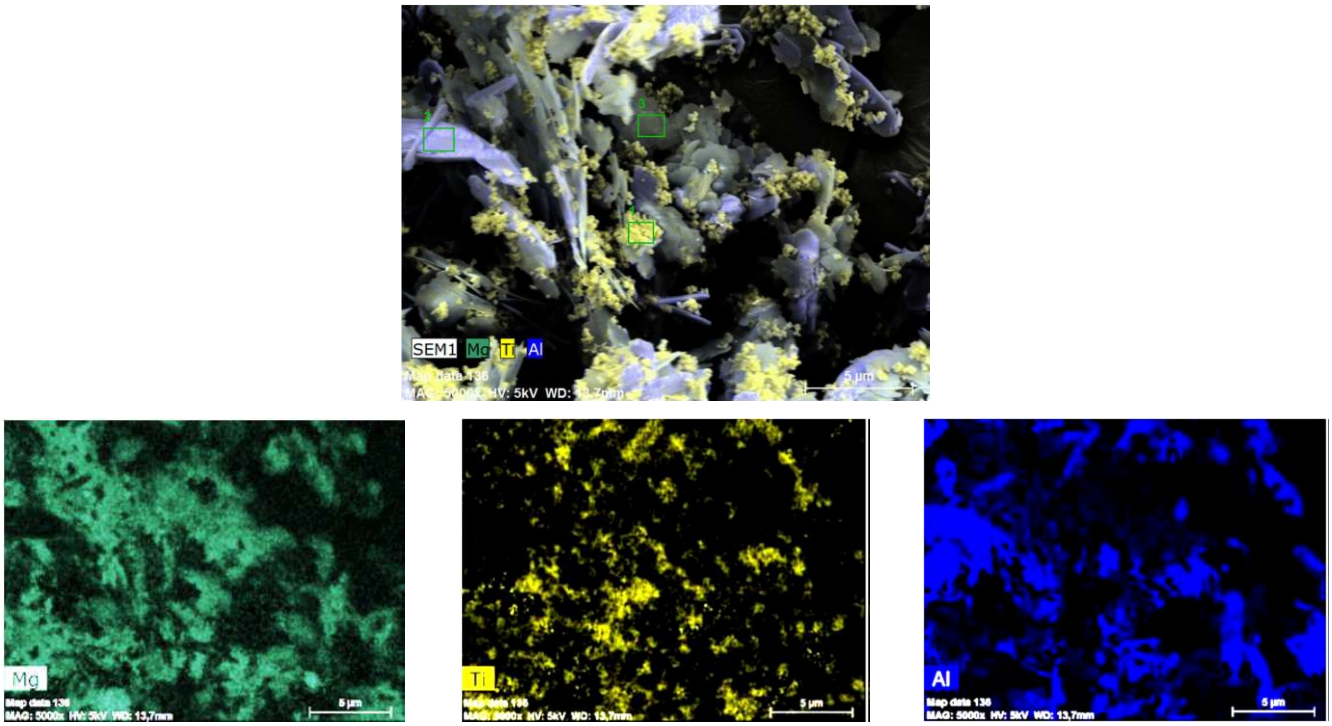

1.

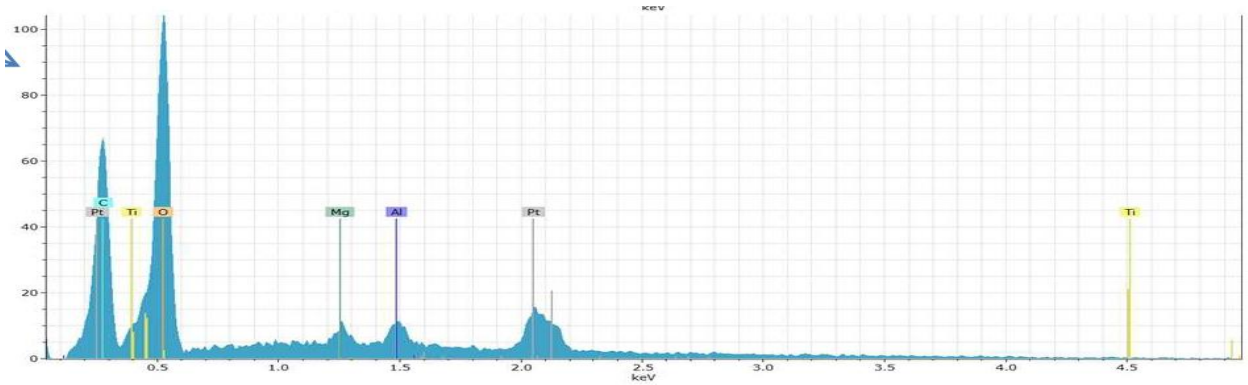

2.

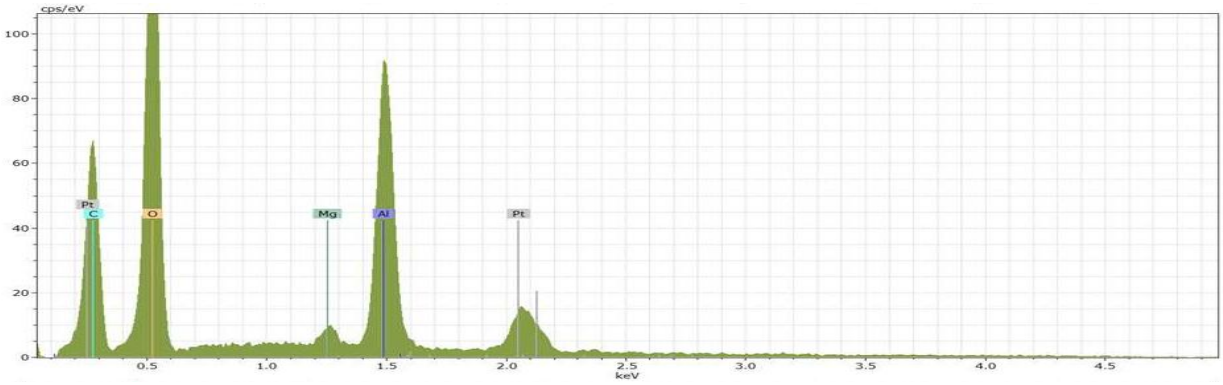

Figure 195: *Mg/Ti* 25 mole% - Inert

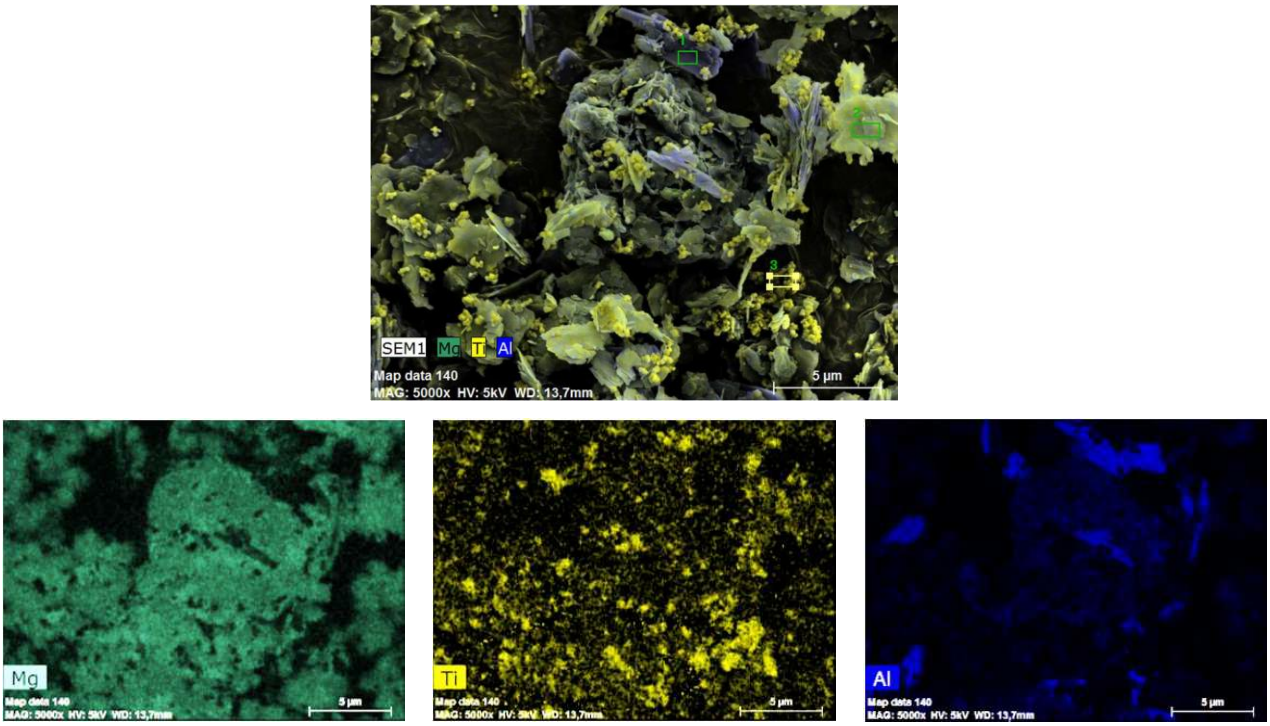

1.

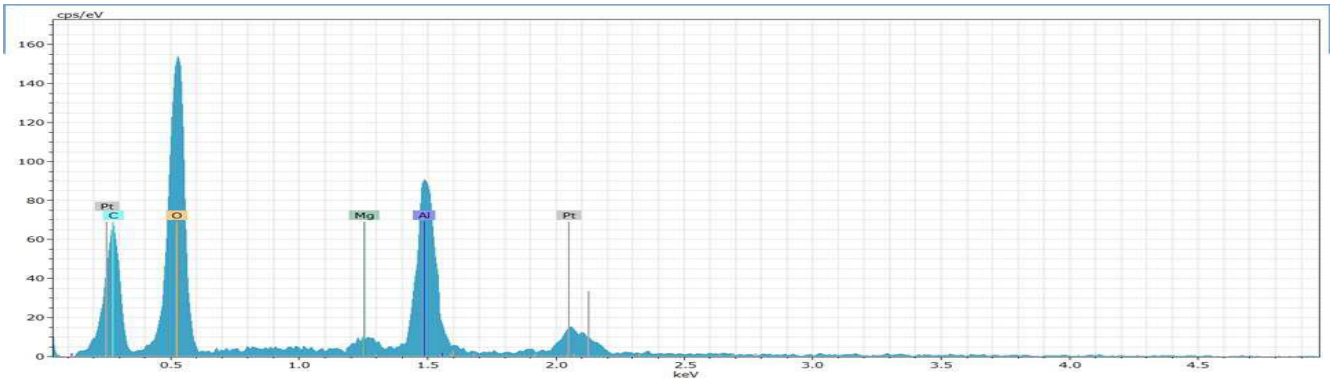

2.

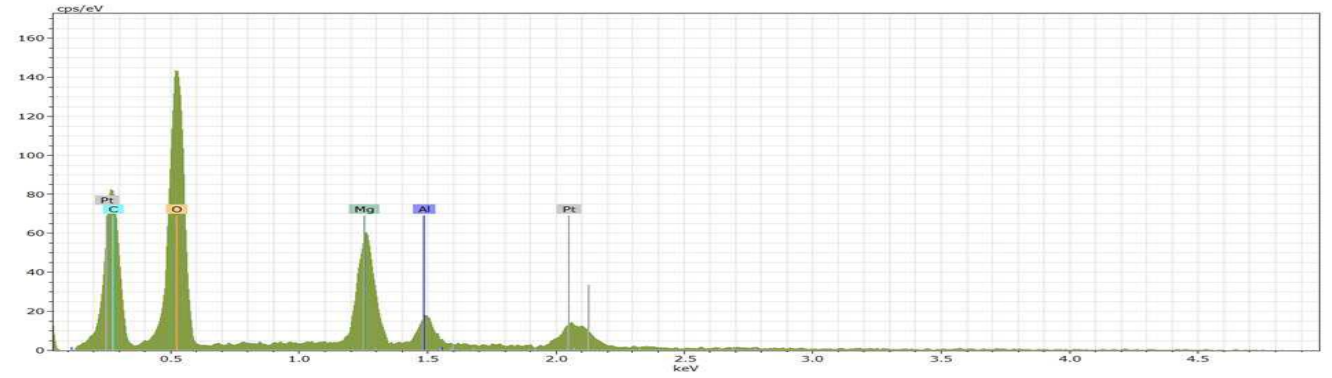

Figure 196: *Mg/Ti* 25 mole% - Carbonate

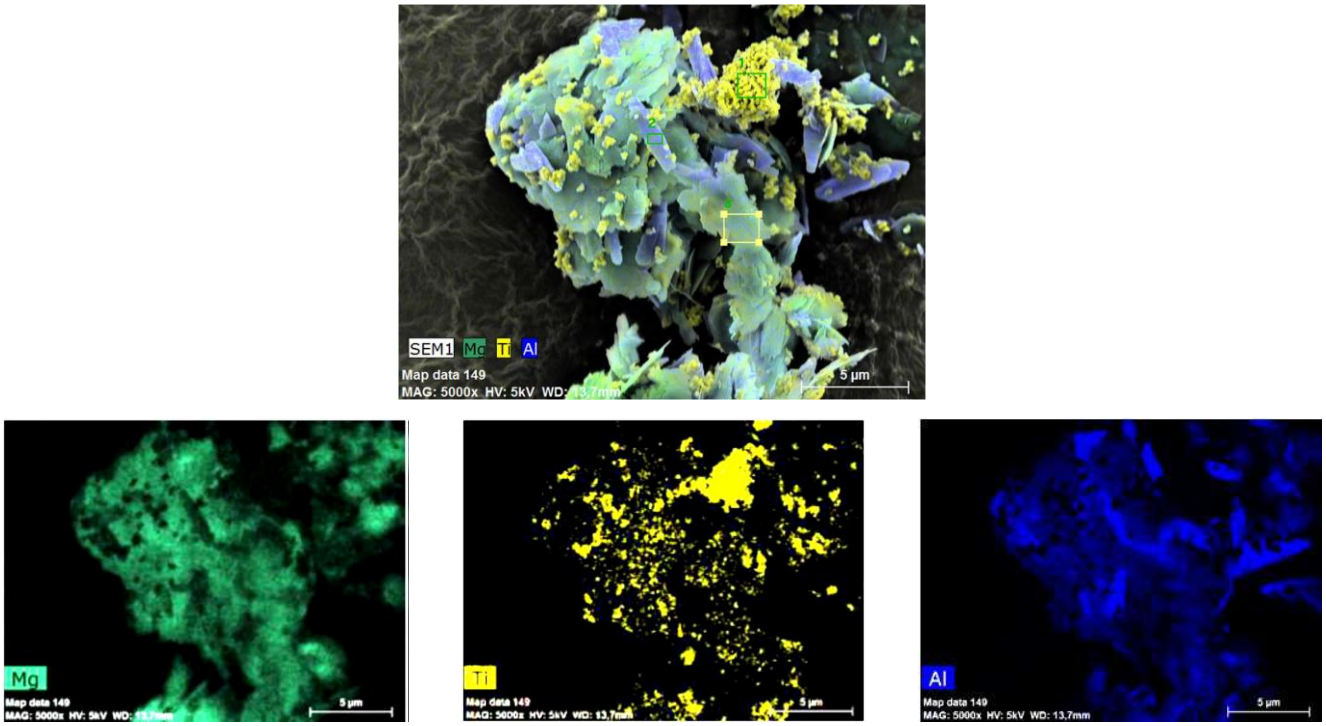

1.

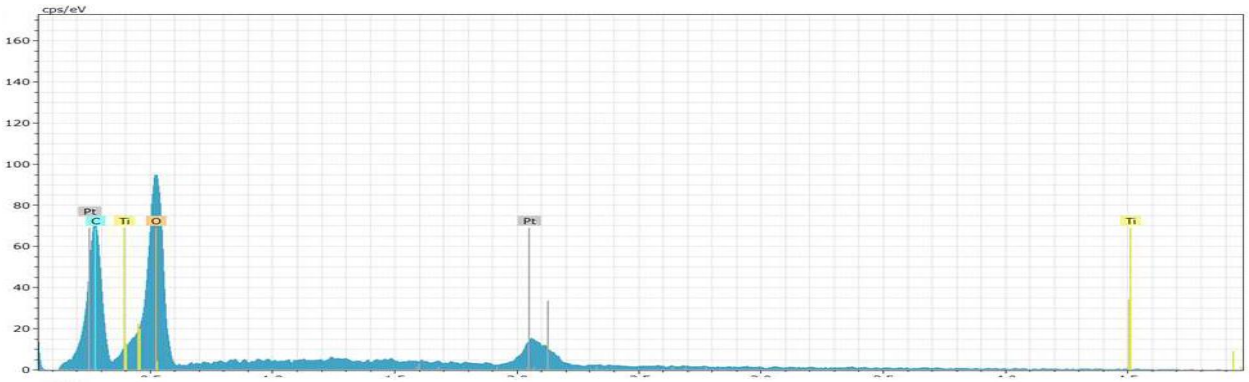

3.

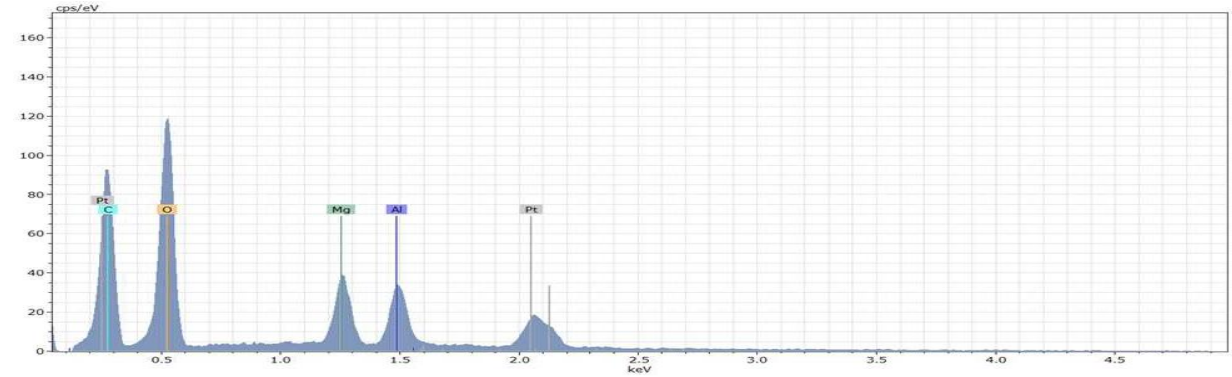

Figure 197: *Mg/Ti* 8.3 mole% - Inert

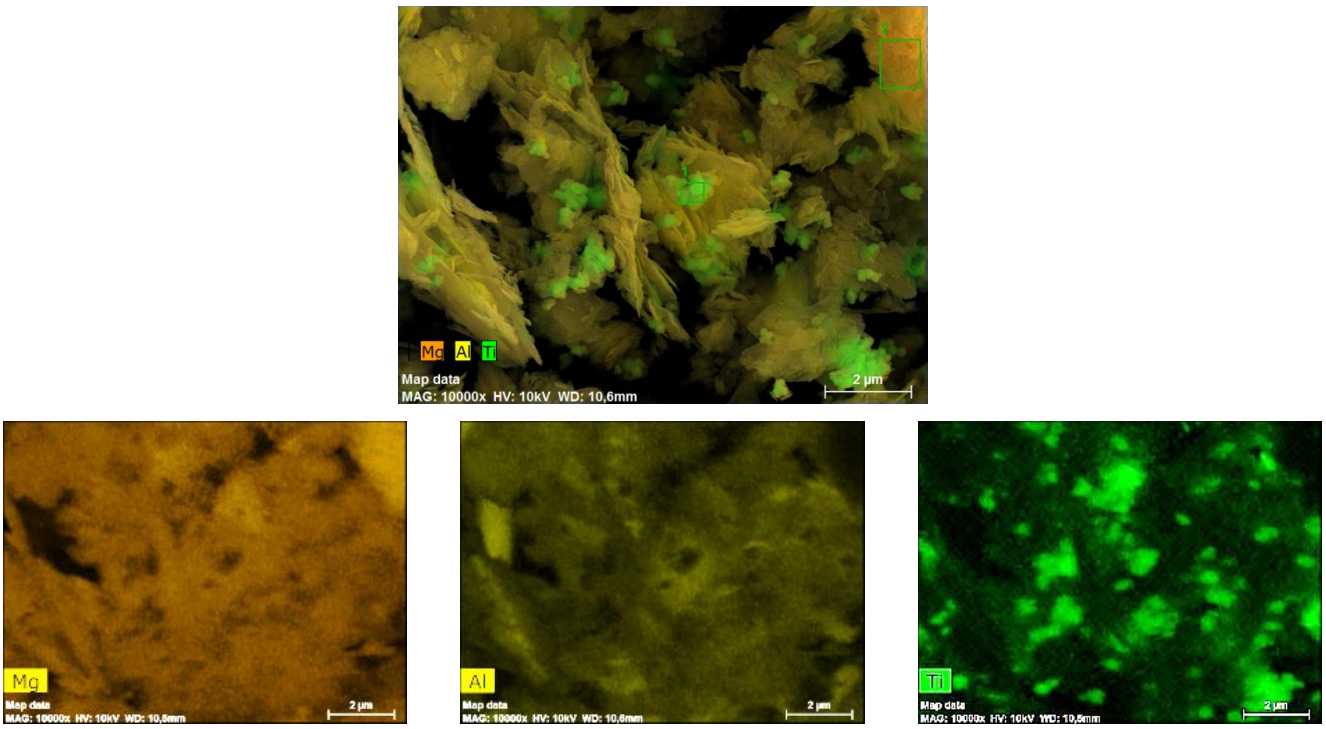

1.

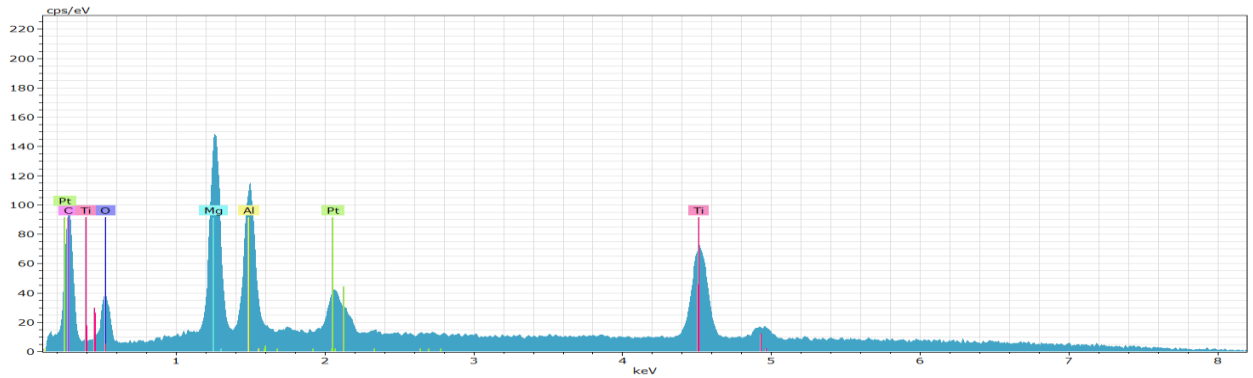

2.

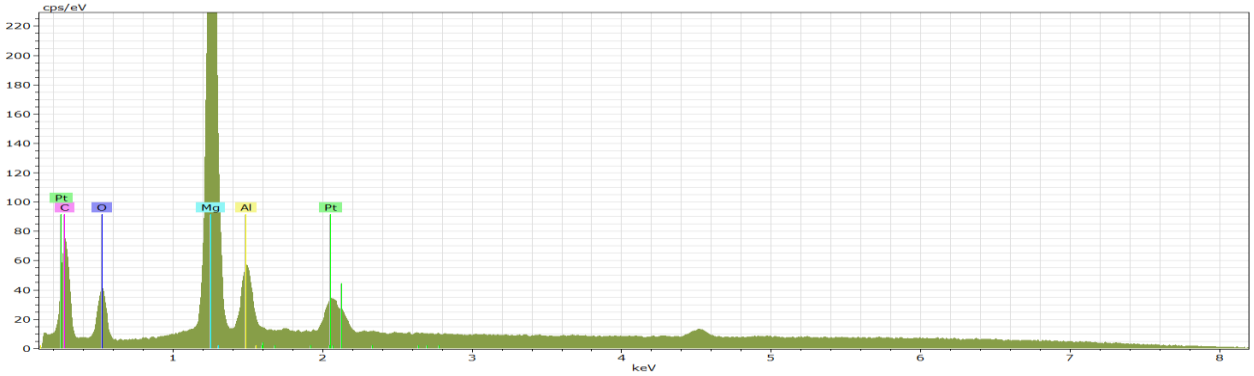

Figure 198: *Mg/Ti* 8.3 mole% - Carbonate

Zinc

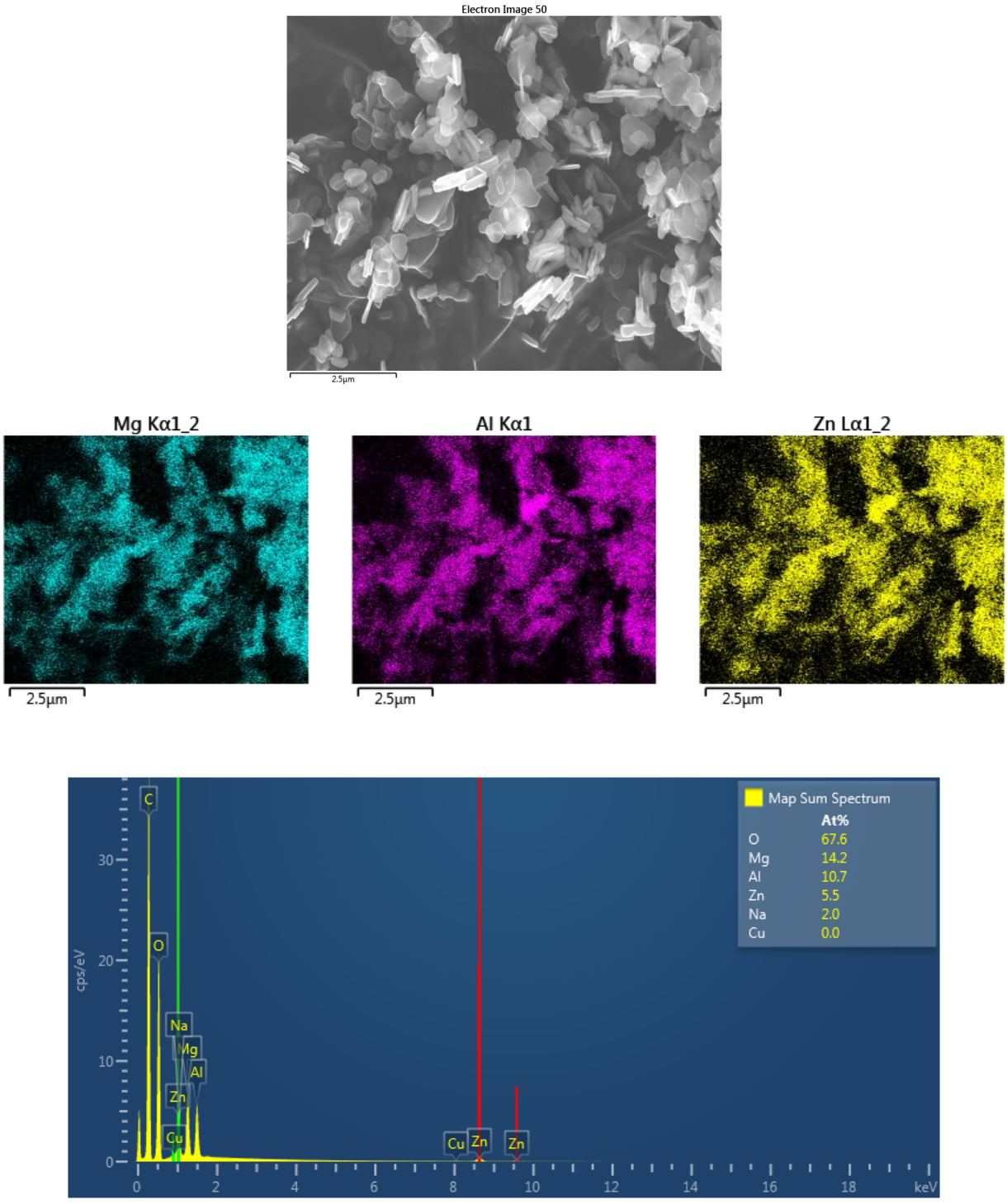

Figure 199: *Mg/Zn* 25 mole% - Carbonate